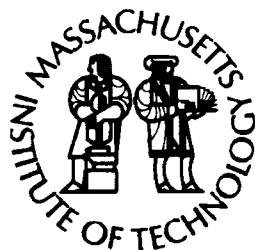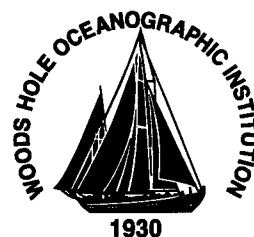MIT/WHOI 97-24

Massachusetts Institute of Technology
Woods Hole Oceanographic Institution

Joint Program in Oceanography/ Applied Ocean Science and Engineering
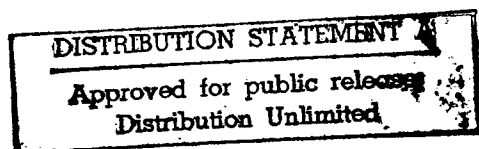
1930

DOCTORAL DISSERTATION

Crustal Structure of Rifted and Convergent Margins:
The U.S. East Coast and Aleutian Margins

by

Daniel Lizarralde

June 1997

DTIC QUALITY INSPECTED

19980505 057

MIT/WHOI

97-24

Crustal Structure of Rifted and Convergent Margins:
The U.S. East Coast and Aleutian Margins

by

Daniel Lizarralde

Massachusetts Institute of Technology
Cambridge, Massachusetts 02139

and

Woods Hole Oceanographic Institution
Woods Hole, Massachusetts 02543

June 1997

DOCTORAL DISSERTATION
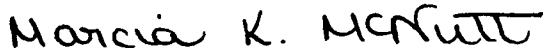
Approved for publication; distribution unlimited.

Approved for Distribution:
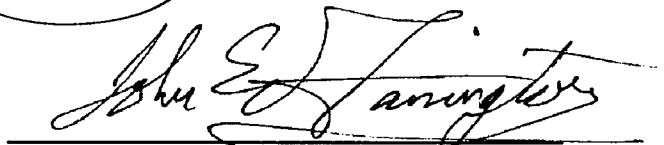
_____
William B. Curry, Chair
Department of Geology and Geophysics

_____
Marcia K. McNutt
MIT Director of Joint Program

_____
John W. Farrington
WHOI Dean of Graduate Studies

Crustal Structure of Rifted and Convergent Margins: The U.S. East Coast and Aleutian Margins

by

Daniel Lizarralde

B. S., Virginia Polytechnical Institite and State University, 1985.
M. S., Texas A&M University, 1990.
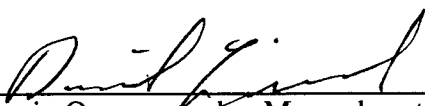
SUBMITTED IN PARTIAL FULFILLMENT OF THE REQUIREMENTS FOR THE

DEGREE OF DOCTOR OF PHILOSOPHY
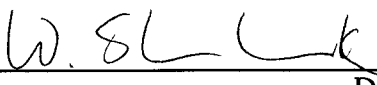
at the
MASSACHUSETTS INSTITUTE OF TECHNOLOGY
and the
WOODS HOLE OCEANOGRAPHIC INSTITUTION

May, 1997

Signature of Author_____
Joint Program in Oceanography, Massachusetts Institute of Technology and
Woods Hole Oceanographic Institution, April 1997

Certified by_____
Dr. W. Steven Holbrook, Thesis Supervisor

Accepted by_____
Deborah K. Smith, Chair, Joint Committee for Marine Geology and Geophysics,
Massachusetts Institute of Technology and Woods Hole Oceanographic Institution

3

Crustal Structure of Rifted and Convergent Margins: The U.S. East Coast and Aleutian Margins

by

Daniel Lizarralde

Submitted to the Department of Earth, Atmospheric, and Planetary Sciences
Massachusetts Institute of Technology
and
Department of Geology and Geophysics
Woods Hole Oceanographic Institution

May, 1997

in partial fulfillment of the requirements
for the degree of Doctor of Philosophy

Abstract

Many of the most important processes that create and modify continental crust occur at continental margins, but recently has the scientific community acquired the necessary intrumentation to image crustal structure across margins in detail. In this thesis we investigate the crustal structure across the U.S. East Coast rifted margin and the convergent margin of southwestern Alaska using modern, deep-penetrating marine seismic reflection/refraction data.

We consider U.S. East Coast margin transects along the shelf offshore Georgia and across the mid-Atlantic margin near Chesapeak bay. Results by other workers, based on data from these transects, have shown that voluminous volcanism accompanied formation of the rifted margin during continental breakup. Results presented in this thesis constrain the landward extent of rift-related magmatic emplacement. We find that magmatic intrusion and underplating of pre-existing continental crust occurs primarily in extended crust and that crustal extension is focused in a 75-km-wide region beneath the shelf and slope. The crust thinned by 50 to 80% within this interval and then seafloor spreading began with an unusually large volume of igneous crust production. The initial volcanic extrusives were emplaced subaerially and are now present beneath the sediments in a thick seaward-dipping wedge. We use post-stack depth migration to image this wedge and use the resulting image to consider the early subsidence of the margin. The geometry of the subaerially extruded rift volcanics sugggest that the margin subsided rapidly once volncanism began. We infer from the subsidence, the along-margin distribution of magmatic material, and the across-margin localization of magmatic emplacement and deformation that the U.S. East Coast rift volcanics had an anomalously-hot mantle source whose distribution beneath the lithosphere prior to rifting was long (the length of the margin) but not deep. We speculate that the distribution of this material was controlled by topography at the base of the lithosphere inherited from the Paleozoic collision of North America and Africa.

Our analysis of the southwestern Alaska convergent margin is based on data from the 1994 Aleutian seismic experiment. The crust of most of Alaska has been built through terrane accretion and arc magmatism, and this experiment was conducted to study the evolution of continental crust through these processes. We consider transects across the westernmost Alaska Peninsula margin, where subduction is occurring beneath proto-continental crust composed of oceanic-arc terranes accreted in the Cretaceous, and across Bristol Bay in the back arc region where the crust has undergone a number of geologic events since accretion. Across the Peninsula, we find that the velocity structure of the accreted terranes differs little from that of the Cenozoic Aleutian oceanic-arc crust west of the Peninsula determined along another transect of this experiment. The accreted oceanic-arc terranes are considerably more mafic than continental crust and the process of accretion has apparently not modified the bulk composition of these terranes toward that of average continental crust. It is possible that Cenozoic arc magmatism has been more felsic in composition than that which formed the accreted terranes and the Aleutian oceanic arc to the west, and that these magmas have been emplaced primarily within the crust inboard of the accreted terranes which lie south of the currently active arc. The geology of the Bristol Bay region suggests that the crustal components here had an origin similar to that of the Alaska Peninsula margin — that is, accreted terranes. We find, however, that the crust beneath Bristol Bay has a typically continental velocity structure. If this crust originally had a structure similar to the Alaska Peninsula margin, then at least two processes must have occured to affect the transformation to its current structure: crustal thickening and removal of the mafic lower crust. The geologic events that have affected this region since accretion are consistent with such and evolution.

Thesis Supervisor: W. Steven Holbrook
                      Associate Scientist
                      Woods Hole Oceanographic Institution

Acknowledgements

"Day. Wheelbarrow sun over arch of bridge."
Ulysses, James Joyce

The ocean-bottom seismology group at WHOI grew from the leadership and vision of Mike Purdy. I am personally indebted to Mike for sitting me down and carefully explaining to me why I should leave Texas and for sharing with me his clarivoyant vision of Steve Holbrook's future, whom Mike had brought to WHOI to deploy instruments across continental margins. Watching the evoluion of Steve's career has been both educational and inspirational, and working with Steve has been pure fun. The relationship that has developed between us has been deeply rewarding, and I have continually drawn motivation from his positive and enthusiastic view of science and of life.

This thesis is based on data, and the data would not exist were it not for the hard work and professionalism of Beecher Wooding, Ken Peal, Dave DuBois, Jim Dolan, and Vee Ann Cross. They provided me with data and with proper examples of how to swagger around a ship. The contributions of Dave and Jim's presence in the lab can not be overestimed. They are the glue.

Much of my education has come from conversations with John Collins, Graham Kent, Steve Swift, Alan Chave, Greg Hirth, Uri ten Brink, Peter Kelemen, Rafi Katzman and Garret Ito. I thank Alan in particular for letting me work on the HAW-1 data. This paper is not part of the thesis, but working on it with Alan and Greg was a lot of fun and I learned volumes from both of them. I also thank Debbie Hutchinson for letting me take the con for a couple of weeks on the *R/V Hatteras* and Tommy O'Brian for watching my back out there.

More than anything else, my time in the Joint Program has been marked by amazing friendships. Parties, dinners, beach cookouts, barbecues, fishing, bachelor send offs, and on and on — these are the basic stuff of student life at WHOI. I will be forever grateful for the friends I have shared this experience with, Gary Jaraslow, Javier Escartín, Gorka Sancho, Rob Evans, Dan Torres, Jun Korenaga, Chris Weidman, Joe Lacasce, Cecilie Mauritzen, Gail Christensen, Emilie Hooft, Chris Bradlee, Rafi Katzman, Bob Greaves, Garrett Ito, Cecily Wolfe, Carl and Marj Freidrich, Cathleen and Miguel Goné. I wouldn't have thought it possible to make this many close friends. My impeccably calm demeanor during the last months of thesis construction has been due to the influence of my bandmates Rob Evans, Dan Torres, Greg Hirth, Glen "the voice", and Gorga Sancho — unquestionably the finest group of musicians I have ever played with. My office mates Gail Christensen, Chris Bradley, and Bob Greaves have also provided me with much appreciated support.

I'll borrow Joyce's line for my one allotted metaphor and use it to acknowledge my wife, Hege. Completing a thesis is an excercise in determination and focus, and she has supplied me with my full share of both, shoving me up the steep front side of this bridge and keeping me from careening down the slippery slope of the back. At the end of this long day I am in awe at her heroic efforts. I am looking forward to emptying out my load of seismic sections and GMT plots and wheeling her around the streets and gardens of Copenhagen.

TABLE OF CONTENTS

Chapter 1
Introduction: Crustal Processes at Continental Margins

This thesis is concerned with the crustal structure of continental margins and the processes that occur there. Continental margins exist at the transition between the two main crustal types covering the earth, continental and oceanic crust. Continental margins are of scientific interest because many of the processes that create and modify continental crust occur there. Margins are also societally relevant, as global petroleum reserves and hazardous tectonic activity are concentrated at continental margins. Only recently, however, has the scientific community acquired the necessary instrumentation — including arrays of ocean bottom seismometers and powerful and economical acoustic sources — to image crustal structure across continental margins in detail. In this thesis we capitalize on this development to investigate crustal structure across the continental margins of the U.S. East Coast and southwestern Alaska using modern, deep-penetrating seismic reflection/refraction data.

An understanding of the formation and evolution of the earth's crust is central to a complete understanding of the dynamics of the earth as a whole, as the existence of the crust is a direct result of deeper mantle processes and because the crust, though volumetrically small, represents an important chemical reservoir within the global geochemical system. The formation of oceanic crust is generally well understood and involves uniform mechanisms that are reflected in the global uniformity of oceanic-crustal structure and composition. The formation of continental crust, in contrast, involves a plethora of geologic processes operating episodically over billions of years. In fact, the term *evolution* is probably more appropriate than *formation* when characterizing the genesis of continental crust. The formation (origin) and composition of the components of

continental crust may differ greatly (magmatic arcs and sedimentary fans, for example), but the tectonic and magmatic processes that amalgamate these components tend to drive continental crust toward a steady-state composition and thickness [e.g. *Christensen and Mooney*, 1995].

The continents have grown through a series of distinct accretionary events since the Proterozoic [*Bickford*, 1988]. The Wilson cycle paradigm explains the growth of continents through repeated opening and closing of ocean basins and provides a convenient framework within which to consider fundamental processes of crustal evolution. The Wilson cycle involves divergent and convergent phases. A divergent phase is initiated through continental rifting and proceeds to seafloor spreading, leaving behind conjugate rifted margins and an ocean basin floored by rift/drift igneous rocks and blanketed by terrigenous and pelagic sediments. A convergent phase begins with the initiation of subduction within the ocean basin or along a continental margin and results in the formation of a magmatic arc. As convergence proceeds, basin-filling sediments, oceanic arcs, and oceanic plateaus are piled up and accreted at the continental margin. The cycle ends when the ocean basin closes, continents collide and accreted material is further amalgamated through the processes of compressional tectonics.

An understanding of continental crustal evolution requires an understanding of each of the fundamental crustal processes operating during the Wilson cycle, including continental rifting, arc magmatism, terrane accretion and orogeny. Basic data required for this understanding is information about the crustal structure and composition of continental margins, where many of these processes operate. This is the motivation behind the research presented in this thesis, where we consider the crustal structure across the rifted margin of the U.S. East Coast and the convergent margin of southern Alaska with the goal of better understanding the fundamental processes of crustal evolution.

The U.S. East Coast Margin

The processes of continental breakup include lithospheric extension, decompression melting, the initiation of seafloor spreading, and lithospheric subsidence. These processes may be manifest in numerous ways depending on the initial rheologic and thermal conditions of the lithospheric and aesthenospheric mantle. Slow extension of homogeneous lithosphere over normal temperature mantle, for instance, will result in a rifted margin structure characterized by progressive thinning of continental crust with little or no addition of volcanic material until rifting is complete and seafloor spreading initiated [*Bown and White*, 1995]. In contrast, a margin formed through rapid extension of lithosphere with a pre-existing weakness over hot aesthenospheric mantle may result in voluminous igneous crustal additions at the initiation of and during lithospheric extension [*White and McKenzie*, 1989]. These two end members are commonly referred to as *non-volcanic* and *volcanic* rifted margins, and their global distribution and details of their formation are only now beginning to be understood. Volcanic rifted margins are particularly intriguing because their formation may represent a volumetrically significant crustal forming process and because the genesis of the voluminous volcanics found on these margins challenges our notions of mantle dynamics [*Coffin and Eldholm*, 1994].

Chapters 2 and 3 address aspects of the U.S. East Coast rifted margin crustal structure. These chapters are based on the analysis of seismic data from two seminal experiments across the Carolina Trough [*Austin et al.*, 1990] and the mid-Atlantic margin [*Sheridan et al.*, 1993]. These seismic experiments were the first across this margin to employ large arrays of ocean-bottom seismic instruments to record wide-angle arrivals from tuned, large-volume airgun arrays. These experiments were proposed primarily to find evidence of remnant convergent structures, but what they revealed was evidence for a voluminous episode of volcanism accompanying Mesozoic continental breakup [*Holbrook et al.*, 1994a, 1994b]. The U.S. East Coast margin was found to be a volcanic rifted margin

[*Holbrook and Kelemen*, 1993] with all the characteristics of the volcanic rifted margins of the North Atlantic [e.g. *Eldholm and Grue*, 1994]. The North Atlantic rift volcanism has been attributed to proximity to the Iceland plume [*White and McKenzie*, 1989]. The U.S. East Coast rift volcanics lack an obvious plume source, however, and the origin of this material remains and important and unsolved geodynamic problem.

We make several contributions to the understanding of U.S. East Coast margin rift and magmatic history in Chapters 2 and 3. In both chapters we consider data that constrain the landward extent of rift-related magmatic emplacement. We find that magmatic underplating and intrusion are localized near the hinge zone of the margin, which marks the onset of significant extensional deformation. We also show that crustal thinning is localized toward the hinge zone. In Chapter 3 we consider the early subsidence of the margin and find that subsidence during the extrusion of the rift volcanics was quite rapid. We infer from the subsidence, the along-margin distribution of magmatic material, and the across-margin localization of magmatic emplacement and deformation that the U.S. East Coast rift volcanics had an anomalously hot mantle source whose distribution beneath the lithosphere prior to rifting was long (the length of the margin) but not particularly deep. We speculate that the distribution of this material was controlled by topography at the base of the lithosphere inherited during the Paleozoic collision of North America and Africa.

The southern Alaska margin

The processes that have been most important to continental growth since the Proterozoic, including terrane accretion and arc magmatism, occur at convergent margins. There is ample geologic evidence that continents have grown in this manner (e.g., Hamilton, 1981), and the processes are observed to be ongoing today in locations such as the southern Alaska margin. Continental growth though these processes is not well understood, however, and this lack of understanding is evident in the so-called

composition paradox of continental crustal [e.g. *Rudnick*, 1995]. The majority of magmatic and accreted material that has grown the continents since the Phanerozoic consists of the products of mantle melting and includes intra-oceanic arcs, oceanic plateaus, continental arcs and associated sediments. The average composition of mantle melts is mafic (basaltic), while, paradoxically, the bulk composition of continental crust is intermediate (andesitic).

The importance of convergent margins to the evolution of continental crust has not been matched with experimental data to provide detailed characterizations of convergent margin crustal structure. Seismic experiments have been conducted across the south-central Alaskan margin, the Trans-Alaskan Crustal Transect (TACT) [*Fuis et al.*, 1991], and along the accreted arc of the Cascades [*Leaver et al.*, 1984]. While these experiments were successful in delineating large-scale crustal structure, it is difficult to disentangle the processes that have modified the crust along the geologically complex TACT profile, and the Cascades transect provides a view of crustal structure from only beneath the arc.

In Chapters 4 and 5 we engage these problems by delineating the crustal structure of the southwestern Alaska convergent margin. These studies are based on data from the 1994 Aleutian seismic experiment, which was conducted to study the evolution of continental crust through the processes of arc magmatism and terrane accretion. In Chapter 4 we determine the seismic structure beneath the western Alaska Peninsula margin, where subduction is occurring beneath proto-continental crust composed of accreted oceanic terranes. We find that the velocity structure of these terranes differs little from *un*-accreted oceanic-arc terranes and is not consistent with an andesitic (i.e., "continental") bulk crustal composition. In Chapter 5, we determine the velocity structure of the crust in Bristol Bay, whose components likely had an origin similar to that of the Alaska Peninsula margin — that is, accreted arc terranes. Here we find that the crust has a typically continental velocity structure: it is 35–40 km thick, with a "silicic" upper crust (P-velocity 6.0–6.3 km/s), and

a lower crust of velocity 6.8 km/s. Transformation of proto-continental crust (Alaska Peninsula margin) to mature continental crust (Bristol Bay) requires at least two processes: crustal thickening and removal of the mafic (>7.0 km/s) lower crust. Crustal thickening may have occurred during Cretaceous and Tertiary crustal rotation associated with opening of the Arctic Ocean basin. Removal of the mafic lower crust may have occurred either by eclogitization and delamination or by incorporation into the upper mantle as the residue of intracrustal melting. We may thus attribute the evolution of mature continental crust to the geologic events that have affected this region since accretion.

References

Austin, J. A. Jr., P. L. Stoffa, J. D. Phillips, J. Oh, D. S. Sawyer, G. M. Purdy, E. Reiter, and J. Makris, Crustal structure of the southeast Georgia embayment–Carolina trough: Preliminary results of a composite seismic image of a continental suture(?) and a volcanic passive margin, *Geology, 18*, 1023-1027, 1990.

Bown, J.W., and R.S. White, The effect of finite duration extension on melt generation at rifted continental margins, *J. Geophys. Res.*, 100, 18,011–18,029.

Bickford, M.E., The formation of continental crust: Part 1. A review of some principles; Part 2. An application to the Proterozoic evolution of southern North America, *GSA Bull., 100*, 1375-1391, 1988.

Christensen, N.I., and W.D. Mooney, Seismic velocity structure and composition of the continental crust: A global view, *J. Geophys. Res., 100*, 9761-9788, 1995.

Coffin, M. F., and O. Eldholm, Large igneous provinces: crustal structure, dimensions, and external consequences, *Rev. Geophys., 32*, 1-36, 1994.

Eldholm, O., and K. Grue, North Atlantic volcanic margins: Dimensions and production rates, *J. Geophys. Res., 99*, 2955-2968, 1994.

Fuis, G.S., E.L. Ambos, W.D. Mooney, N.I. Christensen, and E. Geist, Crustal structure of accreted terranes in Southern Alaska, Chugach Mountains and Copper River Basin, from seismic refraction results, *J. Geophys. Res., 96*, 4187-4227, 1991.

Hamilton, W., Crustal evolution by arc magmatism, *Philos. Trans. R. Soc. London, 301*, 279–291, 1981.

Holbrook, W. S., and P.B. Kelemen, Large igneous province on the U.S. Atlantic margin and implications for magmatism during continental breakup, *Nature, 364*, 433-436, 1993.

Holbrook, W. S., E. C. Reiter, G. M. Purdy, D. Sawyer, P. L. Stoffa, J. A. Austin Jr., J. Oh, and J. Makris, Deep structure of the U.S. Atlantic continental margin, offshore South Carolina, from coincident ocean bottom and multichannel seismic data, *J. Geophys. Res.*, *99*, 9155-9178, 1994a.

Holbrook, W. S., G. M. Purdy, R. E. Sheridan, L. Glover III, M. Talwani, J. Ewing, and D. Hutchinson, Seismic structure of the U.S. Mid-Atlantic continental margin, *J. Geophys. Res.*, 99, 17,871-17,891, 1994b.

Kay, R.W.., and S.M. Kay, Delamination and delamination magmatism, *Tectonophysics*, 219, 177-189, 1993.

Leaver, D.S., Mooney, W.D., and W.M. Kohler, A seismic refraction study of the Oregon Cascades, *J. Geophys. Res.*, *89*, 3121-3134, 1984.

Nelson, J.D., A unified view of craton evolution motivated by recent deep seismic reflection and refraction results, *Geophys. J. Int.*, *105*, 25-35, 1991.

Rudnick, R.L., Making continental crust, *Nature, 378*, 571–578.

Sheridan, R.E., D.L. Musser, L. Glover III, M. Talwani, J. Ewing, W.S. Holbrook, G.M. Purdy, R. Hawman, and S. Smithson, Deep seismic reflection data of the EDGE U.S. Mid-Atlantic continental margin experiment: Implications for Appalachian sutures, Mesozoic rifting and magmatic underplating, *Geology, 21*, 563-567, 1993.

White, R.S., and D. McKenzie, Magmatism at rift zones: the generation of volcanic continental margins and flood basalts, *J. Geophys. Res.*, *94*, 7685-7729, 1989.

CHAPTER 2

Crustal Structure Across the Brunswick Magnetic Anomaly, Offshore Georgia, From Coincident Ocean-bottom and Multi-channel Seismic Data

Crustal structure across the Brunswick magnetic anomaly, offshore Georgia, from coincident ocean bottom and multi-channel seismic data

Daniel Lizarralde

Massachusetts Institute of Technology/Woods Hole Oceanographic Institution Joint Program in Oceanography, Woods Hole, Massachusetts

W. Steven Holbrook

Department of Geology and Geophysics, Woods Hole Oceanographic Institution, Woods Hole, Massachusetts

Jinyong Oh[1]

University of Texas Institute for Geophysics, Austin

Abstract. We present results from a coincident wide-angle and deep-penetrating, multichannel reflection seismic experiment conducted on the continental shelf of the Southeast Georgia Embayment. Over 5000 air gun shots were recorded by a 6-km-long, towed streamer and six ocean bottom seismic instruments along a ~250-km, north-south profile crossing the Brunswick magnetic anomaly (BMA). These data indicate a transition in seismic properties across the BMA, including higher seismic velocities south of the BMA, particularly in the upper crust (7-15 km depth), and a transition from reflective to transparent crust from north to south. We interpret this transition to indicate an increased mafic content in crust south of the BMA. Magnetic modeling based on our seismic results indicates that the BMA may be explained as an edge effect anomaly of the more mafic upper crust. We suggest that the increased mafic content toward the south is due to rift-related mafic intrusion. An alternative interpretation is discussed in which the seismic transition across the BMA is related to an Alleghanian suture. Athough there is no direct indication in the data for the association of the BMA and an Alleghanian suture along our profile, such an association cannot be ruled out. The southern portion of the profile crosses the margin hinge zone, where we observe seaward dipping reflectors similar to those observed along the northern Blake Plateau Basin and Carolina Trough hinge zones, which have been interpreted as volcanic sequences. Our seismic data include no evidence for very high velocity (>7.0 km/s) mid-crust to lower-crust inboard of the hinge zone such as is observed in the Carolina Trough outboard of the hinge zone. This indicates that the volume of emplaced mafic material changes dramatically across the hinge zone and suggests that rift-related magmatic processes along the margin were highly focused.

Introduction

In this paper we discuss the analysis of wide-angle and deep-penetrating, multichannel reflection seismic (MCS) data recorded along a 250-km, north-south transect on the continental shelf offshore South Carolina and Georgia. These data were acquired as part of a larger experiment conducted by the University of Texas Institute for Geophysics and the Woods Hole Oceanographic Institution designed to study the crustal structure across the continental margin and how this structure relates to prominent potential field anomaly trends along the margin [*Austin et al.*, 1990; *Oh et al.*, 1991] (Figure 1). A primary focus of this

experiment was to understand the source of the Brunswick magnetic anomaly.

The Brunswick magnetic anomaly (BMA) extends in an arcuate path from southern Alabama through southern Georgia and then swings northeastward offshore where it tracks inboard of the hinge zone as far as Cape Hatteras (Figure 1). The source of the BMA has been a subject of debate. One interpretation is that the BMA marks the Alleghanian suture of two terranes along which rift-related mafic magmas were emplaced in the early Mesozoic [*McBride and Nelson*, 1988; *Thomas et al.*, 1989; *McBride and Nelson*, 1991]. Results from margin-perpendicular profiles of the seismic experiment mentioned above suggest that along the Carolina Trough and northern Blake Plateau hinge zones the BMA is caused by intruded and extruded mafic material associated with rifting of the margin and that, along these hinge zones, there is no clear association of a Paleozoic suture and the BMA [*Oh et al.*, 1991; *Holbrook et al.*, 1994]. The seismic data discussed below place constraints on the source of the BMA as it extends across the shelf. In addition, these data place constraints on the extent to which rift-related

---

[1]Now at Korean Institute of Geology, Mining and Minerals, Taejon, South Korea

LIZARRALDE ET AL.: COASTAL BRUNSWICK MAGNETIC ANOMALY CRUST
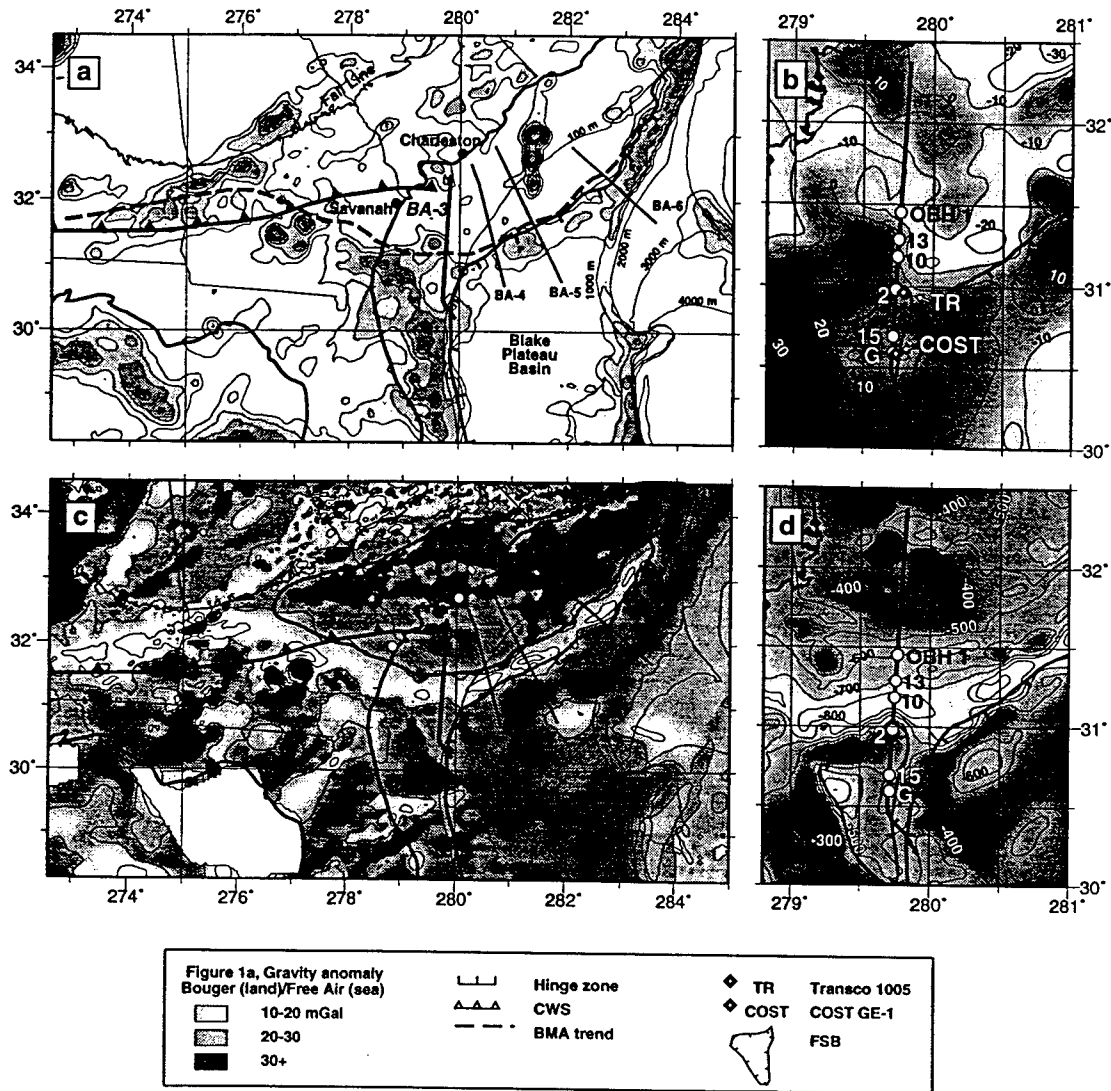
Figure 1. (a) Location and positive gravity anomaly map showing locations of BA seismic lines and Bouguer (land)/free-air (sea) gravity anomaly values of 10 mGal or more. Gravity data are from the gridded, 2.5 arc minute Decade of North American Geology (DNAG) [1987a] compilation. Also shown are bathymetric contours, and trends of the hinge zone [*Uchupi et al.*, 1984], Brunswick magnetic anomaly (BMA), Suwannee-Wiggins suture (CWS) as inferred by *Chowns and Williams* [1983], and the Fall Line. See legend for symbols. (b) Location and free-air gravity anomaly map showing trend of line BA-3, location of ocean bottom instruments, the COST GE-1 (Cost) and Transco TR 1005-1 (TR) wells, hinge zone, and approximate boundaries of the Florida shelf basin (FSB) [*Uchupi et al.*, 1984]. The gravity data were interpolated and gridded from a 10-mGal contour map [*Ewing*, 1984]. (c) Magnetic anomaly map with same features as in Figure 1a and the outline of the Brunswick magnetic terrane. Magnetic data are from DNAG [1987b]. (d) Magnetic anomaly map with same features as in Figure 1b. Magnetic data were interpolated and gridded from a 50-nT contour map [*Heirtzler and Cande*, 1984].

magmatic processes along the margin hinge zone may have extended onto the shelf. We begin with a brief review of the relevant regional tectonic terranes that have been identified from geological and geophysical data. We then describe our analyses of the MCS and wide-angle seismic data and discuss our results.

Suwannee and Brunswick Terranes and Terrane Boundaries

The crustal structure of the southeastern United States has been influenced by two major tectonic events: the Paleozoic Appalachian orogeny and early Mesozoic rifting which led to the formation of the East Coast continental margin. It is believed that the Appalachian orogen was formed by terrane accretion [cf. *Williams and Hatcher*, 1983]. Several terranes have been mapped from exposed outcrops inboard of the Fall Line, which marks the onset of the Coastal Plain sedimentary cover (Figure 1). Outboard of the Fall Line, terranes and terrane boundaries have been inferred from drilling samples and geophysical data. Our seismic profile extends across portions of two of these terranes — the southern Brunswick terrane and the Suwannee terrane.

Drilling samples from beneath the post-Jurassic sedimentary cover of the Georgia and Florida coastal plain have identified a boundary between two distinct terranes [*Chowns and Williams*, 1983]. This boundary, referred to as the Suwannee-Wiggins suture [*Thomas et al*, 1989], separates Piedmont-type basement rocks to the north and basement rocks of African affinity to the south. The terrane to the south of the Suwannee-Wiggins suture is referred to as the Suwannee terrane, which lies beneath the coastal plains of southern Alabama and Georgia and northern Florida. It consists of undisturbed Paleozoic metasediments of the Suwannee basin which occupy the Florida peninsular arch and overlie, and are flanked by, relatively unmetamorphosed granites and felsic volcanic rocks with ages of ~500 Ma [*Chowns and Williams*, 1983].

There is considerable evidence suggesting that the Suwannee terrane was once part of, or adjacent to, the African craton and represents a fragment of Gondwana left behind following the opening of the Atlantic [*Wilson*, 1966; *Chowns and Williams*, 1983]. The trend of the Suwannee-Wiggins suture as inferred by *Chowns and Williams* [1983] is thus taken to represent the Alleghanian North America/Gondwana suture (CWS in Figure 1a). The position of the boundary toward the coast is not well constrained but has been placed between Charleston and Savannah on the basis of felsic volcanics drilled near Savannah and the Piedmont-like lithology of detrital clasts within red beds drilled near Charleston [*Chowns and Williams*, 1983].

Terranes and terrane boundaries have also been identified on the basis of potential field data. Of these, the most relevant to this discussion is the Brunswick terrane, which has been identified principally on the basis of its magnetic anomaly character [*Higgins and Zietz*, 1983]. This terrane, shown outlined in the magnetic anomaly map of Figure 1c, is bounded to the south and east by the BMA and to the west and north by short-wavelength, northeast trending magnetic anomalies associated with Piedmont metamorphic rocks. Various authors have commented on the possible significance of the Brunswick terrane [*Popenoe and Zietz*, 1977; *Higgins and Zeitz*, 1983; *Klitgord et al.*, 1983; *Williams and Hatcher*, 1983]. The noncoincidence of the southern boundary of the Brunswick terrane, the BMA, and the Suwannee-Wiggins suture determined

from borehole data, combined with the distinctly different magnetic anomaly character of the Brunswick terrane relative to the region south of the BMA, has complicated the interpretation of the true position of the Alleghanian North America/Gondwana suture.

In addition, the southern portion of the Brunswick terrane has a much more subdued magnetic anomaly character than the northern portion of the terrane. This has led to speculation that the southern Brunswick terrane may be associated with a series of basins or an aulacogen filled with sedimentary rocks [*Popenoe and Zietz*, 1977; *Higgins and Zeitz*, 1983; *Daniels et al.*, 1983]. Our seismic profile extends across the southern Brunswick terrane and thus directly addresses this issue.

Data Acquisition

In June 1988 the University of Texas Institute for Geophysics shot six deep-penetrating multichannel seismic (MCS) profiles across the BMA [*Austin et al.*, 1990; *Oh et al.*, 1991] (Figure 1). These profiles are referred to as the BA lines, as they were designed to intersect the Brunswick anomaly at a high angle. A 36-element, 10,800-inch^3, tuned air gun array fired every 50 m was used as the seismic source and a 6-km-long, 240-channel streamer was used as the receiver. Ocean bottom hydrophones (OBH) from the Woods Hole Oceanographic Institution and ocean bottom seismometers (OBS) from the University of Hamburg were deployed along lines BA-3 and BA-6. In this paper we present results from line BA-3, which lies entirely on the shelf; results from the margin-perpendicular transect across the Carolina Trough, line BA-6, have been presented by *Austin et al.* [1990], *Oh et al.* [1991], and *Holbrook et al.* [1994]. Presentations of portions of all of the MCS profiles are given by *Oh et al.* [1991].

Line BA-3 trends north-south from 32.7°N to 30.4°N. The profile crosses the southern Brunswick terrane (km 0-130), the BMA (km 130-160), and the eastern edge of a shelf basin (km 160-230) and then turns southeast and crosses the hinge zone near km 235 (Figure 1). Two basement-penetrating wells, the COST GE-1 and Transco TR 1005-1 wells [*Dillon and Popenoe*, 1988], were drilled near the line at the northern and southern limits of the basin south of the BMA (Figure 1). Line BA-3 also lies near single-channel seismic and sonobuoy profiles recorded by *Dillon and McGinnis* [1983] and, at its northern end, ties with deep-reflection profiles recorded offshore Charleston [*Behrendt et al.*, 1983].

Multichannel Data

The line BA-3 MCS data shown in Figure 2 reveal the following general features: a southward thickening sedimentary section 1 to 3 s thick; a reverberatory basement represented by a ~1-s-thick stratified unit that is locally disturbed in places in the north and deformed into a 90-km-long basin in the south; a relatively transparent zone between ~3 and 5 s two-way traveltime (TWT); a middle to lower crust (~5-11 s TWT) that is reflective beneath the northern half of the profile and transparent beneath the southern half, with the reflectivity in the north characterized by broad diffractive bodies; and a ~1- to 2-s-thick reflective zone above Moho that exhibits considerable structure. Localized blanking of crustal reflections due to basement structure is observed at km 132-140, km 162-178, and km 220-227. Apart from these zones, we interpret changes in crustal
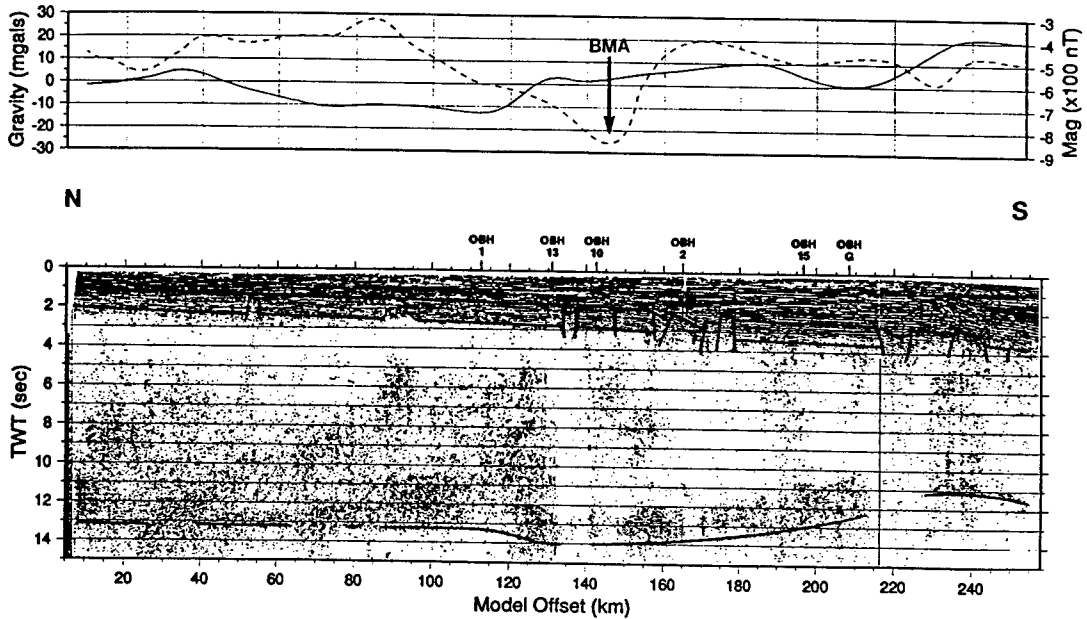
Figure 2a. Stacked MCS data. Data have been corrected for spherical divergence and coherency weighted. No intertrace mixing was performed. Gravity (solid curve) and magnetic (dashed curve) anomalies (interpolated from the 10-mGal and 50-nT contour maps of *Ewing* [1984] and *Heirtzler and Cande* [1984]) along the profile and locations of ocean bottom instruments are also shown.
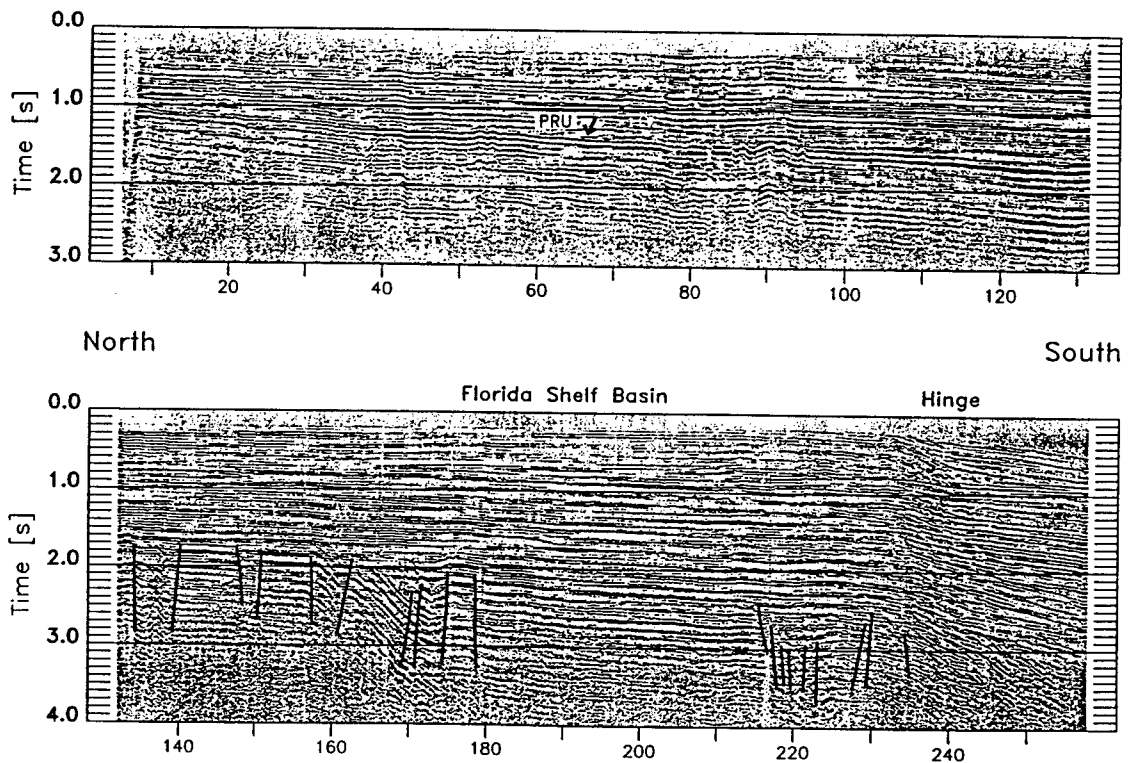
Figure 2b. Enlarged view of the sedimentary and basement sections of the stacked MCS data with interpretted faulting of the Florida shelf basin.

reflectivity to correspond to genuine changes in seismic properties of the crust.

Sedimentary Section and Postrift Unconformity

The sedimentary section thickens southward uniformly from ~1 to 3 s thick. Reflectors in this interval are nearly horizontal but laterally discontinuous, with a number of sedimentary structures such as channels observed along the line. The strata are largely undisturbed, with the exception of some small displacement faulting seen mostly in the north and the more prominent normal faulting near the hinge zone.

We interpret a laterally continuous reflector dipping southward from ~1 to 3 s TWT to mark the postrift unconformity (PRU) (Figure 2b). This reflector is identified by its lateral continuity, the onlapping of sediments from the south, the separation of undeformed reflectors above from strata that are in places intensely deformed below, and an abrupt velocity increase of 2 km/s or more. Over the northern half of the line (to km 135), this reflector has the same high-amplitude, two-cycle character as the "J" reflector of *Shilt et al.* [1983].

Shilt et al. [1983] analyzed shallow MCS data recorded on several lines in the Charleston, South Carolina, area and correlated a strong reflector at ~3 s with a ~300-m-thick sequence of Jurassic basalt flows drilled in the Clubhouse Crossroads wells [*Gottfried et al.*, 1983]. The distinctive J reflector marking the PRU has since been observed on numerous seismic lines shot on the coastal plain and offshore Georgia and South Carolina and is now taken to indicate a regionally extensive, Jurassic basalt flow [*Dillon and McGinnis*, 1983; *Hamilton et al.*, 1983, *Dillon et al.*, 1983; *Behrendt et al.*, 1983; *McBride et al.*, 1987; *Austin et al.*, 1990].

We interpret the southern limit of J to be km 135, where the reflection marking the PRU changes character as it passes over a small basement high. This interpretation is in agreement with that of *Dillon et al.* [1979, 1983]. The basement high lies on the northern flank of a 5-km-wide zone of intensely disturbed basement. This zone, which lies just north of the BMA, marks the northern limit of the extensional features which, 25 km to the south, open into a broad basin bounded by deep grabens (Figure 2b). This basin, which we call the Florida shelf basin, has been discussed by *Kiltgord et al.* [1983, 1988] and *Dillon et al.* [1983] and was the site of a number of petroleum exploration wells drilled in the late 1970s [*Mattick and Libby-French*, 1988].

Stratified, Pre-Cretaceous Basement

The reverberatory character of reflections beneath the PRU makes interpretations of basement reflectivity difficult. The reverberations consist of water bottom and peg-leg multiples from the PRU and strong reflectors in the sedimentary section. It appears, however, that the upper 1 s of basement directly beneath the PRU from the northern end of the line to km 235 is stratified, suggesting a sequence of metasedimentary or layered volcanic rocks. Basement rocks drilled onshore consist of Paleozoic felsic volcanics west of the northern end of the line and Suwannee basin metasediments west of the southern end of the line [*Chowns and Williams*, 1983]. Basement rocks encountered by wells drilled on the flanks of the Florida shelf basin consist of undisturbed Silurian quartzite and shale (TR 1005-1) and upper Devonian argillite (COST GE-1) [*Dillon and Popenoe*, 1988]. As pointed out by *Oh et al.* [1991], these
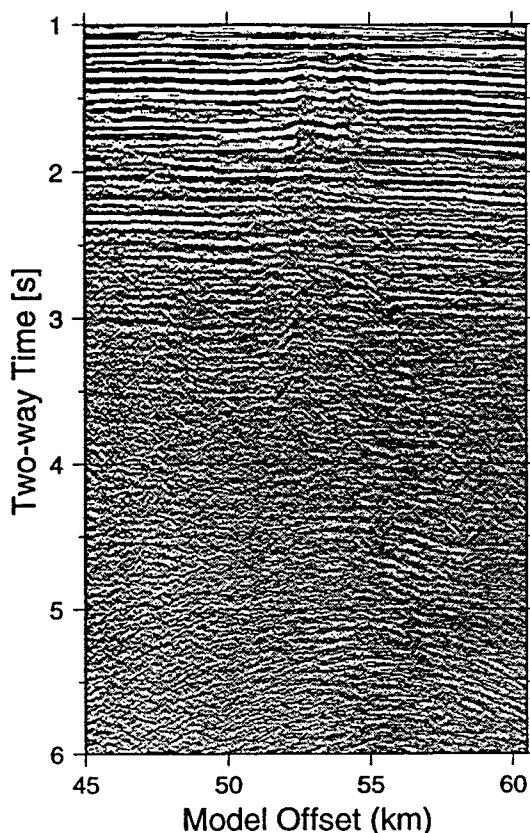

Figure 3. Detail of basement disturbance beneath the PRU near km 53 interpreted as an igneous intrusion. Also note reflections at ~4 s that mark the base of the transparent zone.

lithologies are similar to the Paleozoic metasediments of the Suwannee basin in Florida and may represent a seaward continuation of that basin. It is thought that the Suwannee basin strata fill a syncline of felsic basement rocks [*Chowns and Williams*, 1983]. There is no clear indication, however, of a contact between these two likely basement lithologies, metasediments and felsic volcanics, along BA-3. Along-profile variations of reflectivity within this interval are observed, but they are subtle and may be associated with changes in multiple-reverberation character. Also, there is no indication of significant basement structure associated with the southern Brunswick terrane.

Deformation within the stratified basement interval consists of minor disturbances near km 30 and 41 that may represent small grabens; upwarped disturbances near km 58 and 90 that may represent igneous intrusions (Figure 3) (a similar feature observed by *Behrendt et al.* [1983] was also interpreted as an intrusion); and extensional deformation south of km 135 (Figure 2b) that is probably related to Mesozoic rifting and formation of the hinge zone.
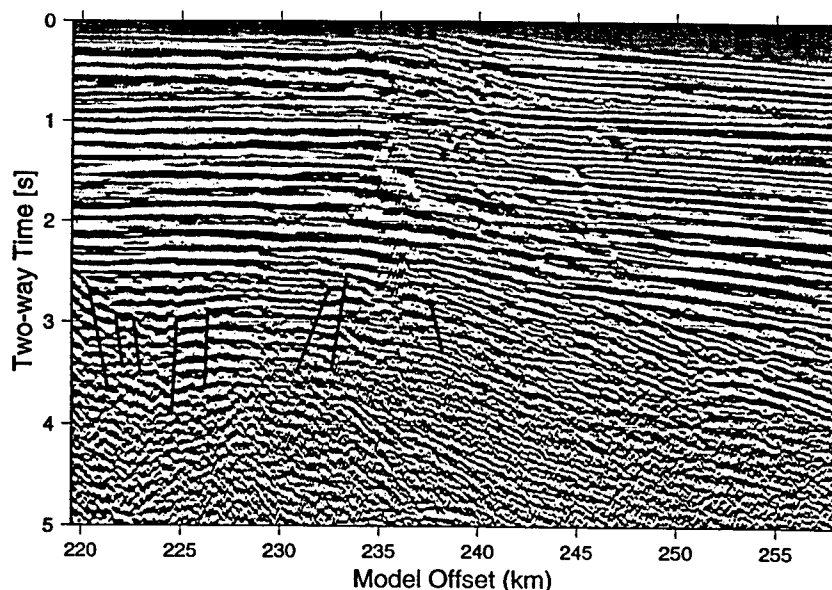
Figure 4. Detail of the southern graben of the Florida shelf basin (km 217-230), the basement hinge (km 235), and the wedge-shaped region of seaward dipping reflectors overlying basement between km 235 and 253. Interpreted basement faulting is indicated.

The hinge zone is marked by an abrupt increase in basement depth across a normal fault on the southern side of the tilted horst block that bounds the southern graben of the Florida shelf basin (Figure 4). Prominent normal faulting is observed within the sediments just above and seaward of the horst. A sequence of seaward dipping reflectors is observed overlying basement beyond the hinge. This sequence has a similar character to seaward dipping reflectors observed on BA lines 4, 5, and 6, which have been interpreted as basaltic flows [Austin et al., 1990; Oh et al., 1991] and thus may also represent a volcanic sequence.

Crystalline Crust and Moho

Deep crustal reflectivity varies significantly along the line. The crust north of the BMA is strikingly more reflective than that south of the BMA (Figure 2a). To the north, a 2- to 3-s-thick transparent zone lies beneath the basement section. The base of this transparent zone is defined by a surface of diffraction tops at ~5 s. This surface is most apparent between km 85 and 135, where two dome-shaped features exhibiting bright, layered reflectivity are observed (Figure 5). South of the BMA the crust is largely transparent down to the lower crustal reflections overlying Moho. The strength of these lower crustal events indicates that the relative transparency of crust south of the BMA represents weaker crustal reflectivity, not energy loss due to attenuation or scattering.

Strong lower crustal reflections are observed overlying Moho along the entire line. These reflections are seen as a steeply dipping sequence cutting Moho near km 35; a thinner, horizontal sequence between km 45 and 70; and thick, wedge-shaped sequences between km 70-120 and 150-215 (Figure 2a). Moho, interpreted as the base of these reflectors, exhibits considerable structure, sagging between km 120 and 160, and

rising steeply between km 180 and 220 (Figure 2a). South of km 220 the reflective character of the Moho changes, possibly due to processes associated with crustal thinning toward the hinge zone.

Wide-Angle Data and Travel Time Modeling

Six ocean bottom seismic instruments recorded airgun shots along BA-3 (Figure 1). OBHs 1, 13, 10, and 2 were located in a 60-km spread about the trough of the BMA. OBH 15 and OBS G were located farther south. This geometry provides very good resolution of seismic velocities within the upper 15 km of the crust between km 80 and 220, from which a variety of reflected and diving-wave phases are observed on all instruments. Analysis of the wide-angle data consisted of identification and digitization of reflected and diving-wave phases followed by a combination of inverse and forward traveltime modeling.

Phase Interpretation and Travel Time Modeling

The coincident MCS data greatly facilitated the interpretation of wide-angle phases by providing constraints on sediment thickness and the effects of basement disturbances and by enabling a general association of wide-angle phases with reflectivity patterns observed on the MCS data. A summary of the wide-angle phases interpreted on all of the instruments is shown in Figure 6. We illustrate the major interpreted phases in Figure 7, where we show the southern portion of the OBH 1 record section. A clear first-arrival branch is observed to offsets of 110 km. The abrupt change in apparent velocity of the first arrivals from ~3.5 to ~5.8 km/s at 6 km range indicates the sediment/basement velocity contrast. Reflection R1 corresponds to the PRU/basement interface discussed above. Local disruptions of the first-arrival branch observed near 26, 60, and
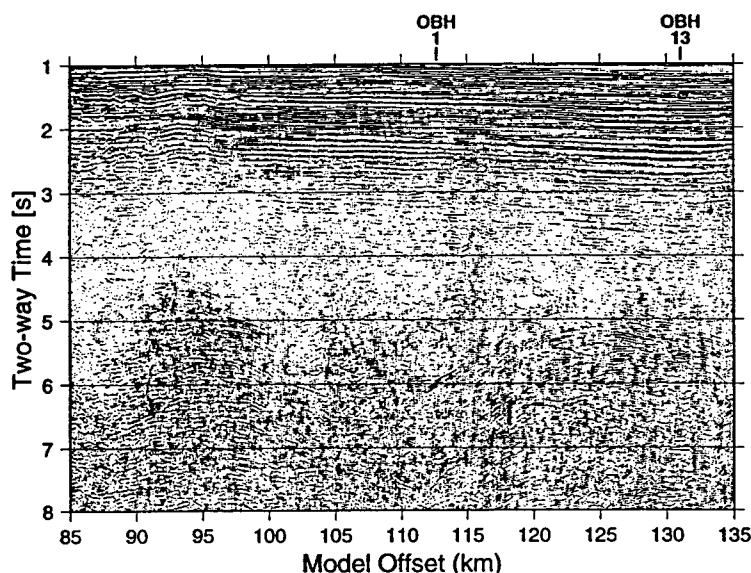
Figure 5. Detail of dome-shaped features exhibiting bright, layered reflectivity beneath the transparent upper-crustal layer.

110 km range are associated with the basement disturbance near km 135 and the bounding grabens of the Florida shelf basin (Figure 2). These basement features give rise to both traveltime delays and diffractions.

We have identified five main wide-angle reflection phases from the crust beneath the basement. These are indicated as R2, R3, R4, $P_M P_1$, and $P_M P_2$ in Figure 7. The R2 phase becomes asymptotic to the first-arrival branch beyond ~20 km range. R3, R4, and $P_M P_1$ represent the earliest arriving phases of multicyclic, wide-angle reflection sequences. We interpret $P_M P_2$ as the latest arriving phase of the $P_M P$ reflection sequence. The multicyclic events of these sequences probably represent both specular reflections and diffractions from laterally discontinuous, layered reflective zones such as observed in the MCS data overlying Moho (Figure 2) and in the midcrust (Figure 5). We have indicated some of the diffractions that merge into the coherent wide-angle reflection sequences in Figure 7.

The picked phases were modeled using a combination of forward and inverse modeling to obtain the velocity model shown in Figure 8a. The inversion scheme of *Zelt and Smith* [1992] was used in a layer-stripping fashion as a rapid means of exploring acceptable velocities and thicknesses for individual layers. The inversion models obtained for each layer were adjusted via forward modeling as necessary to improve the fit to the data. Bold lines along the model interfaces in Figure 8a indicate reflecting points of modeled wide-angle reflection phases and thus give some indication of where the model is well constrained. In Figure 8b we show a contour plot of the interpolated resolution values (model resolution matrix diagonal elements) determined for each velocity node beneath the sedimentary layer of the final model. These resolution values correspond to five seperate inversions, one for each layer, in which all velocity nodes of a given layer were inverted for simultaneously using ray groups corresponding to observed phases. These resolution values indicate the relative number of

rays passing near a given velocity node and are dependent on model parameterization [*Zelt and Smith,* 1992]. Nevertheless, they provide a good qualitative view of which portions of the model are well resolved.

The small-scale velocity anomalies associated with basement disturbances are not formally well resolved by the inversion but are indicated by traveltime delays such as those discussed above and shown in Figure 9. In Figure 9 we show the effects of the basement disturbance near km 135 on basement refractions recorded by OBHs 13 and 10, located on either side of the feature. We note two effects: a local traveltime delay (indicated by an arrow) that probably represents diffraction of the basement diving waves, and a net delay of diving waves that have passed through the disturbed zone (indicated by Δt).

The problem of obtaining quantitative estimates of model parameter uncertainty for two-dimensional velocity models is complicated and has not yet been solved. Qualitative estimates of uncertainty may be obtained through various sensitivity analyses in which the effects of perturbations to model parameters on the fit of the model to the data are considered. We used the inversion code of *Zelt and Smith* [1992] to perform sensitivity analyses on seven discrete portions, or blocks, of the velocity model as indicated in Figure 10a. The velocities of each block were perturbed in increments of 0.05 km/s and held fixed at the perturbed values during inversion for all other model parameters of the given layer. We consider the effect of the perturbation in terms of the RMS misfit of the calculated to the observed traveltimes.

The results of the sensitivity analyses for blocks 1-4 are sumarized in Figures 10b and 10c. In Figure 10b the change in RMS error, δRMS, relative to the final model (Figure 8a) is shown contoured in increments of 0.005 s. Various quantitative features of this error surface, such as curvature near the minima or absolute levels of δRMS misfit or gradient, undoubtedly bear on the uncertainty of the model parameters, but the exact mapping
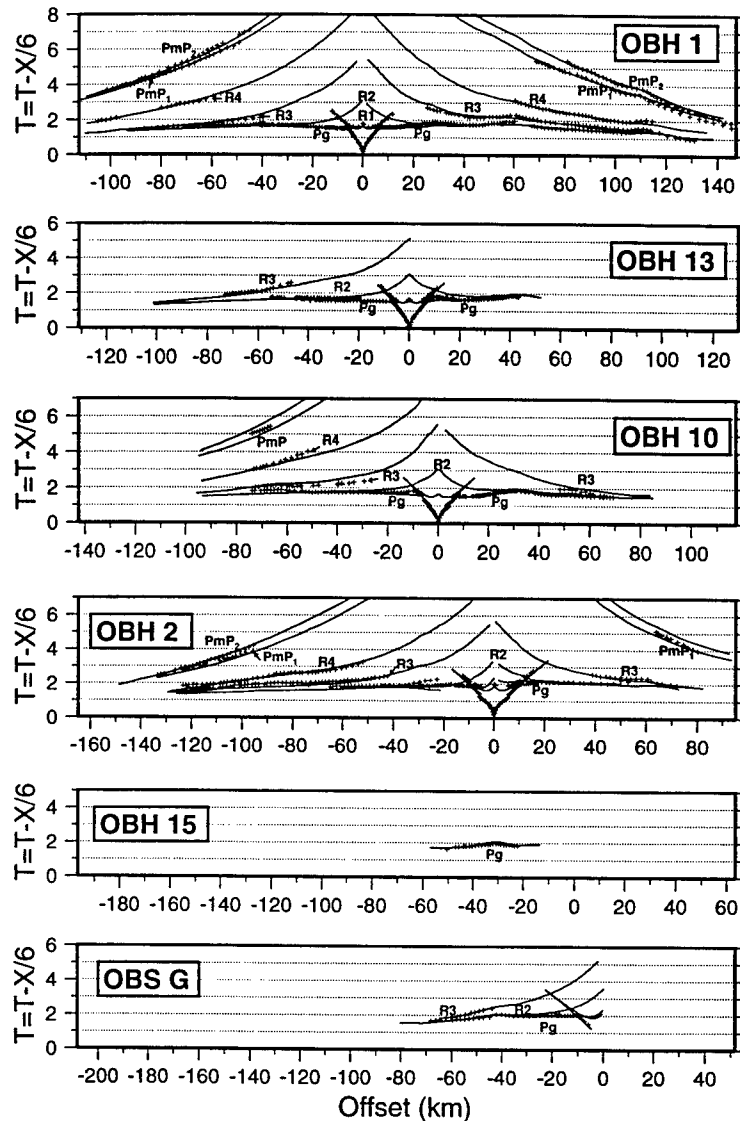
Figure 6. Summary of picked wide-angle events for all ocean bottom instruments (crosses) and the calculated arrival times from the velocity model of Figure 8.

between these quantities and parameter uncertainty is unknown. In our analyses this mapping is based on qualitative considerations. We notice in the consideration of blocks 1-4, for example, that the fit to the data and the geologic reasonableness of the model become noticeably poor for δRMS values above ~0.02 s. At this misfit level the gradient of the δRMS surface also becomes qualitatively significant. In addition, we show in Figure 10c a contour of the percentage of observed traveltimes used in the final inversion for the perturbed blocks 1-4. The decrease in ray coverage indicated in Figure 10c results from accommodation of the velocity perturbations by model parameter adjustments (velocities or interface topography) which are in some sense extreme, preventing rays from being

traced to surface locations where observations exist. We note that for block 2 the δRMS error is relatively insensitive to velocity perturbations, but this is largely due to pathological adjustments to the other parameters. Thus, in evaluating velocity uncertainties for blocks 1-4, we must consider both the δRMS error surface and ray coverage. Considering 0.02 s to be a significant level of misfit for blocks 1-4 and a 15% decrease in ray coverage to be unacceptable, we assign an uncertainty of ± 0.1-0.15 km/s for blocks 1-4. We note that block 1 has a tendency to be more sensitive to velocity increases, whereas block 4 is more sensitive to velocity decreases.

Adjustments for velocity perturbations to blocks 5-7 do not significantly reduce ray coverage, as these layers are both
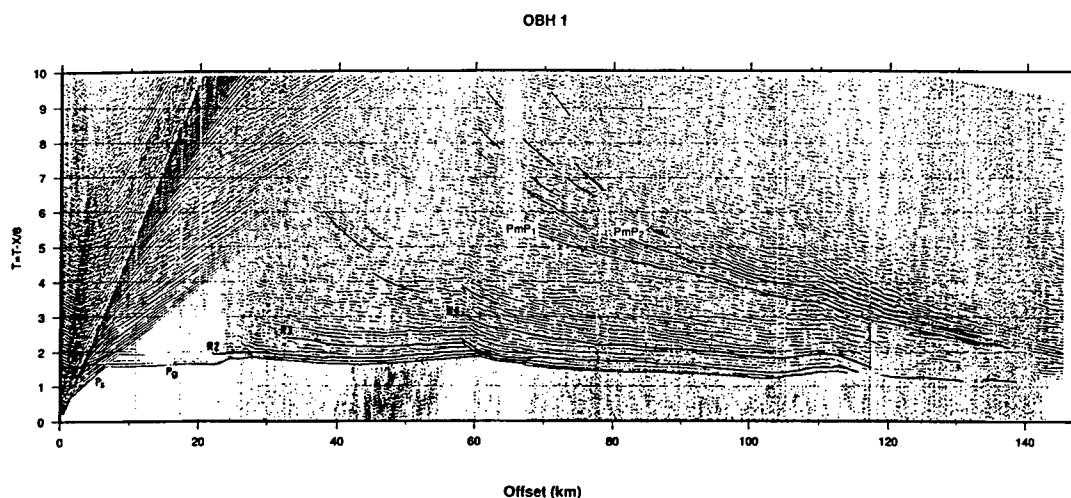
OBH 1

Figure 7. Southern portion OBH 1 profile reduced at 6 km/s with interpreted phases indicated. See text for description.

thicker and involve a smaller range of ray parameter than the upper crustal layer; thus we show only the δRMS error curves in Figures 10d-10f. Again, it is not clear how to determine a statistically meaningful level of δRMS misfit. It is unlikely that a 0.005-s δRMS error is meaningful, and we are not concerned that the δRMS error minima do not coincide exactly with our final model. It is clear that block 5 is more sensitive to velocity perturbations than block 6 and that block 7 is relatively insensitive to perturbations less than 0.20 km/s. Based on a qualitative assessment of the curvature of the δRMS error curves, we assign uncertainties of ±0.1–0.2 km/s to the midcrustal layer and ±0.20–0.25 km/s to the lower crustal layer.

Velocity Model

The velocity model shown in Figure 8a consists of 1.6-2.4 and 3.1-3.6 km/s sedimentary layers, with total sedimentary thickness increasing from 1 to 4 km from north to south; a thin, 5.5 km/s layer beneath the sediments in the south (km 165-260); a 5.8-6.0 km/s basement layer with a marked velocity increase in the hinge zone; an upper crustal layer that varies laterally from 6.1-6.3 km/s in the north to 6.4-6.5 km/s in the south; a midcrustal layer that varies laterally from 6.3-6.6 km/s in the north to 6.5-6.7 km/s in the south; a 6.7-6.8-km/s lower crustal layer; and a thin, 7.1-7.3-km/s layer above Moho. Traveltime curves computed from the model are shown with the traveltime picks in Figure 6 and overlain on the OBH 1 and OBH 2 record sections in Figure 11. The RMS errors of the computed traveltimes for each layer are given in Table 1.

The velocity and thickness of the sediments are constrained by first arrivals on five instruments observed at offsets of ~6 km, the R1 reflector, and the traveltime to the PRU reflector observed on the MCS data.

Velocities within the basement and upper crustal layers are constrained by diving waves observed as first arrivals on all instruments (Figure 6). In particular, the lateral velocity increase of the upper crustal layer across km 145 is indicated by the increased apparent velocity of first arrivals on OBH 1 beyond +60 km range and OBH 10 beyond +30 km range. The

thicknesses and velocities of these layers are constrained by wide-angle reflection phases R2 and R3 (Figure 6) and are well resolved between km 80 and 200 (Figure 8b). The basement velocity increase in the hinge zone is indicated primarily by the increased apparent velocity of $P_M P$ arrivals observed on OBH 1 beyond +110 km range (Figure 11a). The location of this velocity anomaly is not well constrained and could be placed anywhere within the crust south of km 230 between 5 and 25 km depth.

No diving wave phases are observed from the midcrustal and lower crustal layers. Velocities and thicknesses of these layers are constrained by the R4 (midcrustal layer) and $P_M P$ reflections (Figure 6) and are best constrained between km 80 and 180 (Figure 8b). The depths of the lower crustal interfaces are consistent with the two-way traveltime to the lower crustal reflection sequence observed on the MCS data.

The $P_M P$ phases observed on OBHs 1 and 2 appear as multi-cyclic events (Figure 11). We interpret the earliest and latest of these reflections as arising from the top and bottom of the reflective zone at the base of the crust. The ~7.2 km/s velocity assigned to this layer is not constrained, as the thickness and velocity of the layer can be traded off to fit the traveltimes equally well. The strength of the observed $P_M P$ phases, however, suggests a positive velocity step across a lower crustal transition. Thus we believe that 7.2 km/s is a reasonable velocity for this transitional layer.

Discussion

Mafic Composition Crust and Lateral Change in Seismic Properties

The two principal results of this study are the determination of crustal seismic velocities beneath line BA-3 and the identification of first-order differences in seismic properties of the crust across the center of the BA-3 profile. The seismic velocities of the middle to lower crust and the upper crust south of km 150 suggest that the overall composition of the crust beneath line BA-3 is fairly mafic. The increase in upper crustal
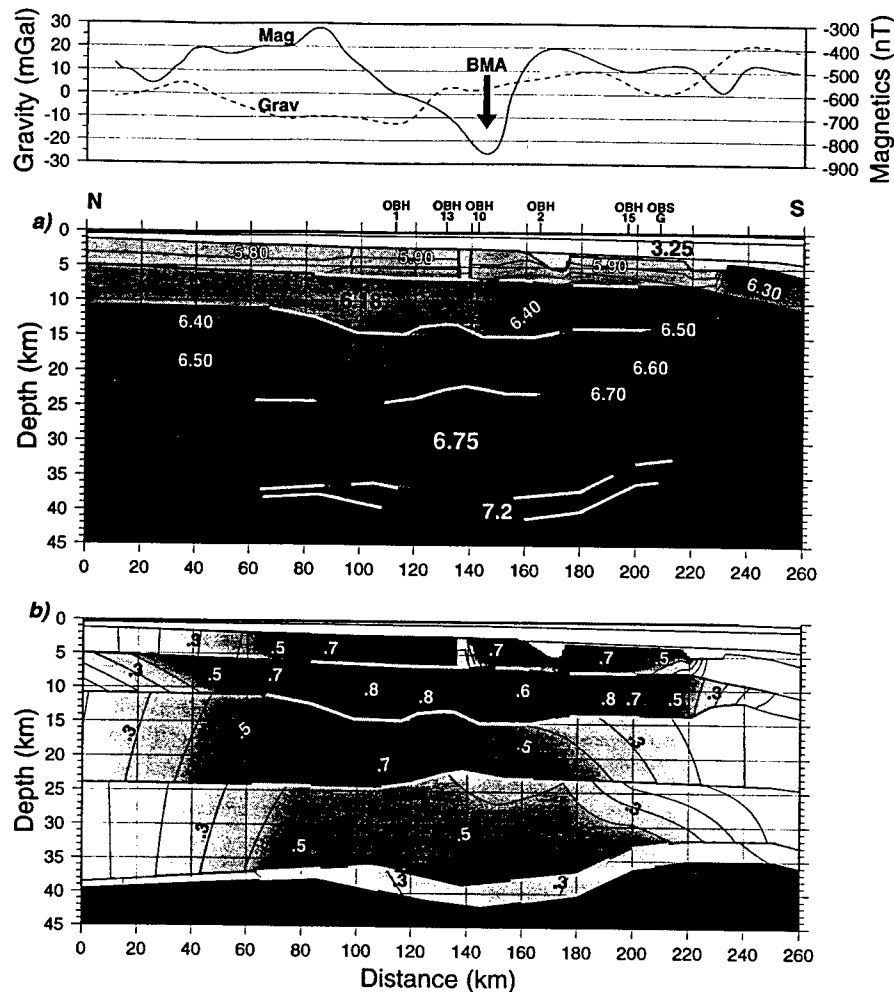
Figure 8. (a) Velocity model determined from trave time modeling of wide-angle phases. Velocity contour interval is 0.1 km/s, gray scale shading proportional to velocity. No velocity contours are shown in the sedimentarty section for simplicity. Bold lines on interfaces indicate reflection points of modeled wide-angle phases. Ocean bottom instruments locations are indicated as are gravity and total intensity magnetic field profiles interpolated along line BA-3 from the 10-mGal and 50-nT contour maps of *Ewing* [1984] and *Heirtzler and Cande* [1984]. (b) Velocity node resolution values obtained from the inversion of individual layers. Resolution values have a range of 0 to 1, with values above 0.5 being well resolved.

seismic velocity across the center of the profile from ~6.18 to ~6.45 km/s suggests a transition from felsic to more mafic rocks. For example, average velocities for granitic to quartz-mica schist composition midcrustal rocks range from 6.07 to 6.26 km/s, whereas greenschist facies metagabbro to gabbroic composition rocks range from 6.49 to 6.95 km/s [*Holbrook et al.*, 1992]. The midcrustal (12-25 km) velocities of ~6.45 km/s to the north and ~6.60 km/s to the south suggest a significant mafic component for rocks at these depths as well, with a slightly increased mafic content towards the south. The lower-crustal velocities of ~6.75 km/s are also consistent with mafic rocks [*Holbrook et al.*, 1992].

We have identified the following differences in seismic properties of the crust across the center of the profile: (1) an abrupt increase in upper crustal velocities from north to south; (2) a less well constrained increase in midcrustal velocities from north to south; (3) a transition in crustal reflectivity patterns from fairly complex in the north to largely transparent down to the lower crustal reflection sequence in the south; and (4) an apparent deepening of the lower crustal reflections overlying Moho across the center of the profile and a corresponding "sag" in the Moho of the velocity model, which is required to fit the observed P_MP phases.

Our results strongly suggest that the increase in seismic velocity across the center of the BA-3 profile between 7 and 15 km depth and the occurrence of the BMA at approximately the same location are both due to an abrupt increase in mafic content of the upper to middle crust south of the BMA. The
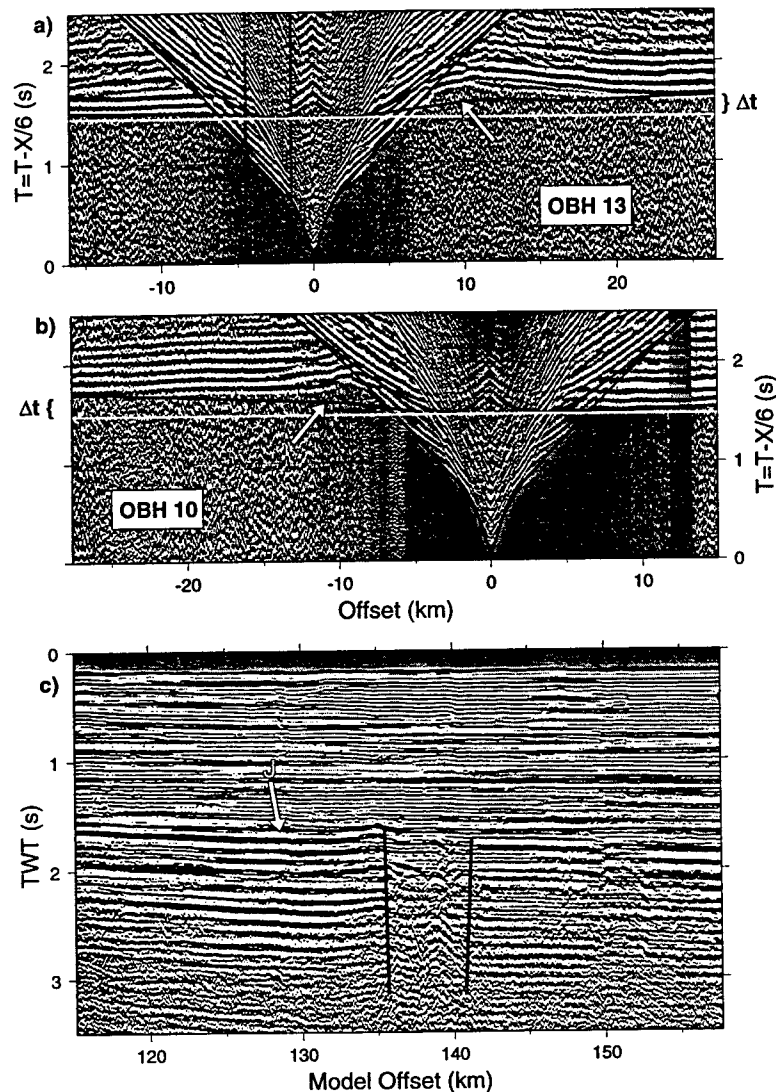
Figure 9. (a) and (b) Trave time delays associated with basement disturbance indicated in Figure 9c. Arrow indicates delay due to diffraction of the basement diving waves. Δt indicates net delay of diving waves which have passed through the disturbed zone. Calculated trave times for the velocity model are indicated in black. (c) Basement disturbance between interpreted faults. Basement reflector and PRU indicated by J.

interpretation of the BMA follows from simple two-dimensional modeling of the anomaly. A magnetic model of the crust beneath BA-3 was constructed by assigning a susceptibility contrast of $3.0 \ A \ m^{-1}$ and no remanant magnetization to crust with velocities ≥ 6.3 km/s and depths ≤ 20 km (the assumed Curie depth based on heat flow data of *Pujol and Fountain* [1985]), with the northern and southern limits of this body extending to infinity. Comparison of the anomaly calculated for this body and the observed anomaly (Figure 12) shows that the salient features of the BMA across line BA-3 can be explained by this model.

There are two end-member explanations for the increased mafic content of the crust beneath the southern portion of BA-3:

(1) intrusion of mafic magmas in the early Mesozoic associated with rifting of the margin; and (2) juxtaposition of terranes of differing composition during the Paleozoic Alleghanian orogeny. The first explanation follows from evidence that the region experienced a period of voluminous igneous activity in the early Mesozoic and from the crustal structure across the Carolina Trough and northern Blake Plateau Basin hinge zones. The second explanation follows from onshore borehole data which suggest that the Suwannee-Wiggins suture crosses the shelf somewhere south of Charleston (Figure 1a) and from the correlation of the BMA onshore with crustal-scale dipping reflection sequences observed on deep MCS profiles in Georgia.
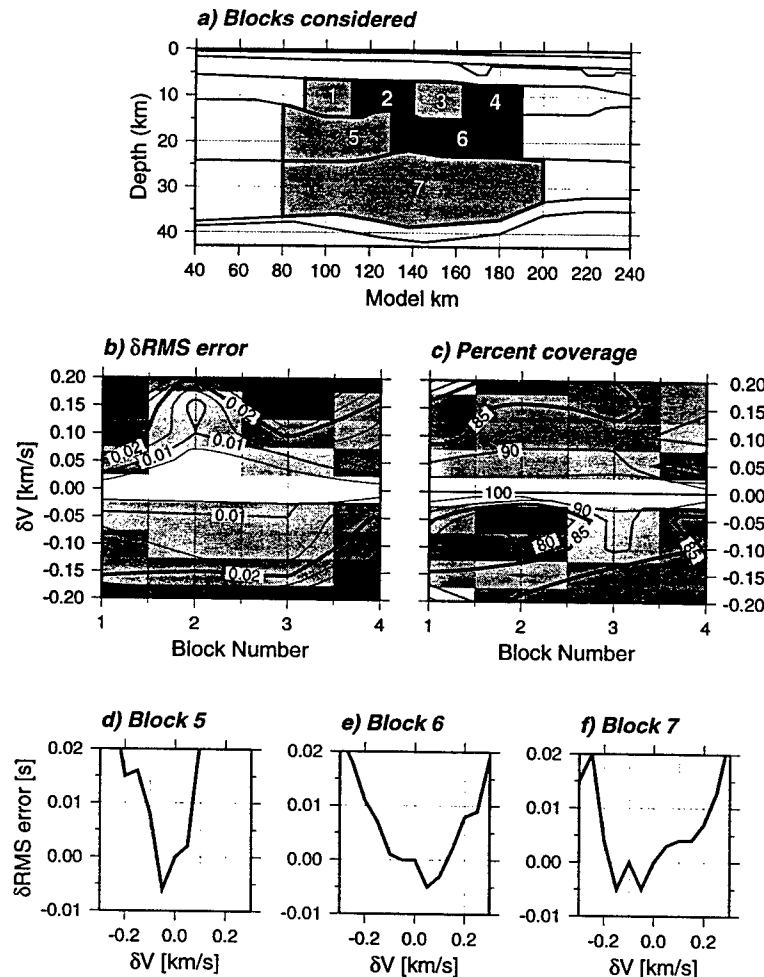
Figure 10. (a) The seven blocks of the velocity model (Figure 8a) for which sensitivity analyses were performed. The velocities of each block were perturbed in increments of 0.05 km/s and then held fixed during inversion for remaining layer model parameters. (b) The change in RMS error, δRMS, relative to the final model for blocks 1-4 contoured in 0.005-s increments. The 0.02-s level, which we consider significant, is shown in bold. (c) Percentage of observed trave times used in final inversions for blocks 1-4. Decrease in ray coverage indicates inability of rays to be traced to observed trave times. The 85% level, which we consider pathological, is shown in bold. (d)-(f) δRMS-error curves for blocks 5-7.

We consider arguments for both explanations as well as a third, intermediate possibility that rift-related mafic material was emplaced along a reactivated suture.

Rift-Related Mafic Intrusion and the Change in Seismic Properties Across the BMA

Evidence that the region experienced a period of voluminous igneous activity in the early Mesozoic includes regional basalt flows as evidenced by borehole and seismic data [Chowns and Williams, 1983; Dillon et al., 1983; McBride et al., 1987; de Boer et al, 1988]; numerous circular, positive magnetic/gravity anomalies interpreted as mafic intrusions [Daniels et al., 1983]; and massive intrusion and extrusion of mafic material outboard of the Carolina Trough and northern Blake Plateau Basin hinge

zones [Tréhu et al., 1989; Austin et al., 1990; Holbrook et al., 1994; Holbrook and Kelemen, 1993]. The massive emplacement of mafic material outboard of these hinge zones is inferred from anomalously high seismic velocities in the midcrust (6.5-6.9 km/s) and lower crust (7.2-7.5 km/s) between the hinge zone and normal oceanic crust in the Carolina Trough [Tréhu et al., 1989; Holbrook et al., 1994] and from the observation of seaward dipping reflectors outboard of the hinge zone on MCS profiles BA-4, 5 and 6 [Austin et al., 1990; Oh et al., 1991].

It is likely that the mafic material outboard of the Carolina Trough and northern Blake Plateau Basin hinge zones is the primary cause of both the BMA and the positive-gravity-anomaly trend which track respectively inboard and outboard of the hinge zone (Figure 1a) [Holbrook et al., 1994]. We may thus
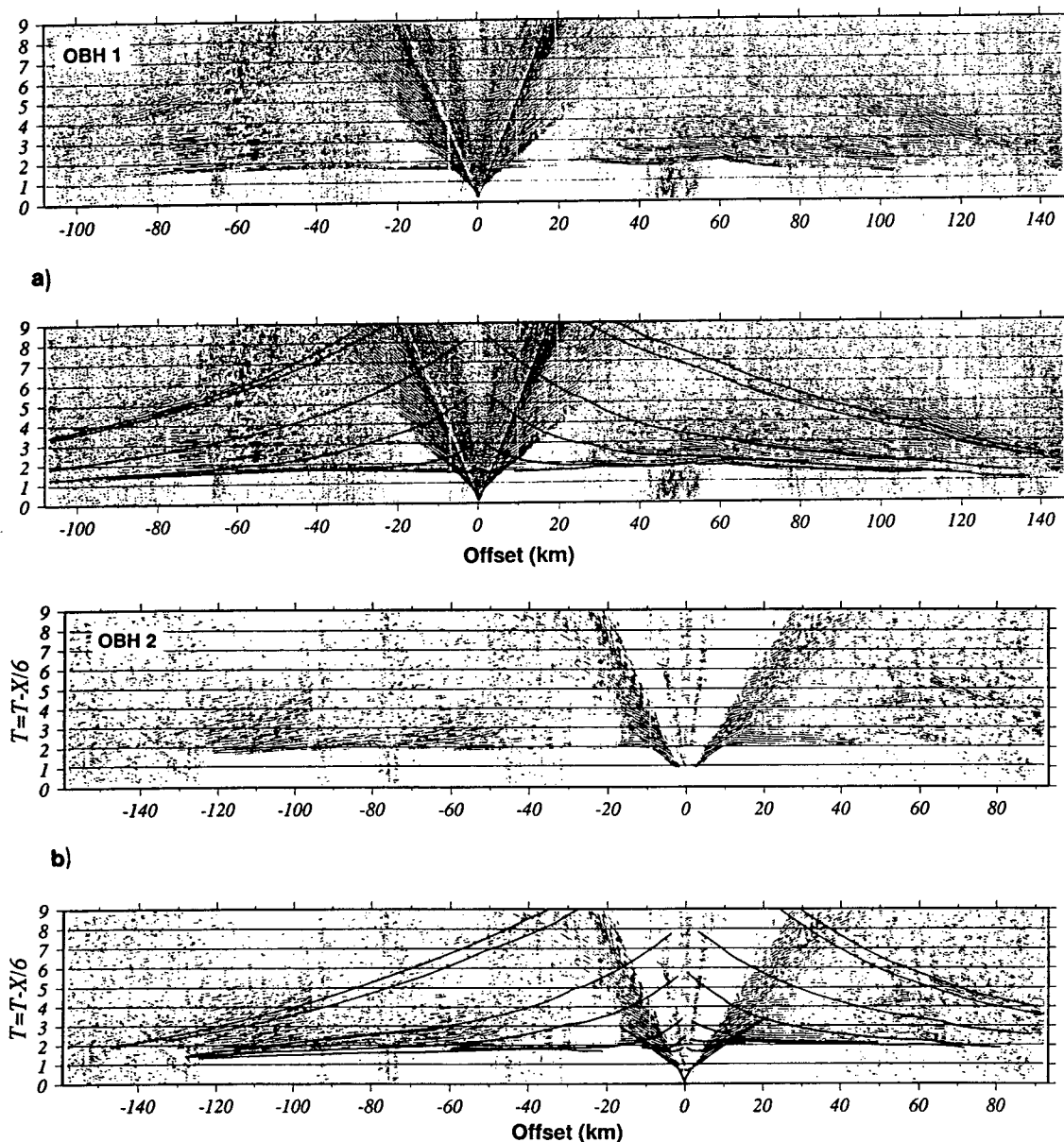
Figure 11. OBH profiles with and without calculated trave time curves overlain: (a) OBH 1, (b) OBH 2. Profile of OBH 2 has been coherency weighted to enhance signal/noise.

argue that the increased mafic content beneath the southern portion of BA-3 represents a continuation of the igneous material emplaced along the Carolina Trough and northern Blake Plateau Basin hinge zones. In support of this argument we point out the continuity of the BMA and the positive gravity anomaly trend and their intersection of line BA-3, as well as the observation of seaward dipping reflections near the hinge zone on line BA-3, which may represent a volcanic sequence. Magmatic emplacement outboard of the hinge zone was probably enabled by fracturing of the crust as it rifted. Intrusion beneath

the southern portion of BA-3 may have accompanied fracturing associated with the formation of the Florida shelf basin, resulting in a gross homogenization and relative transparency of the crust.

As a counter argument we note that the increased midcrustal velocities across the Carolina Trough margin are observed in association with high-velocity (7.3-7.5 km/s) lower crustal material. The presence of this material is evidenced by first-arriving wide-angle phases with apparent velocities of ≥ 7.0 km/s observed within ranges of 35-75 km [*Tréhu et al.*, 1989;

Table 1. Root Mean Squared Travel Time Errors of Modeled Crustal Phases and Velocity Uncertainties of Crustal Layers as Determined From the Sensitivity Analyses Discussed in the Text

Crustal Layer	RMS Error, s	Uncertainty, km/s
Basement		
Diving waves	0.094	
Wide-angle reflections	0.101	
Upper crust		
Diving waves	0.098	± 0.10–0.15
Wide-angle reflections	0.105	
Mid Crust		
Wide-angle reflections	0.077	± 0.10–0.20
Lower Crust		
PmP1 reflection	0.093	± 0.20–0.25
PmP2 reflection	0.093	

Holbrook et al., 1994]. These observations suggest nearly complete replacement of preexisting continental crust with mafic material. It is not clear that such drastic reorganization of the crust is required to effect the increase in upper crustal velocities from 6.18 to 6.45 km/s seen along BA-3, but we see no evidence in the line BA-3 wide-angle data for midcrustal to lower crustal velocities of ≥7.0 km/s, even though the profile trends parallel and in close proximity to the hinge. Moreover, because we have posed the argument based on analogy to processes along the hinge zone, we require additional mechanisms to explain the landward continuation of both the BMA and the positive gravity anomaly trend. Also, neither of the basement-penetrating wells drilled along BA-3 encountered Mesozoic volcanic rocks. Finally, we note that the southern portion of BA-3 lies at the intersection of two positive gravity anomaly trends, that which tracks outboard of the Carolina Trough and northern Blake Plateau Basin hinge zones and a broader anomaly extending along the shelf from just south of the

BMA to 29°N. This anomaly, which we call the Florida shelf gravity high, is not readily explained by rift-related processes, but rather suggests a consideration of juxtaposed terranes.

Suwannee-Wiggins Suture and the Change in Seismic Properties Across the BMA

If the BMA and the change in seismic properties across the center of line BA-3 are caused by the juxtaposition of terranes of different composition, then the Suwannee terrane must be more mafic than crust to the north, and the BMA must mark the terrane boundary. Borehole samples of crystalline basement rocks from the Suwannee terrane consist dominantly of felsic volcanics, rhyolite, and granite. It is possible, however, that a mafic core lies beneath these uppermost felsic rocks. The Florida shelf gravity high may indicate the presence of this mafic material. We note that its peaks generally correlate positively with magnetic anomaly highs (Figure 1). The anomaly is situated inboard of the hinge zone and is not associated with any known basins other than the Florida shelf basin. Thus there is little evidence to suggest that significant extension of the shelf crust took place to make room for a large volume of rift-related mafic material. These arguments suggest an "indigenous" mafic component of the Suwannee terrane unrelated to rifting.

An argument that the BMA marks the Suwannee-Wiggins suture is more difficult to make. The consideration of a suture zone/BMA relation is based primarily on onshore borehole data. These data, however, suggest that the suture passes offshore considerably north of the BMA. We may argue that the change in seismic properties across the BMA represents a terrane boundary because the seismic properties change abruptly. A similar argument can be made based on the differing magnetic anomaly characters of the Brunswick and Suwannee terranes. These arguments are circular, however, and are not particularly satisfying. There are a number of reasons to suspect that the BMA does not represent the Suwannee-Wiggins suture. We consider these in conjunction with the intermediate possibility that rift-related mafic material emplaced along a reactivated suture is the cause of both the BMA and the change in seismic properties along line BA-3.
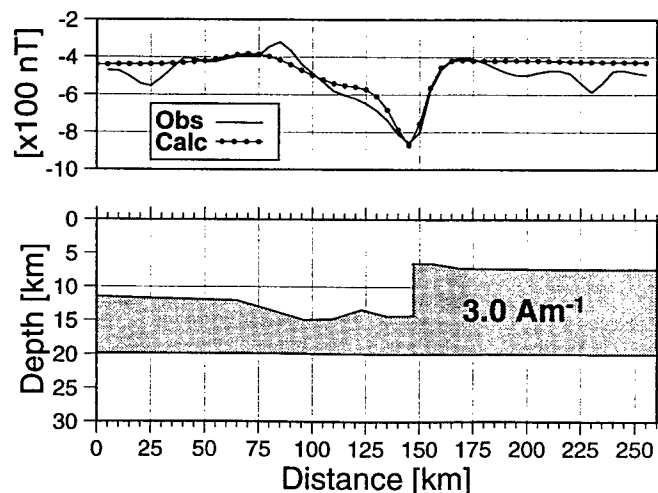

Figure 12. Magnetic model obtained by assigning a susceptibility contrast of 3.0 Am^{-1} and no remanent magnetization to the portion of the crust with velocities ≥ 6.3 km/s and depths ≤20 km.

Magmatic Emplacement Along Reactivated Suture Zones

McBride and Nelson [1991] suggest that mafic material was emplaced in the early Mesozoic along extensionally reactivated mid and late Paleozoic sutures, based on their interpretation of reflection data across the BMA in Georgia and analyses of regional potential field data. The role of suture zones is inferred from *McBride and Nelson's* [1991] interpretation of southward dipping reflection sequences, which bound largely unreflective crust to the south, as suture zones separating North American and African crust, and a correlation between these reflection sequences and the BMA. For this interpretation to apply to line BA-3 we would require the observation of similar dipping reflection sequences. We observe a transition from reflective to nonreflective crust across the BMA on line BA-3, but we do not observe southward dipping reflection sequences which could be interpreted as a suture zone. Southward dipping crustal reflections are observed on BA lines 4, 5 and 6 but show no systematic relationship to the BMA [*Oh et al.*, 1991].

As counter arguments to the coincidence of the BMA and a suture zone, we point out the apparent continuity of the layered sequence of Paleozoic basement reflectors immediately beneath the PRU and the absence of substantial compressional structures within this sequence. Additionally, correlation of the southward dipping reflections observed on BA-4 and BA-5 reveals an approximate east-west trend passing over BA-3 near km 35, which is also the intersection of the offshore projection of the suture based on borehole data with line BA-3. Other features near km 35 include a sequence of reflectors between 7 and 9 s, an inboard-vergent, steeply dipping reflector between km 20 and 30 at 5 to 8 s TWT, and a thick sequence of outboard-vergent, lower crustal reflections crosscutting Moho (Figure 2). It is not apparent that these features represent a suture, but if they do, a relationship between a suture in this location and the change in crustal properties across the BMA is unlikely. Finally, it is unlikely that mafic material emplaced along a suture zone would result in increased upper crustal velocities beneath the entire southern portion of the BA-3 profile.

The arguments put forth for possible causes of the crustal transition observed across the BMA on the BA-3 profile involve considerable speculation. To distinguish between them requires an even greater level of speculation. Hot spots, stike-slip motion along landward extensions of fracture zones, the Paleozoic distribution of island arcs, and thin-skinned tectonics, for example, can be and have been invoked to help explain the regional geologic and geophysical data [cf. *de Boer et al.*, 1988; *Tauvers and Muehlberger*, 1987; *Klitgord et al.*, 1983]. With appropriate caution, then, we prefer the interpretation of rift-related mafic intrusion as the dominant cause of the crustal transition observed across the BMA.

Conclusions

We have presented results from a coincident MCS/wide-angle seismic experiment conducted along a north-south transect on the southeastern U.S. continental shelf, crossing portions of the southern Brunswick terrane, the Suwannee terrane, and the Brunswick magnetic anomaly. The two principal results of this study are the determination of crustal seismic velocities beneath the profile and the identification of first-order differences in crustal seismic properties across the Brunswick magnetic anomaly. The velocity model is well resolved in the upper 15 km between ~60 km north and ~60 km south of the BMA. The transition in seismic properties across the BMA includes higher

seismic velocities south of the BMA, particularly in the upper crust (7-15 km depth), and a transition from reflective to transparent crust from north to south.

We interpret these results to indicate an abrupt increase in the mafic component of the upper to midcrust from north to south. Magnetic modeling indicates that association of increased magnetic susceptibility with this higher velocity material results in an edge effect anomaly which explains the BMA quite well. These results strengthen the proposition that the BMA is due to more mafic material south of the anomaly [*McBride and Nelson*, 1991; *Holbrook et al.*, 1994] and not due to basins or particularly nonmagnetic material within the southern Brunswick terrane [*Higgins and Zeitz*, 1983; *Daniels et al.*, 1983; *Klitgord et al.*, 1983].

We considered arguments for two possible causes of the increased crustal mafic content south of the BMA: rift-related mafic intrusion and juxtaposed terranes of differing crustal composition. Arguments for mafic intrusion follow from evidence of voluminous, regional, early Mesozoic igneous activity and analogy to crustal structure along the Carolina Trough and northern Blake Plateau Basin hinge zones. Counter arguments include the lack of evidence for very high-velocity (≥7.2 km/s), midcrustal to lower crustal material such as that observed outboard of the hinge zones [*Tréhu et al.*, 1989; *Holbrook et al.*, 1994], suggesting that the massive igneous intrusion associated with the continent-ocean transition zone is confined to the region of highly extended crust outboard of the hinge zone.

Arguments for juxtaposed terranes follow from our interpretation of the Florida shelf gravity high as indicating a dense, mafic crustal composition for the eastern Suwannee terrane. Counter arguments include the continuity of thickness, velocity, and reflection character within the stratified basement section, which we interpret, based on seismic velocity and borehole samples along our profile, to represent a Paleozoic metasedimentary/ volcanic sequence. Also, no dipping crustal reflection sequences are observed associated with the BMA, in contrast with reflection data onshore Georgia [*McBride and Nelson*, 1988].

Although an unequivocal distinction between these two causes cannot be made, we prefer the interpretation of rift-related mafic intrusion as the dominant cause of the crustal transition observed across the BMA.

References

Austin, J. A. Jr., P. L. Stoffa, J. D. Phillips, J. Oh, D. S. Sawyer, G. M. Purdy, E. Reiter, and J. Makris, Crustal structure of the southeast Georgia embayment–Carolina trough: Preliminary results of a composite seismic image of a continental suture(?) and a volcanic passive margin, *Geology, 18*, 1023-1027, 1990.

Behrendt, J. C., R. M. Hamilton, H. D. Ackermann, V. J. Henry, and K.

36

C. Bayer, Marine multichannel seismic-relfection evidence for Cenozoic faulting and deep crustal structure near Charleston, South Carolina, in Studies Related to the Charleston, South Carolina, Earthquake of 1886 — Tectonics and Seismicity, edited by G. S. Gohn, *U.S. Geol. Surv. Prof. Pap., 1313*, J1-J29, 1983.

Chowns, T. M., and C. T. Williams, Pre-Cretaceous rocks beneath the Georgia Coastal Plain – regional implications, in Studies Related to the Charleston, South Carolina, Earthquake of 1886 — Tectonics and Seismicity, edited by G. S. Gohn, *U.S. Geol. Surv. Prof. Pap., 1313*, L1-L42, 1983.

Daniels, L. D., I. Zietz, and P. Popenoe, Distribution of subsurface lower Mesozoic rocks in the southeastern United States, as interpreted from regional aeromagnetic and gravity maps, in Studies Related to the Charleston, South Carolina, Earthquake of 1886 — Tectonics and Seismicity, edited by G. S. Gohn, *U.S. Geol. Surv. Prof. Pap., 1313*, K1-K24, 1983.

de Boer, J. Z., J. G. McHone, J. H. Puffer, P. C. Ragland and D Whittington, Mesozoic and Cenozoic magmatism, in *The Geology of North America*, vol. I-2, *The Atlantic Continental Margin: U.S.*, edited by R.E. Sheridan and J. A. Grow, pp. 217-241, Geological Society of America, Boulder, Colo., 1988.

Decade of North American Geology Committee for the Gravity Anomaly Map of North America, Gravity anomaly map of North America, Geol. Soc. of Am., Boulder, Colo., 1987a.

Decade of North American Geology Committee for the Magnetic Anomaly Map of North America, Magnetic anomaly map of North America, Geol. Soc. of Am., Boulder, Colo., 1987b.

Diebold, J.B., P. L. Stoffa, and the LASE Study Group, A large aperture seismic experiment in the Baltimore Canyon Trough, in *The Geology of North America*, vol. I-2, *The Atlantic Continental Margin: U.S.*, edited by R.E. Sheridan and J. A. Grow, pp. 387-398, Geological Society of America, Boulder, Colo., 1988.

Dillon, W. P., C. K. Paull, A. G. Dahl, and W. C. Patterson, Structure of the continental margin near the COST No. GE-1 well, United States South Atlantic outer continental shelf area, U.S. Geol. Surv. Circ., 800, 97-114, 1979.

Dillon, W. P., K. D. Kiltgord, and C. K. Paull, Mesozoic development and structure of the continental margin off South Carolina, in Studies Related to the Charleston, South Carolina, Earthquake of 1886 — Tectonics and Seismicity, edited by G. S. Gohn, *U.S. Geol. Surv. Prof. Pap., 1313*, N1-N16, 1983.

Dillon, W. P., and L. D. McGinnis, Basement structure indicated by seismic-reflection measurements offshore from South Carolina and adjacent areas, in Studies Related to the Charleston, South Carolina, Earthquake of 1886 — Tectonics and Seismicity, edited by G. S. Gohn, *U.S. Geol. Surv. Prof. Pap., 1313*, O1-O7, 1983.

Dillon, W. P., and P. Popenoe, The Blake Plateau Basin and Carolina Trough, in *The Geology of North America*, vol. I-2, *The Atlantic Continental Margin: U.S.*, edited by R.E. Sheridan and J. A. Grow, pp. 291-328, Geological Society of America, Boulder, Colo., 1988.

Ewing, V. M., Gravity anomalies, in *Ocean Drilling Program Regional Atlas Series*, Atlas 5, *Eastern North American Continental Margin and Adjacent Ocean Floor, 28° to 36° N and 70° to 82° W*, edited by G. M. Bryan and J. R. Heirtzler, pp. 2, Marine Science International, Woods Hole, Mass., 1984.

Gottfried, D., C. S. Annes, and G. R. Byerly, Geochemistry and tectonic significance of the subsurface basalts near Charleston, South Carolina: Clubhouse Crossroads test holes #2 and #3, in Studies Related to the Charleston, South Carolina, Earthquake of 1886 — Tectonics and Seismicity, edited by G. S. Gohn, *U.S. Geol. Surv. Prof. Pap., 1313*, A1-A19, 1983.

Hamilton, R. M., J. C. Behrendt, and H. D. Ackermann, Land multichannel seismic-reflection evidence for tectonic features near Charleston, South Carolina, in Studies Related to the Charleston, South Carolina, Earthquake of 1886 — Tectonics and Seismicity, edited by G. S. Gohn, *U.S. Geol. Surv. Prof. Pap., 1313*, I1-I18, 1983.

Heirtzler, J. R. and S. C. Cande, Magnetic total intensity anomalies, in *Ocean Drilling Program Regional Atlas Series*, Atlas 5, *Eastern North American Contiental Margin and Adjacent Ocean Floor, 28° to 36° N*

and 70° to 82° W, edited by G. M. Bryan and J. R. Heirtzler, pp. 3, Marine Science International, Woods Hole, Mass., 1984.

Higgins, M., and I. Zietz, Geological interpretation of geophysical maps of the pre-Cretaceous "basement" beneath the coastal plain of the southeastern United States, Mem. Geol. Soc. Am., 158, 125-130, 1983.

Holbrook, W. S., and P.B. Kelemen, Large ingeous province on the U.S. Atlantic margin and implications for magmatism during continental breakup, Nature, 364, 433-436, 1993.

Holbrook, W. S., W. D. Mooney, and N. I. Christensen, The seismic velocity structure of the deep continental crust, in *Continental Lower Crust*, edited by D. M. Fountain, R. Arculus, and R. Kay, pp. 1-43, Elsevier, New York, 1992.

Holbrook, W. S., E. C. Reiter, G. M. Purdy, D. Sawyer, P. L. Stoffa, J. A. Austin Jr., J. Oh, and J. Makris, Deep structure of the U.S. Atlantic continental margin, offshore South Carolina, from coincident ocean bottom and multichannel seismic data, J. Geophys. Res., 99, 9155-9178, 1994.

Klitgord, K. D., W. P. Dillon, and P. Popenoe, Mesozoic tectonics of the Southeastern United States Coastal Plain and continental margin, in Studies Related to the Charleston, South Carolina, Earthquake of 1886 — Tectonics and Seismicity, edited by G. S. Gohn, *U.S. Geol. Surv. Prof. Pap., 1313*, P1-P15, 1983.

Klitgord, K. D., R. D. Hutchinson, and H. Schouten, U.S. Atlantic continental margin; Structural and tectonic framework, in *The Geology of North America*, vol. I-2, *The Atlantic Continental Margin: U.S.*, edited by R.E. Sheridan and J. A. Grow, pp. 19-55, Geological Society of America, Boulder, Colo., 1988.

Mattick, R. E., and J. Libby-French, Petroleum geology of the United States Atlantic continental margin, in *The Geology of North America*, vol. I-2, *The Atlantic Continental Margin: U.S.*, edited by R.E. Sheridan and J. A. Grow, pp. 445-467, Geological Society of America, Boulder, Colo., 1988.

McBride, J. H., and K. D. Nelson, Integration of COCORP deep reflection and magnetic anomaly analysis in the southeastern United States: Implications for origin of the Brunswick and East Coast magnetic anomalies, Geol. Soc. Am. Bull., 100, 436-445, 1988.

McBride, J. H., and K. D. Nelson, Deep seismic reflection constraints on Paleozoic crustal structure and Moho from the buried southern Appalachian orogen, in *Continental Lithosphere: Deep Seismic Reflection*, edited by R. Meissner, et al., pp. 9-20, Geodyn. Ser., vol. 22, AGU, Washington, D. C., 1991.

McBride, J. H., K. D. Nelson, and L. D. Brown, Early Mesozoic basin structure and tectonics of the southeastern United States as revealed from COCORP reflection data and the relation to Atlantic rifting, in Sedimentary Basins and Basin-Forming Mechanisms, edited by C. Geaumone and A. J. Tankard, Mem. Can. Soc. Pet. Geol., 12, 173-184, 1987.

Morel, P., and E. Irving, Paleomagnetism and the evolution of Pangea, J. Geophys. Res, 86, 1858-1872, 1981.

Nelson, K. D., J. A. Arnow, J. H. McBride, J. H. Willemin., J. Huang, L. Zheng, J. E. Oliver, L. D. Brown, and S. Kaufman, New COCORP profiling in the southeastern United States, I, Late Paleozoic suture and Mesozoic rift basin, Geology, 13, 714-718, 1985a.

Nelson, K. D., J. A. Arnow, J. H. McBride, J. E. Oliver, L. D. Brown, and S. Kaufman, New COCORP profiling in the southeastern United States, II, Brunswick and east coast magnetic anomalies, opening of the north-central Atlantic Ocean, Geology, 13, 718-721, 1985b.

Oh, J., J. D. Phillips, J. A. Austin Jr., and P. L. Stoffa, Deep penetration seismic reflection profiling across the southeastern United States continental margin, in *Continental Lithosphere: Deep Seismic Reflections*, Geodyn. Ser., vol. 22, edited by R. Meissner et al., pp. 225-240, AGU, Washington, D. C., 1991.

Popenoe, P., and I. Zietz, The nature of the geophysical basement beneath the Coastal Plain of South Carolina and northeastern Georigia, in Studies Related to the Charleston, South Carolina, Earthquake of 1886 — A Preliminary Report, edited by D. W. Rankin, U.S. Geol. Surv. Prof. Pap., 1028, 119-138, 1977.

Pujol, J., and D. M. Fountain, Statistical analysis of the mean heat flow/reduced heat flow relationship for continents and its

tectonophysical implications, *J. Geophys. Res.*, *90*, 11,335-11,344, 1985.

Shilt, F. S., L. D. Grown, J. E. Oliver, and S. Kaufman, Subsurface structure near Charleston, South Carolina — Results of COCORP reflection profiling in the Atlantic Coastal Plain, in Studies Related to the Charleston, South Carolina, Earthquake of 1886 — Tectonics and Seismicity, edited by G. S. Gohn, *U.S. Geol. Surv. Prof. Pap., 1313*, H1-H19, 1983.

Tauvers, P. R., and W. R. Muehlberger, Is the Brunswick magnetic anomaly really the Alleghanian suture?, *Tectonics, 6*, 331-342, 1987.

Thomas, W. A., T. M. Chowns, D. L. Daniels, T. L. Neathery, L. Glover III, and R. J. Gleason, The subsurface Appalachians beneath the Atlantic and Gulf Coastal Plains, in *The Geology of North America, vol. F-2, The Appalachian-Ouachita Orogen in the United States*, edited by R. D. Hatcher Jr., W.A. Thomas, and G. W. Viele, pp. 445-458, Geological Society of America, Boulder, Colo., 1989.

Tréhu, A. M., A. Ballard, L. M. Dorman, J. F. Gettrust, K. D. Klitgord, and A. Shreiner, Structure of the lower crust beneath the Carolina trough, U.S. Atlantic continental margin, *J. Geophys. Res., 94*, 10,585-10,600, 1989.

Uchupi, E., J. T. Crosby, S. T. Bolmer Jr., J. D. Eusden, Jr., J. I. Ewing, J. K. Costain, R. J. Gleason, and Lynn Glover, III, Tectonic features, in *Ocean Drilling Program Regional Atlas Series*, Atlas 5, *Eastern North American Contiental Margin and Adjacent Ocean Floor, 28° to 36° N and 70° to 82° W*, edited by G. M. Bryan and J. R. Heirtzler, pp. 36, Marine Science International, Woods Hole, Mass., 1984.

Van der Voo, R., F. J. Mank, and R. B. French, Permian-Triassic continental configureations and the origin of the Gulf of Mexico, *Geology, 4*, 177-180, 1976.

Williams, H., and R. D. Hatcher Jr., Applachian suspect terranes, *Mem. Geol. Soc. Am., 158*, 33-53, 1983.

Wilson, J. T., Did the Atlantic close and then reopen?, *Nature, 211*, 676-681, 1966.

Zelt, C. A., and R. B. Smith, Seismic traveltime inversion for 2-D crustal velocity structure, *Geophys. J. Int., 108*, 16-34, 1992.

W. Steven Holbrook, Deptartment of Geology and Geophysics, Woods Hole Oceanographic Institution, Woods Hole, MA 02543

Daniel Lizarralde, Massechusetts Institute of Technology / Woods Hole Oceanographic Institution Joint Program in Oceanography, Woods Hole, MA 02543 (e-mail: danl@azure.whoi.edu)

Jinyong Oh, Korean Institute of Geology, Mining and Minerals, P.O. Box 14, Taedok Science Town, Taejon, South Korea

Chapter 3

Structure and early thermal evolution of the U.S. Mid Atlantic margin

Abstract

Marine seismic experiments have revealed that the U.S. East Coast rifted margin crustal structure is dominated by voluminous volcanics emplaced during continental breakup. We present results from seismic data recorded onshore during the 1990 EDGE Mid-Atlantic seismic experiment that extend the margin crustal profile westward 180 km across the Coastal Plain and place the offshore results into a broader tectonic context. The onshore/offshore crustal model defines the crustal thinning profile across the margin, enabling the calculation of total extension based on direct measurements of crustal thickness. We find that the crust beneath the Coastal Plain is largely unextended, has a uniform thickness of ~35 km, shows no evidence for magmatic additions of sufficient volume to affect seismic velocity, and that the total half-extension of the crust is 30 to 40 km, less than previous estimates by a factor of 3 to 4. We also present results of depth migration of the offshore vertical-incidence and wide-angle seismic data that yield the most complete and accurate image to date of reflectivity across the U.S. East Coast margin. We use this image to analyze margin subsidence by exploiting the stratigraphy of the subaerially-extruded basalts beneath the sediments. We find that (1) margin subsidence is consistent with a petrogenetic model for initial seafloor-spreading magmatism involving high average melting pressures (3.5-4.0 GPa) and potential temperatures (>1500°C) for a present-day thermal lid thickness of ~225 km; (2) it is difficult to explain margin subsidence with a present-day lid thickness much less than ~175 km; and (3) rapid subsidence following breakup suggests the initially hot mantle underlying the rifting margin cooled very quickly, implying a limited and finite initial distribution of hot mantle, rather than a continuous upwelling or a ubiquitously warm upper mantle.

Introduction

Several seminal marine seismic experiments across the U.S. Atlantic rifted margin have demonstrated the importance of voluminous magmatism during rifting, imaging thick sequences of extrusive volcanics underlain by high velocity, mafic crust at the

continent/ocean transition [*Diebold et al.*, 1988; *Tréhu et al.*, 1989a; *Austin et al.*, 1990; *Sheridan et al.*, 1993; *Holbrook et al.*, 1994a, 1994b]. The implications of these results for rift processes and mantle dynamics cannot be fully explored, however, without a knowledge of Coastal Plain crustal structure to constrain the style and magnitude of extension, the landward extent of magmatism, and the distribution of accreted terranes and their potential involvement in margin development. In this paper we present results from a transect across the Coastal Plain near the Chesapeake Bay (Figure 1) that for the first time delineates Coastal Plain crustal structure based on active-source crustal refraction data.

Prior to this study, our knowledge of Coastal Plain crustal structure in the U.S. Mid-Atlantic region had been based primarily on multi-channel seismic (MCS) profiles [*Nelson et al.*, 1985; *Behrendt*, 1986; *Pratt et al.*, 1988] and a time-term seismic experiment [*James et al.*, 1968]. The often featureless Coastal Plain crust revealed by many of the MCS profiles may have more to due with signal loss in the sedimentary cover than to actual crustal reflectivity. Along the I-64 transect (Figure 1), for instance, a vertical boundary between highly reflective and completely transparent crust is observed at the Fall Line [*Pratt et al.*, 1988]. The results of the *James et al.* [1968] time-term study are equally ambiguous in their characterization of Coastal Plain crustal thickness, as the time-term technique depends on an assumed velocity structure and is particularly sensitive to sediment-thickness variations.

There are two major seismic results presented in this paper. The first is the determination of the crustal structure beneath the Coastal Plain along a 180-km transect — completing a 420-km seismic transect across the rifted margin, from unextended crust west of the Fall Line to oceanic crust offshore, that is based on data from the 1990 EDGE Mid-Atlantic seismic experiment [*Sheridan et al.*, 1993]. The second is the depth migration of the offshore MCS and wide-angle seismic data from this experiment, resulting in the most accurate and complete reflectivity image to date across the U.S. East Coast margin.

The seismic results define the crustal thinning profile across the rifted margin, clarify the complex structure at the continent-ocean transition, and provide a basis for estimating crustal extension and subsidence. A thick sequence of extrusive rift volcanics covers the most extended portion of thinned continental crust along this profile and spans the continent-ocean boundary. The migrated MCS data image the extended continental crust surface beneath the volcanics, and the velocity model constrains the seaward extent of thinned continental crust. We are thus for the first time equipped with all of the data required to accurately calculate crustal extension. In addition, we exploit the stratigraphy of the subaerially extruded basalts that underlie the sediments to calculate total margin subsidence and the history of earliest margin subsidence. These results have implications for pre-rift plate reconstructions, the strength of the lithosphere prior to rifting, the current thermal state of the margin lithosphere and the distribution of hot material beneath the margin at the time of crustal breakup.

Wide-angle data description and interpretation

Three multichannel seismic transects were acquired during the 1990 EDGE Mid-Atlantic seismic experiment using the industry seismic vessel *Geco Searcher's* 36-element, 10,800 cu. in. airgun array firing at 50 m intervals (Figure 1) [*Sheridan et al.*, 1993]. Ten ocean-bottom instruments from the Woods Hole Oceanographic Institution and the U.S. Geological Survey were deployed along Line 801 to record wide-angle arrivals. In addition, ten Reftek seismic recorders were deployed at six stations along an onshore extension of Line 801. Analyses of the offshore multichannel and wide-angle data sets are reported by *Sheridan et al.* [1993] and *Holbrook et al.* [1994b]. Here we present the first analyses of the land seismic stations.

Four of the six onshore stations yielded data ranging from fair to high quality (Figure 2). Data processing consisted of bandpass filtering, deconvolution, amplitude balancing,

and coherency filtering. Seismic phases from three crustal layers as well as an upper mantle diving-wave phase were correlated on these four record sections. The nomenclature we adopt for these phases is as follows: diving wave phases from within Layers 1, 2 and 3 and the upper mantle are referred to as Pg, D2, D3, and Pn, respectively; reflections from the base of Layers 1, 2, and 3 are referred to as R1, R2, and PmP, where PmP is the interpreted reflection from the base of the crust.

Station 2 (Stn 2) suffers from coastal noise, but phases Pg and R1 can be confidently identified. Proceeding westward, Stn 5 is of excellent quality and all correlated phases are observed with the exception of Pn. The blanked region between 120 and 140 km offset represents an interval of high-amplitude noise which has been suppressed by the coherency filter. The diving-wave phases display clear changes in apparent velocity. Numerous diffractions are associated with events observed within the 50 to 110 km offset range — the disruption of PmP between 80 and 110 km offset is particularly pronounced. The effect of the shelf edge is apparent at 150 km offset, and the increase in apparent velocity of the PmP phase beyond 160 km is characteristic of the lateral increase in velocity and seaward shallowing of Moho beyond the shelf edge, as observed on the offshore wide-angle profiles [*Holbrook et al.*, 1994b].

The Stn 7 profile is noisy, but all of the expected phases are observed. The D2, D3 and Pn phases are readily identified and associated with clear breaks in apparent velocity. The effect of the shelf slope on the Pn arrival beyond 200 km offset is apparent. The R2 and PmP phases are clear, though picking of these events is complicated by poor lateral phase continuity. The Stn 11 profile, recorded by geophones cemented in outcropping granite, is of excellent quality. Again all the expected phases are observed. The D3 and Pn phases are clear and the PmP phase is strong, though complicated by a multicyclic signature and interference from the D2 phase.

Velocity Modeling

The velocity model shown in Figure 3 was derived from inversion of the picked traveltimes using the code of *Zelt and Smith* [1992]. The velocity model of *Holbrook et al.* [1994b], based on the offshore instruments, was used as the starting model for the inversion for kms 0-240, and a one-dimensional (1D), landward continuation of this model was used as the starting model for kms -180 to 0. The velocity parameterization of the model is indicated in Figure 3b along with a gray-shade, contoured image of the "resolution" associated with this parameterization. The parameterization of the landward portion of the model was kept sparse, as the land stations are unreversed, and the data therefore only constrain large-scale averages of crustal velocity. In addition, the wide-angle data do not provide strong constraints on the sediment thickness or basement structure west of Line 801. We have assumed a smooth basement shallowing westward towards the Fall Line, consistent with an erosional post-rift unconformity surface [*Klitgord et al.*, 1988].

The resolution plot of Figure 3b is a contour of the model resolution matrix diagonal elements associated with each velocity node of the model. The resolution values are based on both the onshore and offshore wide-angle data and provide a view of the relative constraints that the traveltime data place on the model's velocity parameters. These resolution values indicate that the velocity model is not overparameterized and that the traveltime data place significant constraints on crustal velocity between km -100 and km 200. In particular, the onshore data constrain velocity in a wedge-shaped region extending from the upper crustal layer between km -50 and km 40 down to the lower crustal layer between km -100 and km 50.

Resolution diagrams such as Figure 3b must be interpreted with caution, as they depend on both ray coverage and parameter distribution. Ray diagrams are another means of illustrating the constraints the traveltime data place on crustal velocity and are also useful

in interpreting the contoured resolution values. In Figures 4 and 5 we show ray diagrams and traveltime fits to the picked phases. The traveltime data are most sensitive to crustal velocity in regions bounding ray bottoming points. The resolution plot of Figure 3b represents the density of these bottoming points for all the instruments averaged over the local model parameters. The high resolution values of the landward portion of the model are due in part, then, to the sparse parameterization of this portion of the model, and the closely spaced nodes required to define the velocity gradient near km 60 result in lower resolution values in this region.

The fit to traveltime picks (Figures 4 and 5) and the overlay of computed traveltime curves on the data (Figure 6) indicate that the velocity model explains the observed data very well. The final model is identical to the starting model east of km 80, is only slightly changed in the km 20 to km 80 region, and is similar to a 1D continuation of the *Holbrook et al.* [1994b] model west of km 20. The two significant differences west of km 20 are the thinning of the upper crustal layer to the west and the much shallower depth to Moho. The upper crustal layer (Layer 1) velocity and thickness are constrained between kms -40 and 40 by the Stn 2 and Stn 5 D1 and R1 phases and the Stn 5 D2 phase. This layer is characterized by a 9-km-thick, 5.90- to 6.05-km/s velocity gradient near km 0, thinning to 6 km towards the west with velocities increasing slightly to 5.95 to 6.10 km/s. The inversion introduced the dipping structure at the base of the layer near km -40 to accommodate the Stn 5 R1 phase. The continued westward shallowing of the layer is not constrained by the data, but it provides a positive gravity gradient that may explain the observed positive westward gradient (Figure 1). The velocity structure between km -20 and km 30 is clearly indicated by the Stn 2 and Stn 5 traveltime data given the basement and sedimentary configuration assumed for the model and a degree of off-axis uniformity to the structure. The lower velocities of this region correlate with a local, northeast-trending

gravity low observed crossing the profile on the shelf and continuing southward inboard of the Outer Banks (Figure 1).

The velocity and thickness of Layer 2 are constrained by D2 and R2 phases observed on Stn 5 and Stn 7. The D2 phase is also observed on the Stn 11 record as a secondary arrival, and its arrival time is consistent with the velocity model, though we have not used this phase to constrain the Layer 2 velocity. The layer is characterized by a 6.15- to 6.30-km/s velocity gradient and thickens to the west. Again, this thickening is consistent with both the traveltime and gravity data but is not strictly required by either.

The velocity and thickness of Layer 3 are well constrained by D3 and PmP phases observed on Stns 5, 7 and 11, and by Pn phases observed on Stns 7 and 11. The layer has a uniform thickness and velocity gradient of 6.60 to 6.80 km/s. This landward Moho structure differs from that predicted by the *Holbrook et al.* [1994b] model, which dips down to the west from a depth of 35 km near km 30 to a depth of 42 km at km 0. The structure of the *Holbrook et al.* [1994b] model is not constrained by the offshore wide-angle data, but was incorporated to explain the gravity low which, as mentioned above, has a trough near model km 0. We see now that the gravity low is a local feature apparently associated with a low velocity region in the upper crust.

The Moho is nearly flat between kms -100 and 10, rises to 30 km depth near km 40, deepens again between kms 60 and 80, and finally begins the marked shallowing towards normal oceanic crustal thickness. The shallowing of Moho between kms 40 and 50 is a robust feature of the velocity model. The eastern flank of this mantle "bulge" is well constrained by the offshore wide-angle data; the flat, 35-km-deep Moho west of the bulge is well constrained by the onshore data; and the depth to the top of the bulge is constrained by PmP reflections of Stn 5, Stn 7, and OBH 16 offshore and Pn arrivals of Stn 7. The shape of the bulge corresponds with the shape of interpreted Moho reflections on the depth-migrated MCS data presented below. We show below that this feature is a result of crustal

loading by the thick sedimentary sequence. The details of the western flank of this Moho feature, between km 10 and km 40, are not precisely resolved by the data, however. The PmP arrival most directly imaging the western flank of the Moho bulge is observed on Stn 5 between 80 and 110 km offset and is strongly diffracted in two locations (Figure 2). A traveltime triplication can in part explain the PmP character, but finite-difference wavefield modeling indicates that the PmP diffractions do not arise from Moho structure as smooth as the final velocity model. It is possible that the disruptions to PmP, and to earlier arriving phases, are due to basement structure between Stn 5 and Line 801.

Depth migration of MCS and wide-angle data

The highly complementary nature of coincidentally acquired MCS and wide-angle seismic data has become clear after many such experiments. Wide-angle data provide images of the integrated seismic properties of the crust while multi-fold vertical-incidence seismic data record the crust's differential properties. Interpreted together, these data can place strong compositional and geometric constraints on crustal structure. To yield the full benefit of these data sets, however, the MCS data must be depth migrated so that observed reflections can be assigned to particular locations within the crust and correlated with velocity information derived from the wide-angle data.

We have depth migrated the MCS data using velocities from the model of Figure 3 and the extended split-step migration algorithm of *Kessinger and Stoffa* [1992]. In addition, because the MCS data do not image the Moho seaward of km 70, we have migrated the wide-angle PmP reflections recorded by the offshore instruments using a similar algorithm and merged this Moho image with the migrated MCS data. Extended split-step migration is a frequency-wavenumber algorithm in which the observed seismic data are downward continued by small depth steps using a reference velocity. The downward continuation is followed by spatial Fourier transform and a vertical phase shift of each trace to provide a

first-order correction for lateral velocity variation. For each depth step, several downward continuations are performed, each with a different reference velocity, corresponding to the distribution of lateral velocity variation across a given depth step. Arbitrary migration accuracy can be achieved by increasing the number of reference velocities used. We employed an automated approach in which a new reference velocity was chosen for every 0.1 km/s lateral change in velocity. Deviation from the model velocity was thus never more than 0.05 km/s, so that even at very wide angles, where the vertical traveltime correction is less important, the migration error over a given depth interval was very small. An exploding-reflector imaging condition was used for the MCS migration, and a cross-correlation with a downward-continued point source initiated at the receiver was used as the imaging condition for the wide-angle migration.

The resulting migrated image (Figure 7) reveals crustal features that neither the unmigrated data nor the velocity model show. One important feature is the abrupt decrease in crustal reflectivity seaward of km 40. The observation of a very bright sequence of lower-crustal reflections beneath the region of subdued reflectivity east of km 40 suggests that the observed reflectivity is characteristic of crustal impedance constrasts, not complications due to basement structure, and that the crust here is more homogeneous than the crust to the west, which displays a bright, complex reflectivity pattern. This transition was pointed out by *Holbrook et al.* [1994b], who showed that the decrease in reflectivity appeared to correspond to an increase in velocity, though their resolution of velocity west of km 40 was limited. Their suggestion is borne out by our model, and it is reasonable to conclude that both the velocity increase and the reduction in reflectivity east of km 40 are due to intrusion of mafic material.

The migrated image reveals that the transition in reflectivity across km 40 is quite abrupt. In fact, the ramp-like appearance of the unmigrated diffraction pattern associated with this abrupt transition led *Sheridan et al.* [1993] to relate the diffractions to a Taconic

suture. The arguments for a Taconic suture in this location based on the MCS data now seem less compelling. There is a tendency toward eastward dips in the migrated image west of km 40, but neither the presence of complex reflectivity nor a fabric in the reflectivity are prima facie evidence for a crustal suture.

The migrated image also more clearly delineates the geometry of the seaward-dipping wedge. The wedge is seen to consist of two structural units. Between km 40 and km 75 the wedge thickens to about 5 km. The base of the wedge in this region is defined by downlapping reflection terminations and by short, disrupted reflections, which may represent the basement surface upon which the basalts were extruded, bounded by an apparent basement high near km 75. The crust beneath this portion of the wedge thins progressively towards the east, displays a subdued but discernible reflectivity pattern with the base of the crust defined by a particularly bright sequence of Moho reflections, and has an eastward increasing velocity and density structure. This portion of crust probably represents faulted, heavily intruded continental crust, with basaltic flows ponded in a basement low forming this portion of the wedge and with sills at the base yielding a bright reflection signature.

The seaward-dipping wedge thickens dramatically between km 75 and km 85. The base of the wedge is defined here by reflection terminations. No coherent crustal reflectivity is observed beneath the wedge. It is likely that little or no preexisting continental crust is present beneath this portion of the wedge, as the underlying velocities increase dramatically to 7.3-7.5 km/s. Within this portion of the wedge at least three distinct units are observed, bounded by apparent unconformity surfaces with upper and lower reflection terminations. These surfaces presumably represent periods of volcanic hiatus accompanied by erosion at or near sea level. The seaward limit of the wedge is well defined in the migrated section at km 95 along the post-rift unconformity surface. This point probably represents the location where volcanism became primarily submarine.

There is no readily identifiable Moho reflection observed in the MCS data east of km 70. Strong post-critical Moho reflections are characteristic of the wide-angle data, however, and we have migrated these reflections into the depth image. There are several reasons for doing this which we believe are borne out by the resulting image (Figure 7b). One reason is to generate a more complete reflectivity image. The reflectivity images of multi-fold seismic profiling inform us about crustal structure, and inspire our interpretations of that crustal structure, by means of the visual presentation of reflector geometries. By migrating the wide-angle PmP events into the image, we increase its visual impact and information content. The bulge in the Moho near km 50, for example, is now apparent. The basement east of the seaward-dipping wedge is placed in context with respect to the Moho, rendering the seaward thinning of the igneous crust a striking feature of the image. The migrated Moho image also provides a view of the data coverage associated with this reflector. In this case, we see that the coverage is complete between kms 50 and 200, but not overly redundant. If the coverage were more redundant, a situation achieved through increased instrument density, then wide-angle migration would provide a means of refining crustal velocities via focusing analyses, as well as a more detailed image of crustal reflectivity. At the present level of data redundancy, however, interpretations based on the character of the Moho image are not justified.

Gravity modeling

The images of seismic velocity and reflectivity we have presented, together with gravity measurements along the profile, provide a basis for crustal density modeling. The density model shown in Figure 8 is based on the seismic results and agrees well with the density model presented by *Holbrook et al.* [1994b]. The gravity response of the model, calculated using the Fourier method described by *Parker* [1973], is compared to the gravity profile extracted from the gridded *DNAG* [1987] compilation of gravity measurements. The

principal features of the observed data include a gravity high bounded by steep gradients between kms 20 and 100, a gravity low between kms -40 and 20, and a gentle positive gradient westward of km -40 punctuated by three short-wavelength anomalies. The density model demonstrates that the shelf-edge gravity high is due to dense material associated with the high velocity material of the Figure 3 model. The steep gradient inboard of the high is due to the abrupt increase in density near km 40. The seaward gradient is due to deepening water across the shelf edge. The gravity low between kms -40 and 20 is due to low density material in the upper crust and not a landward deepening of Moho as presented in the *Holbrook et al.* [1994b] model. The positive westward gradient may be explained by a thinning upper crustal layer, though this thinning is not well constrained by the seismic data.

The gridded density model enables us to evaluate the current state of crustal isostatic equilibrium by balancing the "columns" of the density model with a mantle density of 3.3 gm/cc. The difference between the balanced Moho structure and the Moho structure of the density model represents the surface topography of a crust in local isostatic equilibrium with respect to the mantle (Figure 8a). The crust is nearly in isostatic equilibrium, but a ~0.5 km high near km 0 and a ~0.8 km low near km 75 are required for complete Airy equilibrium. This suggests that the crust is at present exerting a moment on the margin lithosphere. The isostatically balanced crust with the sedimentary burden removed has a monotonically shallowing Moho (Figure 8c). The mantle bulge observed in the present day crust is thus due primarily to the sedimentary load of the marginal basin.

Subsidence modeling

The high quality image of the seaward-dipping wedge (SDW), the likelihood that features within the wedge represent paleo-depth markers, and the crustal density model based on seismic velocities enable estimation of the total thermal subsidence of the margin

and provide a unique opportunity to characterize subsidence during the first several million years following breakup. The total thermal subsidence constrains the range of possible mantle thermal structures that are consistent with the subaerial basalt extrusion that accompanied crustal breakup. Margin uplift and melt chemistry and volume are related to mantle potential temperature and thermal lid thickness [*White and McKenzie,* 1989]. *Kelemen and Holbrook* [1995] have shown that the seismic velocities observed along this and other U.S. East Coast margin transects imply a chemistry that requires melting at high average pressures, and they suggest a petrogenetic model where melting occurs at elevated potential temperatures (~1500°C) beneath an extending but still thick (~100 km) thermal lid. We will demonstrate the conditions required for consistency of this type of model with the total margin subsidence. The abrupt seaward termination of the SDW and the submarine formation of normal mid-ocean ridge crust only ~20 m.y. after emplacement of the SDW basalts suggests that mantle temperatures quickly cooled to those of the normal mid-ocean ridge basalt source (~1300°C). The early subsidence history of the margin constrains the rate of mantle cooling and, indirectly, the general distribution of hot mantle material at breakup.

Our subsidence analysis is based on interpretations of the structure and stratigraphy of the seaward-dipping wedge. Our key interpretive assumptions are: 1) the SDW represents a layered sequence of subaerially extruded basalts, 2) the outboard unit of the SDW overlies crust comprised entirely of accreted igneous material, 3) the seaward termination of the SDW along the basement surface represents the transition to predominantly submarine volcanism, and 4) prominent sequence boundaries within the SDW represent paleo-sealevel surfaces marking periods of volcanic hiatus, possibly accompanied by erosion and/or sediment deposition, during ongoing subsidence. The first of these interpretations has been discussed at length by *Sheridan et al.* [1993], *Holbrook et al.* [1994b], and *Talwani et al.* [1995], and is based on, among other things, the velocity of the SDW and the similarity

of this unit to seaward-dipping wedges of the North Atlantic margins which have been drilled and found to be subaerial basalts [cf. *Eldholm and Grue*, 1994]. The basis for our second interpretation was discussed in a previous section where we noted that two distinct units within the SDW, an inboard and outboard, span the continent-ocean transition, that the inboard unit rests on thinned continental crust, and that the much thicker outboard unit overlies crust with seismic velocities of ~7.5 km/s and is therefore very likely comprised only of accreted igneous material. Our third interpretation follows from the second and from the *Mutter et al.* [1985] model for seaward-dipping wedge formation in which the wedge basalts represent the extrusive component of "subaerial seafloor spreading" and the seaward termination of the SDW represents the submergence of the spreading center.

The fourth interpretation follows from the second and third and from the seismic character of the SDW. The submergence of the margin a short time after crustal breakup suggests that the margin and the SDW began to subside upon crustal failure. The lack of evidence for faulting within the SDW suggests that this subsidence was in response to a continuous, long wavelength subsidence mechanism, such as mantle cooling, as opposed to a crustal-scale mechanism. Subsidence would have continued through periods of volcanic hiatus, and it is reasonable to assume that during extended periods of hiatus the SDW may have subsided to near sealevel and experienced erosion and possibly shallow marine deposition. Drilling results from ODP Site 642 on the Vøring volcanic margin reveal that basaltic flow units of the SDW there are commonly separated by erosional features and sediments deposited in both subaerial and shallow-water environments [*Shipboard Scientific Party*, 1987; *Planke and Eldholm*, 1994; *Planke* 1994]. At the Clubhouse Crossroads drill site near Charleston, S.C., similar sediments were found separating basalt flows thought to be related to the offshore Carolina Trough SDW [*Gottfried et al.*, 1983; *Austin et al.*, 1990]. While the majority of these sediments seem to be subaerial, some are shallow marine. Volcanic hiatus accompanied by ongoing

subsidence and erosion, followed by renewed volcanic activity, would result in sequence boundaries within the SDW characterized by onlapping reflectors above the boundary and truncated reflectors below the boundary. Several sequence boundaries of this character are readily identified in the migrated MCS image, and these are taken to represent paleo-sealevel surfaces (Figure 9).

A possible crustal configuration at the time the volcanic center subsided below sealevel is illustrated in Figure 9 using the depth-migrated MCS data. In generating Figure 9, we first used the density model and local isostasy to remove the sedimentary load. We then removed the crust east of km 95, the seaward termination of the SDW along the basement, and, assuming symmetric rifting and volcanic deposition, mirrored the remaining crust about the km-95 point. The point at the surface in the center of Figure 9, labeled point III, represents the center of volcanism at the time just prior to the onset of submarine volcanism. The current unloaded depth of point III in Figure 10, ~2.8 km, therefore represents the thermal subsidence of the margin since the time when the volcanic center was at this location.

Two prominent sequence boundaries and the points I and II at the distal end of these boundaries are also indicated in Figure 9. In accord with the above assumptions, we interpret points I and II to have been at or near sealevel at the time the unconformity surfaces were cut and, at that time, to have been at or near the volcanic center. As for point III, the change in depth of points I and II to their current position below sealevel is due to overburden and thermal contraction of the crust and mantle. Crustal thinning played no role in the subsidence of the crust seaward of about km 90: crustal rifting was complete by this point and igneous accretion was taking place. The amount of thermal subsidence the margin has undergone since these surfaces were cut is obtained as for point III, by unloading the material above and isostatically balancing the crust (Table 1).

The calculated subsidence for points I, II, and III is dependent upon the crustal densities determined from gravity-anomaly modeling. As these determinations are nonunique, we demonstrate the sensitivity of the calculated subsidence on the density model and determine extremal bounds on the subsidence by considering a variety of velocity/density relationships determined for sedimentary and igneous rocks. The vertical column of velocity and density values extracted from the gridded models of Figures 3 and 8 at the point-I horizontal location are plotted against each other in Figure 10. The bars on these cross-plotted values represent 5 percent variation in density for the sedimentary rocks and 3 percent variation for the igneous rocks. The range of laboratory-determined velocity/density relationships suggests that density profiles using values 5 and 3 percent below the model values and 5 and 3 percent above should effectively encompass the entire range of reasonable density variation insofar as the subsidence calculation is concerned. The subsidence calculated using these extremal density profiles are given in Table 1.

Total thermal subsidence

The total thermal subsidence of the margin constrains the range of past mantle thermal structures. We are interested in how hot or cold and how thick or thin the lithosphere could have been at the time of crustal breakup. In particular, we would like to test whether *Kelemen and Holbrook's* [1994] petrogenetic model is consistent with margin subsidence. We consider the total thermal subsidence of point I, the point closest in space and time to crustal failure. We employ the concept of isostatic compensation to relate the measured subsidence to density variations by requiring the mass in a given vertical column of the earth to remain constant [cf. *Turcotte and Schubert*, 1982]. As it is unlikely that significant compositional variations have occurred since margin rifting, we may confidently ascribe density variations to variations in thermal structure, and, as we are at present only interested in the total subsidence that has occurred since point-I time and not the pattern of

subsidence, our analysis only requires a reasonable parameterization of past and present thermal structure. The thermal structure of the present-day, ~190-m.y.-old margin lithosphere is well approximated by a linear, steady-state conductive geotherm overlying an adiabatic mantle with a "normal" potential temperature of ~1300°C. This is consistent with either a "plate" [*Parsons and Sclater*, 1977; *Sclater et al.*, 1981] or a "half-space" model [*Chapman and Pollack*, 1977] of cooling. Previous studies of Atlantic margin subsidence have assumed plate cooling with an asymptotic plate thickness of 125 km [e.g. *Sawyer*, 1982; *Keen and Dehler*, 1993]. There is considerable seismological evidence [cf. *Jordan et al.*, 1989], however, that suggests an asymptotic thickness of ~250 km [e.g. *Burov and Diament*, 1995] or a half-space cooling model is more appropriate for continental lithosphere. We therefore parameterize the present-day thermal structure by a linear geotherm extending to some unspecified depth, Z_B, with a basal temperature, T_B (Figure 11). With ρ_0 as the mantle density at $T=0°C$, we take the density above Z_B to be $\rho(z)=\rho_0(1-\alpha T(z))$, with a coefficient of thermal expansion $\alpha=dV/VdT$, and the density below Z_B to be $\rho(z \geq Z_B)=\rho_0(1-\alpha T_B)$.

The designation of a reasonable density profile for the time represented by point I requires several other considerations, including the thermal structure of the lithosphere, the temperature of the convective mantle, and the depth of aesthenospheric compensation. *White and McKenzie* [1989] point out that melt-depletion density reduction of the mantle and magmatic additions to the crust also affect buoyancy at volcanic rifted margins. We need not consider these factors at present, however, as mantle depletion beneath point I has presumably remained constant since point-I time, and our interpretation of crustal accretion involves additions only on top and to the east of point I with time, in conjunction with the *Mutter* [1985] model. It is thus reasonable to parameterize the density profile in terms of a thermal structure consisting of a conductive lid of some thickness, Z_L, overlying an adiabatic region with potential temperature T_0. We will assume a linear conductive

geotherm with basal temperature $T_{B'}$, consistent with instantaneous extension of a thermal lid in equilibrium with an aesthenospheric temperature $T_{B'}$. While the actual shape of the extended thermal-lid geotherm may have been concave, linear or convex depending on, among other things, the state of thermal equilibrium prior to extension, the history of temperature variation in the convective mantle, and the rate of extension, variations from linearity in the lid would have a relatively small effect on the total buoyancy of the column. In the convective mantle beneath the thermal lid, the effective depth of compensation may be limited by viscous stresses of convection that tend to balance thermal buoyancy forces [*Parsons and Daly*, 1983]. Studies of hotspot swells suggest compensation depths of 70 to 200 km [e.g. *Haxby and Turcotte*, 1978; *Detrick et al.*, 1986; *Courtney and White*, 1986; *McNutt and Shure*, 1986]. We consider compensation down to a depth Z_C such that for depths $Z_L \leq z \leq Z_C$, $\rho = \rho(T=T_{B'})$, and for depths $z > Z_C$, $\rho = \rho(T=T_B)$, making no requirement that Z_C be either greater or less than the current lid thickness Z_B (Figure 11). Given these assumptions, it is straightforward to calculate the paleo potential temperature required to explain a given thermal subsidence, Z_T, for a given set of values Z_B, T_B, Z_L, Z_C, and Z_S, the rebounded height of the overburden, as

$$T_0 = T_{B'} - AZ_L \tag{1a}$$

$$T_{B'} = \frac{-(I + C - Z_C)}{\alpha(Z_C - \frac{1}{2}Z_L)} \tag{1b}$$

$$I = (Z_B - Z_T)\left\{1 - \frac{\alpha T_B}{(Z_B + Z_S)}\left[Z_S + \frac{1}{2}(Z_B + Z_T)\right]\right\} \tag{1c}$$

$$C = (Z_C - Z_B)(1 - \alpha T_B), \tag{1d}$$

where A is the adiabatic geothermal gradient.

We solve (1) for the bounded values of point-I subsidence, Z_{T-} and Z_{T+}, from Table 1, and for a family of discrete current lid thicknesses Z_B=150, 175, 200, 225, and 250 km over a range of values for Z_L, with T_B=1330°C, $A = .3°C/km$ and α=3.2x10^{-5} °C^{-1} [*Turcotte and Schubert*, 1982]. The results of these calculations are shown in Figure 12 for various values of Z_C. A box designating the pressure/temperature conditions for the initially-emplaced melts as determined by *Kelemen and Holbrook* [1995], defined by a potential temperature range of 1450-1550°C and an average pressure of melting of 3.5-4.0 GPa, is also shown. The pressure scale is determined by assuming that melting begins at 120 km depth, proceeds at a rate of 12% per gigapascal of decompression [*McKenzie and Bickle*, 1985], and ends at the base of the conductive geotherm, Z_L. This gives an average pressure of melting of $P_{avg}[GPa] = 2+Z_L/60$. This pressure scale is approximate and only applicable to temperatures between 1450-1550°C.

The results of Figure 12 demonstrate that the *Kelemen and Holbrook* [1995] model of high temperature melting beneath a thick thermal lid is consistent with a current thermal lid thickness of 200-250 km. Thicknesses on this order are consistent with the age of the margin and plate cooling with an asymptotic thickness of 250 km [*Burov and Diament*, 1995] and are generally consistent with seismological determinations of continental thermal-lid thickness [e.g. *Jordan et al.*, 1989; *Polet and Anderson*, 1995]. We may therefore conclude that the results of *Kelemen and Holbrook* [1995] are consistent with the subsidence of the margin. In addition, we point out that the commonly assumed present-day thermal-lid thickness of 125 km requires past conditions that are in some sense extreme - near infinite lithospheric extension at point-I time, potential temperatures exceeding estimates of maximum mantle temperature variations (~350°C, *Sleep* [1992]), and deep compensation depths.

Early subsidence of the basaltic wedge

We now consider the pattern of subsidence during the deposition of the seaward-dipping wedge. Table 1 indicates that there was ~0.90 km of subsidence between point-I time and point-III time in addition to subsidence from loading. The small lateral separation between these points (~2 km) suggests that this subsidence occurred quite rapidly. The rapidity of this initial subsidence has important implications for the distribution of aesthenospheric buoyancy sources, and it is thus important to estimate the time separating points I, II, and III.

Bounds on the duration of time seperating points I, II, and III can be estimated by considering spreading rates before and after the time of crustal failure. The 2 km seperation between points I and III is too small to reasonably constrain a minimum time of seperation between these points based on spreading, as volcanism at active spreading centers commonly occurs over lateral distances of this order. We are more interested in the maximum bound on this time, however, as a conservative bound on the rapidity of subsidence, and we may estimate this bound by considering the minimum spreading rate. Spreading rate may constrained by the date of the onset of crustal rifting, the age of the oldest dateable oceanic magnetic lineation, and a knowledge of the extension that took place between these two times. Triassic basin sediment ages indicate that rifting began at ~225 Ma [*Manspeizer* et al., 1989]. We show below that 60 to 80 km of extension occurred prior to crustal failure. A seafloor-spreading type of crustal emplacement followed crustal failure (the lithospheric mantle was probably still thinning during this time), leading eventually to true seafloor spreading. The oldest dateable oceanic magnetic lineation is the Blake Spur Magnetic Anomaly (BSMA) at ~170 Ma [*Klitgord and Schouten*, 1986]. The BSMA lies ~220 km east of the continent-ocean transition (near km 80). An age of 190 Ma for crustal failure, corresponding to the end of onshore igneous activity [*Manspeizer* et al., 1989], implies a spreading half-rate of 11 mm yr^{-1} based on the distance to the BSMA and

0.86 mm yr^{-1} based on 60 km of pre-rift extension. The 190 Ma age for the onset of seafloor spreading is somewhat arbitrary, but it provides a conservatively small spreading rate during crustal extension. Using this minimum spreading rate estimate, we determine a conservative bound on the maximum time seperating points I and three of 2.3 m.y. The 11-mm-yr^{-1} rate gives a seperation time of 0.2 m.y. which may serve as a minimum bound, though this time is not well constrained. We point out that the duration of most flood basalt events rarely exceeds 5 m.y. [*Coffin and Eldholm*, 1994], and, as the igneous production between point-I and point-III time clearly represents less than half of that for this large igneous event, we see that our 2.3 m.y. estimate is conservative with respect to observations from other large igneous provinces.

The rapidity of the SDW subsidence is demonstrated in Figure 13, where we plot the subsidence of points I, II, and III as of function of time calculated using the minimum and maximum spreading rate estimates. For reference, we also show the subsidence predicted for one-dimensional cooling of lithosphere extended by factors of $\beta=2$ and $\beta=\infty$ using *McKenzie's* [1978] uniform extension model, and the maximum subsidence rate observed by *Farnetani and Richards* [1994] in numerical models of hot blobs impacting lithosphere from below, ~0.1 km m.y.$^{-1}$. The subsidence from the numerical models represents the decrease in dynamic uplift as the plume head disperses in the aesthenospheric low-viscosity channel. A similar rate was found by *Christensen* [1992] in modeling a plume from the 660 km discontinuity. Clearly, the initial subsidence of the wedge proceeded at a much faster rate than either of these two mechanisms can account for.

Discussion

Crustal thickness

The crust beneath the mid-Atlantic Coastal Plain has a fairly uniform thickness of ~35 km with an overlying sedimentary section that thickens to ~2 km from the Fall Line to the

coast. This result is in contrast to previous crustal thickness estimates for the Coastal Plain, which are based primarily on a regional time-term experiment (where crustal thickness is inferred from mantle diving-wave phase, P_n, delay times) carried out in the 1960's [*James et al.*, 1968]. *James et al.* [1968] show variations in crustal thickness from 30 to 45 km beneath the Coastal Plain from North Carolina to Maryland, with considerable variation in the Chesapeake Bay area. These values depend on an assumed velocity structure, however, and are particularly sensitive to sediment-thickness variations. Along the I-64 reflection seismic line [*Pratt et al.*, 1988] (Figure 1), *James et al.* [1968] show crustal-thickness variations from 32 to 45 km, with a prominent 45-km-thick bulge near the coast. As this type of variation is not observed beneath the EDGE line, and as the gravity profile along the I-64 transect differs little from that along the EDGE line, it is likely that the P_n traveltime anomalies observed in the time-term study were not due to variation in crustal thickness, but rather to the Triassic basin imaged along the I-64 line. In fact, the two stations used to infer the 45-km-thick bulge are situated directly over this basin.

The uniformity of Coastal Plain crustal thickness is probably pervasive throughout the Chesapeake Bay area and possibly as far south as Georgia. The best constrained observation of the early Chesapeake Bay explosion studies is the P_n crossover distance of ~150 km [*Tatel et al.*, 1951; *Hart*, 1954; *Tuve et al.*, 1954]. This is consistent with our observations for Stn 7 and Stn 11 and the crossover distance predicted from our velocity model. The I-64 reflection data show essentially no reflections beneath the basement on the Coastal Plain, and therefore provide no constraint on Moho depth there. Reflection data from near the coast in New Jersey, however, show laminated lower-crust reflections that terminate at ~12 s two-way traveltime, consistent with a 35-km-deep Moho [*Sheridan et al.*, 1991]. Refraction surveys just west of the Fall line in Georgia [*Hawman*, 1996] and on the shelf offshore Georgia [*Lizarralde et al.*, 1994] reveal crustal structure very similar to that of the EDGE line, and all observed reflection-Moho events from deep seismic

surveys on the mid-Atlantic Coastal Plain occur at 12-13 s [*Cook et al.*, 1979, 1981; *Behrendt et al.*, 1983; *Nelson et al.*, 1985].

Crustal thinning and extension,

The majority of crustal thinning was confined to a 75-km-wide region beneath the shelf, where the crust thinned by 50 to 85% and then failed. The thinned crust appears to be heavily intruded but not significantly underplated. The only evidence for underplating is the bright sequence of lower crustal reflections underlying the thinned crust. Beyond km 82 the extrusive volcanics dramatically thicken with respect to those extruded onto extended continental crust, and the crust beneath the extrusives has velocities of ~7.5 km/s. This high velocity material is the plutonic counterpart to the extrusives and not underplated material [*Holbrook et al.*, 1994b; *Talwani et al.*, 1995].

The migrated MCS data delineate the top of thinned continental crust beneath the volcanic wedge, enabling an accurate determination of crustal extension. Considering only the portion of the crust beneath the sediments and the volcanic wedge, the crust has apparently thinned from 34 km to 15 km between km 10 and km 84. Significant magmatic intrusion of the crust in this region, implied by the laterally increasing velocity, may mask a larger extension. A crustal thinning profile based on the present-day Moho will thus yield a minimum estimate for crustal extension. Using the present-day Moho to define the crustal-thinning profile in terms of the extension factor, β, for an unextended thickness of 35 km, we determine a minimum estimate of ~30 km for crustal extension by integrating $(1-1/\beta)$ from km -180 to km 84 (Figure 14). Total extension is thus ~60 km if, as *Dunbar and Sawyer* [1989] have demonstrated, the thinning profile is more or less symmetric on the conjugate margin. We can calculate a maximum estimate for crustal extension by assuming that the average crustal velocity between km 10 and km 84 reflects mixing between 6.4 km/s material, the average velocity of the unextended crust, and 7.5 km/s material, the

lower crustal velocity east of km 84. Using this mixing line, shown dashed in Figure 14, to define the thinning profile, we calculate a maximum crustal exension of ~40 km, giving 80 km of total extension for symmetric thinning (Figure 14).

The observed half-extension of 30 to 40 km is considerably less than the ~110 km extension determined by *Sawyer* [1985] and *Dunbar and Sawyer* [1989] from an analysis of total tectonic subsidence. There are two reasons for this discrepancy. First, these workers used a relation between total tectonic subsidence (TTS) and β, TTS=7.82 (1-1/β), that is based on a pre-extensional crustal thickness of 30 km [*Le Pichon and Sibuet*, 1981]. A pre-extensional crustal thickness of 35 km changes the multiplicative factor F=7.82 km to F=9.2 km. More significantly, these workers determined the transition from thinned-continental to oceanic crust from the seawardmost inflection in their TTS profiles. We demonstrate in Figure 14 that this inflection occurs near km 165, considerably seaward of the last occurrence of continental crust. The TTS profile of Figure 14 was determined by multiplying the sediment-unloaded basement depth of Figure 8b by $\rho_{mantle}/(\rho_{mantle}-\rho_{water})$=1.65. The extension determined from this TTS profile using the *Le Pichon and Sibuet* [1981] relation and integrating from km -180 to km 165 is 95 km for F=7.82 and 80 km for F=9.2.

Our new estimate of total crustal extension has implications for Atlantic basin plate reconstructions. *Dunbar and Sawyer* [1989] found that a non-rigid plate reconstruction, using their TTS-determined extension values and *Klitgord and Schouten's* [1986] pole of rotation, required and an additional 155 km of closure beyond *Klitgord and Schouten's* [1986] maximum closure position. This difference is very similar to the 145- to 165-km discrepancy between our 60- to 80-km estimate of total extension and *Dunbar and Sawyer's* [1989] average value of 225 km. This result thus supports the original maximum closure determination of *Klitgord and Schouten* [1986].

The Coastal Plain crust, in addition to being relatively unextended, shows no evidence of significant mafic intrusion or underplating. Significant magmatic additions to the crust are constrained to a region extending only 45 km inboard of the point of crustal failure. There is no evidence for high velocity material (> 7.0 km/s) within the lower crust landward of model km 40, confirming the analysis by *Holbrook et al.* [1992] from EDGE strike Line 802. *Tréhu* [1987] and *Lizarralde et al.* [1994] presented similar results for the Gulf of Maine and along the shelf near the Carolina trough off of Georgia. It would seem that highly focused magmatism is characteristic of the U.S. East Coast rifted margin.

Gravity anomalies and isostatic equilibrium of the crust

A crustal density model that includes lateral density variation consistent with velocity variation reproduces the observed gravity anomaly pattern and is nearly in local isostatic equilibrium (Figures 3 and 8). It is likely that large lateral constrasts in velocity and density are characteristic of the U.S. East Coast margin [*Holbrook and Kelemen*, 1993]. Density models for the margin that fit observed gravity by exclusively invoking crustal-thickness variations, such as *Watts and Marr's* [1995] model for the Baltimore Canyon, are therefore probably not correct. Not surprisingly, *Watts and Marr* [1995] find that fitting gravity with only crustal thickness variations results in an isostatically unbalanced crust. They then infer variations in lithospheric mechanical strength from the pattern of mass disequilibrium. This type of analysis seems questionable given our results from the nearby EDGE Line.

Margin subsidence

Taking advantage of the high quality MCS and wide-angle seismic data along this transect, we have for the first time used structural information from beneath the sedimentary section to characterize total margin subsidence and the earliest subsidence history of a volcanic margin. We have shown that a petrogenetic model for the initially emplaced igneous material involving high average pressures of melting (3.5-4.0 GPa) and

high mantle potential temperatures (~1500°C) [*Kelemen and Holbrook*, 1995] is consistent with the total subsidence of the margin. This consistency requires a present-day thermal lid thickness of ~225 km, considerably thicker than the commonly assumed 125 km. We emphasize that a 225-km-thick present-day thermal lid is not required by the subsidence data. Figure 12 demonstrates that a wide range of reasonable past and present thermal structures may explain the subsidence, with the thickness of the present-day lid scaling nearly linearly with paleo-lid thickness. A 125-km-thick present-day lid, however, requires somewhat extreme conditions at the time of crustal failure. A thicker present day thermal lid is consistent with the notion that significant lateral variations in lithospheric-mantle structure occur across rifted continental margins [e.g. *Jordan*, 1979].

The early subsidence history of the volcanic wedge provides a set of observations against which dynamic models of volcanic-margin formation can be tested (Figure 13). The main factors that may have contributed to the rapid early subsidence of the SDW include cooling of the thermal lid, cooling of the aesthenospheric mantle, reduction of the compensation depth in the aesthenospheric mantle, and reduction in the fraction of melt retained in the mantle. The effects of these mechanisms are buffered by the mantle-depletion density reduction that accompanies melting. While a complete evaluation of these factors requires dynamical modeling, some of the possible effects can be deduced from simple reasoning. For example, cooling or thickening of the thermal lid is unlikely to have contributed to the early SDW subsidence. It is likely that the lid was thinning during this time and still warming toward equilibrium with the abnormally hot underlying mantle. Reduction in the fraction of retained melt is also an unlikely contributor to subsidence. If some change in the fraction of retained melt was associated with the removal of the overlying continental crust upon crustal failure (i.e. if crustal failure represented a change in the effective permeability of the lithosphere), a sufficient volume of melt had already been extruded by point-I time for this change to have occurred, given magma ascent rates on the

order of meters per year [*Turcotte and Schubert*, 1982]. Crustal-level magma resevoir deflation is also an unlikely contributor, as more than 70 years of observations in Hawaii demonstrate that these mechanisms produce subsidence on the order of centimeters [*Ryan et al.*, 1983].

Cooling of the hot underlying mantle and/or reduction of the effective compensation depth of this layer are probably the two largest contributors to the early SDW subsidence. Ascribing all of the early subsidence to the region beneath the thermal lid, we may relate subsidence to temperature and compensation depth variation simply as $Z_T = \alpha\, \Delta T\, Z_H$, where Z_H is either the change in the compensation depth of the hot column and ΔT is the temperature contrast between hot and normal mantle, or Z_H is the height of the compensating column and ΔT is the amount of cooling required to explain the subsidence Z_T. Thus, for a temperature contrast of 300°C we would require a change in compensation depth of ~95 km to explain 0.9 km of subsidence.

Cooling of the hot aesthenospheric mantle may occur through conduction, advection, and convection. Figure 13 suggests that conductive cooling is unlikely to have contributed significantly to the early subsidence. Advective cooling is likely to have occurred via melt extraction and extension. Melting affects mantle buoyancy by absorbing latent heat, decreasing the density of the residuum, and advecting heat out of the system. While the first two effects tend to produce nearly equal but opposite changes in density [*Watson and McKenzie*, 1991], advection of heat to the surface can have a dramatic impact on the average temperature of the hot region provided the initial volume of hot material is not too large and that it is not resupplied with hot material from below, in that every unit volume of melt extracted from the system must be replaced by a unit volume of mantle with normal temperature. Extension produces a similar effect if a finite volume of hot material is considered. Hot mantle will flow to fill the space created by extension, and the thickness of the hot region will decreases in direct proportion to the space created. Small-scale

convection, being more than an order of magnitude more efficient than conduction, undoubtedly had a significant impact on cooling the hot region, and some form of active upwelling is probably required to explain the volume of melt produced [*Kelemen and Holbrook*, 1995]. The vigor of convection also affects the effective compensation depth of the hot region, as the intrinsic buoyancy of the material is countered by viscous stresses. Again, the rate of convective cooling and the vigor of convection are both dependent on the dimensions of the hot region.

From these qualitative considerations of the initial volcanic-wedge subsidence, and from the distribution of volcanics along the margin [*Holbrook and Kelemen*, 1993], we may conclude that the initial spatial distribution of hot material in the upper mantle was long, but not wide or deep. We speculate that this situation may be explained by topography at the base of the lithosphere prior to rifting. The thinner lithosphere of accreted Appalachian terranes, situated between the thicker cratonic lithospheres of Africa and North America, may have provided a "thin spot" [*Thompson and Gibson*, 1991] in which buoyant mantle material could accumulate. A uniform distribution of material in such a thin spot is generally consistent with several of the sources that have been proposed for large-igneous-province (LIP) magmatism, including the "incubation" [*Kent et al.*, 1992] of a tail-less plume, or blob (or series of small blobs), risen from a deeper thermal boundary layer, and the "perisphere" model of *Anderson* [1994, 1995] in which a hot, enriched reservoir is common to most continental sublithospheric mantle.

The U.S. East Coast LIP, once viewed as problematic for hot-spot theories of LIP magmatism, is in fact consistent with elements of most theories for LIP formation [cf. *Coffin and Eldholm*, 1994] and is probably a typical volcanic margin. The primary arguments against applying the early plume theories [e.g. *White and McKenzie*, 1989] to the U.S. East Coast are the lack of independent evidence for a hot-spot track and the linear shape of the igneous province [*Holbrook and Kelemen*, 1993]. *White* [1992] points out,

however, that the most important factors in the formation of volcanic margins are the presence of a widely distributed region of hot material beneath a locus of rifting, and that rapid, lateral, sub-lithospheric flow of this material is likely. Thus, while plumes are a reasonable source for hot mantle material, the material's ultimate distribution probably depends more on relief at the base of the lid channeling the material's lateral flow than on either the location or the plume-, blob-, or sheet-like geometry of the upwelling. In this sense the plume and perisphere theories are essentially equivalent. Moreover, as thinner lithosphere will often be weaker lithosphere, hot material will tend to come to rest beneath the likeliest locations of future rifting. It is not surprising, then, that voluminous initial volcanism is common to many rifted margins, and we may speculate that this systematic process is fundamental to the evolution of continental lithosphere.

Conclusions

We have presented results from a 420-km-long seismic transect across the U.S. East Coast rifted margin, extending eastward from the Fall Line across the Coastal Plain to oceanic crust offshore. These results reveal the crustal structure beneath the mid-Atlantic Coastal Plain, define the crustal-thinning profile from non-extended continental crust to the continent-ocean transition, clarify the relationship between imaged crustal reflectivity and seismic velocity offshore, and have implications for the style and localization of rifting, total margin extension, pre-rift plate reconstructions, the onshore extent of rift magmatism, the state of stress along the present-day margin, and the thermal structure of margin lithosphere. The major conclusions of this study are:

1) The crust beneath the Coast Plain is ~35 km thick, largely unextended, and shows no evidence for magmatic additions of sufficient volume to affect seismic velocity.

2) Rift-related crustal thinning was focused in a 75-km-wide region extending from beneath the shelf to the slope. The crust thinned by 50 to 80% and then failed.

3) The total half-extension of the crust is 30 to 40 km. This is significantly less than the ~110 km of half-extension estimated from studies based on sediment thickness and is consistent with a non-rigid Jurassic plate reconstruction to the *Klitgord and Schouten* [1986] maximum closure position.

4) High quality seismic data can be used to exploit the stratigraphy of subaerially-extruded basalts on volcanic rifted margins for analyses of margin subsidence.

5) A petrogenetic model for initial seafloor-spreading magmatism involving high average pressures of melting (3.5-4.0 GPa) and high mantle potential temperatures (~1500°C) is consistent with the total subsidence of the margin for a present-day thermal lid thickness of ~225 km. It is difficult to explain both the early margin subsidence and the formation of the initial melts with a present-day lid thickness much less than ~175 km.

6) The rapid initial subsidence of the margin following crustal failure suggests that the initially hot underlying mantle cooled very quickly, implying an initial distribution of hot mantle that was of limited and finite extent rather than a continuous deep upwelling or a ubiquitously warm upper mantle.

References

Anderson, D.L., The sublithospheric mantle as the source of continental flood basalts; the case against the continental lithosphere and plume head reservoirs, *Earth Planet. Sci. Lett.*, *123*, 269-280, 1994.

Anderson, D.L., Lithosphere, asthenosphere, and perisphere, *Rev. Geophys.*, *33*, 125-149, 1995.

Austin, J. A. Jr., P. L. Stoffa, J. D. Phillips, J. Oh, D. S. Sawyer, G. M. Purdy, E. Reiter, and J. Makris, Crustal structure of the southeast Georgia embayment–Carolina trough: Preliminary results of a composite seismic image of a continental suture(?) and a volcanic passive margin, *Geology, 18*, 1023-1027, 1990.

Behrendt, J.C., Structural interpretation of multichannel seismic reflection profiles crossing the Southeastern United States and the adjacent continental margin-Decollements, Faults, Triassic(?) basins and Moho reflections, in *Reflection Seismology: The Continental Crust, Geodyn. Ser.*, vol. 14, edited by M. Barazangi and L. Brown, pp. 201-214, AGU, Washington, D.C., 1986.

Burov, E.B., and M. Diament, The effective elastic thickness (T_e) of continental lithosphere: What does it really mean?, *J. Geophys. Res.*, *100*, 3905-3927, 1995.

Cambell, I. H., and R. W. Griffiths, Implications of mantle plume structure for the evolution of flood basalts, *Earth Planet. Sci. Lett.*, *99*, 79-93, 1990.

Chapman, D.S., and H.N. Pollack, Regional geotherms and lithospheric thickness, *Geology, 5*, 265-268, 1977.

Christensen, U.R., An Eulerian technique for thermomechanical modeling of lithospheric extension, *J. Geophys. Res.*, *97*, 2015-2036, 1992.

Christensen, N.I., and D.M. Fountain, Constitution of the lower continental crust based on experimental studies of seismic velocities in granulite, *Geol. Soc. Am. Bull.*, *86*, 227-236, 1975.

Christensen, N.I., and W.D. Mooney, Seismic velocity structure and composition of the continental crust: A global view, *J. Geophys. Res.*, *100*, 9761-9788, 1995.

Coffin, M. F., and O. Eldholm, Large igneous provinces: crustal structure, dimensions, and external consequences, *Rev. Geophys.*, *32*, 1-36, 1994.

Cook, F.A., D.S. Albaugh, L.D. Brown, S. Kaufman, J.E. Oliver, and R.D. Hatcher, Thin-skinned tectonics in the crystalline southern Appalachians; COCORP seismic-reflection profiling of the Blue Ridge and Piedmont, *Geology*, *7*, 563-567, 1979.

Cook, F.A., L.D. Brown, S. Kaufman, J.E. Oliver, and T.A. Petersen, COCORP seismic reflection profiling of the Appalachian orogen beneath the Coastal Plain of Georgia, *Geol. Soc. Am. Bull.*, *92*, 738-748, 1981.

Courtney, R. C., and R. S. White, Anomalous heat flow and geoid across the Cape Verde Rise: evidence for dynamic support from a thermal plume in the mantle, *Geophys. J. R. astr. Soc.*, *87*, 815-867, 1986.

Detrick, R.S., R.P. Von Herzen, B. Parsons, D. Sandwell, and M. Dougherty, Heat flow observations on the Bermuda Rise and thermal models of midplate swells, *J. Geophys. Res.*, *91*, 3701-3723, 1986.

Diebold, J.B., P. L. Stoffa, and the LASE Study Group, A large aperture seismic experiment in the Baltimore Canyon Trough, in *The Geology of North America*, vol. I-2, *The Atlantic Continental Margin: U.S.*, edited by R.E. Sheridan and J. A. Grow, pp. 387-398, Geological Society of America, Boulder, Colo., 1988.

DNAG, Decade of North American Geology Committee for the Gravity Anomaly Map of North America, Gravity anomaly map of North America, Geol. Soc. of Am., Boulder, Colo., 1987.

Dunbar, J.A., and D.S. Sawyer, Patterns of continental extension along the conjugate margins of the Central and North Atlantic oceans and Labrador sea, *Tectonics*, *8*, 1059-1077, 1989.

Eldholm, O., and K. Grue, North Atlantic volcanic margins: Dimensions and production rates, *J. Geophys. Res.*, *99*, 2955-2968, 1994.

Forsyth, D.W., Geophysical constraints on mantle flow and melt generation beneath mid-ocean ridges, *AGU Monograph*, *71*, 1-65, 1992.

Gottfried, D., C.S. Annes, and G.R. Byerly, Geochemistry and tectonic significance of the subsurface basalts near Charleston, South Carolina: Clubhouse Crossroads test holes #2 and #3, in Studies Related to the Charleston, South Carolina, Earthquake of 1886 — Tectonics and Seismicity, edited by G.S. Gohn, *U.S. Geol. Surv. Prof. Pap.*, *1313*, A1-A19, 1983.

Grand, S.P., and D.V. Helmberger, Upper mantle shear structure of North America, *Geophys. J. R. Astr. Soc.*, *76*, 399-438, 1984.

Gurnis, M., Large-scale mantle convection and the aggregation and dispersal of supercontinents, *Nature*, *332*, 695-699, 1988.

Hamilton, E.L., Sound velocity-density relations in sea-floor sediments and rocks, *J. Acoust. Soc. Am.*, *63*, 366-377, 1978.

Harry, D. L., and D. S. Sawyer, A dynamic model of lithospheric extension in the Baltimore Canyon Trough region, *Tectonics*, *11*, 420-436, 1992.

Hart, P.J., Variation of velocity near the Mohorovicic discontinuity under Maryland and northeastern Virginia, Ph.D. thesis, Harvard University, Cambridge, 1954.

Hawman, R.B., Wide-angle, three-component seismic reflection profiling of the crust along the East Coast Gravity High, southern Appalachians, using quarry blasts, *J. Geophys. Res.*, *101*, 13,933-13,945, 1996.

Haxby, W. F., and D.L. Turcotte, On isostatic geoid anomalies, *J. Geophys. Res.*, *83*, 5473-5478, 1978.

Hill, R. I., Starting plumes and continental breakup, *Earth Planet. Sci. Lett.*, *104*, 398-416, 1991.

Holbrook, W.S., G.M. Purdy, J.A. Collins, R.E. Sheridan, D.L. Musser, L. Glover III, M. Talwani, J. Ewing, R. Hawman, and S.B. Smithson, Deep velocity structure of rifted continental crust, U.S. Mid-Atlantic margin, from wide-angle reflection/refraction data, *Geophys. Res. Lett.*, *19*, 1699-1702, 1992.

Holbrook, W. S., and P.B. Kelemen, Large igneous province on the U.S. Atlantic margin and implications for magmatism during continental breakup, *Nature*, *364*, 433-436, 1993.

Holbrook, W. S., W. D. Mooney, and N. I. Christensen, The seismic velocity structure of the deep continental crust, in *Continental Lower Crust*, edited by D. M. Fountain, R. Arculus, and R. Kay, pp. 1-43, Elsevier, New York, 1992.

Holbrook, W. S., E. C. Reiter, G. M. Purdy, D. Sawyer, P. L. Stoffa, J. A. Austin Jr., J. Oh, and J. Makris, Deep structure of the U.S. Atlantic continental margin, offshore South Carolina, from coincident ocean bottom and multichannel seismic data, *J. Geophys. Res.*, *99*, 9155-9178, 1994a.

Holbrook, W. S., G. M. Purdy, R. E. Sheridan, L. Glover III, M. Talwani, J. Ewing, and D. Hutchinson, Seismic structure of the U.S. Mid-Atlantic continental margin, *J. Geophys. Res.*, 99, 17,871-17,891, 1994b.

Hutchinson, D.R., J.A. Grow, K.D. Klitgord, and B.A. Swift, The deep structure and evolution of the Carolina trough, *Mem. Am. Assoc. Pet. Geol.*, *34*, 129-152, 1983.

Jarvis, G., and D. McKenzie, Sedimentary basin formation with finite extension rates, *Earth Planet. Sci. Lett.*, *48*, 42-52, 1980.

James, D.E., T.J. Smith, and J.S. Steinhart, Crustal structure of the middle Atlantic states, *J. Geophys. Res.*, *73*, 1983-2007, 1968.

Jordan, T.H., The deep structure of the continents, *Sci. Am.*, *240*, 92-107, 1979.

Jordan, T.H., A.L. Lerner-Lam, and K.C. Creager, Seismic imaging of boundary layers and deep mantle convection, in *Mantle Convection: Plate Tectonics and Global Dynamics*, edited by W.R. Peltier, pp. 98-201, Gordon and Breach, New York, 1989.

Keen, C. E., and S. A. Dehler, Stretching and subsidence: Rifting of conjugate margins in the North Atlantic region, *Tectonics*, *12*, 1209-1229, 1993.

Kelemen, P. B., and W. S. Holbrook, Origin of thick, high-velocity igneous crust along the U.S. East Coast Margin, *J. Geophys. Res.*, *100*, 10,077-10,094, 1995.

Kent, R.W., M. Storey, and A.D. Saunders, Large igneous provinces: Sites of plume impact or plume incubation?, *Geology*, *20*, 891-894, 1992.

Kessinger, W., and P.L. Stoffa, Extended split-step Fourier migration, *Proc. of the Int. Soc. of Expl. Geophys.*, *62*, 917-918, 1992.

Klitgord, K.D., D.R. Hutchinson, and H. Schouten, U.S. Atlantic continental margin; Structural and tectonic framework, in *The Geology of North America*, vol. I-2, *The Atlantic Continental Margin: U.S.*, edited by R.E. Sheridan and J. A. Grow, pp. 19-53, Geological Society of America, Boulder, Colo., 1988.

Le Pichon, X., and J.C. Sibuet, Passive margins: A model of formation, *J. Geophys. Res.*, *86*, 3708-3720, 1981.

Lizarralde, D., W. S. Holbrook, and J. Oh, crustal structure across the Brunswick magnetic anomaly, offshore Georgia, from coincident ocean bottom and multi-channel seismic data, *J. Geophys. Res.*, 99, 21,741-21,757, 1994.

Ludwig, W.J., J.E. Nafe, and C.L. Drake, Seismic refraction in the sea, in *The Sea*, vol. 4, edited by A.E. Maxwell, pp. 53-84, Wiley, New York, 1970.

Manspeizer, W., J. DeBoer, J.K. Costain, A.J. Froelich, C. Çoruh, P.E. Olson, G.J. McHone, J.H. Puffer, and D.C. Prowell, Post-Paleozoic activity, in *The Geology of North America*, vol. F-2, *The Appalachian-Ouachita Orogen in the United Sates*, edited

by R.D. Hatcher, Jr., W.A. Thomas, and G.W. Viele, pp. 319-374, Geological Society of America, Boulder, Colo., 1989.

McKenzie, D., Some remarks on the development of sedimentary basins, *Earth Planet. Sci. Lett.*, *40*, 25-32, 1978.

McKenzie, D., and M.J. Bickle, The volume and composition of melt generated by extension of the lithosphere, *J. Petrol.*, *29*, 625-679, 1988.

McNutt, M., and L. Shure, Estimating the compensation depth of the Hawaiian Swell with linear filters, *J. Geophys. Res.*, *91*, 13,915-13,923, 1986.

Mutter, J. C., Seaward dipping reflectors and the continent-ocean boundary at passive continental margins, *Tectonophys.*, *114*, 117-131, 1983.

Nelson, K.D., J.A. Arnow, J.H. McBride, J.H. Willemin., J. Huang, L. Zheng, J.E. Oliver, L.D. Brown, and S. Kaufman, New COCORP profiling in the southeastern United States, I, Late Paleozoic suture and Mesozoic rift basin, *Geology*, *13*, 714-718, 1985.

Nolet, G., and A. Zielhuis, Low S velocities under the Tornquist-Teisseyre zone: Evidence for water injection into the transition zone by subduction, *J. Geophys. Res.*, *99*, 15,813-15,820, 1994.

Parsons, B. and J.G. Sclater, An analysis of the variation of ocean floor bathymetry and heat flow with age, *J. Geophys. Res.*, *82*, 803-827, 1977.

Parsons, B. and S. Daly, The relationship between surface topography, gravity anomalies, and temperature structure of convection, *J. Geophys. Res.*, *88*, 1129-1144, 1983.

Parker, R. L., The rapid calculation of potential anomalies, *Geophys. J. R. Astr. Soc.*, *31*, 447-455, 1973.

Planke, S., and O. Eldholm, Seismic response and construction of seaward dipping wedges of flood basalts: Vøring volcanic margin, *J. Geophys. Res*, *99*, 9263-9278, 1994.

Planke, S., Geophysical response of flood basalts from analysis of wire line logs: Ocean Drilling Program Site 642, Vøring volcanic margin, *J. Geophys. Res*, *99*, 9279-9296, 1994.

Polet, J., and D.L. Anderson, Depth extent of cratons as inferred from tomographic studies, *Geology*, *23*, 205-208, 1995.

Pratt, T.L., C. Çoruh, J.K. Costain, and L. Glover III, A geophysical study of the Earth's crust in central Virginia: implications for Appalachian crustal structure, *J. Geophys. Res.*, *93*, 6649-6667, 1988.

Royden, L., and C.E. Keen, Rifting process and thermal evolution of the continental margin of Eastern Canada determined from subsidence curves, *Earth Planet. Sci. Lett.*, *51*, 343-361, 1980.

Ryan, M.P., J.Y.K. Blevins, A.T. Okamura, and R.Y. Koyanagi, Magam reservoir subsidence mechanics: theoretical summary and application to Kilauea Volcano, Hawaii, *J. Geophys. Res.*, *88*, 4147-4181, 1983.

Sawyer, D.S., Total tectonic subsidence: A parameter for distinguishing crust type at the U.S. Atlantic continental margin, *J. Geophys. Res.*, *90*, 7751-7769, 1985.

Sclater, J.G., B. Parsons, and C. Jaupart, Oceans and continents: Similarities and differences in the mechanisms of heat loss, *J. Geophys. Res.*, *86*, 1031-1052, 1981.

Sheridan, R.E., R.K. Olsson, and J.J. Miller, Seismic reflection and gravity study of proposed Taconic suture under the New Jersey Coastal Plain: Implications for continental growth, *Geol. Soc. Amer. Bull.*, *103*, 402-414, 1991.

Sheridan, R.E., D.L. Musser, L. Glover III, M. Talwani, J. Ewing, W.S. Holbrook, G.M. Purdy, R. Hawman, and S. Smithson, Deep seismic reflection data of the EDGE U.S. Mid-Atlantic continental margin experiment: Implications for Appalachian sutures, Mesozoic rifting and magmatic underplating, *Geology*, *21*, 563-567, 1993.

Shipboard Scientific Party, Site 642, *Proc. Ocean Drill. Program Initial Rep., 104,* 53-213, 1987.

Sleep, N. H., Thermal effects of the formation of Atlantic continental margins by continental break-up, *Geophys. J. R. astr. Soc., 24,* 325-350, 1971.

Sleep, N.H., Hotspot volcanism and mantle plumes, *Annu. Rev. Earth Planet. Sci., 20,* 19-43, 1992.

Talwani, M., J. Ewing, R.E. Sheridan, W.S. Holbrook, and L Glover III, The EDGE experiment and the U.S. East Coast magnetic anomaly, in *Rifted Ocean-Continent Boundaries,* edited by E. Banda, M. Torné, and M. Talwani, Kluwer Acad. Publ., the Netherlands, 155-181, 1995.

Tatel, H.E., L.H. Adams, and M.A. Tuve, Studies of the Earth's crust using waves from explosions, *Proc. Amer. Phil. Soc., 97,* 658-669, 1951.

Thompson, R.N., and Gibson, S.A., Subcontinental mantle plumes, hotspots, and pre-existing thinspots, *Geol. Soc. Lon. Journal, 148,* 973-977, 1991.

Tréhu, A. M., Data report for large offset OBS data collected during cruise GYRE-85-11 in the Gulf of Maine, *U.S.G.S. Open-File report 87-644,* 56 p., 1987.

Tréhu, A. M., A. Ballard, L. M. Dorman, J. F. Gettrust, K. D. Klitgord, and A. Shreiner, Structure of the lower crust beneath the Carolina trough, U.S. Atlantic continental margin, *J. Geophys. Res., 94,* 10,585-10,600, 1989.

Tréhu, A. M., K. D. Klitgord, D. S. Sawyer, and R. T. Buffler, Atlantic and Gulf of Mexico continental margins, *Mem. Geol. Soc. Am., 172,* 349-381, 1989.

Turcotte, D.L., and G. Schubert, *Geodynamics,* John Wiley, New York, 1982.

Tuve, M.A., H.E. Tatel, and P.J. Hart, Crustal structure from seismic exploration, *J. Geophys. Res.,* 59, 415-422, 1954.

Van der Hilst, R., R. Engdahl, W. Spakman, and G. Nolet, Tomographic images of subducted lithosphere below northwest Pacific island arcs, *Nature, 353,* 37-43, 1991.

Vogt, P., and N. Ostenso, Steady state crustal spreading, *Nature*, *215*, 810, 1967.

Watson, S., and D. McKenzie, Melt generation by plumes: a study of Hawaiian volcanism, *J. Petrol.*, *32*, 501-537, 1991.

Watts, A.B., and C. Marr, Gravity anomalies and the thermal and mechanical structure of rifted continental margins, in *Rifted Ocean-Continent Boundaries*, edited by E. Banda, M. Torné, and M. Talwani, Kluwer Acad. Publ., the Netherlands, 65-94, 1995.

White, R.S., and D. McKenzie, Magmatism at rift zones: the generation of volcanic continental margins and flood basalts, *J. Geophys. Res.*, *94*, 7685-7729, 1989.

White, R.S., Magmatism during and after continental breakup, in *Magmatism and the Causes of Continental Break-up*, edited by B.C. Storey, T. Alabaster, and R.J. Pankhurst, pp. 1-16, Geological Society Special Publication, 68, 1992.

Zelt, C. A., and R. B. Smith, Seismic traveltime inversion for 2-D crustal velocity structure, *Geophys. J. Int.*, *108*, 16-34, 1992.

	Z_T- (km)	Z_T (km)	Z_T+(km)
I	4.03	3.65	3.30
II	3.20	2.97	2.74
III	3.02	2.75	2.55
I-II	0.83	0.68	0.56
I-III	1.00	0.90	0.75

Table 1. Thermal subsidence, Z_T, of basaltic wedge points I, II, and III, and the differential subsidence between point I and points II and III. Thermal subsidence was computed as the unloaded, isostatically balanced depth using Figure 8 density model. Subsidence calculated using the lower and upper bounds on the density model is indicated as Z_T- and Z_T+.

Figure Captions

Figure 1. a) Shaded relief map of gravity anomalies from the *DNAG* [1987] compilation. Note the continuity of the shelf-edge gravity high. The coast, the Fall Line, and the locations of published coincident MCS/wide-angle seismic experiments are indicated. b) Enlarged view of the 1990 EDGE experiment region with positions of offshore and onshore seismic instruments indicated.

Figure 2. Record sections for land seismic stations a) Stn 2, b) Stn 5, c) Stn 7, and d) Stn 11. Interpreted phases are indicated.

Figure 3. a) Gray-shade image of the velocity model obtained from traveltime modeling. Velocities are indicated in km/s. Triangles show instrument locations. b) Gray-shade image of parameter resolution for the igneous crust. Bold lines indicate reflection points of modeled wide-angle reflections.

Figure 4. Observed and fit traveltime curves for Stn 2 and Stn 5 with raypaths for the fit phases shown on a gray-shade plot of the velocity model.

Figure 5. Observed and fit traveltime curves for Stn 7 and Stn 11 with raypaths for the fit phases shown on a gray-shade plot of the velocity model.

Figure 6. Record sections with overlain traveltimes computed for the velocity model of Figure 3 for a) Stn 2, b) Stn 5, c) Stn 7, and d) Stn 11.

Figure 7. a) Depth migrated MCS data computed using the velocity model of Figure 3. b) Composite depth migrated image of MCS data and wide-angle reflections recorded by the ocean-bottom instruments. The basement surface is indicated.

Figure 8. a) Observed gravity values (dots), calculated gravity anomaly for the density model (dark solid line), and elevation required to place crust in local isostatic equilibrium (light line and scale to the right). b) Crustal density model with densities

indicated in gm/cm^3. c) Crustal density model with sedimentary load removed and isostatically balanced.

Figure 9. Hypothetical crustal configuration at the time rift volcanism became primarily submarine produced from the migrated seismic data unloading the sediments, rebounding the crust, and mirroring the data west of km 95, the seaward terminus of the volcanic wedge along the basement. Points I, II, and III picked at the ends of sequence boundaries interpreted as paleo-sealevel surfaces, with reflection terminations indicated. Bold line indicates the faulted basement of extended continental crust.

Figure 10. Cross-plot of velocity and density values at point-I (Figure 9) overlain on a variety of velocity/density relationships for sediments (left) and igneous rocks (right). For sediments, shaded region bounds *Ludwig, Nafe and Drake* [1970] data with center line their preferred curve. Other curves from *Hamilton* [1978] for clay/mud/shale, calcareous, and siliceous sediments. For igneous rocks, shaded regions bound *Birch* [1961] fits for mean-atomic-weight-21 rocks (upper), gabbros (center) and all rocks (lower). Other curves are *Christensen and Mooney* [1995] non-linear fit for 20 km and 30 km depth (upper) and *Christensen and Fountain* [1975] for granulite facies rocks at 6 kb (lower). There are 1601 velocity/density points plotted with bars corresponding to 5% (sediments) and 3% (igneous) variation in density.

Figure 11. Parameterization of thermal structure used to model total thermal subsidence of point I. Z_S is the rebound from removal of overburden, Z_T the thermal subsidence, Z_B the current thermal-lid thickness, Z_L the paleo-lid thickness, Z_C the paleo compensation depth, T_B the current basal temperature, $T_{B'}$ the paleo basal temperature, and T_O the paleo potential temperature. Z_C does not necessarily equal Z_B.

Figure 12. Calculated past potential temperature required to explain the thermal subsidence of points I, for five discrete values of current lid thickness over a range of past lid thicknesses. The four plots represent different values of past compensation

depth, Z_C. Shaded regions indicate effect of extremal bounds on density. Average pressure of melting scales linearly with past lid thickness for temperatures near 1500°C. Bold box indicates bounds of *Kelemen and Holbrook* [1995] petrogenetic model for earliest melts. Point-I subsidence is consistent with these bounds for a current lid ~225 km thick.

Figure 13. Early subsidence history from point-I to points II and III using minimum and maximum spreading-rate estimates. Predicted subsidence for 1D conductive cooling and aesthenospheric dispersal of impacting plume head also shown.

Figure 14. Calculation of total extension. a) sediment-unloaded crust with extended continental crust distinguished from new igneous additions. Minimum extension calculated from thickness of gray region; maximum extension calculated using dashed "mixing" line instead of Moho to define thinning profile. b) Total tectonic subsidence (TTS) determined from unloaded basement with seaward inflection point indicated. c) Extension determined from TTS using *Le Pichon and Sibuet* [1981] equation (light lines) for 30 km (upper) and 35 km (lower) pre-extensional thickness. Extension calculated by integrating $(1-1/\beta)$ from seismic model (heavy line) line is 30 to 40 km. d) β from seismic model using the "mixing" line (upper) and the Moho (lower) to define thinning profile.
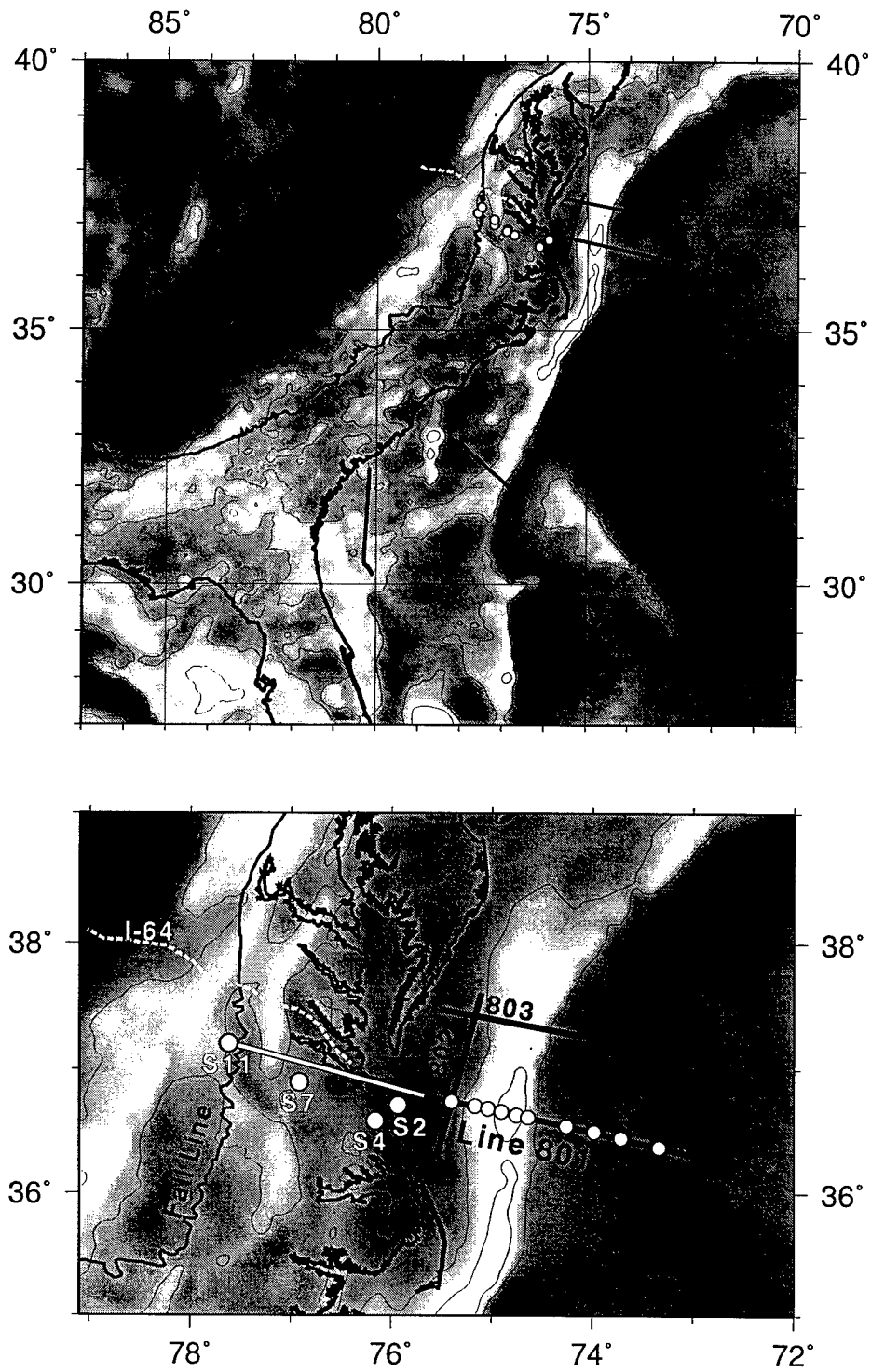
Figure 3.1
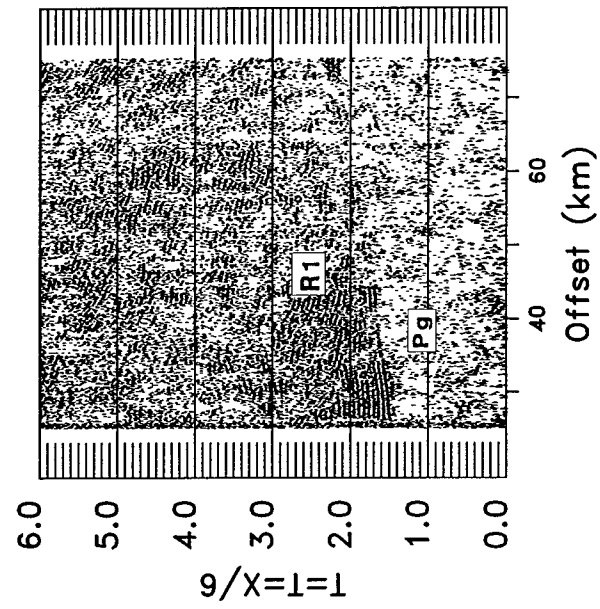
Figure 3.2a
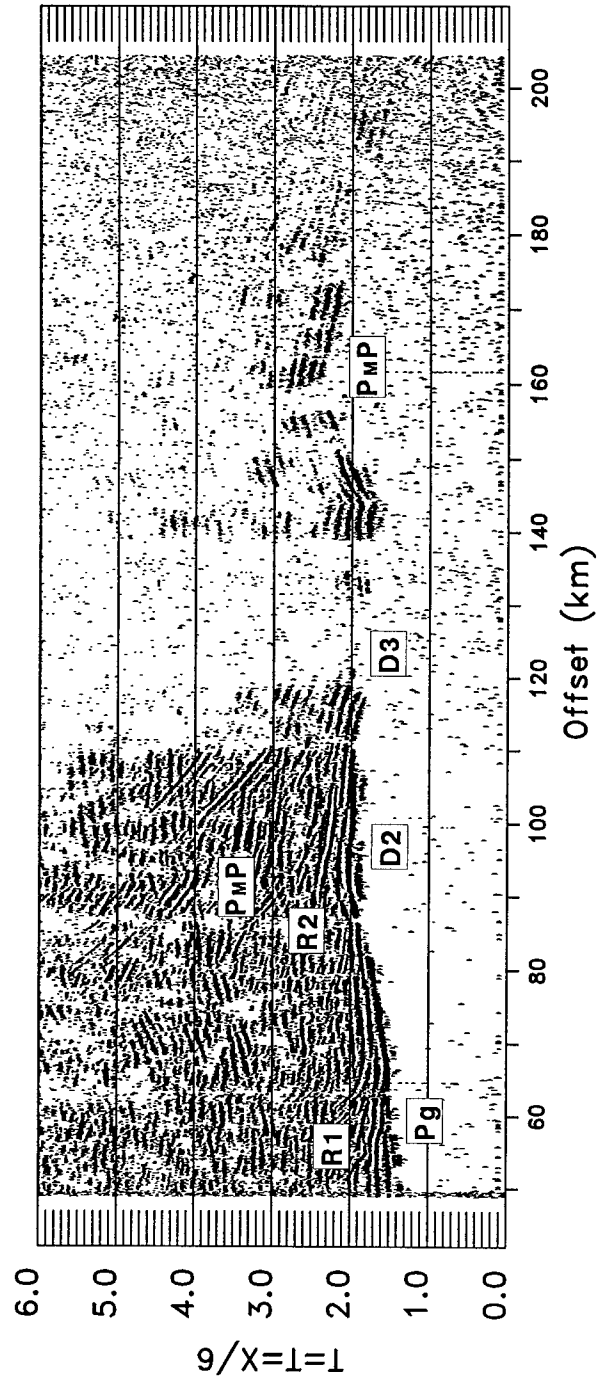
Figure 3.2b
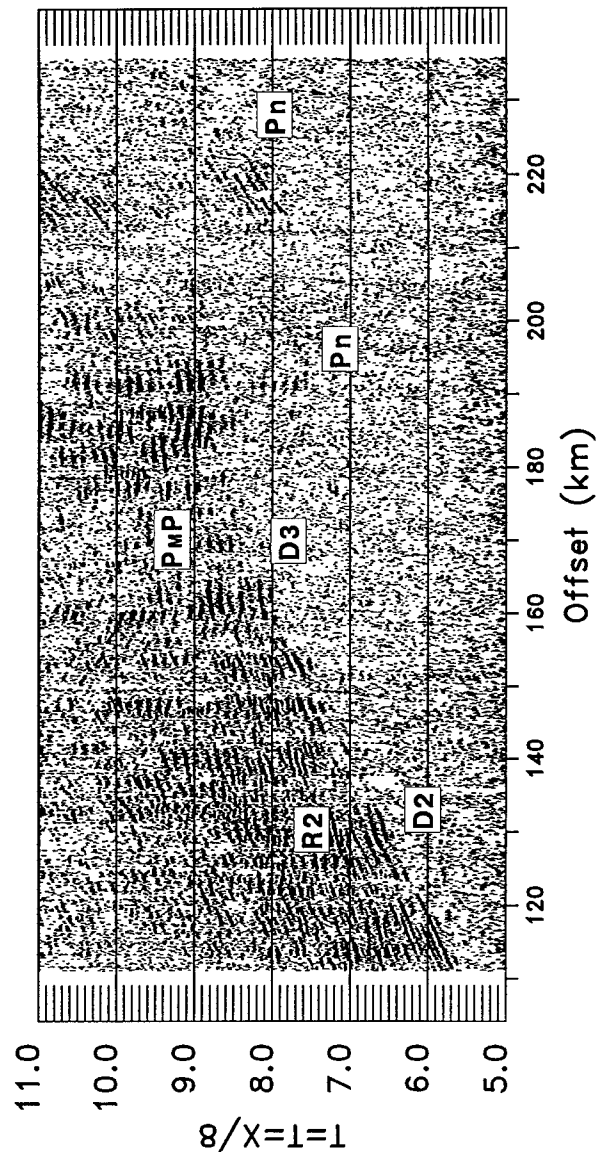
Figure 3.2c
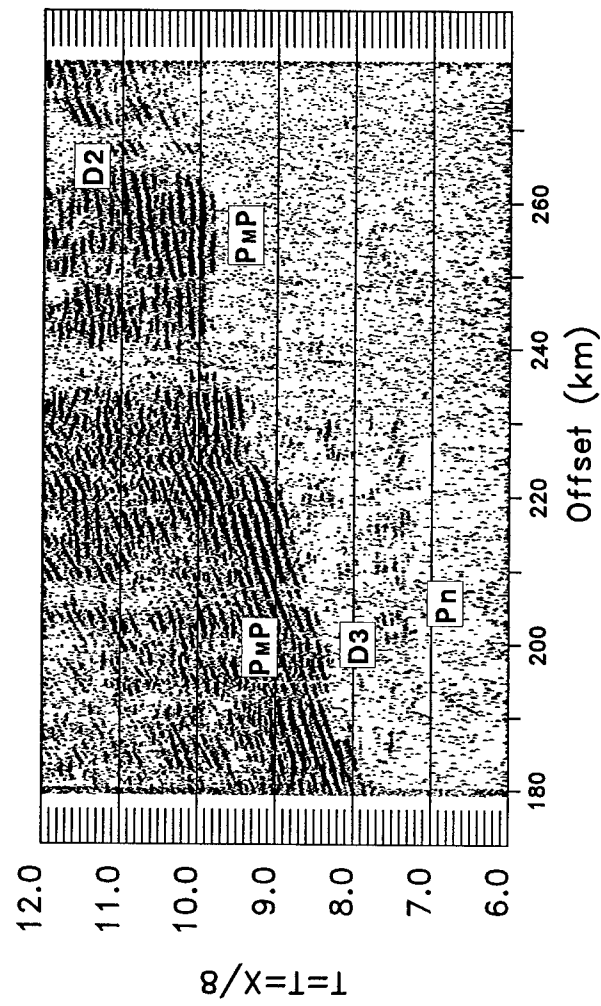
Figure 3.2d
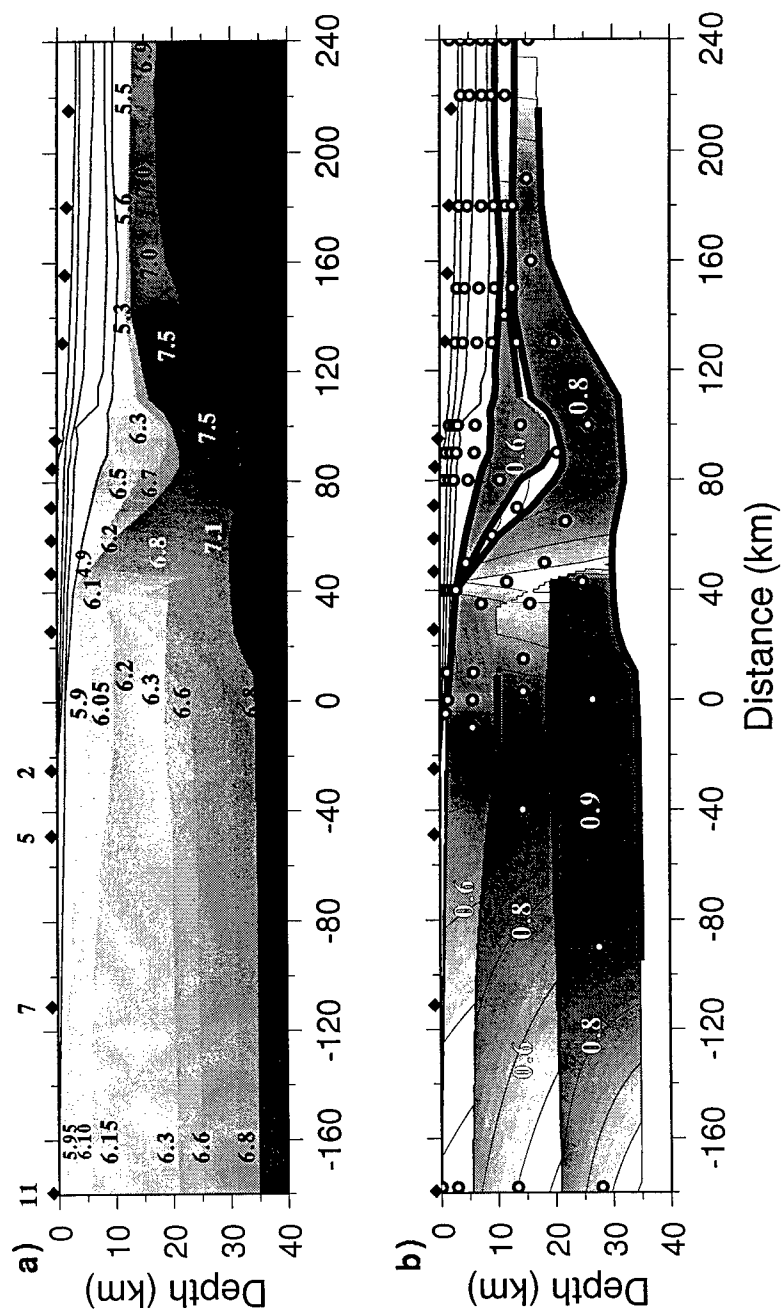
Figure 3.3
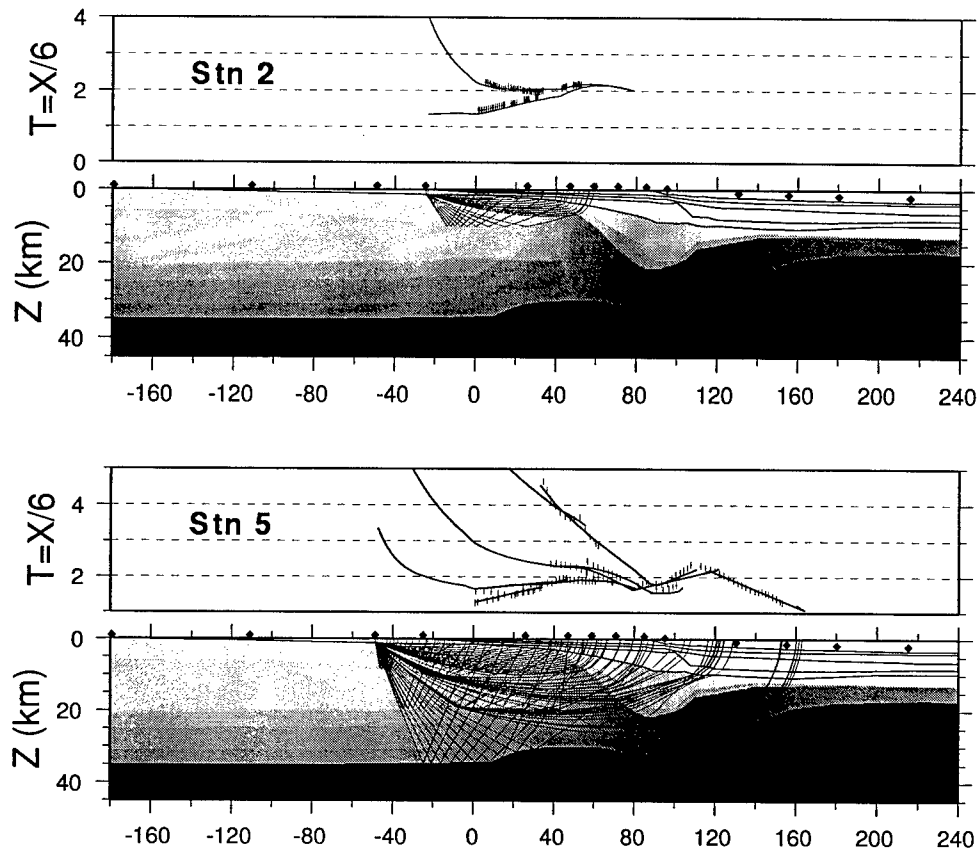
Figure 3.4
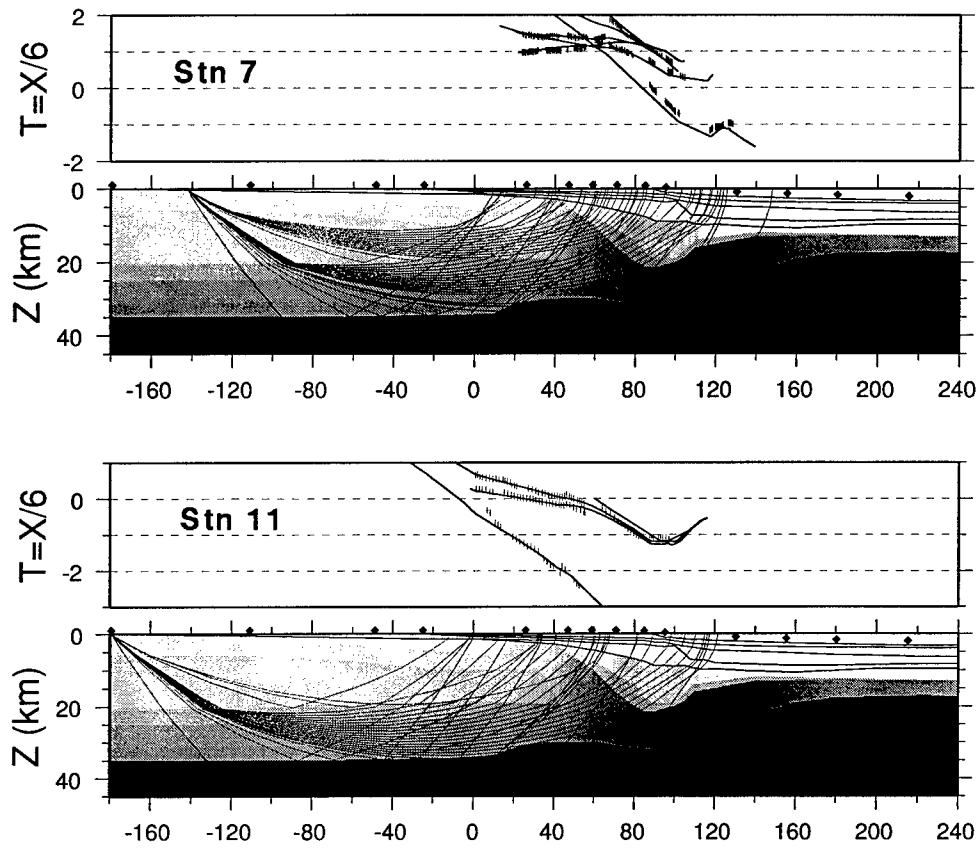
Figure 3.5
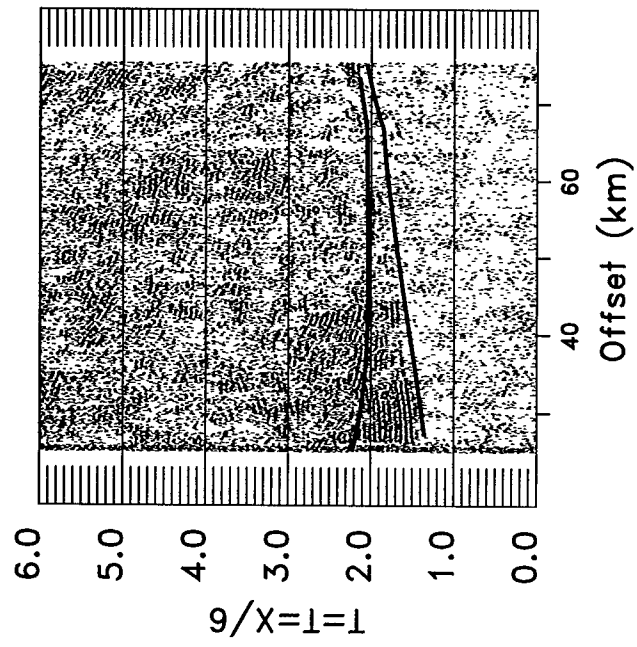
Figure 3.6a
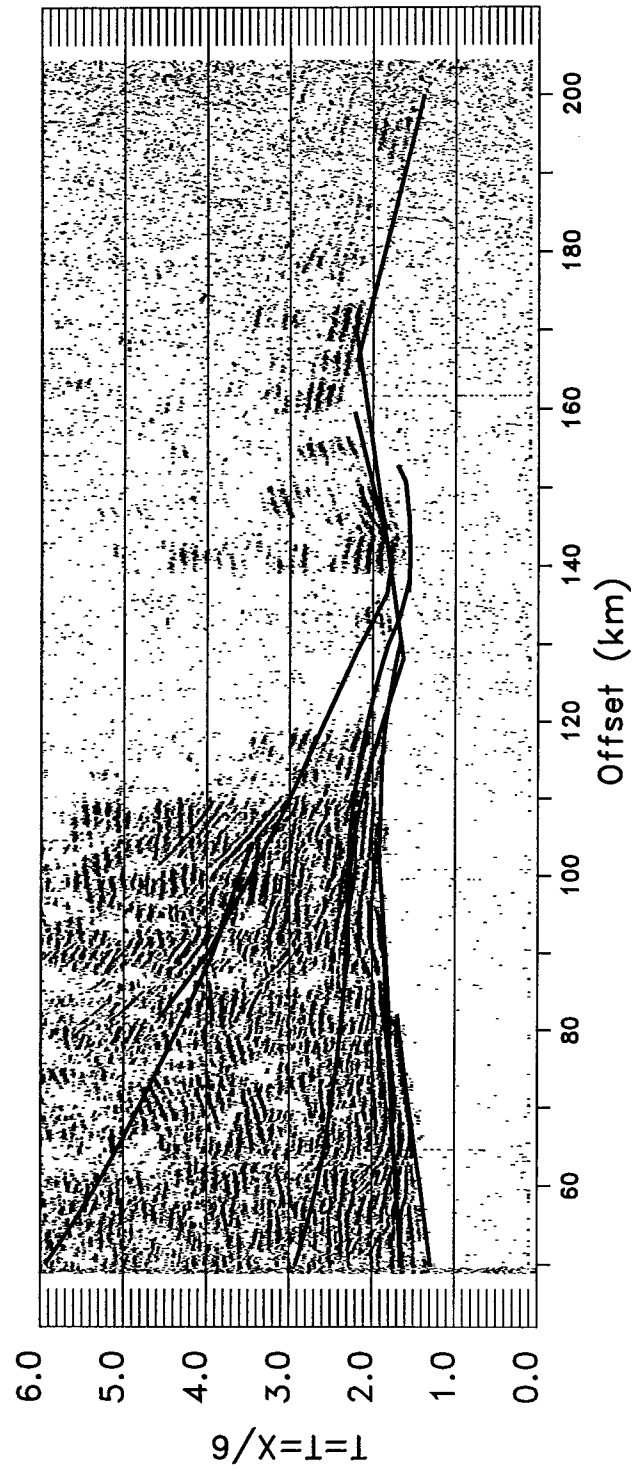
Figure 3.6b
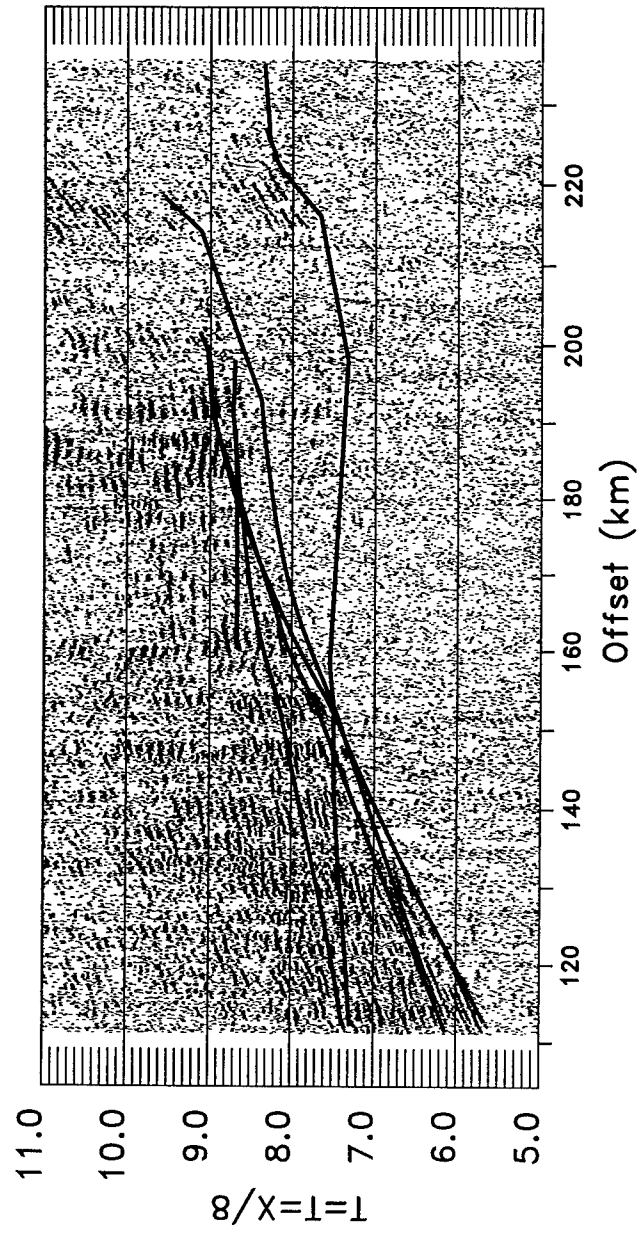
Figure 3.6c
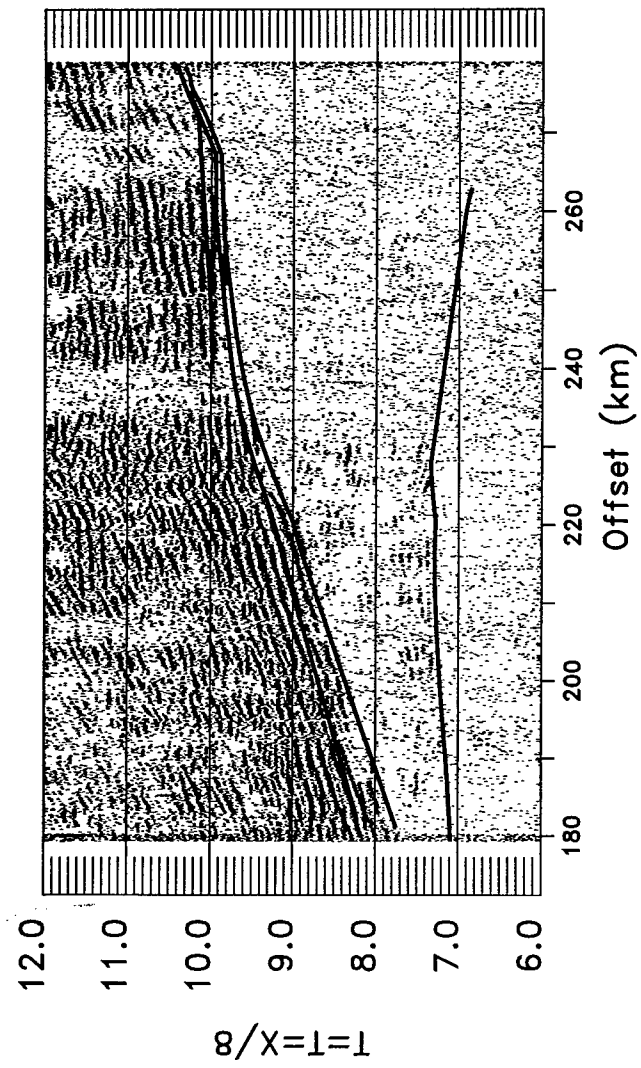
Figure 3.6d
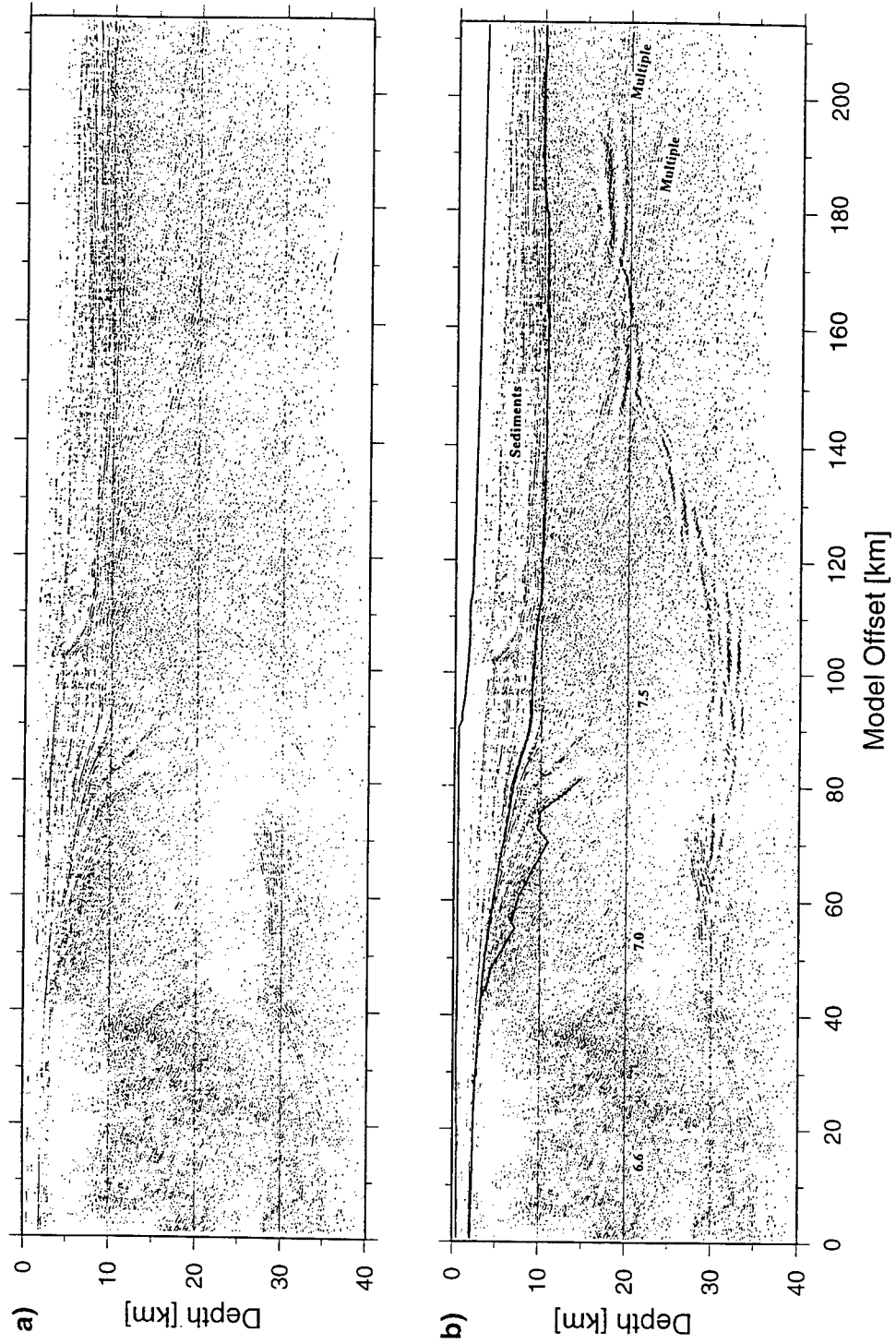
Figure 3.7
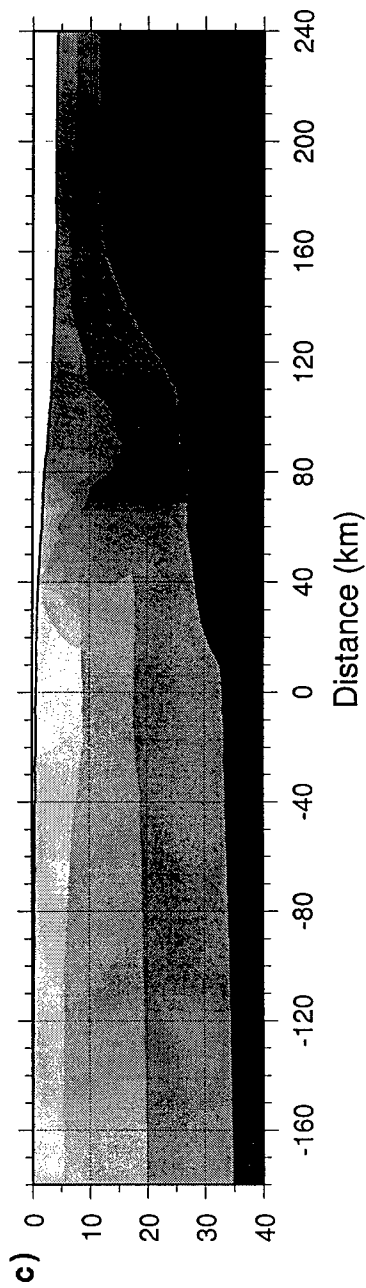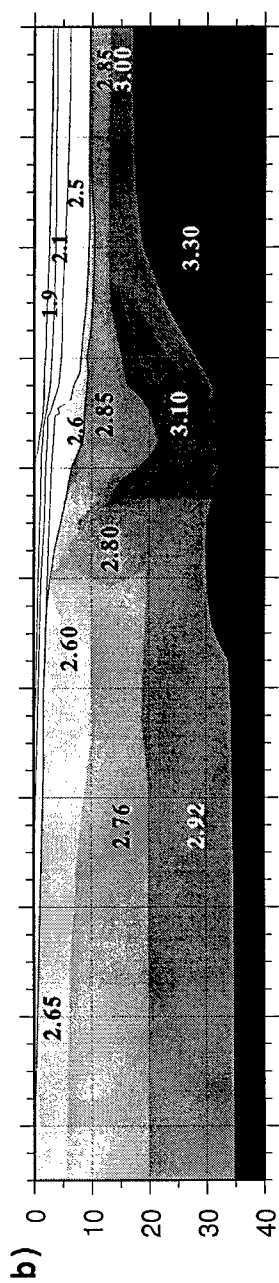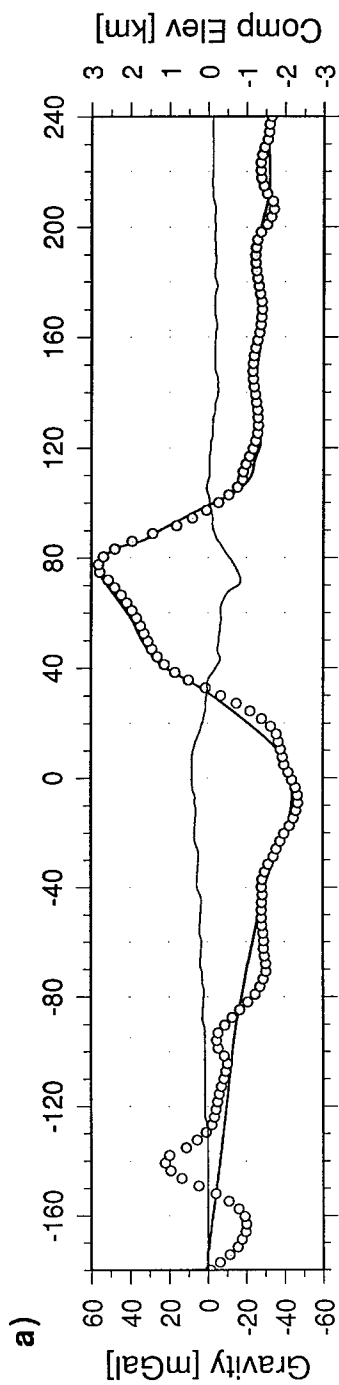
Figure 3.8
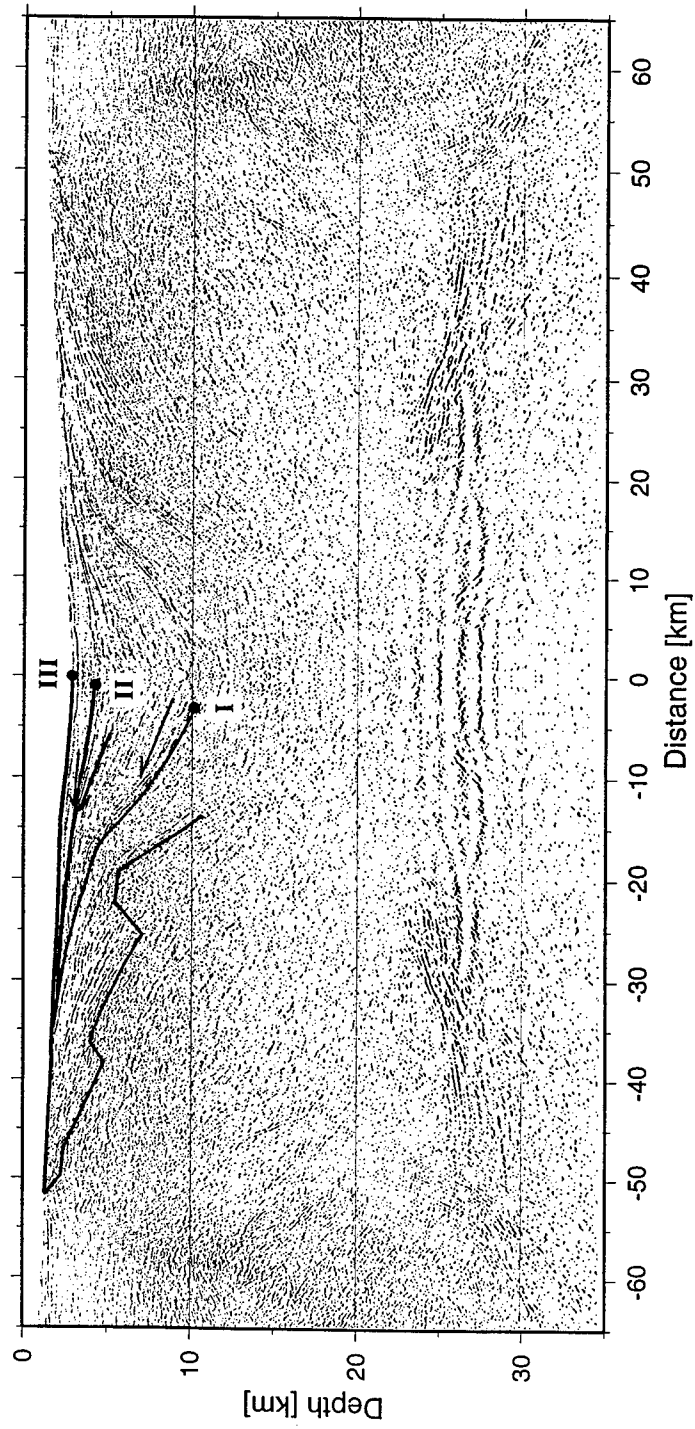
Figure 3.9
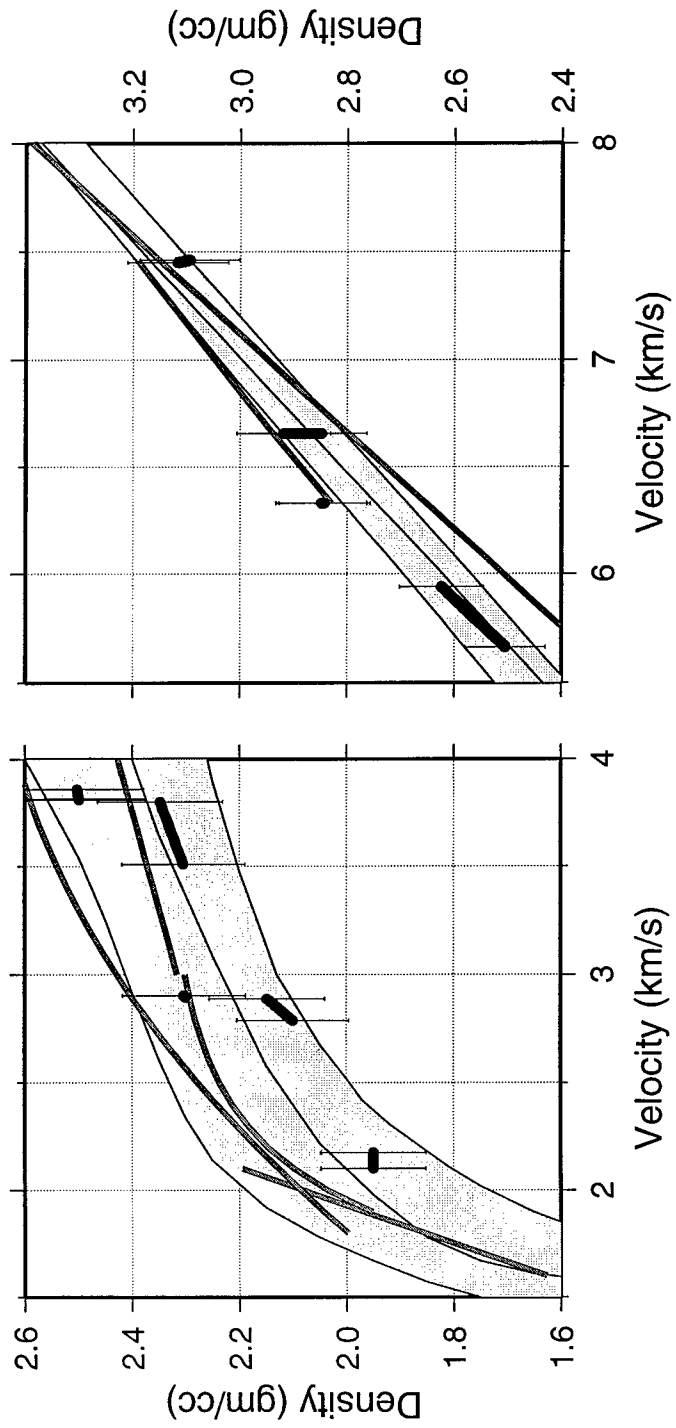
Figure 3.10
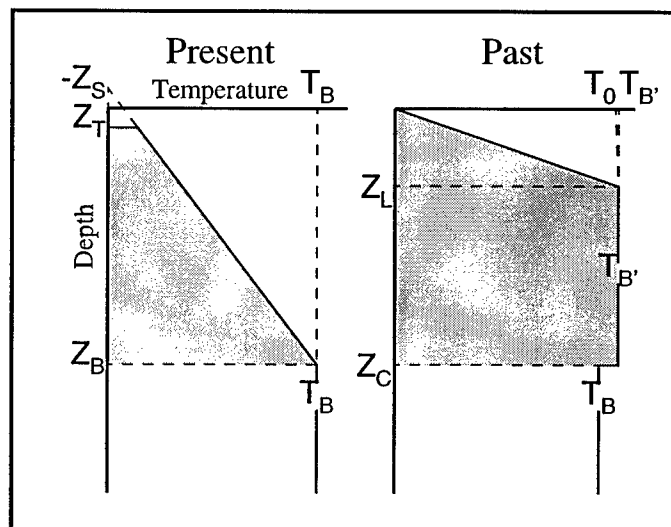
Figure 3.11
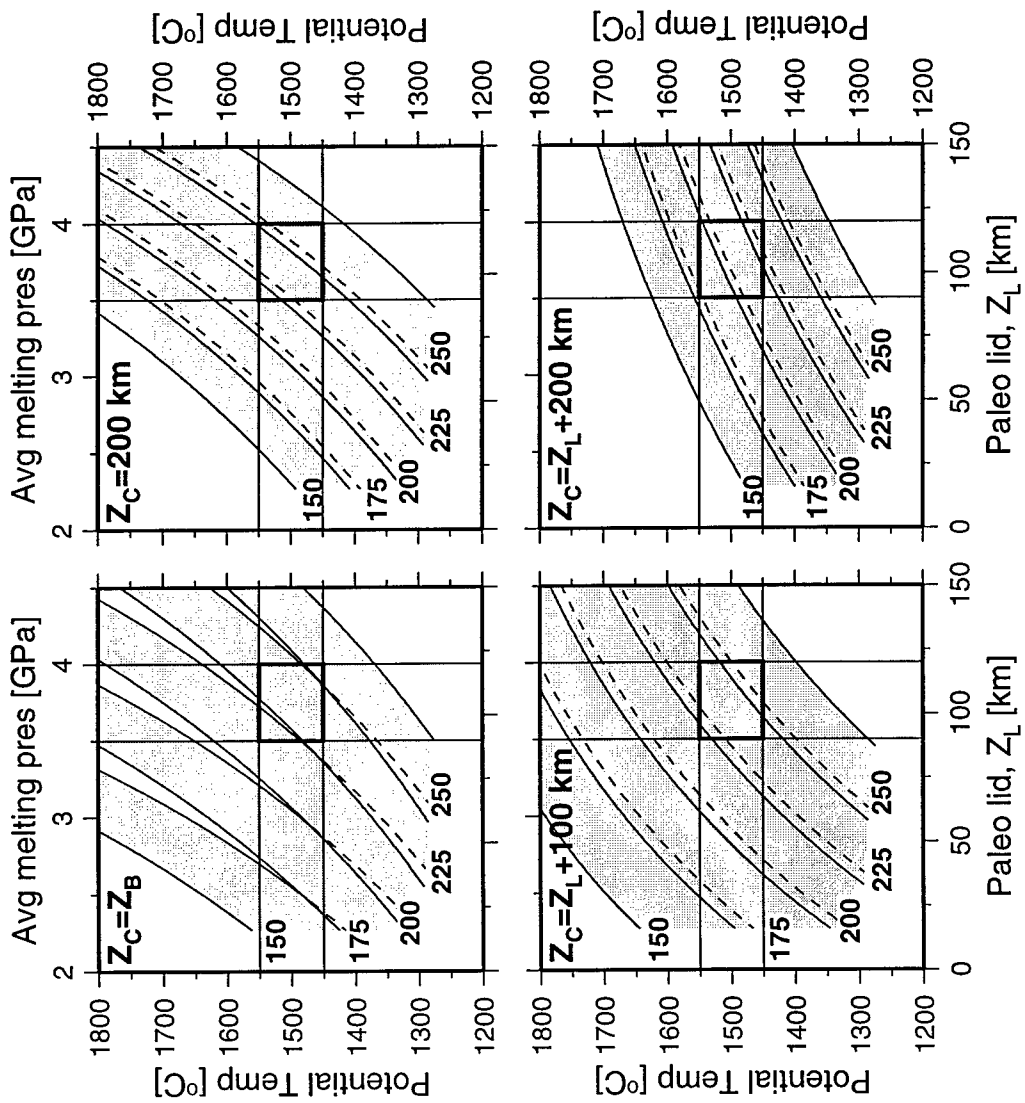
Figure 3.12
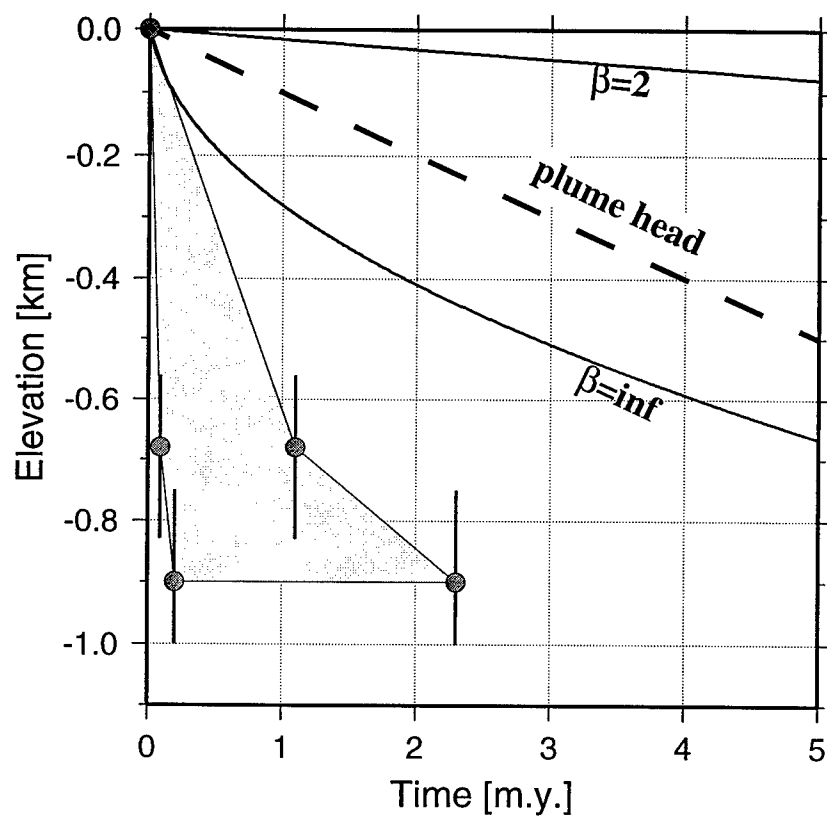
Figure 3.13
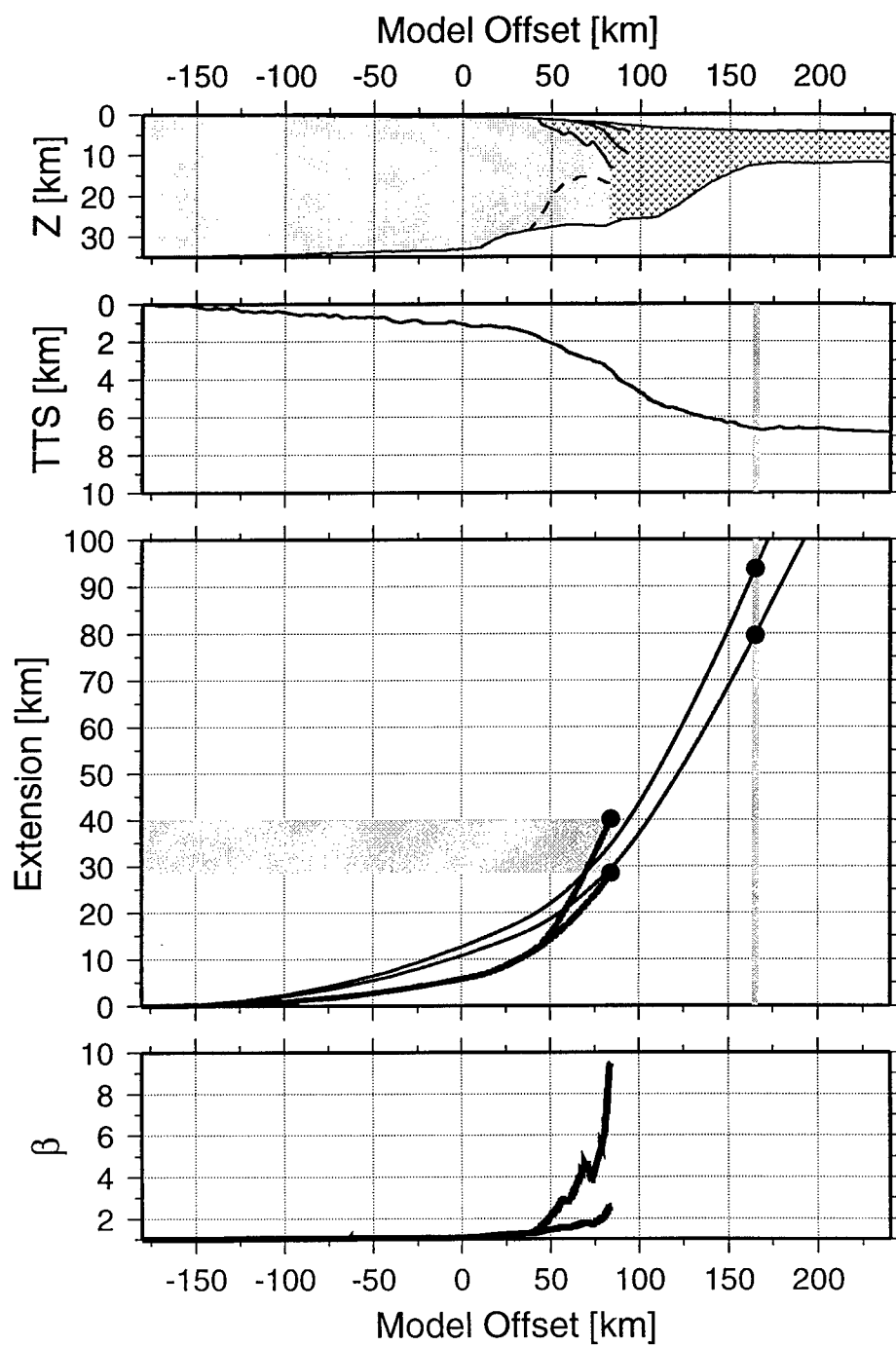
Figure 3.14

Chapter 4

Crustal Structure of a Proto-Continental Volcanic Arc: Alaska Peninsula

Introduction

The formation of stable continental crust occurs through a variety of processes operating episodically over 10s to 100s of millions of years. In contrast to the formation of oceanic crust, which is reasonably well understood, there is currently no generally agreed upon scenario for the formation and evolution stable continental crust. There is widespread agreement, however, that one of the earliest and most important stages of continental-crustal growth occurs at convergent margins through magmatism and terrane accretion. In this chapter we present results from a seismic experiment across the Aleutian arc (Figure 1) and investigate the structural and compositional evolution of continental crust at its earliest stages of formation.

The paramount unanswered question of crustal evolution is how the continental crust acquires its bulk compositional properties. The bulk major-element composition of the continental crust has been robustly estimated by a variety of approaches to be andesitic, intermediate between rhyolite and basalt [e.g. *Rudnick*, 1995; *Christensen and Mooney*, 1995]. The primary mechanism of continental crustal growth since the early Archean is thought to be arc magmatism and magmatic-arc-terrane accretion at convergent margins [e.g. *Condie*, 1989]. However, evidence from exposed sections of arc crust [*Pearcy et al.*, 1990], melting experiments with mantle rocks [e.g. *Kelemen*, 1995], and observed distributions of arc lavas [e.g. *Kay and Kay*, 1994] suggests that the bulk composition of subduction-related magmatic arcs is basaltic. This raises the question, how does crust built mostly of basaltic magmatic-arc terranes evolve towards the andesitic composition of stable continental crust?

Several hypotheses have been proposed to explain the evolved character of continental crust, in terms of both bulk composition and enrichment in incompatible trace-elements — for which the continental crust is a globally significant reservoir. The merits of these various hypotheses, including their implications for continental iron-enrichment and light-rare-earth-element trends, have been discussed by several authors [e.g. *Kelemen*, 1995; *Rudnick*, 1995] and need not be repeated here. We are primarily interested in the evolution of the bulk composition of the crust, and hypotheses for this evolution are of three basic types: 1) Differentiation occurs in the crust as the magmatic arc is forming, resulting in a lower-crustal, ultramafic residuum that may be seismically indistinguishable from the upper mantle and may at some point delaminate and return to the mantle [*Kay and Kay*, 1985]. 2) Differentiation occurs by melting the lower crust at some time after the arc crust is formed, possibly in association with compressional orogeny during accretion, forming an ultramafic, lower-crustal residuum that behaves as in (1) [e.g. *Meissner et al.*, 1987]. 3) Differentiation occurs in the mantle via melt/rock interactions, and the bulk composition of arcs is andesitic [*Kelemen*, 1995].

One of the primary goals of the 1994 Aleutian seismic experiment was to determine the seismic velocity structure of crust at various stages of magmatic/accretionary evolution, enabling constraints to be placed on bulk crustal composition at these stages and providing tests to the evolutionary hypotheses. Line A1 of the experiment crosses the Aleutian arc where intra-oceanic subduction occurs, Line A3 crosses the arc where subduction is beneath proto-continental crust, and Line BA3 crosses more mature continental crust of the back arc (Figure 1). Line A1 is one of only two high-quality seismic transects across an intra-oceanic arc, the other being across the Izu-Ogasawara arc [*Suyehiro et al.*, 1996]. Line A1 is thus of primary importance in defining the deep structure and bulk composition of oceanic arcs. The Line A1 seismic data have been analyzed by *W.S. Holbrook*

[unpublished manuscript], and we will use these results as a reference for the structure of intra-oceanic-arc crust.

In this chapter we consider results from Line A3, a transect crossing the Aleutian arc through Unimak pass at the westernmost end of the Alaskan Peninsula. Here the crust of the overriding plate is probably best characterized as proto-continental crust, lying below sea level and lacking the dramatic mountain belts that characterize the continental arcs of Northwest America and the Andes. This nascent crust has formed through successive and ongoing episodes of magmatism and terrane accretion [*Plafker et al.*, 1994], and we hope to find in its seismic structure evidence for evolution from the properties observed on Line A1 to the properties of average, stable continental crust. Toward this end, it is important to establish the geologic framework of this margin, and we will begin with a brief review of its history.

Geologic and tectonic setting

The Aleutian arc is a band of mountainous crustal constructions built from the volcanic and tectonic activity associated with Pacific plate subduction along a more than 3000-km-long subduction zone extending from the Kamchatcka Peninsula to the Gulf of Alaska. The current configuration of the arc dates back to the Eocene, when a change in plate motions forced a reorganization in subduction from its paleo location along the Beringian margin and Alaska Peninsula (Figure 2). Unimak Pass thus represents a fundamental boundary along the Aleutian arc. West of Unimak Pass, oceanic lithosphere of the Pacific plate is subducted beneath oceanic lithosphere of the relic Kula plate (trapped by the subduction-zone jump), and the arc is composed of volcanic flows, plutons and volcaniclastic sediments that are Eocene and younger in age. East of Unimak Pass, the crust of the overriding plate is composed of an amalgamation of several magmatic-arc/accretionary-complex terranes of Mesozoic age that formed ~30° to the south, accreted

to the southern Alaska margin during the Cretaceous, and are now being reintruded and tectonically modified.

The Peninsular terrane

At present we are primarily concerned with the general geologic framework of the Alaska Peninsula and southern margin, which we may consider as consisting of two main units, the Peninsular terrane and the Southern Margin Composite terrane. The Peninsular terrane encompasses the Alaska Peninsula and is bounded to the south by the Border Ranges Fault (BRF in Figure 2). The northern boundary of the Peninsular terrane is uncertain, but probably tracks just north of the Alaska Peninsula. Little is known about the Bering Sea shelf crust to which the Peninsular terrane is attached except that its thickness is estimated, primarily from gravity models, to be ~30 km [*Cooper et al.*, 1987]. The westward extent of the Peninsular terrane is also uncertain, and it is not clear whether it extends as far west as Umnak Island. If the terrane extends beyond the Alaska Peninsula, then it probably continues along the Beringian margin, the westward trend of subduction during the Cretaceous when the terrane was accreted [*Cooper et al.*, 1987].

The Peninsular terrane consists of volcanic and volcaniclastic rocks of the Jurassic-age Talkeetna intra-oceanic arc [*Plafker et al.*, 1994]. These rocks include basalt, andesitic and dacitic flows and volcaniclastic rocks of the Early Jurassic Talkeetna Formation and the plutonic rocks of the Alaska-Aleutian batholith, which intrude the Talkeetna Formation and may represent the core of the magmatic arc [*Miller*, 1994]. The Alaska-Aleutian batholith consists of mid- to late-Jurassic plutons that define a calc-alkaline magmatic suite of intermediate composition (mean SiO_2 content of 58%) [*Miller*, 1994]. Two phases of intrusion at 83-58 Ma and 38-26 Ma, following the accretion of the arc terrane to North America, involved rocks of a somewhat more evolved composition [*Miller*, 1994].

The intermediate composition of the Alaska-Aleutian batholith and subsequent plutons are probably not indicative of the bulk composition of the Peninsular terrane. An ultramafic-mafic suite of Peninsular terrane lower-crustal rocks (the Tonsina assemblage) is exposed along the Border Ranges Fault north of Cook Inlet [*DeBari and Coleman*, 1989], and the composition of these rocks and a similar assemblage in Oregon led *Pearcy et al.* [1990] to suggest that the bulk composition of intra-oceanic island arcs is basaltic. In addition, the most reliable measurements of the seismic structure of the Peninsular terrane reveal an upper-crustal structure with velocities of 6.3-6.6 km/s, considerably higher than those of average continental crust [*Ambos et al.*, 1989].

Southern margin composite terrane

The Southern Margin Composite terrane is an assemblage of accretionary-complex terranes consisting of the Triassic-Cretaceous Chugach terrane, which lies immediately south of the Border Ranges Fault, and various outboard Cenozoic terranes [*Plafker et al.*, 1994]. The Cenozoic terranes are more voluminous towards the east where accretionary rocks from the western North American margin have been transported northward on the Pacific plate and incorporated into the southern margin. At the western end of the Alaskan Peninsula, the Southern Margin Composite terrane is dominated by Chugach terrane rocks [*Vallier et al.*, 1994]. The Chugach terrane consists of three main units, by far the most voluminous of which is the flysch and basalt assemblage [*Plafker et al.*, 1994]. This unit includes a number of mapped formations, the westernmost being the Shumagin formation whichs crops out on Sanak Island, located just south of Umnak Island (Figure 2). Rocks of the Shumagin formation probably are the basement beneath at least the southern portion of Line A3 and consist of predominantly of deep-water volcaniclastic sediments [*Berg et al.*, 1994; *Bruns et al.*, 1987; *Vallier et al.*, 1994].

The deeper structure of the Chugach terrane is uncertain toward the southwestern end of the Alaska Peninsula but has been seismically determined onshore along the Trans-Alaskan Crustal Transect (TACT) north of the Gulf of Alaska [*Fuis et al.*, 1991]. Here the deep structure of the Chugach terrane is dominated by what appears to be a relic fragment of oceanic crust dipping northward, beneath the surficial flysch, from the terrane's southern boundary fault (the Contact Fault). A strike line crossing the TACT profile towards the southern edge of the Chugach terrane convincingly demonstrates the velocity structure of this ophiolitic(?) fragment as a 15-km-thick sequence of alternating high- and low-velocity layers, with an average aggregate velocity of ~6.9 km/s [*Fuis et al.*, 1991].

Seismic data acquisition and processing

The seismic data collected along Lines A3 and BA1 (Figure 1) consist of multichannel-streamer and ocean-bottom-instrument recordings of shots fired at ~50-m intervals by the R/V *Ewing's* 20-element, 8000-in^3, tuned airgun array. The ocean-bottom instruments along Line A3 were spaced 10 to 20 km apart and consisted of 11 Woods Hole Oceanographic Institution ocean-bottom hydrophones (OBHs) and 5 U.S. Geological Survey ocean-bottom seismometers (OBSs) (Figure 3). The ocean-bottom instruments along Line BA1 consisted of the northern OBH of Line A3 (OBH19) and two additional instruments spaced ~70 km apart. The multichannel-seismic (MCS) data for all lines were recorded by a 4-km-long, 164-channel streamer towed behind the *Ewing*.

Processing of the MCS data is being carried out by other investigators. Figures of MCS data presented in this paper are post-processed brute stacks. The complete section shown in Figure 4 is processed with predictive deconvolution, a 4- to 30-Hz, zero-phase, bandpass filter and a time-varying ($t^{0.8}$) gain. Other figures include a water-velocity Stolt migration.

The MCS data reveal the flexed subducting oceanic plate, a fairly complex crust beneath the forearc terrace (km 75-125), a ~3-s-thick stratified section beneath the slope and outermost shelf (km 125-175), a mostly transparent section beneath the shelf in the vicinity of the arc (km 175-250), and an abrupt thickening to ~3 s of the stratified section beyond km 250 (Figure 4). We demonstrate below that the transparency of the profile between km 175 and 250 correlates with the absence of a significant thickness of low-velocity sedimentary strata along the shelf platform. It is possible that subsequent processing will reveal features beneath the platform, as reflections from the subducting slab are observed for shots near km 210. At this stage of processing, however, we are not inclined to interpret any upper crustal events observed in this interval.

The ocean-bottom data processing flow consisted of previous-shot suppression, predictive deconvolution, 3- to 18-Hz zero-phase bandpass filter, and a range-varying ($X^{1\cdot}$) gain. The acausal precursor to the zero-phase filter is significant at one to two cycles before the first break at small offsets on many of the record sections, giving the false impression that traveltime fits arrive too late.

The turn in Line A3 through Unimak pass, near the center of the line, presents a complication to two-dimensional modeling. For our modeling, we have chosen the obvious profile extending between the southern and northern endpoints of the line, and model offset is defined as distance along this profile from the southern endpoint. All MCS data are plotted as a function of model offset, with data from shots fired during the turn projected onto this profile. The wide-angle data are plotted and modeled as a function of range from the shot to the recording instrument. The line configuration thus guarantees traveltime-data misfits for shots fired in the turn, barring a highly fortuitous three-dimensionality to the subsurface structure.

Seismic data and velocity model

The voluminous Line-A3 and Line-BA1 seismic datasets enable the determination of the large-scale (kms to 10s of kms) seismic velocity structure beneath Line A3 (Figure 5). The velocity model of Figure 5 is based on wide-angle traveltimes with incorporated constraints from the MCS data. The analyses and modeling of the seismic data followed a similar approach to that described in preceding chapters of this thesis, including phase identification and traveltime picking, model parameterization, and a layer-stripping application of inverse and forward traveltime modeling to arrive at a final model. The most significant difference between the Line A3 dataset and those of the previous chapters is the size and superior spatial sampling of the wide-angle dataset. This volume of data greatly facilitates the seismic interpretation and modeling while at the same time complicating the discussion of the results. Our discussion proceeds with detailed descriptions of key aspects of the model combined with a comprehensive presentation of of the wide-angle data with and without fit traveltime curves (Figures 6) and plots of the picked traveltimes with fits (Figure 7), enabling the interested reader to consider undiscussed portions of the model.

The primary focus of this paper is the arc crust of the overriding plate, though the data place significant constraints on the location of the subducting slab and the structure of the forearc accretionary complex. We thus only discuss the modeling of data north of km 150 and present figures of wide-angle profiles to the south for completeness. The arc-crust model consists of 4 upper crustal layers with velocities <6.0 km/s, a middle-crustal layer and a lower-crustal layer. Wide-angle traveltimes are used to constrain all aspects of this model, and MCS traveltime data are used to constrain the geometries of the upper 3 layers. Wide-angle and MCS data along Line BA1 were used to constrain the structure at the

northern end of Line A3. We will mention modeling results from Line BA1 in this section but postpone a thorough review of the Line BA1 data and results to a later section.

The upper arc crust

The upper arc crust consists of four seismic layers that have a fairly uniform total thickness of ~10 km but thin to ~3 km across the basement high near km 225. The upper two layers have velocities of ~2.0 km/s and ~3.0 km/s, and the lower two have velocities of ~4.7 km/s and ~5.6 km/s. Velocity constraints for these layers come from arrivals at offsets as great as 52 km, but mostly less than 25 km. The disappearance of the upper two low-velocity layers across the basement high is apparent in the near-offset arrivals. The slow phases of Layers 1 and 2 observed on instruments between OBH19 and OBSA1 (Figures 7a and 7e) are absent on instrument OBH22 and OBSA3 (Figures 7f and 7h) , reappearing again on OBH21 (Figure 7i). The small basin beneath OBH17 (Figure 7g) is indicated from the slow phases here out to 2- to 5-km offset.

The upper three layers of the arc-crust velocity model have a direct relationship to units imaged by the MCS data (Figure 8 and Figure 9), and the geometry of these seismic units was used to constrain the velocity model. The upper two layers have sedimentary seismic character and velocity and are generally consistent in character with the regional designations of *upper* and *middle series* seismic units [e.g. *Bruns et al.*, 1987]. The upper two layers pinch out near km 185 and thicken again beyond km 285. The absence of these units apparently inhibits seismic penetration beneath most of the shelf platform (Figure 4).

The near offset arrivals observed on OBSA1 and OBSC3 are more complex in detail than those observed on other instruments, with phases suggestive of high- and low-velocity layering. We have not incorporated these details into our model, but note here that this near-offset complexity correlates with the disturbed character of the Layer-1/Layer-2 sedimentary sequence between km 250 and km 285 (Figure 9). These features also

correlate with a distinct character to the underlying Layer 3 in this interval and a high frequency component in the magnetic anomaly profile, both discussed below. The km 250-285 interval lies within the trend of the currently active arc, and it is thus possible that the Layer-1/Layer-2 features here are associated with arc-related intrusions.

Layer 3 is characterized by a strong velocity gradient, with velocity increasing from 4.2 to 5.2 km/s over a few kilometers depth, giving rise to a strong refraction, P_3, on the wide-angle profiles, many of which display considerable curvature. The velocity structure of Layer 3 is similar over the northern and southern portions of the line, but the geologic makeup of this layer may be quite different. Over the northern portion of Line A3 (km 300-341) and along Line BA1 (Figure 18), Layer 3 corresponds to a 1- to 2-s-thick reflective zone beneath a well defined acoustic basement. A borehole located ~100 km northwest of the end of Line A3 encountered basalt, basalt breccia and tuff at 3.2 km depth beneath marine sediments, consistent with the depth to the top of Layer 3 [*Marlow et al.*, 1987]. Thus, Layer 3 probably consists of an assemblage of flows, volcaniclastic sediments and small plutons beneath the northernmost portion of Line A3 and along Line BA1, and the gradation in velocity and the disappearance of reflectivity in this layer are probably due to compaction-induced loss of porosity and an increasing incidence of intrusive rocks.

The seismic character of Layer 3 beneath the slope and the southern end of the shelf platform is characterized by more continuous reflections and a smoother upper surface than observed in the north (Figure 8). This character is consistent with the regional *lower series* seismic unit described on a number of MCS profiles across the southern margin. The lower series horizon has been traced to outcrops on Sanak Island and the southern Shumagin Islands and found to be correlative with the Shumagin formation of the Chugach terrane which consists of deformed Mesozoic deep-water turbidite sequences [*Bruns et al.*, 1987; *Vallier et al.*, 1994]. Numerous sonobuoy profiles along the margin to the south and

southeast of Umnak Island indicate an average velocity of 4.6 km/s for the *lower series* unit, consistent with Layer 3. Thus, Layer 3 beneath the slope and southern end of the shelf is probably correlative with the deep-water flysch deposits of the Chugach terrane.

The seismic character and velocity structure of Layer 3 between km 250 and km 285 is distinct from that in other portions of the MCS profile and velocity model. The layer is seismically transparent in this interval with a strong, low-frequency reflection defining its base. The velocity is slower on average, and the layer is nearly twice as thick here than elsewhere. As mentioned previously, these changes in character are correlated with changes in character in the overlying strata and a distinct magnetic anomaly pattern.

Layer 4 has a nearly constant velocity of 5.5 km/s along the northern end of the profile. On OBH19 (Figure 7a), the Layer 4 refraction, P_4, is observed between -27 km and -50 km offset and is more linear and lower amplitude than the P_3 phase. The P_4 phase has a similar expression on OBSC4 (Figure 7b) and the positive offsets of OBH27 and OBSC3 (Figures 7c and 7d), but is complicated with the P_3P and P_4P reflections and structure of the basement high on the negative offsets of OBSC3, and is a "hidden" arrival on the positive offsets of OBSA1 (Figure 7e). Consequently, the velocity and thickness of Layer 4 between km 250 and km 275 is constrained mostly by its effect on the delay times of other arrivals passing through from below.

The P_4 phase is expressed clearly on the Line BA1 OBH19 profile between 15 km and 50 km offset (Figure 19a). The velocity of Layer 4 here is determined to be gradational from 5.6 to 6.0 km/s. This velocity structure is similar to that observed on Line A3 south of the basement high. Because the basement characterization from the MCS data along Line BA1 is very good and the reversal of P_4 between OBH27 and OBH19 is complicated by structure near km 300, it is possible that the Layer-4 velocities beneath the northern end of Line A3 have been somewhat underestimated. The P_4 phase is well expressed south of the basement high in the negative offsets of OBH17 and OBSA3 and the positive offsets of

OBH21, and is important in establishing the delays to the Layer 5 refraction on OBH16 and OBSA2.

The mid crust

The mid-crustal Layer 5 is characterized by two distinct velocity regimes on either side of an arc-centered mid-crust high. The mid-crust south of km 250, including the mid-crust high, has a gradational velocity of 6.5-6.85 km/s. North of km 250 the velocity is 6.15-6.40 km/s. Layer 5 is 13 km thick at its thickest point, and averages 7 km thick in the south and 9 km thick in the north.

The arrivals constraining the Layer 5 structure, P_5 and P_5P, are the predominant crustal phases observed on most of the wide-angle profiles. The P_5 and P_5P phases are best distinguished from one another on OBSC4 and OBH22 (Figures 7b and 7f), where the reflected rays traverse the thickest sections of Layer 5 and thus attain the greatest delay with respect to the refracted P_5 phase. These phases are also well distinguished on OBH27, OBSA3, OBH16, and OBSA2 (Figures 7c, 7h, 7j, and 7k). In other cases the distinction is difficult either because the phases arrive too closely in time or are complicated by shallower structure, as is the case for the positive offsets of OBH21.

Ray coverage for interpreted P_5 and P_5P phases is dense between km 150 and km 325. In Figures 10a and 10b we show point-to-point raypaths to the P_5 and P_5P traveltime picks. The white dots in Figure 10a indicate ray bottoming points, which are, to first order, the locations where the traveltime data are most sensitive to velocity. While this dense ray coverage imparts a high resolution to the velocity determinations for this layer, we have somewhat underparameterized the layer to avoid overfitting expected misfits resulting from the 2-D approximation of a 3-D ray geometry in the vicinity of the line turn.

The shallowing of the mid-crustal layer between km 225 and km 250 is clearly indicated by wide-angle traveltimes. This is illustrated in Figure 11, where we plot

reversing profiles OBSA3-OBSA1 and OBH21-OBSC3 located on either side of the layer high. First-arrival traveltimes advance and then delay with increasing range as they pass over the shallowing feature, obtaining an apparent phase velocity of ~6.5 km/s directly over it. These traveltime effects are more dramatic to the north due to the greater thickness of slower Layer 2 sediments there.

There is no question that the Layer 5 high is a required element of the model. Traveltime fits for rays passing through this feature are quite good, though fits to traveltimes associated with rays passing through or near the northern flank of the high are generally poor due to the steepness of the flank and, presumably, the line turn across it. Rays traveling to the south tend to require the flank be shifted northward (OBH19, OBH27, OBSC3), whereas rays traveling to the north generally require a greater delay across the northern flank (OBH17, OBH21). This misfit complicates, but does not preclude, an estimation of traveltime-fit sensitivity to the velocity near the peak of the high.

We investigate the sensitivity of RMS traveltime residuals to the velocity structure of the thickest portion of Layer 5 by perturbing the velocity at the top of the layer high point. Images of the perturbed velocity structure for upper velocities of 6.0, 6.4, and 6.8 km/s are indicated in Figure 12 along with the RMS error of the P_5-phase fits to the four instruments most sensitive to velocity in this portion of the model, OBSA3, OBH22, OBSA1, and OBSC3. This is perhaps the simplest test one could construct, as we did not modify any aspect of the overlying model and did not consider a comprehensive suite of vertical velocity gradients. The resulting misfit curves demonstrate the basic sensitivity of the data, however, and show that the 6.5-km/s estimate for the velocity at the top of the layer yields an RMS minimum for this suite of models. Qualitative considerations suggest that the 6.5-km/s velocity estimate for the top of the layer is bounded by ±0.20 km/s. The RMS-error curves are symmetric, suggesting that an upper velocity of 6.3 km/s will fit the data equally

well as an upper velocity of 6.7 km/s, and qualitative assessment of the misfit for these models is consistent with this symmetry.

Layer-5 velocities south of km 200 are 6.5-6.9 km/s and are probably somewhat higher than indicated in the model; the layer may include an isolated high velocity body. The requirement for high Layer-5 velocities south of km 200 is indicated by the P_5 and P_5P phases of OBSA2 and OBH16. Computed traveltimes for these events arrive considerably too late beyond 50 km offset. Rays for events at these ranges bottom within the lower half of Layer 5 between km 175 and km 200 and then pass through and emerge above the mid-crust high. Layer-5 phases at negative offsets of OBSA3 and OBH21 also suggest that the velocities south of km 200 may be faster than those of the model, though the fit to OBH17 is good. The addition of a thin (perhaps 3-km-thick) layer with velocities of 7.2-7.3 km/s within the base of the present Layer 5 between km 175 and km 200 would satisfy the OBSA2 and OBH16 Layer-5 traveltimes. Such a body would result in a lower-crustal low-velocity zone, however, and therefore, as these phases are unreversed, we have not included such a body in the final model.

The Layer 5 velocity north of km 250 is determined primarily from the linear, 7-km/s-apparent-velocity P_5 phase observed on instruments OBH19, OBSC4, and OBH27 (Figures 7a, 7b, and 7c) within ranges of -25 to -90 km, reversed by the slower, ~5.5-km/s-apparent-velocity P_5 phase observed on OBSC3 and OBSA1 (Figures 7d and 7e). Rays to these phases bottom mostly within the upper half of the layer, and the traveltime fit is most sensitive to velocity at the top of the layer. Inspection of the model fit to these phases suggests that somewhat higher velocities at the top of the layer may be acceptable, and this is borne out by qualitative assessments of sensitivity tests. A velocity increase from 6.15 km/s to 6.30 km/s at the top of the layer does not significantly degrade the overall traveltime fit. A decrease in the upper velocity to 6.00 km/s, however, has a marked effect on the traveltime fit.

Lower crust

The lower crust is characterized by velocities of 7.0-7.2 km/s seaward of the arc, decreasing velocity across km 250 near the arc, and velocities of 6.8-7.0 km/s at the northern end of the profile. Total crustal thickness increases northward to a maximum of 35 km at km 250, just seaward of the arc, and then thins to ~32 km thick beyond km 300, resulting in a slight downward bulge near km 250. This structure is constrained by Moho reflections (PmP) observed on eight of the wide-angle profiles with bottoming points between km 180 and km 280 (Figure 10). Multiple reciprocity ties between the observed PmP events enable unambiguous correlation of this phase. The OBSC4 and OBH21 profiles (Figures 13 and 14), for example, provide correlation ties to all the observed PmP phases. The resulting ray coverage (Figures 10 and 15) provides reasonable constraints on lower crustal structure. In addition, PmP phases observed on the end-line instruments of Line BA1 were modeled to constrain the velocity and thickness of the lower crustal layer at the northern end of the line.

Lower-crustal diving-wave phases, P_6, were not interpreted on any of the wide-angle profiles. The final model predicts traveltimes for P_6 phases that are potentially observable, however, and we have distinguished these traveltime curves in Figure 7 by plotting them in gray. The calculated P_6 traveltimes are generally consistent with first-arrival branches of the wide-angle data. This consistency suggests that the lower-crust velocities are neither considerably too fast nor considerably too slow. The most serious apparent discrepancies between calculated P_6 traveltimes and observed first-arrival times occur for OBH19 and OBSC4, where the phase emerges near -130 km range ~0.4 s ahead of the first arrivals. The lateral velocity contrasts of the model in Layers 5 and 6 create a shadow zone for the P_6 phase up to these ranges, and the amplitude of this phase beyond the shadow zone should be small. This is consistent with the ray synthetic calculated for OBH19 using the

Zelt and Smith [1991] code (Figure 16). It would not be surprising if this phase is present but unobservable.

The downwarping of the Moho in the vicinity of km 250 is a forward-modeled feature whose presence is suggested by the traveltime curvature of the PmP phase observed on OBH19 and OBSC4 and by strong secondary arrivals observed on OBH21 and OBH16. In Figure 16 we show the raypaths and traveltimes for PmP to OBH19 calculated for the final model. In models without a downwarped Moho, PmP arrives considerably too early between km 200 and km 225. This behavior is true for OBSC4 as well, and we note that the errant early-arriving rays would not be passing entirely through the Layer 5 high, but mostly south of it. Models that accommodate the required PmP delays in this interval, such as the downwarped Moho, are complex by virtue of their short wavelength and the resulting ray geometries — in this case a traveltime triplication — which are very difficult to invert for. This is illustrated in the ray diagram for the point-to-point raytraced PmP events (Figure 10c) where no bottoming points are found within the downwarped section of Moho because events from here are secondary arrivals of the triplication (Figure 16). Reflections from here would thus be ignored in most inversion schemes, including the *Zelt and Smith* [1991] scheme, and thus such a structure could only result pathologically from any given inversion step.

We have included a downwarped Moho (as opposed to a lower-crustal low-velocity zone) to explain the traveltimes of the OBH19 and OBSC4 PmP phases because this feature gives rise to a traveltime triplication that might explain the secondary arrivals observed on OBH21 and OBH16 (Figures 14 and 7j) as well as the anomalous character of the OBH19 PmP phase near -160 km range (Figure 7a). The downwarped Moho near km 250 has moderate success in modeling these PmP features. The secondary events observed on OBH21 and OBH16 are strong and continuous, however, and though the retrograde

branch of the downwarp triplication generally coincides with these arrivals, we cannot consider these features fully explained.

An additional interesting aspect of the PmP reflection is the amplitude behavior observed on OBH22, OBH17, and OBSA3 (Figures 7f, 7g, and 7h). On these instruments we observe a strong variation in PmP amplitude for reflections observed at the same range but on different instruments (i.e. different bottoming points). This behavior suggests that impedence constrasts vary laterally along the Moho and are particularly strong near km 265, the reflection point of the OBH22 PmP arrivals (Figure 3). This location lies beneath the axis of the active volcanic arc and on the northern flank of the downwarped Moho. The characteristics of the observed PmP reflections thus suggest the presence of complex structure and bright reflectivity in the lowermost crust or upper mantle in the vicinity of the currently active arc.

Line BA1

The primary goal of the analysis of the Line BA1 wide-angle data is to constrain the velocity structure at the northernmost end of Line A3. Line BA1 trends along the strike of the primary tectonic fabric and so should present a structural profile that is considerably more one-dimensional (1D) than that of Line A3. However, there is a prominent gravity lineation that extends along the length of the Beringian margin and crosses the center of Line BA1 (Figures 3 and 17). This gravity low is associated with a deep graben that has a dramatic expression in the Line BA1 MCS profile (Figure 18). This graben may represent the extensional reactivation of a relic crustal boundary fault of the paleo-Beringian convergent margin [e.g. *Cooper et al.*, 1987]. It is possible, then, that significant changes in crustal structure occur across the center of Line BA1. Nevertheless, the data quality of the three instruments along this line is good, and the coverage is sufficient to place bounds on the thickness and average velocity of the crust here.

The Line BA1 MCS profile reveals features with a direct correlation to the upper three layers defined for Line A3, including two distinct sedimentary units (Layers 1 and 2) and a 1- to 2-s thick reflective zone at the top of acoustic basement (Layer 3) (Figure 18). The character of these units remains more or less constant across the central graben, though there are differences in detail to either side. The wide-angle data are of moderate quality and display events correlative to those observed on Line A3 (Figure 19). A noisy interval between km 75 and km 125 obscures the P_5 and P_5P phase on OBH19 and the P_4 and P_4P phase on OBH20. A weak lower-crustal diving-wave phase, P_6, is observed on OBH19, and PmP is observed on both OBH19 and OBH20.

Constraints on the velocity and structure of the lower crust come from the observed PmP events and the interpreted OBH-19 P_6 event. These observations are too sparse to place unambiguous constraints on the structure of the lower crust, but we may place some bounds on possible structures by considering a suite of simplified models. Our approach was to invert for Moho depths with depth nodes defined at only three locations, the ends and center of the model, for a suite of effectively 1D layer velocity structures. Holding the velocity at the top and the bottom of the layer fixed, we first inverted for a two-node Moho parameterization with depth nodes only at the ends of the model, and then inserted a depth node at the center of the model and inverted again. We performed this inversion for velocities at the top of the layer ranging from 6.6 to 6.9 km/s and a 6.8- to 8.0-km/s range for the base.

The inversion results indicate that, for a uniform velocity layer, virtually no long-wavelength Moho structure is required to best fit the traveltime data. The relief on the Moho was never found to be more than 1.5 km and was less than 0.5 km for 90% of the imposed velocity profiles. We also observe that minimum misfits are obtained for thicker, high velocity crust (Figure 20b). The best fit model under this parameterization includes a 36-km-thick crust with a lower crustal velocity increasing linearly with depth from 6.7 to

7.7 km/s. The RMS misfit for this model, 0.07 s, is quite small. This is an unrealistic velocity structure, however, and this model is probably not correct. It is more likely that the parameterization is faulty, and that some combination of short-wavelength Moho structure and lateral velocity variation are required. This model is instructive, however, in that it is probably a reasonable approximation to the thickest, fastest velocity model consistent with the data. To move out of this RMS-misfit minimum we must consider thinner, slower models.

A variety of models can satisfy the traveltime constraints when a priori conditions are not imposed on the velocity structure and Moho relief. Imposing the qualitative constraint that predicted P_6 arrival times for OBH 20 be "close" to the observed first-arrival traveltimes, we obtained the velocity model in Figure 20a through forward modeling. This model has an RMS error of 0.072 s for the lower-crustal phases and predicts a larger amplitude P_6 phase for OBH19 than for OBH20 due to the lateral velocity gradient.

Gravity and magnetic anomalies

The correlation between velocity and density for crustal rocks [e.g. *Christensen and Mooney*, 1995] provides a check for consistency of a seismically determined velocity model with observed potential field anomalies. We converted the velocities of the Line A3 model to densities using the relationships described in Chapter 3 and calculated the predicted gravity anomalies for this model using the method of *Parker* [1973] (Figure 21). The predicted gravity anomaly matches the observed free-air anomaly calculated from shipboard data well over most portions of the model. The gravity-anomaly profile is dominated by the low of the trench, the gradient of the slope, the edge-effect high of the outer shelf (due to the asymmetric northward thinning of low-density slope sediments and thickening of the crust), and the back-arc low due to thickening sediments.

The most serious discrepancy between predicted and observed gravity anomalies occurs in the vicinity of the Layer 5 high where the calculated anomaly is nearly 50 mGal too high. Three-dimensionality undoubtedly plays a role in this misfit. It is clear from the satellite-derived local gravity-anomaly map (Figure 3) that the anomaly pattern between km 220 and km 265 is considerably three dimensional. Three-dimensionality does not provide a complete explanation for the misfit near km 230, however, as there are no obvious off-line, non-2-D gravity highs that we can readily ascribe to the Layer-5-high anomaly. A possible candidate is the north-south trending gravity high that extends northward from between OBH22 and OBSA1, crosses the western tip of Umnak Island and then turns northeastward. A high-velocity body strictly associated with this anomaly may not satisfy the traveltime data, however.

The well-resolved shallowing of the high-velocity Layer 5 near km 230 does not have an apparent expression in the regional satellite-derived gravity anomaly data. This indicates that the feature is either highly localized or simply does not represent a density contrast to the surrounding material. There is a dramatic change in magnetic anomaly character across the feature, however. The high-frequency character of the magnetic anomaly pattern between km 200 and km 300 suggests a shallowing of the magnetic source layer, which is probably Layers 3 and 4. The large-amplitude anomalies between km 220 and km 250 may reflect increased magmatic activity in this interval, across the Layer 5 high, or may simply reflect the shallowing of Layers 3 and 4 in this location. Further study of the regional potential field data is required, as these data may help determine whether the Layer 5 high is a localized magmatic construction or a tectonic feature perhaps associated with the Border Ranges Fault.

Constraints on the subducting slab

We note here briefly that the Line A3 MCS data provide constraints on the location of the slab out to km 180 at ~50-km depth. The top of the subducting crust is well imaged in the MCS data between km 50 and km 110 (Figure 22). The two-way times to this horizon, in combination with wide-angle arrivals observed on OBH25, OBSC1, and OBSA2, provide a very good estimate of the depth to the top of the slab out to km 125. Northward-dipping reflection events associated with the downgoing plate are observed on the MCS profile between km 190 and km 220 at 12-17 s two-way time (Figure 23). The association of these events with the slab has been clearly demonstrated through correlations with the along-arc Line A2 MCS profile [*S. McGeary*, unpublished manuscript]. We are able to constrain the location of the downgoing plate in the vicinity of km 180 by interpreting these events as reflections from the top of the slab, assuming a mantle-wedge velocity of 7.9 km/s, and modeling the reflection points for the length of the sequence as a single, dipping reflector (Figure 23). The deeper position of the slab was fixed so that the top of the slab corresponds to the location of the single deep-focus earthquake located by *E.R. Engdahl* [personal communication] at ~100 km depth.

Discussion

The focus of this paper is the genesis of continental crust at a convergent margin through terrane accretion and magmatism. It is thus important to consider the distribution of accreted terranes beneath Line A3, what the original structure of these terranes might have been, and what modifications have attended the accretion and reintrusion of this crust. There are indications in the velocity model that at least two distinct crustal provinces form the crust beneath the transect, one that is apparently quite mafic and one that is more similar to mature continental crust. We will consider the implications of this lateral heterogeneity, and what it tells us about crustal evolution at this margin, by comparing the crustal structure

beneath Line A3 with that beneath Line A1, an active intra-oceanic arc, and with the average velocity structure of continental crust.

Accreted terranes

An understanding of the processes attending terrane accretion depends upon the identification and characterization of terranes and terrane boundaries. The terranes we might expect to comprise the crust beneath Line A3 are the Peninsular and Chugach terranes, but the available geologic evidence provides only sketchy clues about the position of these crustal units beneath the transect. The Peninsular terrane is known to extend down the length of the Alaska Peninsula and is thought to include Umnak Island and then swing northwestward along the Beringian margin [*Cooper et al.*, 1987]. Umnak Island is covered in Tertiary and Quaternary volcanic and intrusive rocks, however, and the westernmost disposition of this terrane along the peninsula and of its southern boundary, the Border Ranges fault, is unclear. It is thus likely that Peninsular-terrane crust underlies a portion of Line A3, but it is unclear how much Peninsular-terrane material is present and under what portion of the transect. Similarly, rocks of the Chugach terrane are known on Sanak Island (Figure 3), but the width of the shelf, and thus the Southern Margin Composite terrane, decreases southwestward and it is unlikely that significant pre-Cretaceous accreted material exists west of Unimak pass.

There are several significant lateral changes in crustal seismic properties beneath Line A3 that may be related to distinct crustal units. The primary lateral variation occurs in the mid-crust across km 250. South of km 250 the mid-crust has velocities of 6.5-6.9 km/s whereas in the north the mid-crustal velocities are 6.15-6.40 km/s. This contrast is mimicked in the lower crust, though resolution here is much poorer than in the mid-crust. These two main crustal units, on either side of km 250, may in turn each be divided in two. To the south, the region between km 220 and km 250 is a structurally distinct unit, and the

small basin beneath OBH17 may be the surface expression of a fault bounding this unit (Figure 3). To the north, the region between km 250 and km 300 is distinguished by the character of Layer 3, and the abrupt transition in Layer-3 character across km 300 may represent a tectonic boundary.

We interpret the primary transition in crustal properties across km 250 to represent the boundary between the accreted Chugach and Peninsular terranes to the south and the pre-Cretaceous North American margin to the north (Figure 24). This interpretation is based largely on the properties of the upper crust. The upper crust south of km 220, in particular between km 125 and km 220, probably consists of Chugach-terrane rocks. The similarity of seismic character and velocity of Layer 3 to the character and velocity of the *lower series* unit observed in seismic lines and sonobuoy profiles on the Shumagin margin is compelling [*Bruns et al.*, 1987], and the correlation of the *lower series* with Shumagin formation rocks on Sanak Island makes it difficult to argue against an association of Layer 3 with Chugach-terrane rocks. The mid-crust south of km 220 resembles sediment-loaded, underplated oceanic crust, similar to what is observed for the Chugach terrane along the TACT Chugach profile [*Fuis et al.*, 1991]. It is thus possible, perhaps likely, that the Chugach terrane comprises most of the upper and middle crust between km 125 and km 220.

The upper crust between km 220 and km 250 is dominated by the thickened and elevated Layer 5. This structure has several possible interpretations. It may be a Cenozoic magmatic construction, an upthrust mid- to lower-crustal assemblage of the Peninsular terrane along the Border Ranges fault as observed onshore near Cook Inlet [*DeBari and Coleman*, 1989], or it may be the western expression of the Peninsular terrane's plutonic core, as the velocity structure here is similar to that determined for Peninsular-terrane crust near Cook inlet [*Ambos et al.*, 1989]. An association of the crust in this interval with the Peninsular terrane is natural given the likelihood that the crust south of km 220 corresponds

to the Chugach terrane. In this case, it is plausible to interpret the small basin beneath OBH17 as the surface expression of the Border Ranges fault.

We interpret the crust north of km 250 to be pre-Cretaceous North American crust that is overlain and intruded by Cenozoic volcaniclastic and volcanic rocks (Figure 24). This interpretation is based largely on the differences in seismic structure between this crust and that expected for oceanic-arc crust. This interpretation obviously depends on our expectation of oceanic-arc crustal structure, which is based on the structure observed beneath the intra-oceanic arc transect Line A1 (Figure 1). It is thus appropriate at this point to consider the comparison between Line-A1 and Line-A3 crustal structure.

Comparison with Line A1

The Line A1 profile across the Aleutian arc provides an important reference for interpreting the crustal structure of Line A3. The Peninisular terrane is thought to be an accreted oceanic arc, and thus we expect it to have had a structure similar to the crust beneath Line A1 prior to its accretion and reintrusion. In addition, we can ascribe the differences between Line A1 crustal structure and the structure of average oceanic crust to the Cenozoic flux of melt out of the mantle wedge. We would expect a similar volume of melt to have affected the Line A3 crust.

South of km 220, the crustal structures of the two transects are similar (Figure 25). Both profiles reveal a thick pile of <6.0-km/s material overlying a mid-crustal layer with oceanic-crustal velocity and thickness and a lower crust with velocities of 7.0-7.2 km/s. Several differences exist, however. The Layer-4 velocities south of km 220 on Line A3 are higher (5.5-6.0 km/s) than the corresponding layer beneath Line A1 (5.2-5.5 km/s). This increase may be due to the greater age of the Layer-4 material, a fundamentally different geologic make up, or a more pervasive plutonism within the upper crust of Line A3. The Southern Margin Composite terrane experienced episodes of granitic plutonism in the early

Cretaceous along the Border Ranges fault and during the late Paleocene to early Eocene along a 2100-km-long belt that extends as far west as Sanak Islands [*Plafker et al.*, 1994]. In addition, the thickness of material above Layer 4 is greater than the thickness of material above the 5.2-5.5 km/s along Line A1, and the amount of crust seaward of the arc is considerably greater along Line A3 than along Line A1. These differences are all consistent with the presence of accreted crust south of the arc on Line A3.

Another important difference between these two profiles is the Layer 5 structure between km 220 and km 250. An interesting feature of the Line A1 model is the absence of a massive plutonic core beneath the arc. It is possible that the absence of massive plutonism in the upper crust is characteristic of oceanic arcs in general, and that it is only upon accretion and reintrusion that seismically-resolvable volumes of plutonic material are emplaced in the upper crust. This possibility is purely speculative, however, as it is equally likely that upper-crustal plutonism varies along the length of the arc and that the Layer 5 structure is a localized feature. Moreover, as described above, the Layer 5 structure may not be a magmatic construction at all but a tectonic feature. A regional, along-arc characterization of upper-most crustal structure is necessary to define the nature and importance of this feature.

The most significant differences between the crustal structure beneath Line A3 and Line A1 exist north of km 250. Along Line A1, the mid-crustal layer thins and the lower-crustal layer thickens, whereas the mid-crustal layer along Line A3 remains nearly constant but the velocities of this layer decrease from those of mafic rocks to velocities consistent with intermediate-composition rocks. Thus, the mid crust north of km 250 is compositionally more similar to mature continental crust than is the crust to the south, which is more similar to the intra-oceanic-arc crust of Line A1.

The interpretation of the origin of the crust north of km 250 is particularly important to our understanding of crustal evolution of this margin. If this crust belongs to the oceanic-

arc Peninsular terrane, then comparison with Line A1 would suggest that the bulk composition of this crust has undergone considerable evolution. We believe that this is unlikely, however, because of the apparent lack of significant upper crustal plutonism along Line A3 north of km 250. A magmatic modification of Line-A1-type crust to that of Line A3 would require substantial melting and fractionation of both the middle and lower crust and the removal of an ultramafic residue. As crustal thickness is approximately the same for both Line A1 and Line A3, a magmatic flux from the mantle would presumably be required to offset the loss of the residuum. Substantial melting and fractional recrystallization of a 30-km-thick crust are dramatic modifications, and we would expect to see some effect of them in Layers 3 and 4, most likely in the form of significant plutonic intrusion of these basement layers. No modifications of this type are suggested by the velocities (4.5-5.5 km/s), which are similar to those observed both to the south and along Line A1 and are consistent with a mixture of flows, volcaniclastic sediments, and small isolated plutons. It is therefore more likely that the crust north of km 250 was not originally oceanic-arc crust, but thin crust of the pre-Cretacous North American margin that has been thickened through foreland deposition during accretion of the southern terranes and through Cenozoic arc magmatism.

In summary, we interpret much of the crust south of km 250 to be comprised of the accreted Chugach and Peninsular terranes based on the likely association of Shumagin formation rocks with Layer 3 south of km 220 and the similarity of the crust to seismic observations along the TACT seismic lines onshore to the east [*Fuis et al.*, 1991; *Ambos et al.*, 1995]. The general similarity of the accreted crust to that of Line A1 suggests that the accreted material has an oceanic-arc origin, as expected for the Chugach and Peninsular terranes, and that this material has undergone limited modifications since accretion. We interpret the crust north of km 250 to be pre-Cretaceous North American margin crust that was perhaps thickened during accretion of the outboard terranes. We do not believe that

this crust has been modified from a more mafic composition through magmatic processes because the upper crustal velocities are inconsistent with the massive plutonism expected to accompany such a transformation.

These interpretations must be tempered with a final observation from the comparison of Line A3 to Line A1. As stated above, we can ascribe the differences between Line-A1 crustal structure and the structure of average oceanic crust to the Cenozoic flux of melt out of the mantle wedge. We would expect a similar volume of melt to have affected the Line A3 crust. If we interpret most of the crust south of km 250 to be accreted terranes, then a simple comparison of the structure beneath the two profiles (Figure 25) suggests that a substantial amount of Cenozoic material is missing beneath Line A3. There are several possible explanations for this discrepancy. Cenozoic melt production may have been anomalously small beneath Line A3 or anomalously large beneath Line A1; the lower crust of the Peninsular and Chugach terranes may have delaminated upon accretion and been replaced with Cenozoic material; Cenozoic melts may be more widely distributed north of the Alaskan Peninsula; a larger proportion of Cenozoic material may be present below the Moho beneath Line A3 than beneath Line A1; or our interpretation of accreted crust south of km 250 may be in error.

This final possibility, that our interpretation of the terrane components of the Line-A3 crust is in error, has serious implications for the crustal evolution across this margin and requires some consideration. An extreme possibility is that the similarity of Layer 3 and the *upper series*/Shumagin formation is coincidental and that no crust of the Chugach or Peninsular terranes is present beneath Line A3. This scenario requires a jump in subduction from somewhere south of km 250 to approximately the current location of the trench, trapping a length of Kula Plate oceanic crust as the current mid-crustal layer. A reorganization of this type presumably occured somewhere near Unimak Pass during the Eocene initiation of subduction along the Aleutian arc. If this reorganization occurred east

of Unimak Pass, the relic subduction zone should be present beneath Line A3 and as a margin-oblique structure beneath the Cenozoic sediment cover south of Umnak Island. Further processing of the Line A3 and Line A2 MCS may reveal evidence for a relic subduction zone, but at present there is no indication of a relic subduction zone beneath or east of Line A3, and we remain confident in our interpretation of accreted terranes south of km 250.

Comparison to average continental crust

The average composition of continental crust and its compositional variation with depth have been estimated from a variety of methods [e.g. *Rudnick*, 1995]. Continental crust has an average thickness of 41 km, an intermediate bulk composition, and is compositionally layered, with the upper third having a felsic composition (>70% SiO_2), the middle an intermediate composition, and the lower third of the crust having a mafic composition (<53% SiO_2) [*Christensen and Mooney*, 1995]. The first-order correlation of seismic velocity with composition enables compositional inferences to be made based on comparisons of observed crustal seismic structure with the well-defined average seismic structure of continental crust [e.g. *Christensen and Mooney*, 1995].

Comparison of vertical velocity profiles at km 200, km 225, and km 300 with the average-continental-crust profile of *Christensen and Mooney* [1995] (Figure 26) shows that the Line-A3 crust is thinner and more mafic than average continental crust and lacks a 5- to 10-km thick, 5.8-6.2 km/s, granitic-tonalitic, upper-crustal layer characteristic of continental crust [e.g. *Fountain and Christensen*, 1989]. The crust south of km 250 is considerably faster, and thus more mafic, than continental crust. We have interpreted this crust to consist of accreted oceanic-arc and accretionary complex terranes, and comparison with Line A1 shows the structure here to be very similar to that of a currently active oceanic arc. If this interpretation is correct, then we can conclude that the processes of terrane

accretion and reintrusion along this margin have not substantially modified the composition of these terranes toward that of continental crust.

To the north, the mid-crust has velocities similar to continental crust at these depths, but the lower crust is somewhat faster than continental crust. We have suggested that this may have been initially thin crust of the North American margin, perhaps covered with a thick wedge of flysch [*Plafker and Berg*, 1994], prior to the accretion of the Peninsular terrane. The 10-km-thick mid-crustal layer may thus represent a tectonically thickened flysch layer whose felsic to intermediate composition may be representative of the composition of the ~10-km-thick blanket of low-velocity material covering the crust along both Line A1 and Line A3. While this interpretation is speculative, it emphasizes the importance of geologic setting in determining dramatic lateral heterogeneity of bulk crustal properties.

Conclusions

The objectives of this study were to define the crustal structure across the Aleutian arc at the western end of the Alaskan Peninsula, where crustal growth has occured through arc volcanism and the accretion of oceanic-arc and accretionary-complex terranes, and to interpret these results in terms of evolution from oceanic-arc-crust properties towards those of mature continental crust. Our major conclusions include:

1) The crust south of the currently active arc probably consists of the accreted Peninsular and Chugach terranes. The structure of these terranes is similar in most respects to the intra-oceanic-arc crust of Line A1, and the composition of this crust is mafic.

2) The crust north of the active magmatic arc is compositionally more evolved than that to the south, though probably more mafic than average continental crust. Lack of evidence for massive upper-crustal plutonism suggests that this crust has not evolved from oceanic-arc crust through magmatic differentiation but instead was probably thin crust of the North American margin prior to the accretion of the southern terranes. The intermediate-

composition mid-crust layer may be dominated by thickened volcaniclastic sequences and thus may be characteristic of the composition of the low-velocity layers currently blanketing the arc.

3) The crust along the entire transect lacks a granitic (5.8-6.2 km/s) upper layer characteristic of mature continental crust. This layer thus presumably evolves from tectonic and magmatic events which have not occured along this margin.

4) With respect to proposed mechanisms for the genisis of continental crust from oceanic arc magmatism, we can conclude that the crustal structure observed for Line A1 and Line A3 are generally inconsistent with a net flux of intermediate composition melt from the mantle wedge across the Moho, or the so-called andesite model and its variants [e.g. *Kelemen et al.*, 1995]. In addition, the processes of accretion and reintrusion along this margin have been insufficient to substantially modify the bulk composition of the accreted crust, either through delamination or widespread crustal melting. If lower-crustal delamination occured upon accretion, this material has since been replaced by a mafic lower crust. We may tentatively conclude that continental crust does not acquire its bulk compositional properties in either an intra-oceanic arc or upon accretion of an oceanic arc. It is arguable that accretion at the westernmost end of the Alaska Peninsula is not typical, however, and that "hard" accretion, characterized by considerable crustal thickening, may occur under different conditions. Likewise, Cenozoic magmatic crustal construction along the Aleutian arc, as characterized by the Line A1 results, may not be typical of all oceanic arcs. Crust of the Izu-Ogasawara arc, for example, appears to be considerably more felsic than the Aleutian arc crust [*Suyehiro et al.*, 1996].

5) Rocks associated with Cenozoic magmatism beneath Line A3 may be located within the lower crust south of the current active magmatic arc, throughout the crust north of the arc, and possibly beneath the seismic Moho. If a substantial volume of Cenozoic subduction-related igneous rocks is present within the crust north of the arc along Line A3,

then the composition of Cenozoic arc magmas beneath Line A3 is probably more felsic than beneath Line A1 and may, in fact, be similar to the average composition of continental crust.

These conclusions tend to say more about where continental crust is *not* formed than about the genesis of continental properties. One may wonder if the growth of continental crust from oceanic arcs is in fact a viable model. There is no cause for concern in this regard, however, as we will see in Chapter 5 that crust of a similar origin to Line A3 has evolved a characteristic continental velocity structure, complete with a granitic upper crustal layer.

134

References

Ambos, E.L., W.D. Mooney, and G.S. Fuis, Seismic refraction measurements within the Peninsular terrane, south central Alaska, *J. Geophys. Res.*, *100*, 4079-4095, 1995.

Bruns, T.R., R. von Huene, R.C. Culotta, S.D. Lewis, and J.W. Ladd, Geology and petroleum potential of the Shumagin margin, Alaska, in *Earth Science Series*, vol. 6, *Geology and Resource Potential of the Continental Margin of Western North America and Adjacent Ocean Basins - Beaufort Sea to Baja California*, edited by D.W. Scholl, A. Grantz, and J.G. Vedder, pp. 157-189, Council for Energy and Mineral Resources, Houston, Texas, 1987.

Christensen, N.I., and W.D. Mooney, Seismic velocity structure and composition of the continental crust: A global view, *J. Geophys. Res.*, *100*, 9761-9788, 1995.

DeBari, S.M., and R.G. Coleman, Examination of the deep levels of an island arc: evidence from the Tonsina ultramafic-mafic assemblage, Tonsina, Alaska, *J. Geophys. Res.*, *94*, 4373-4391, 1989.

Fountain, D.M., and N.I. Christensen, Composition of the continental crust and upper mantle: A review, in Geophysical Framework of the Continental United States, edited by L. C. Pakiser and W.D. Mooney, *Mem. Geol. Soc. Am.*, *172*, 711-742, 1989.

Fuis, G.S., E.L. Ambos, W.D. Mooney, N.I. Christensen, and E. Geist, Crustal structure of accreted terranes in Southern Alaska, Chugach Mountains and Copper River Basin, from seismic refraction results, *J. Geophys. Res.*, *96*, 4187-4227, 1991.

Fuis, G.S., and G. Plafker, Evolution of deep structure along the Trans-Alaska Crustal Transect, Chugach Mountains and Copper River Basin, Southern Alaska, *J. Geophys. Res.*, *96*, 4229-4253, 1991.

Kay, S.M., and R.W. Kay, Aleutian magmas in space and time, in *The Geology of North America*, vol. G-1, *The Geology of Alaska*, edited by G. Plafker, and H.C. Berg, pp. 687-722, Geological Society of America, Boulder, Colo., 1994.

Kelemen, P.B., Genesis of high Mg# andesites and the continental crust, *Cont. Min. Petr.*, *120*, 1-19, 1995.

Miller, T.P., Pre-Cenozoic plutonic rocks in mainland Alaska, in *The Geology of North America*, vol. G-1, *The Geology of Alaska*, edited by G. Plafker, and H.C. Berg, pp. 535-554, Geological Society of America, Boulder, Colo., 1994.

Miller, T.P., and D.H. Richter, Quaternary volcanism in the Alaska Peninsula and Wrangell Mountains, Alaska, in *The Geology of North America*, vol. G-1, *The Geology of Alaska*, edited by G. Plafker, and H.C. Berg, pp. 759-776, Geological Society of America, Boulder, Colo., 1994.

Moll-Stalcup, E.J., Latest Cretaceous and Cenozoic magmatism in mainland Alaska, in *The Geology of North America*, vol. G-1, *The Geology of Alaska*, edited by G. Plafker, and H.C. Berg, pp. 589-619, Geological Society of America, Boulder, Colo., 1994.

Mooney, W.D., and R. Meissner, Continental crustal evolution observations, EOS. Trans., 72, 537-585, 1991.

Parker, R.L., The rapid calculation of potential anomalies, *Geophys. J. R. Astr. Soc., 31*, 447-455, 1973.

Pearcy, L.G., S.M. DeBari, and N.H. Sleep, Mass balance calculations for two sections of island arc crust and implications for the formation of continents, *Earth. Planet. Sci. Lett., 96*, 427-442, 1990.

Plafker, G., H.C. Berg, Overview of the geology and tectonic evolution Alaska, in *The Geology of North America*, vol. G-1, *The Geology of Alaska*, edited by G. Plafker, and H.C. Berg, pp. 989-1021, Geological Society of America, Boulder, Colo., 1994.

Plafker, G., J.C. Moore, and G.R. Winkler, Geology of the southern Alaska margin, in *The Geology of North America*, vol. G-1, *The Geology of Alaska*, edited by G. Plafker, and H.C. Berg, pp. 389-449, Geological Society of America, Boulder, Colo., 1994.

Rudnick, R.L., Making continental crust, *Nature, 378*, 571-577, 1995.

Suyehiro, K., N. Takahashi, Y. Ariie, Y. Yokoi, R. Hino, M. Shinohara, T. Kanazawa, N. Hirata, H. Tokuyama, A. Taira, Continental crust, crustal underplating, and Low-Q upper mantle beneath and oceanic island arc, *Science, 272*, 390-392, 1996.

Vallier, T.L., D.W. Scholl, M.A. Fisher, T.R. Gruns, F.H. Wilson, R. von Huene, A.J. Stevenson, Geologic framework of the Aleutian arc, Alaska, in *The Geology of North America*, vol. G-1, *The Geology of Alaska*, edited by G. Plafker, and H.C. Berg, pp. 367-388, Geological Society of America, Boulder, Colo., 1994.

Zelt, C.A. and R.B. Smith, Seismic traveltime inversion for 2-D crustal velocity structure, *Geophys. J. Int., 108*, 16-34, 1992.

Figure Captions

Figure 1: Location map of the 1994 Aleutian seismic experiment. MCS track lines and ocean-bottom instruments (white circles) are indicated on the gray-shaded relief map of bathymetry.

Figure 2: Cenozoic and Pre-Cenozoic magmatic belts of southwestern Alaska. The pre-Eocene location of subduction along the Beringian margin, the location of the Border Ranges Fault (BRF), the Southern Margin Composite terrane, and the tracks of the instrumented lines of the 1994 Aleutian seismic experiment are also indicated. [Adapted from *Plafker et al,* 1994; *Plafker and Berg,* 1994; and *Moll-Stolcup,* 1994]

Figure 3: Ocean-bottom instrument locations along Line A3 and Line BA1 plotted on satellite-based free-air gravity anomaly pattern. Gravity contours are 10 mGal.

Figure 4: Brute stack of the Line A3 MCS data plotted with a 4- to 30-Hz bandpass filter and $t^{.8}$ time-varying gain.

Figure 5: Gray-shade and contour plot of the Line A3 final velocity model. Velocities are indicated in km/s and contoured at 0.5 km/s. Bold lines on mid-crust and Moho interfaces represent reflection points of P_5P and PmP reflections. Gray bold line on Moho corresponds to PmP triplication bounce points. Arrow at top indicates position of magmatic arc, with vertical lines indicating line turn through Unimak pass. White circles indicate earthquake events within 50 km of the line (gray in the inset map view) located by Engdahl [personal communication] with a depth error of less than 3 km. Circle sizes are for events with body-wave magnitudes $mb \leq 5$, $5 < mb < 6$, $mb \geq 6$. Mantle velocities are assumed, and depth of subducting slab is constrained to model km 185.

Figure 6: Traveltime picks and fit traveltime curves for all Line A3 ocean-bottom instruments. Reduction velocity is 7 km/s.

Figure 7: Record sections with and without calculated traveltime curves overlain for Line A3 ocean-bottom instruments. Reduction velocity is 7 km/s for all sections, but horizontal and vertical scales vary. Calculated traveltime curves for the P6 lower-crustal diving-wave phase indicated in gray.

Figure 8: Detailed view of the Line A3 MCS data across the slope with velocity-model interfaces indicated.

Figure 9: Detailed view of the Line A3 MCS data north of the arc with velocity-model interfaces indicated. Note change in character of both the sedimentary sequences and the basement across km 305, as well as the unusual disturbance within the sedimentary sequence near km 305.

Figure 10: Two-point ray diagrams (i.e. only rays to traveltime picks) for the (a) P_5, (b) P_5P and (c) PmP phases. White dots in (a) mark the bottoming points of the diving-wave phases and indicate very good velocity resolution of the mid crust. No PmP reflection points are indicated for the depressed Moho near km 250 (gray bold line) are reflections from here secondary-arrival triplications.

Figure 11: Reversed profiles located on either side of the Layer 5 high. First arrivals traveling to both the north and south show a decrease in apparent velocity at ranges beyond the Layer 5 high, requiring the presence of the high. The effect is more dramatic to the north where the thickness of the slowest velocity upper layers is greatest.

Figure 12: RMS misfits of traveltime picks most sensitive to the velocity at the top of the Layer 5 high due to perturbing the velocity at the top of the layer. Perturbed models for top velocities of 6.0, 6.4 and 6.8 km/s are shown. Results of two runs are indicated, with and without traveltime picks from OBSC3 which has large misfits near the

northern flank of the high. These results demonstrate the sensitivity of the data, and qualitative considerations suggest an uncertainty of ±0.20 km/s for the upper velocity of the high.

Figure 13: Detail of OBSC4 indicating the PmP phase, the location of the inferred triplication, and the reversal points for other instruments.

Figure 14: Detail of OBH21 indicating the PmP phase, the location of the inferred triplication, and the reversal points for other instruments. Note that at the OBSC4 reversal point it is the strong, continuous event at ~4.6 s that reverses with the strong PmP phase of OBSC4 (Figure 14).

Figure 15: Ray diagrams for OBH19 and OBH21 illustrating PmP-triplication bottoming points.

Figure 16: Ray synthetic for a portion of the OBH19 demonstrating the relative strength of the P_6 lower-crustal diving wave phase. The most serious discrepancy between predicted P_6 traveltimes and observed first arrivals occurs for OBH19 and OBSC4, but the predicted amplitudes for these phases is relatively small due to a shadow-zone effect associated with lateral velocity variations in Layers 5 and 6, as suggested by this figure.

Figure 17: Shaded-relief image of satellite-derived free-air gravity anomalies illustrating, among other things, the gravity-low trend that tracks inboard of the Beringian margin and crosses the center of Line BA1. This low is associated with a steep-sided graben and may represent a major crustal boundary.

Figure 18: Line BA1 MCS brute stack. Note the prominent steep-sided graben in the center of the profile and the well defined reflectivity of the upper 1 to 2 s of basement which we associate with Layer 3.

Figure 19: Wide-angle profiles for Line BA1 ocean-bottom instruments. Processing and display are the same as for Line A3 except that a minimum-phase (instead of a zero-phase) bandpass filter was used.

140

Figure 20: a) Final velocity for Line BA1. b) Contour of RMS error (s) of constrained inversions for Moho structure including only three depth nodes and laterally constant velocity for a suite of fixed top and bottom velocities. White numbers indicate the RMS error in seconds. Labeled diagonal lines indicate the Moho depth for each inversion result - introduce Moho structure was negligible for each of these runs.

Figure 21: (Top) Observed (shipboard) and calculated free-air gravity anomaly as well as magnetic anomaly along Line A3. (Bottom) Density model based on seismic velocities.

Figure 22: Line A3 MCS profile across the trench and forearc. Reflections from the subducting slab are visible beneath the forearc at ~10 s to near km 110.

Figure 23: (Top) Inboard dipping reflection sequence associated with the subduction slab observed on Line A3 MCS profile with calculated vertical-incidence-ray traveltime curve overlain. (Bottom) Vertical incidence rays reflecting off linear slab segment used to model depth of slab between km 150 and 200.

Figure 24: Cartoon illustrating preferred interpretation of major crustal components and terranes. Evidence for the lateral transition across the arc from accreted to non-accreted terranes comes from the lateral transition in velocity and the distribution of Chugach and Peninsular terrane material east of the transect. The depth extent of these terranes is uncertain. A shallower extent for this accreted material would imply a large proportion of Cenozoic (Cz) lower crustal magmatic additions.

Figure 25: Comparison of Line A3 and Line A1 velocity structure. Arrows indicate location of active arc. Line A1 velocity structure from *W.S. Holbrook* [unpublished manuscript].

Figure 26: Comparison of Line A3 vertical velocity profiles from km 200, km 225, and km 300 (circles with thin lines) with the in-situ velocity structure of average continental crust [*Christensen and Mooney*, 1994] shown with standard deviations.

Figure 4.1

142

Figure 4.2

Cenozoic Magmatic Belts

Alaska Range - Talkeetna Mts (50-75 Ma)

Yukon-Kanuti Belt (65-56 Ma)

Kuskokwim Mts (72-60 Ma)

TACT Seismic Lines

Pre-Cenozoic Terranes

Peninsular Terrane

Chugach Terrane

Togiac Terrane

Kahiltna Terrane

Beringian Margin

200 m

Unimak Pass

Relic Kula Plate Oceanic Crust
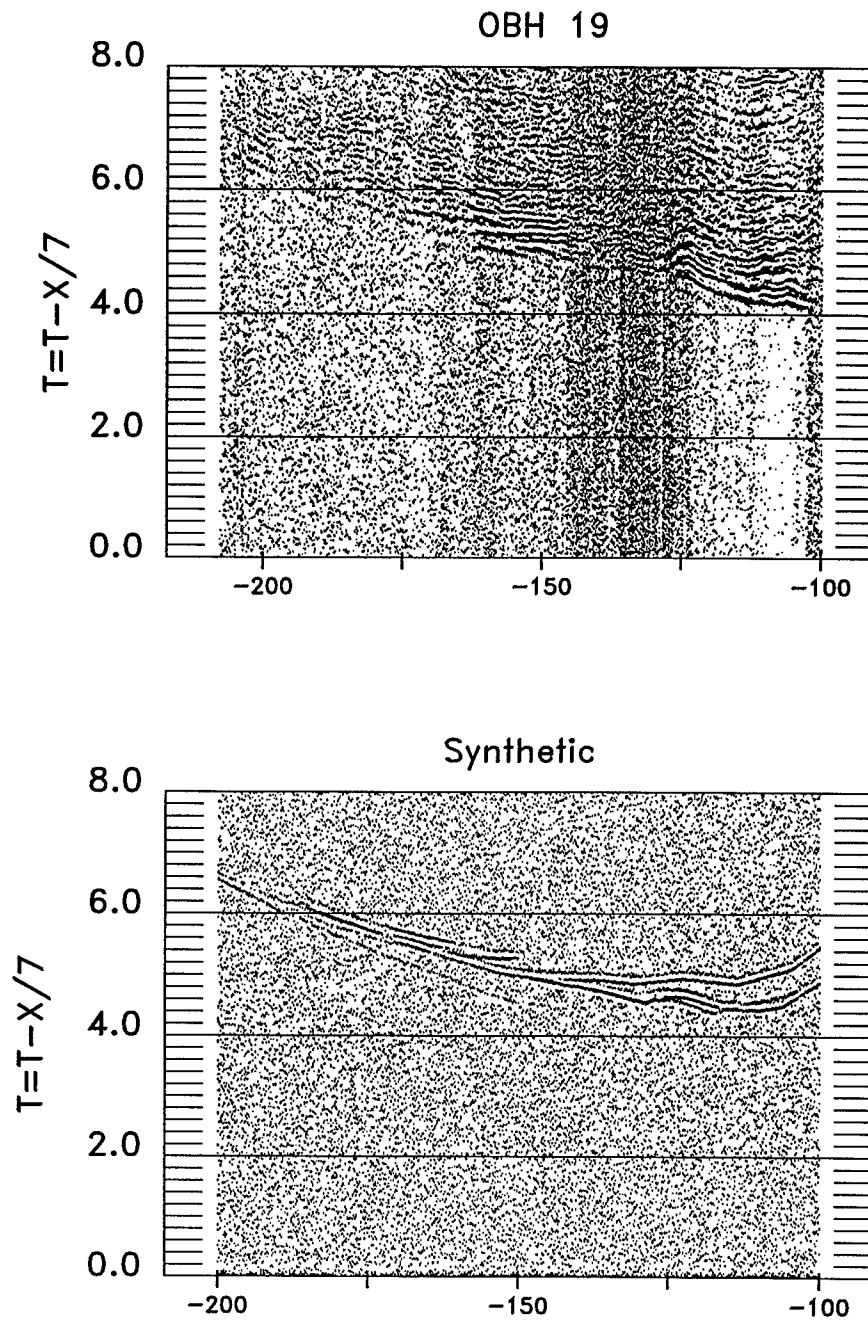
Aleutian Trench

Umnak Is.

Sanak Is.

BRF

Figure 4.3

Line A3 Mcs
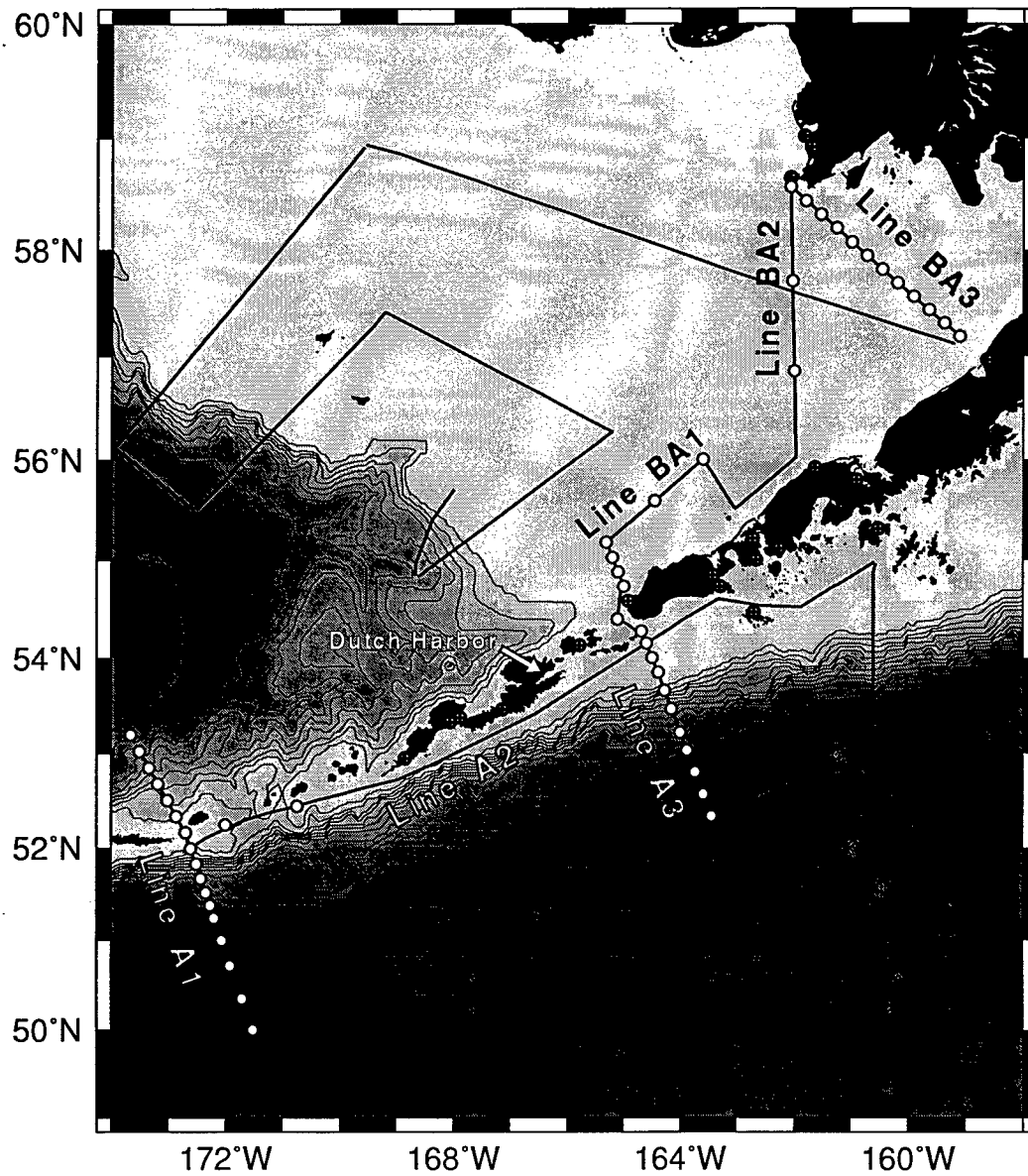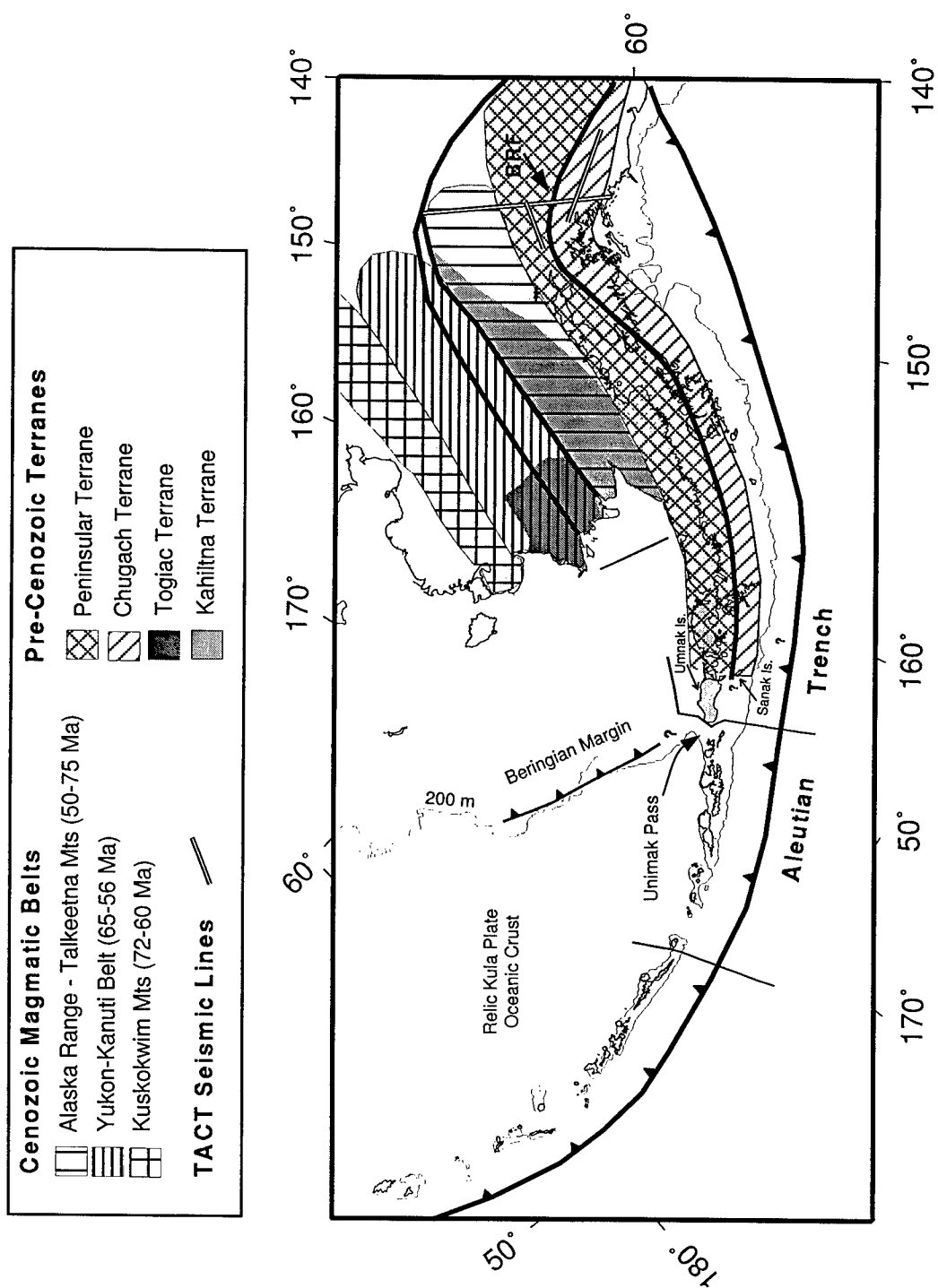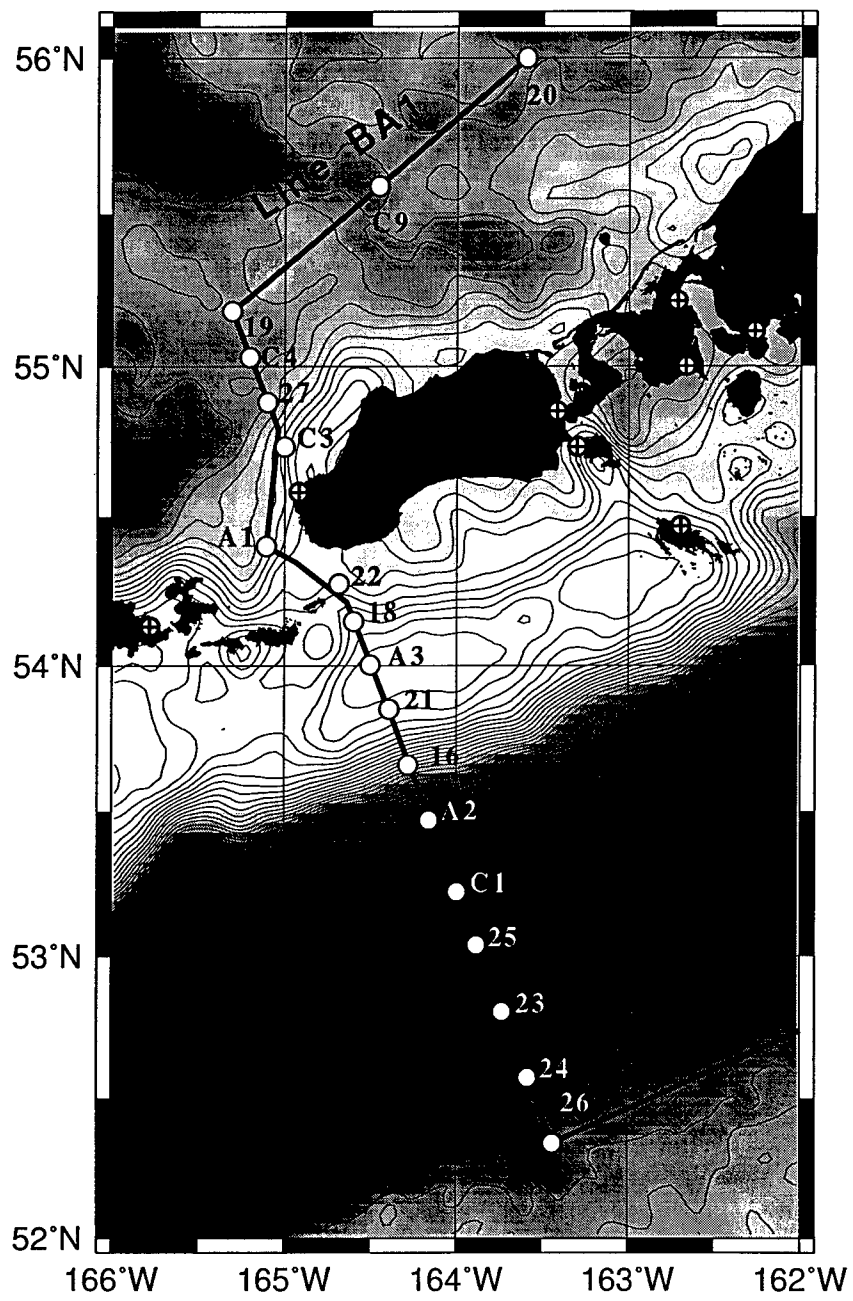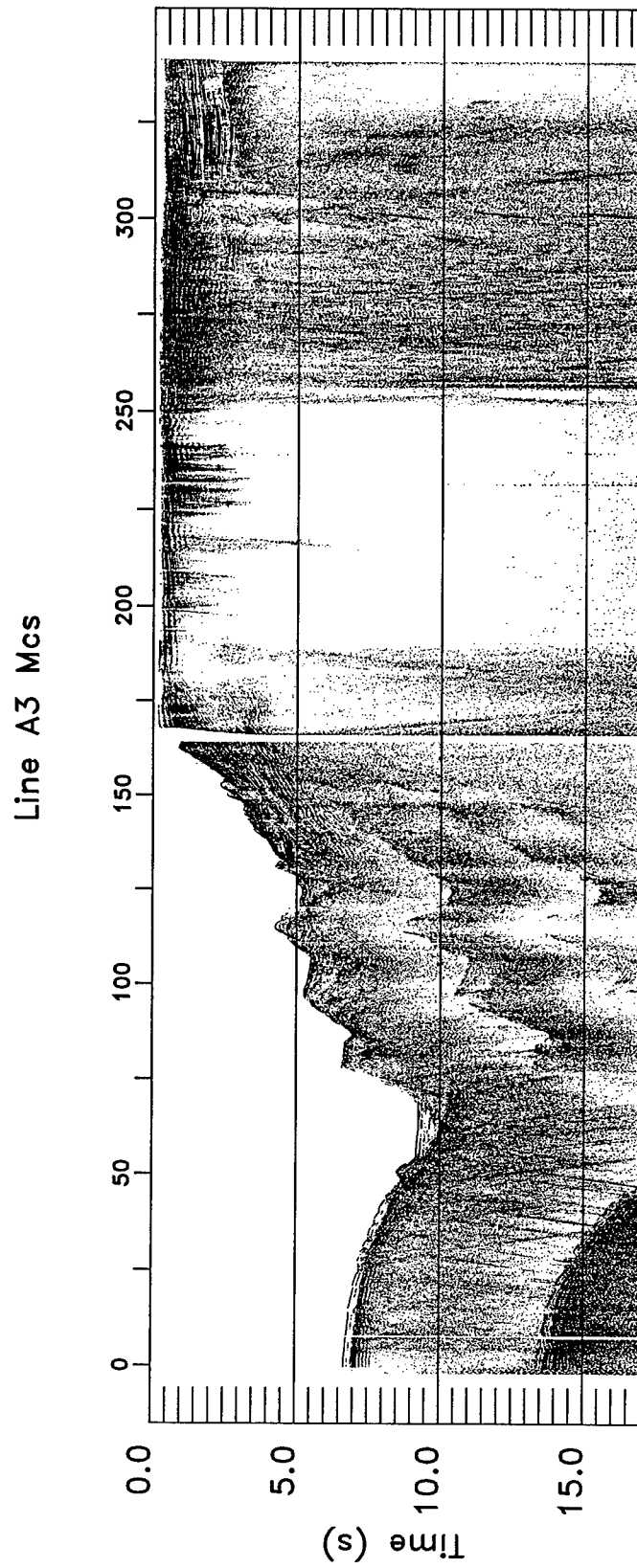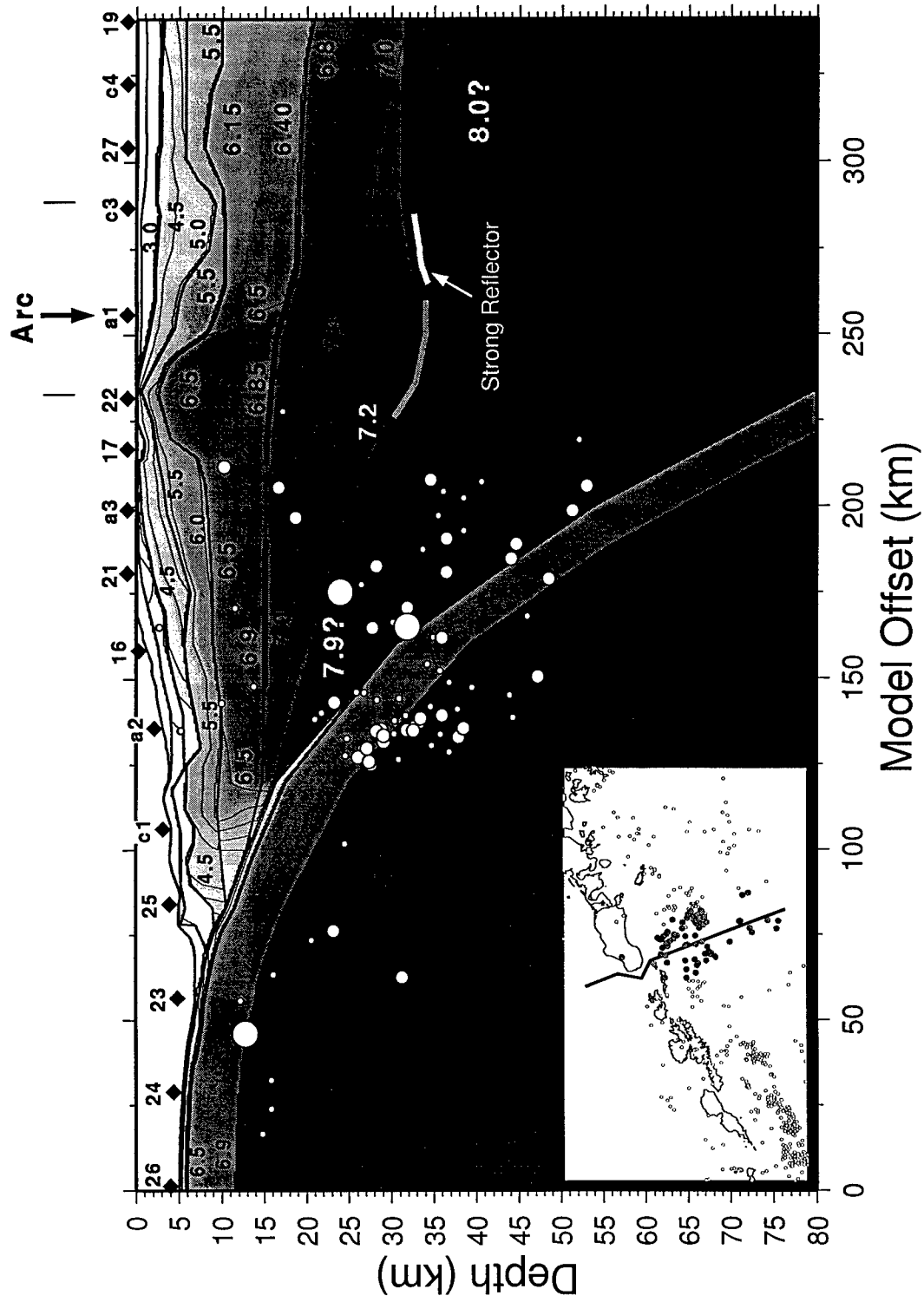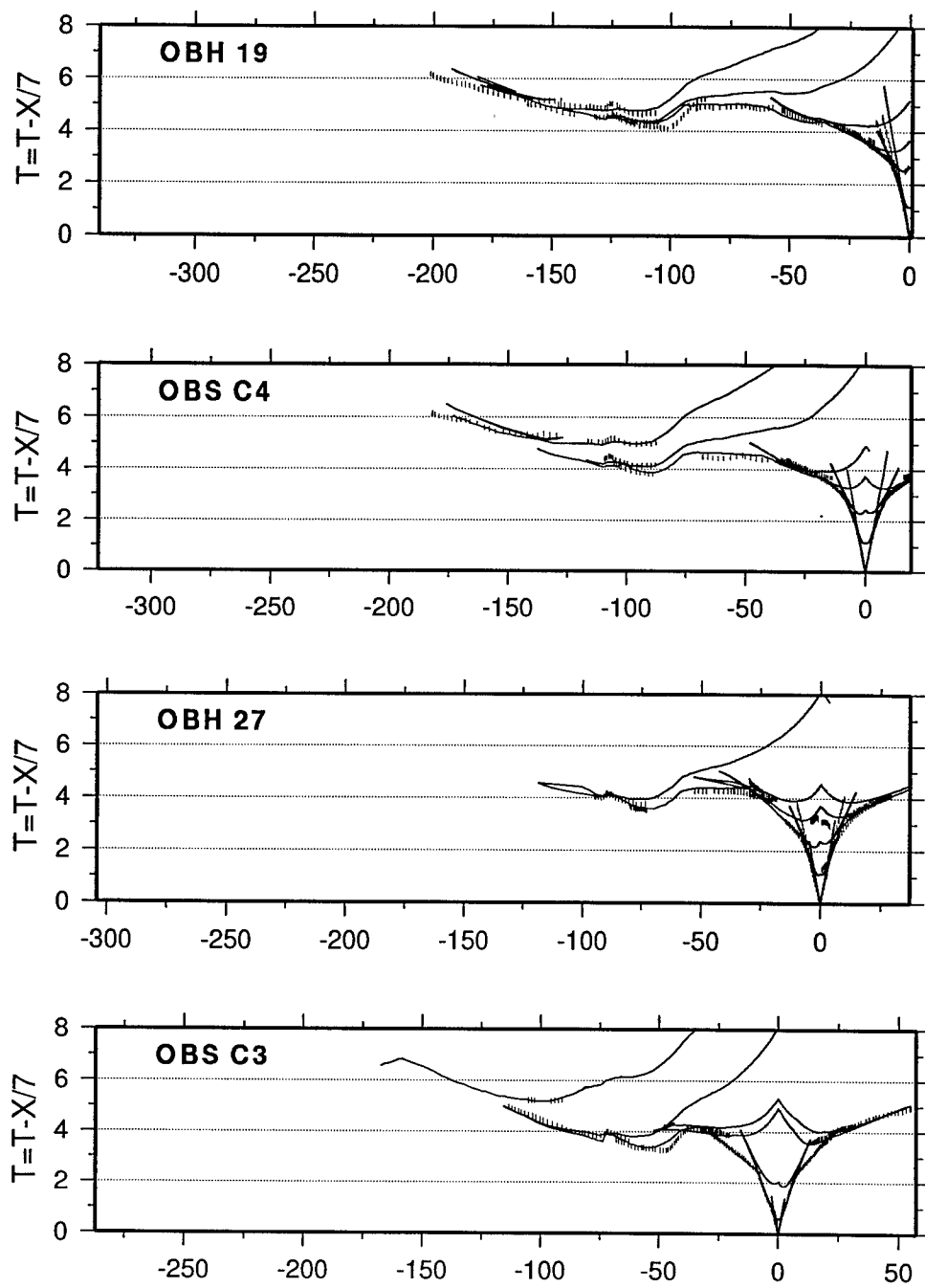
Figure 4.4

Figure 4.5

Figure 4.6
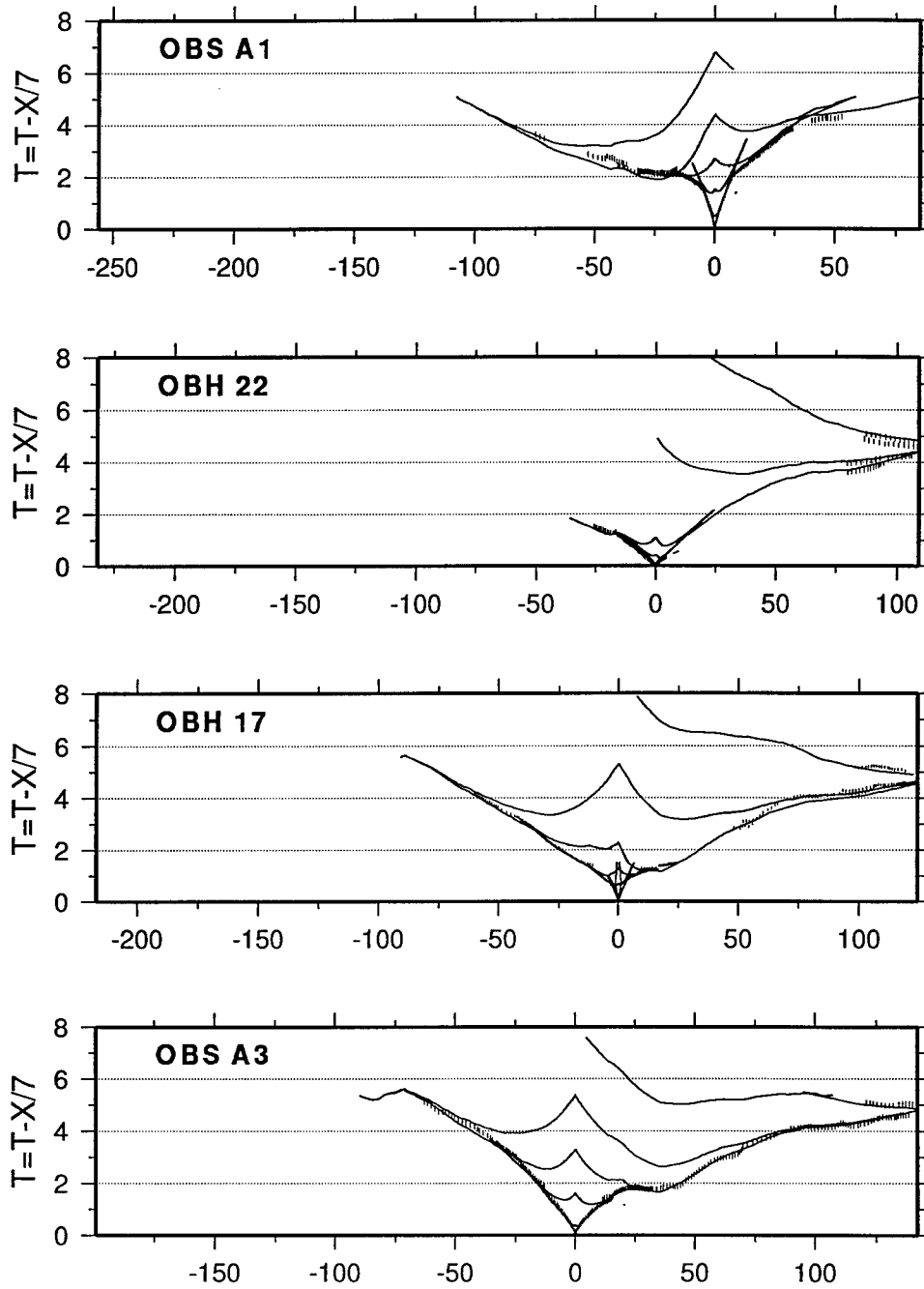
Figure 4.6 cont.
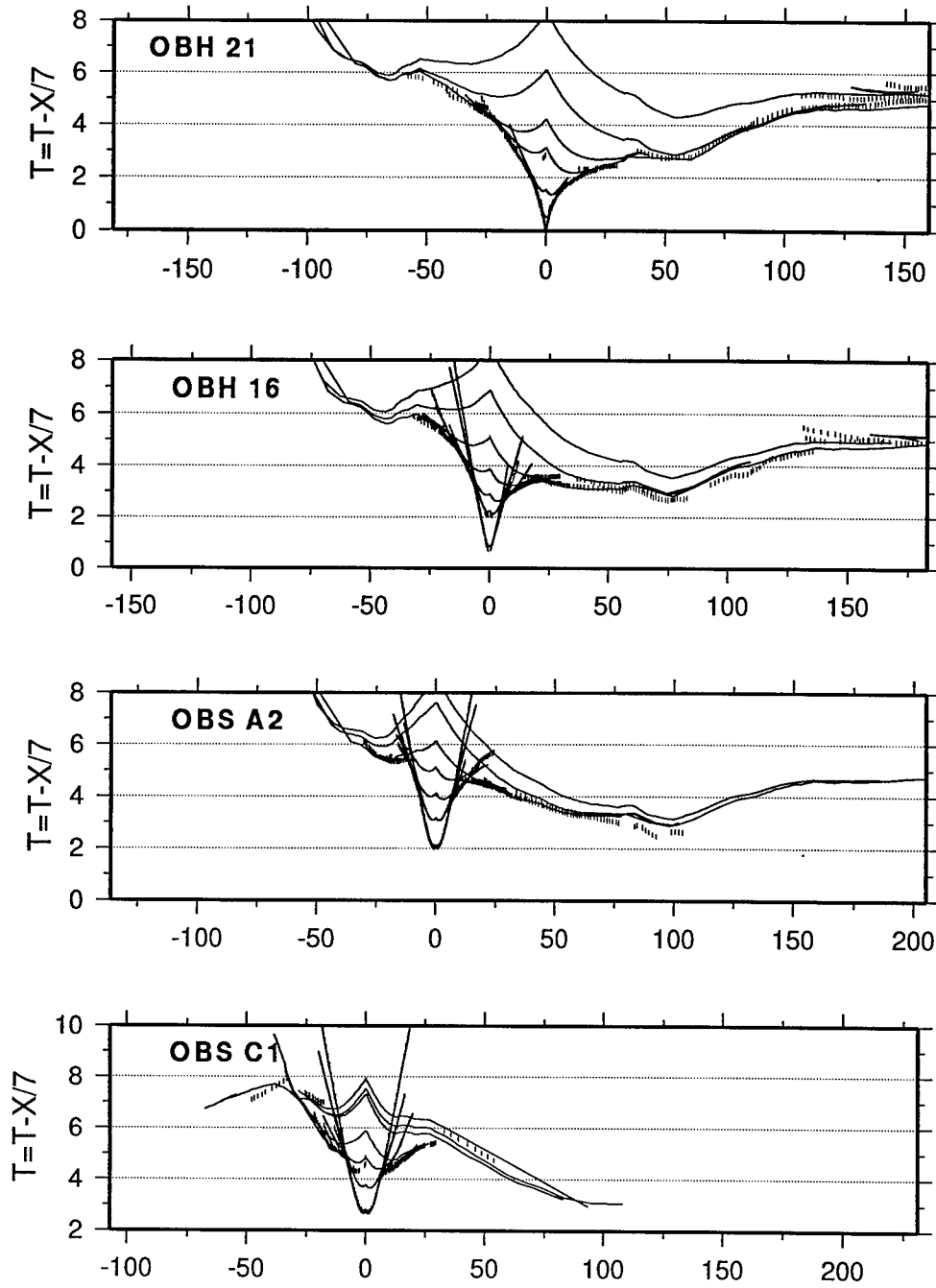
Figure 4.6 cont.
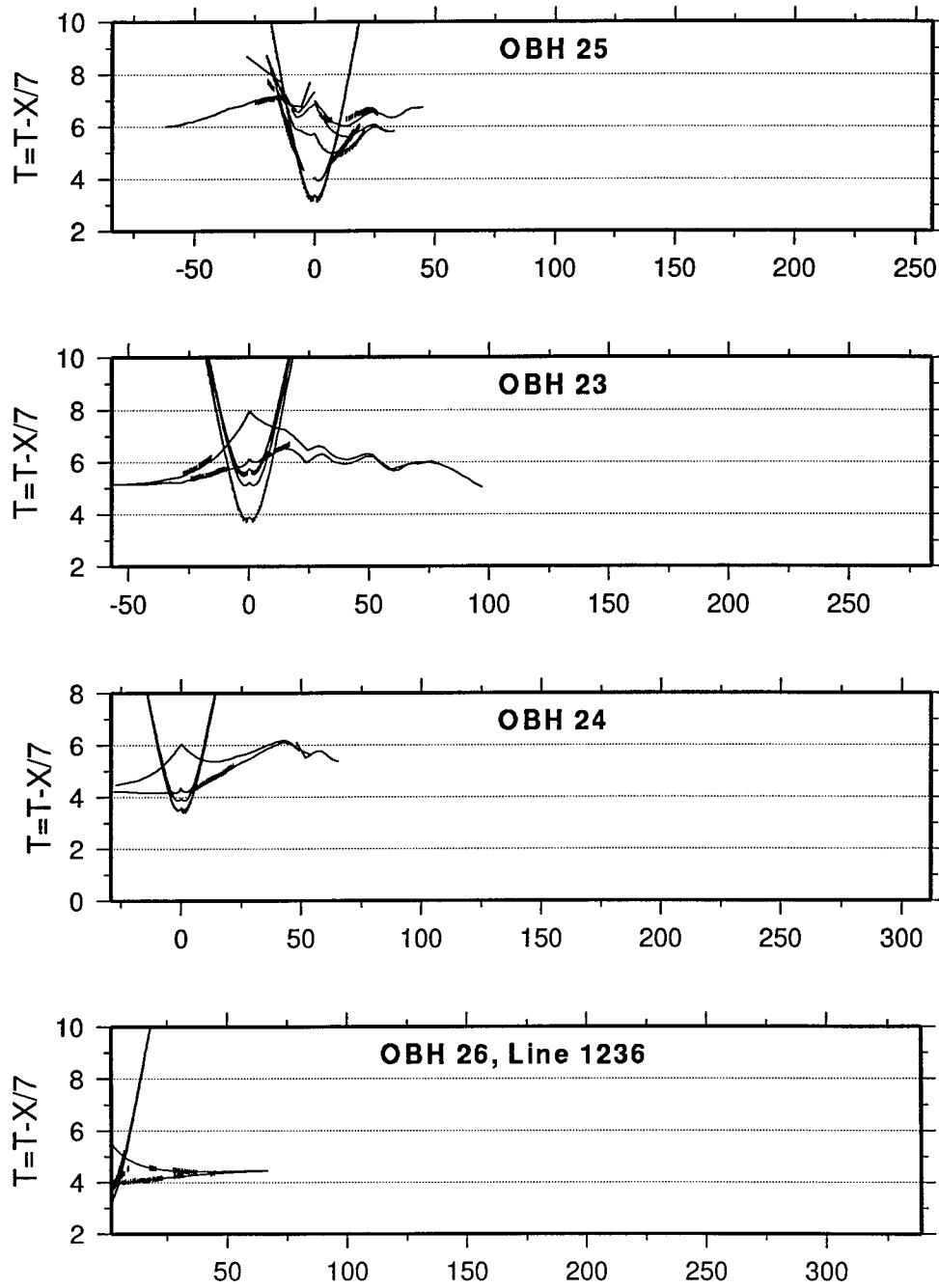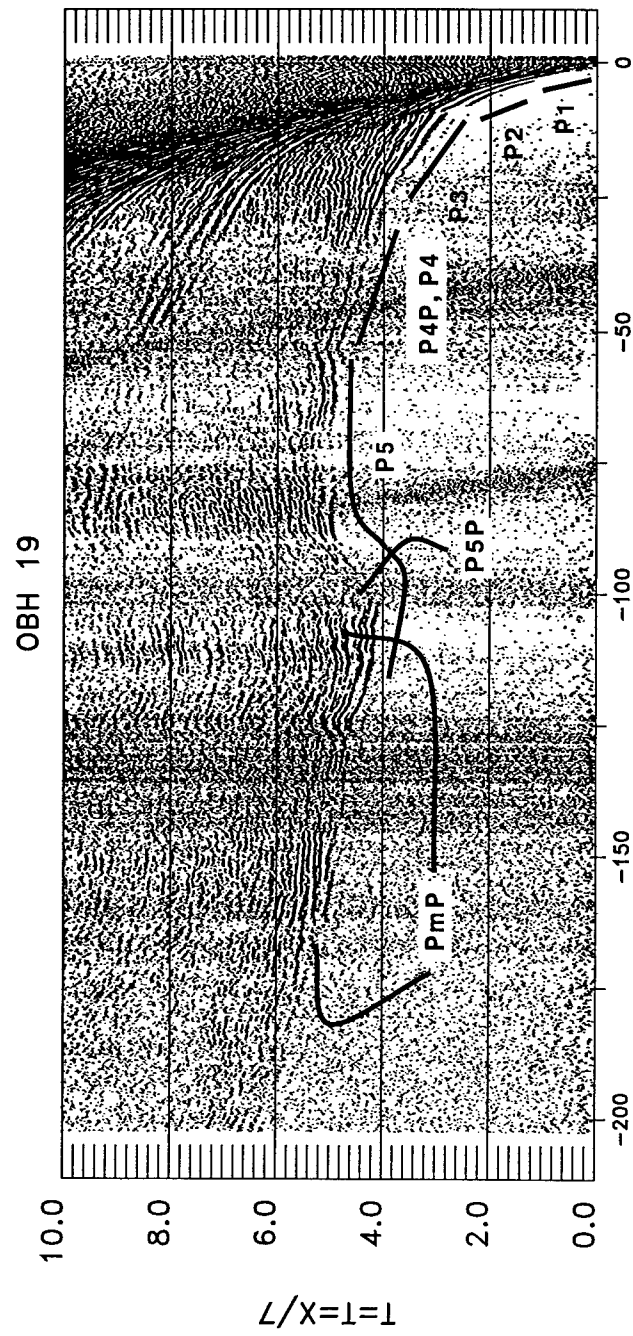
Figure 4.6 cont.

Figure 7a,1
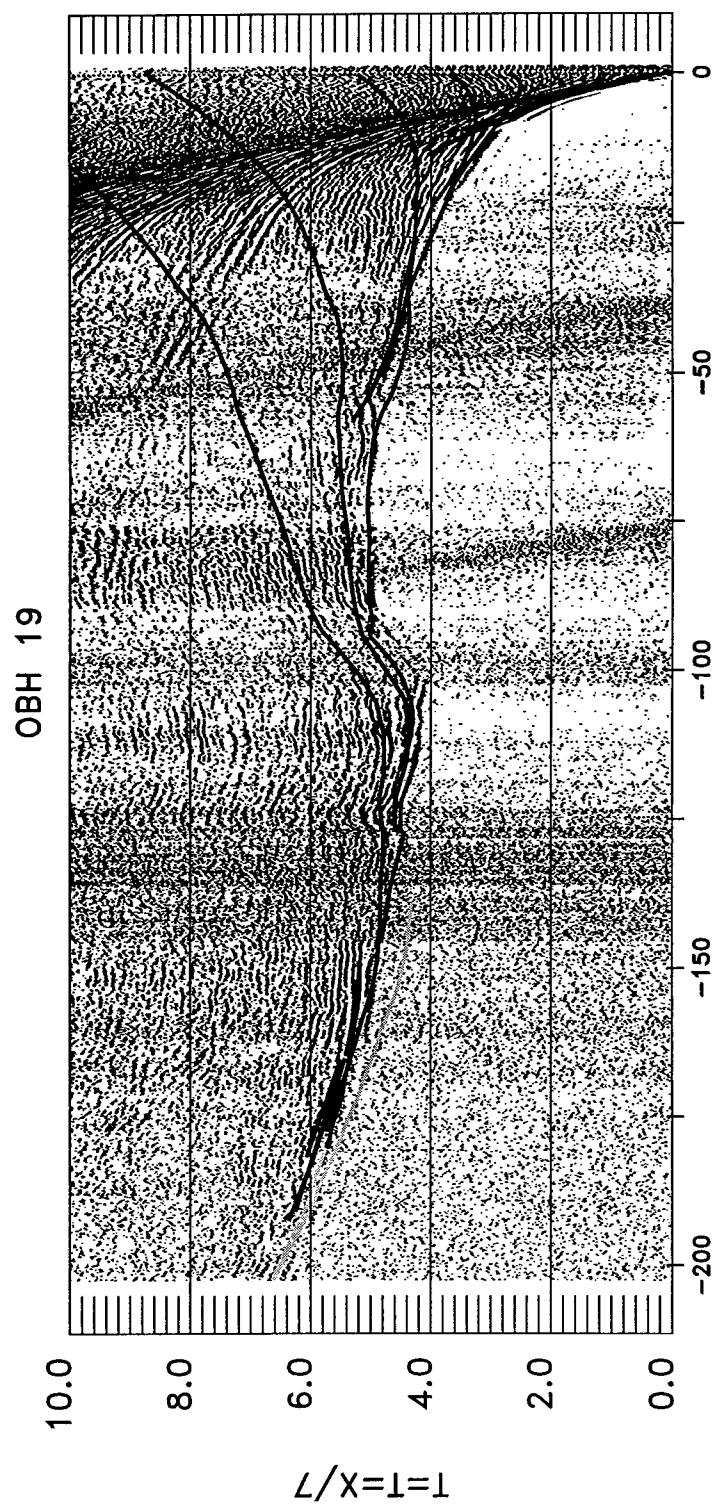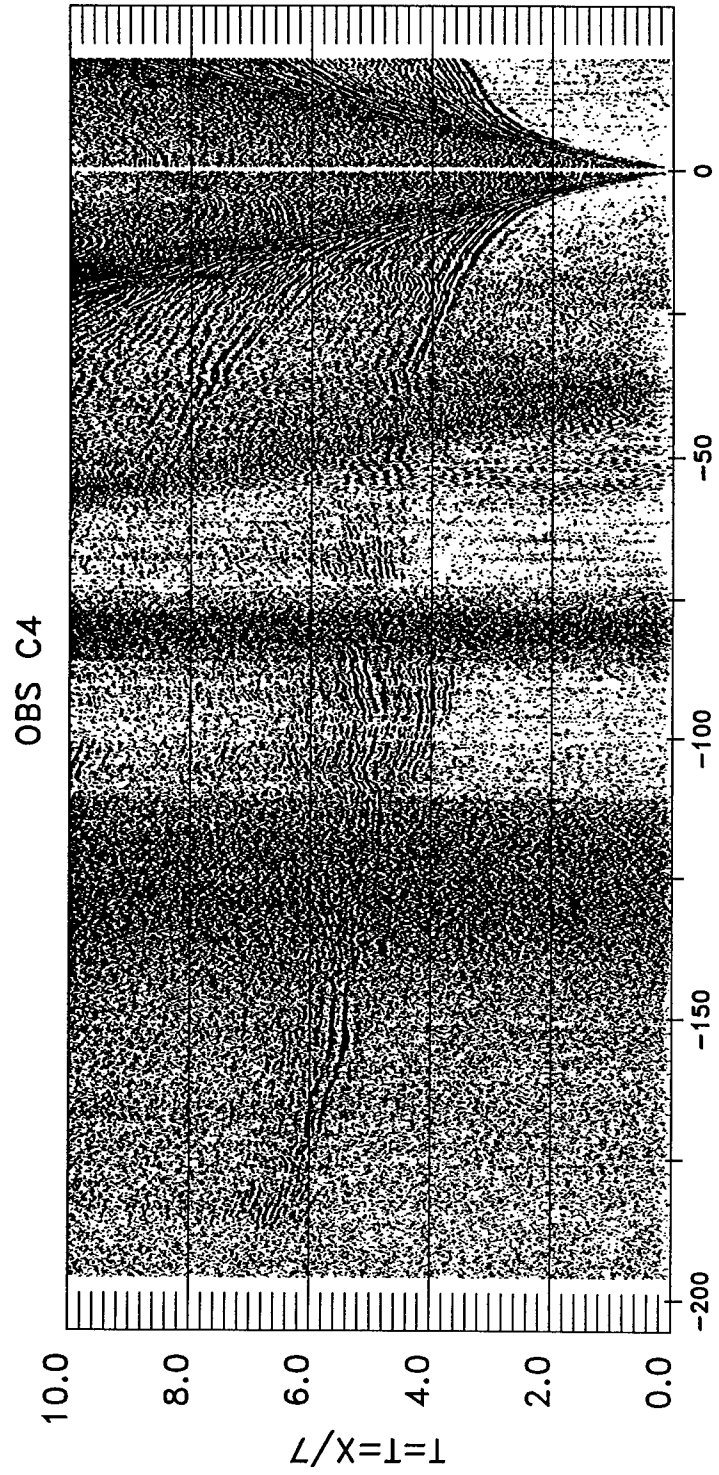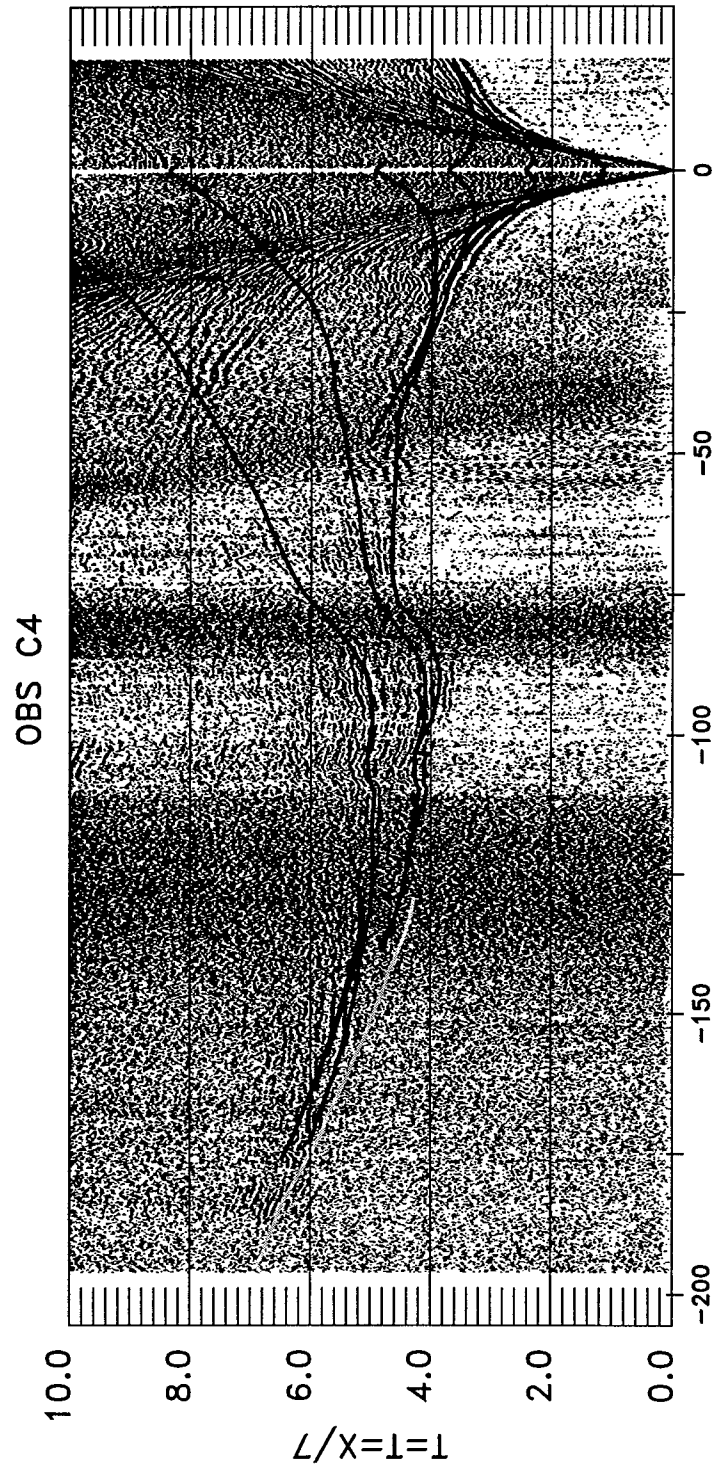
OBH 19

Figure 4.7a,2

OBS C4

$T=T-X/7$

Figure 4.7b,1

OBS C4

Figure 4.7b,2

T=T=X/7

OBS 27

$T=T-X/7$

Figure 4.7c,1

OBS 27

$T=T-X/7$

Figure 4.7c,2

OBS C3

Figure 4.7d,2

$T=T-X/7$

OBS C3

$T=T-X/7$

Figure 4.7d,1

OBS A1

T=T=X/7

Figure 4.7e,2

OBS A1

T=T=X/7

Figure 4.7e,1

OBH 22

T=T=X/7
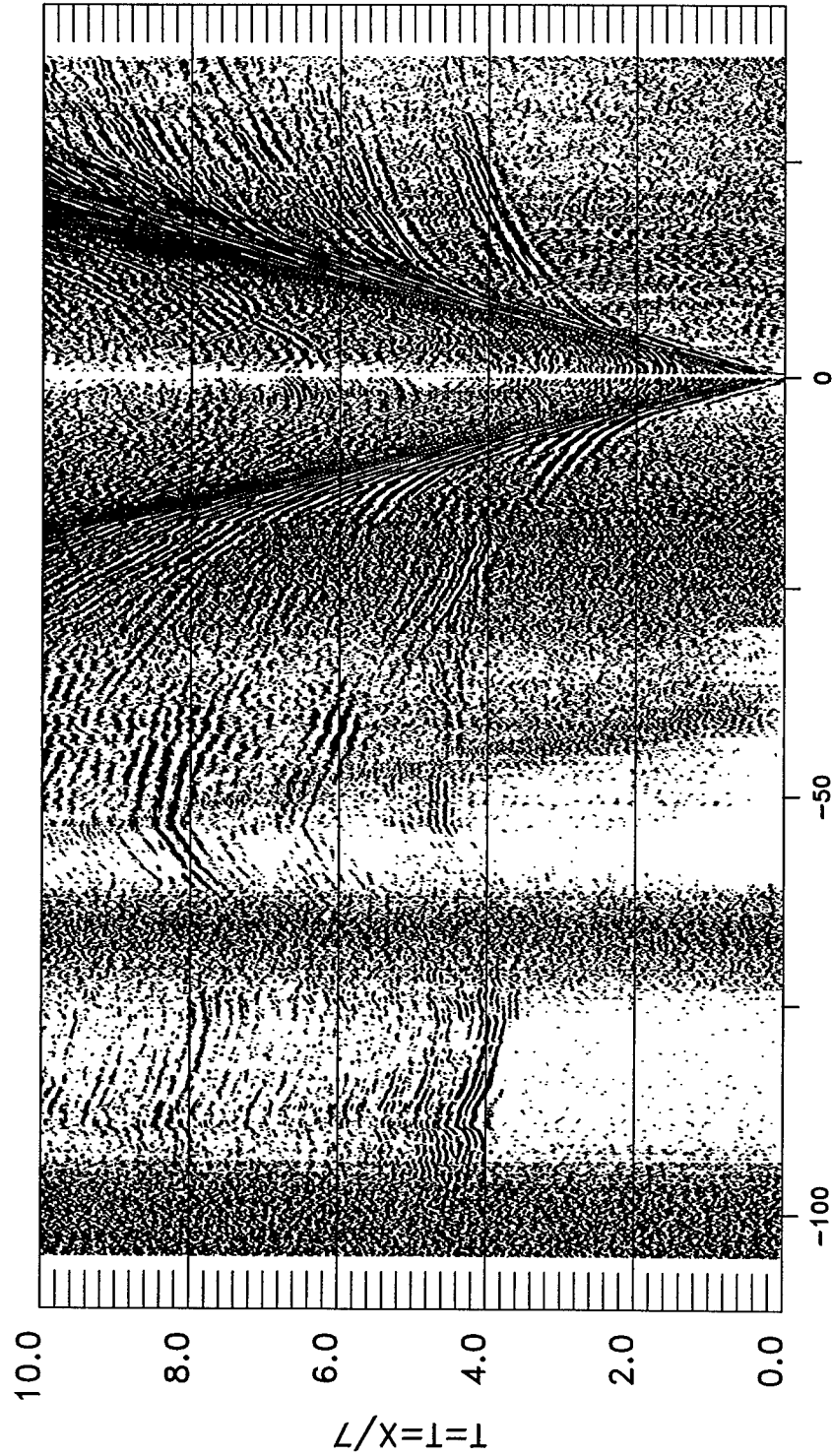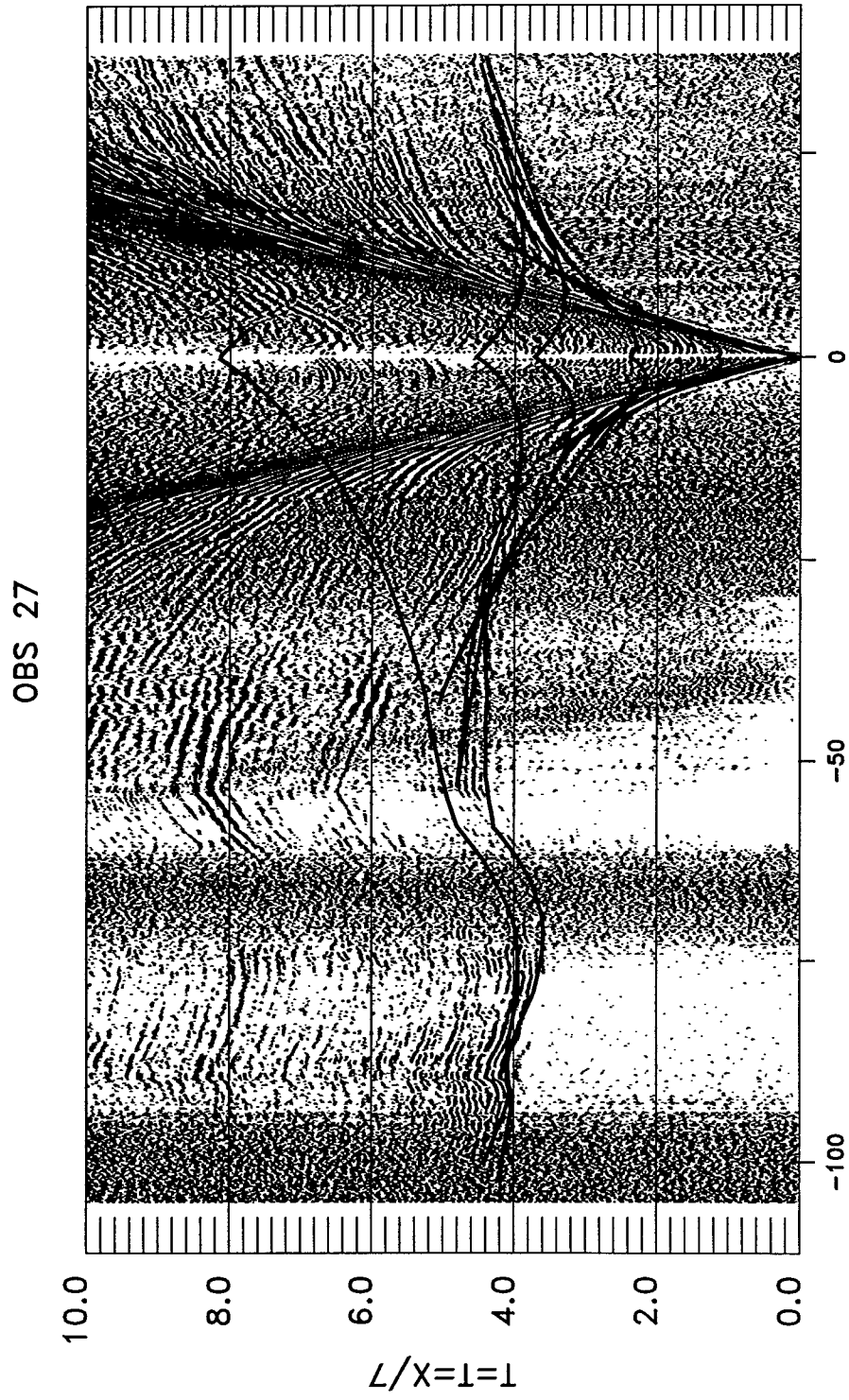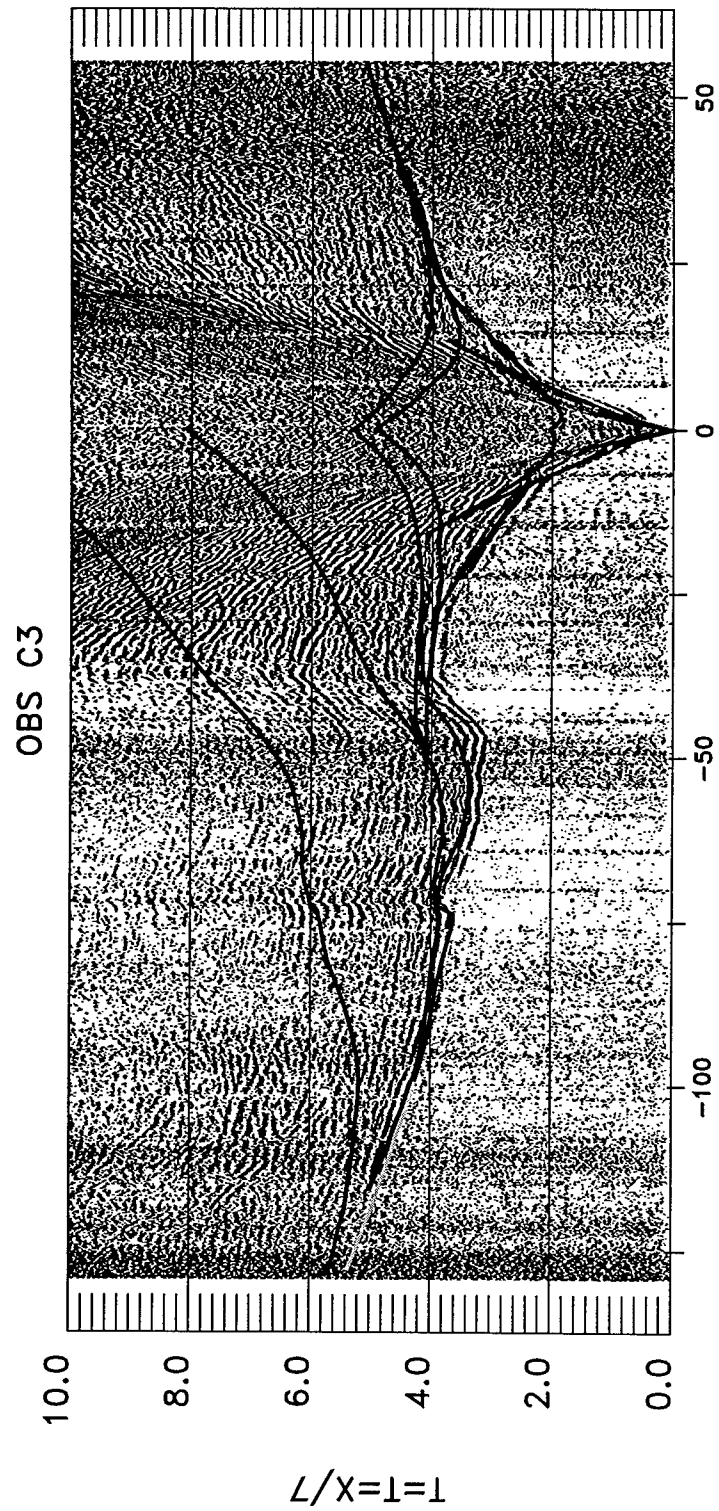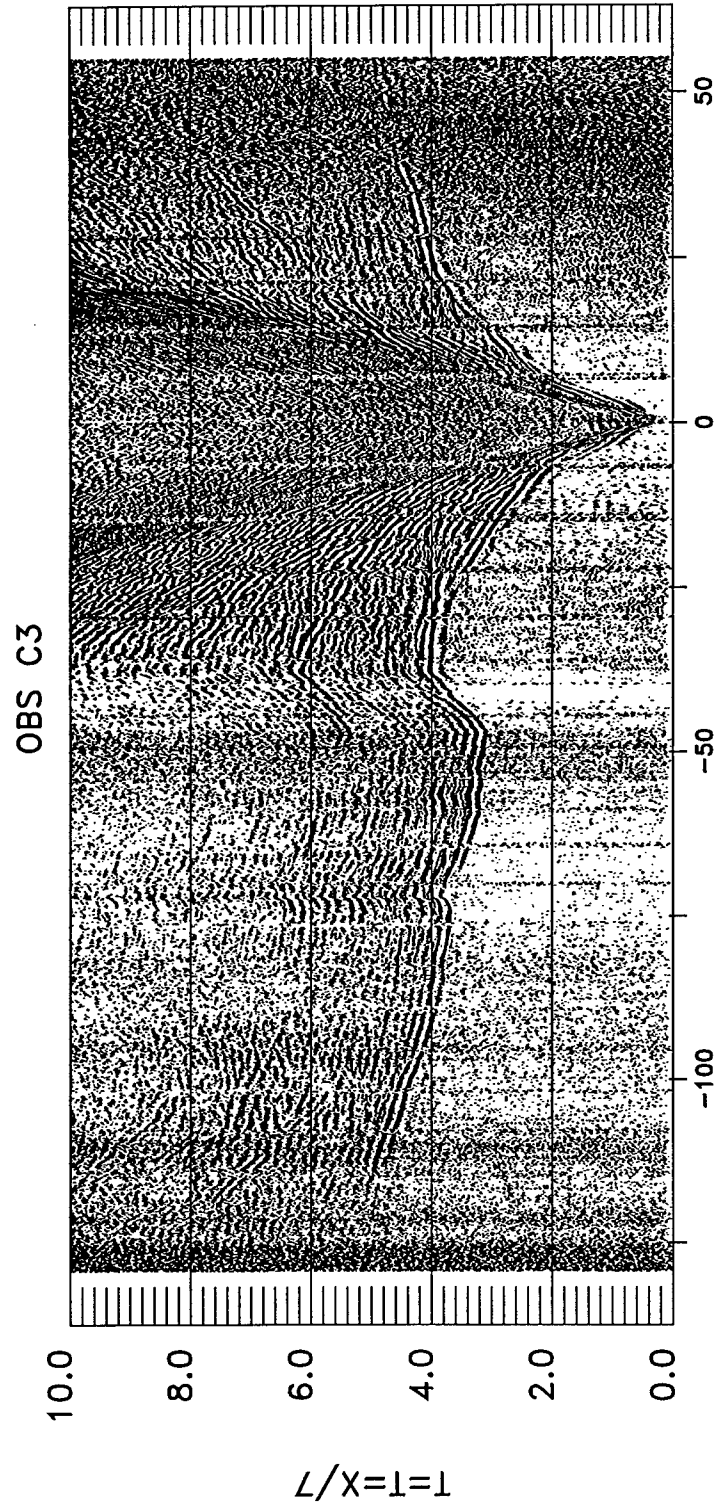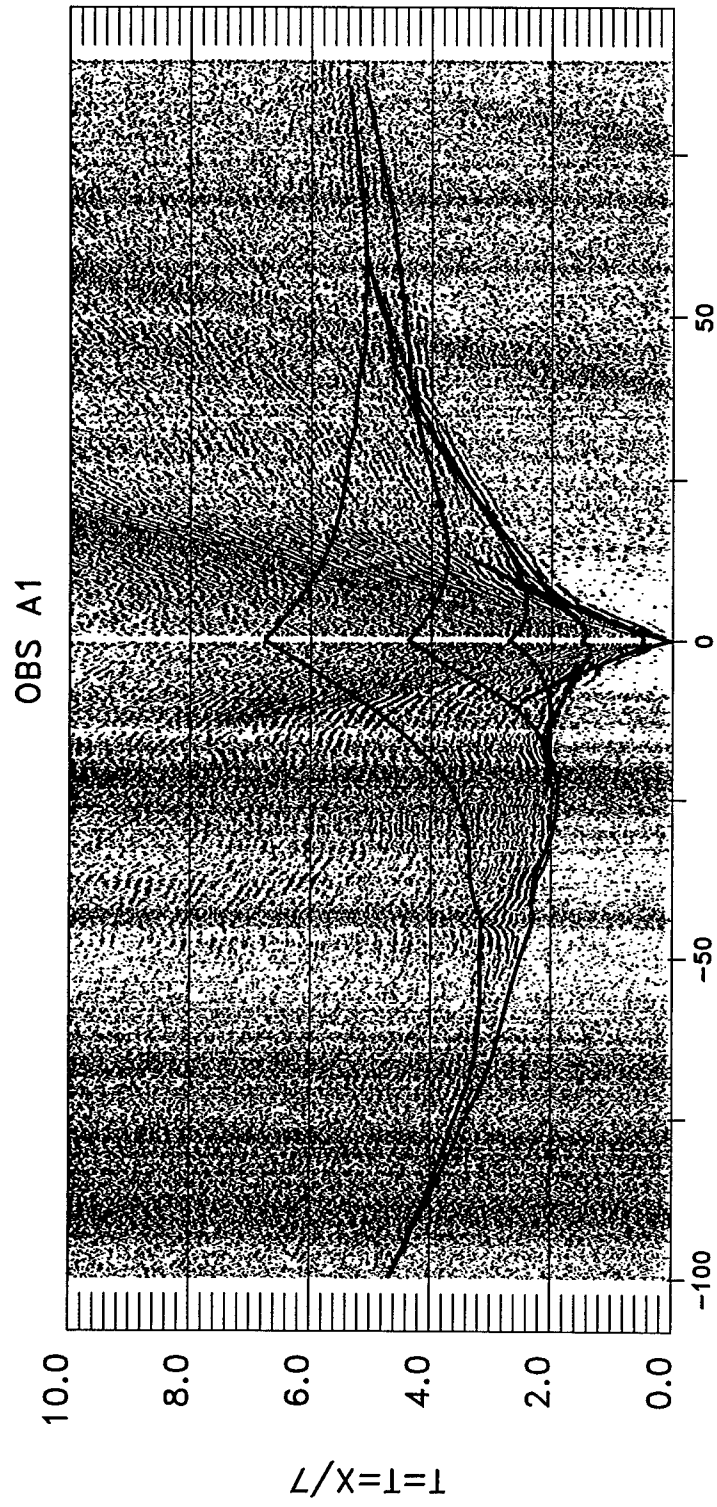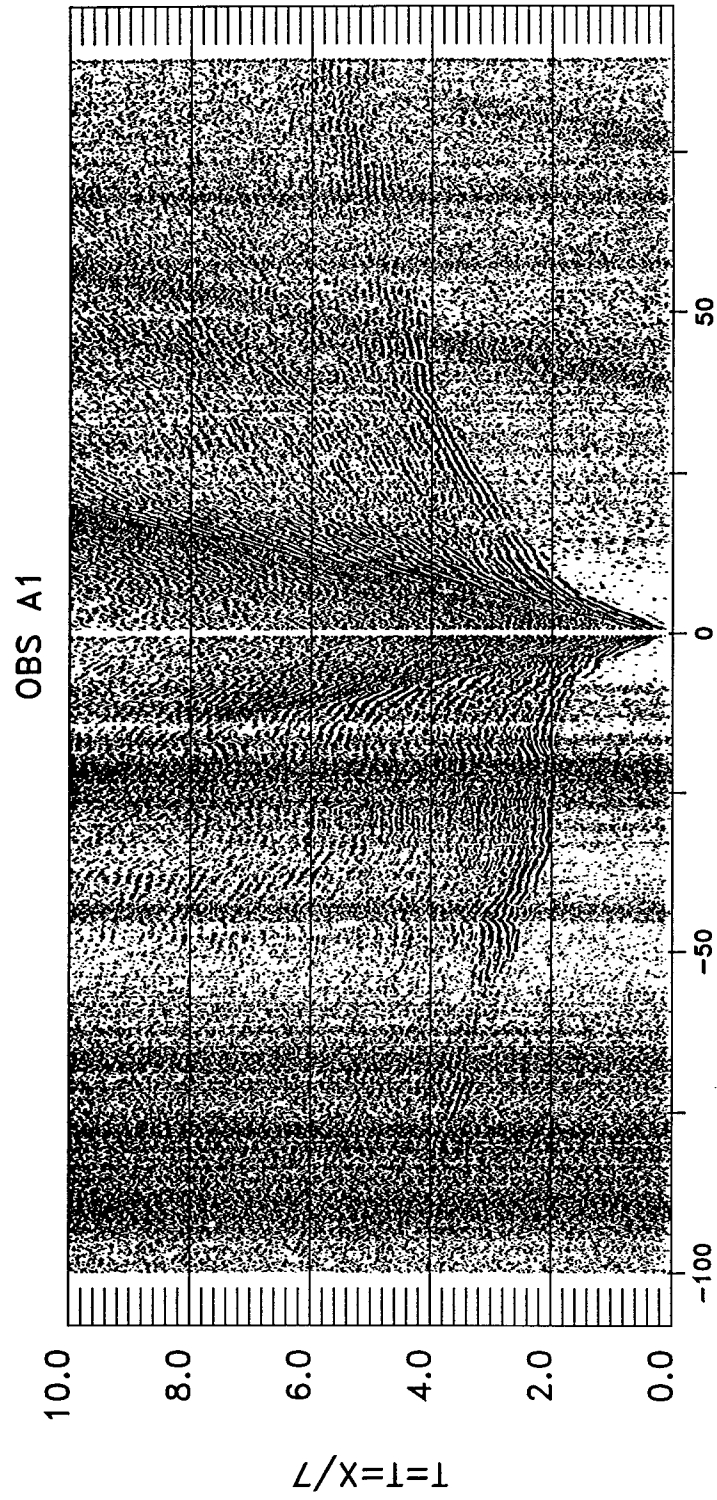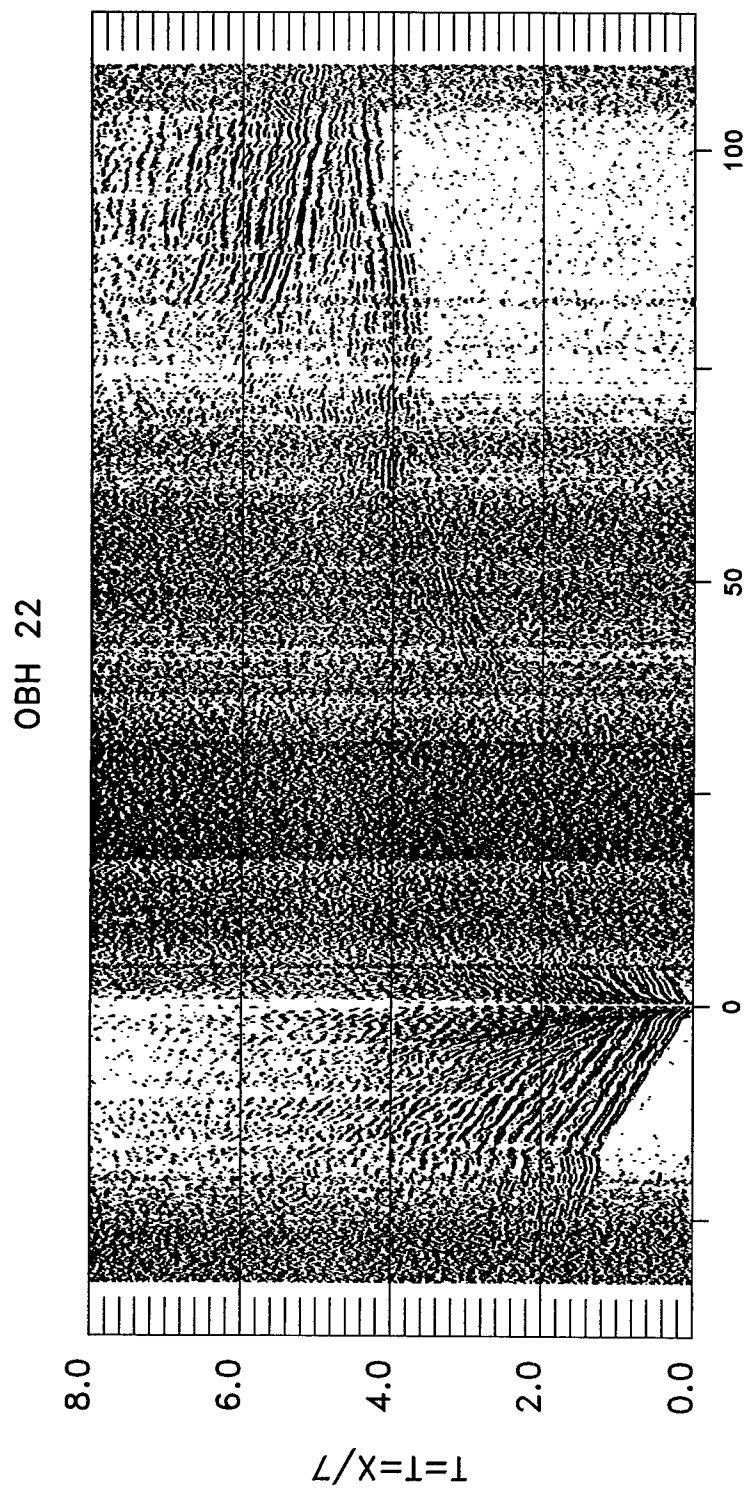
Figure 4.7f,1

OBH 22

Figure 4.7f,2
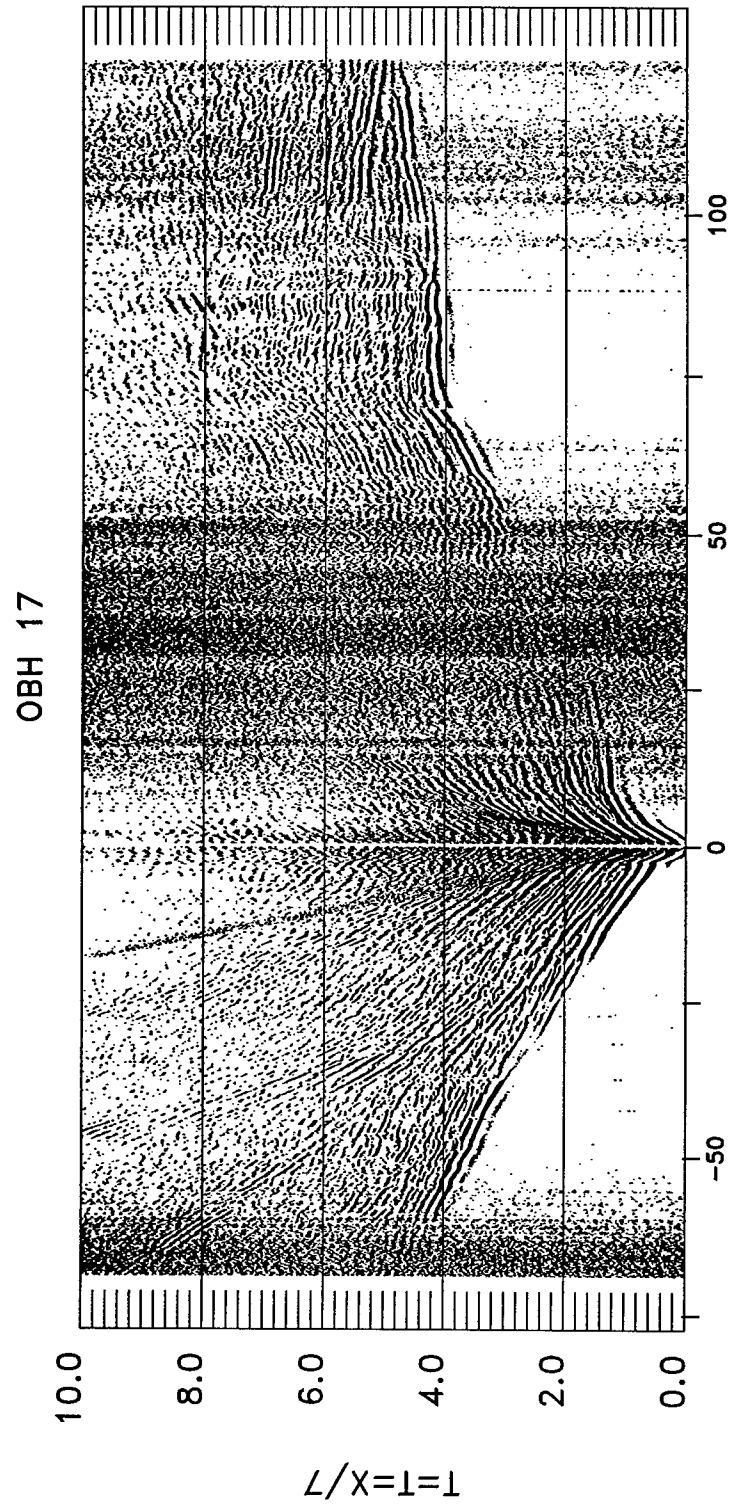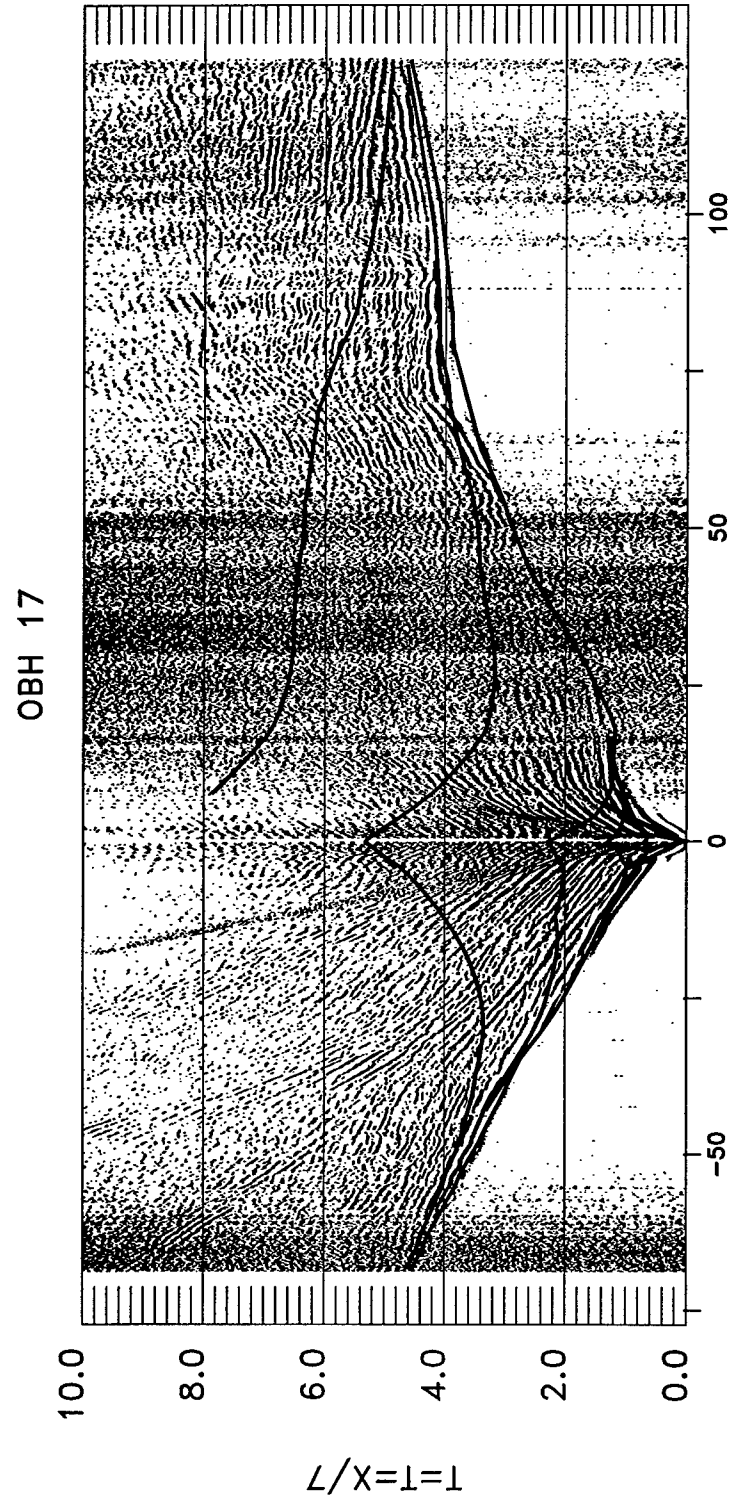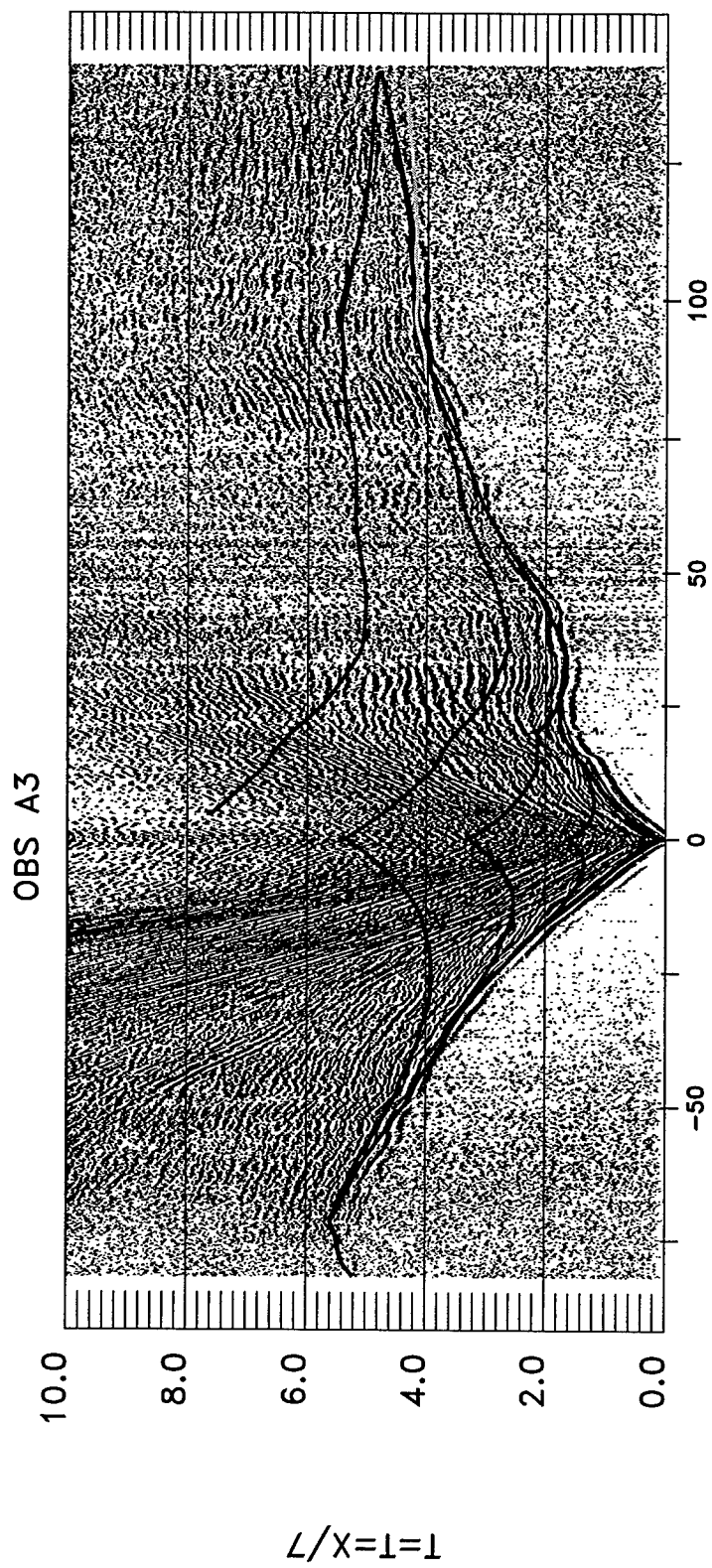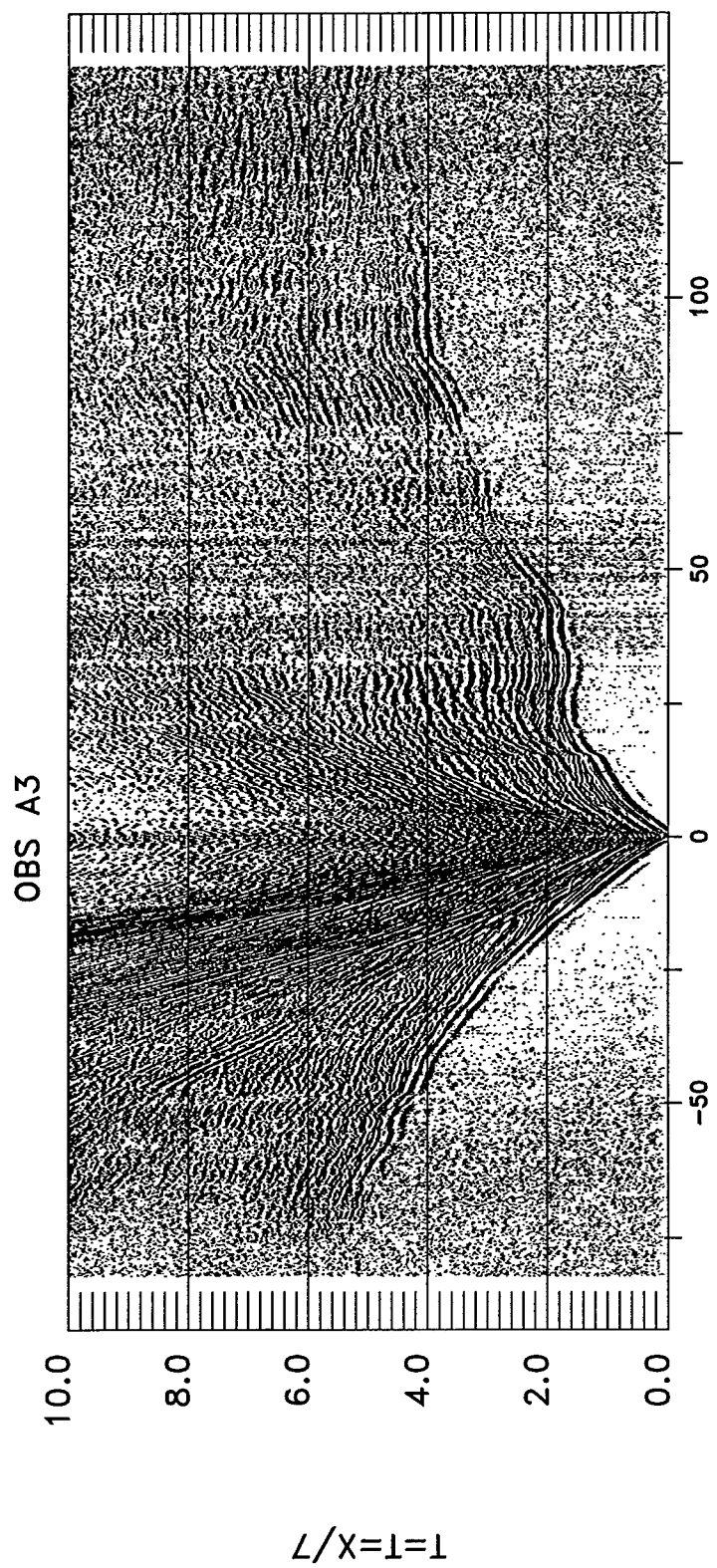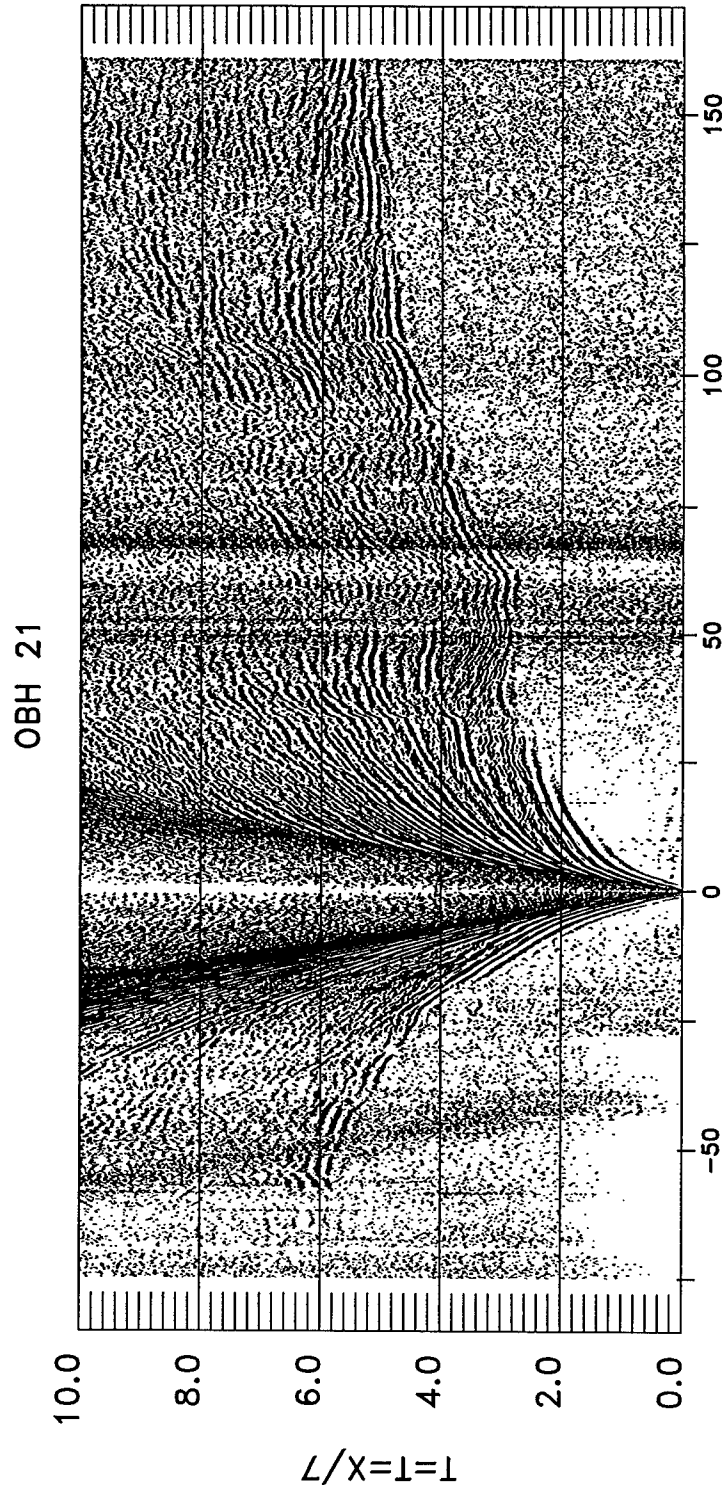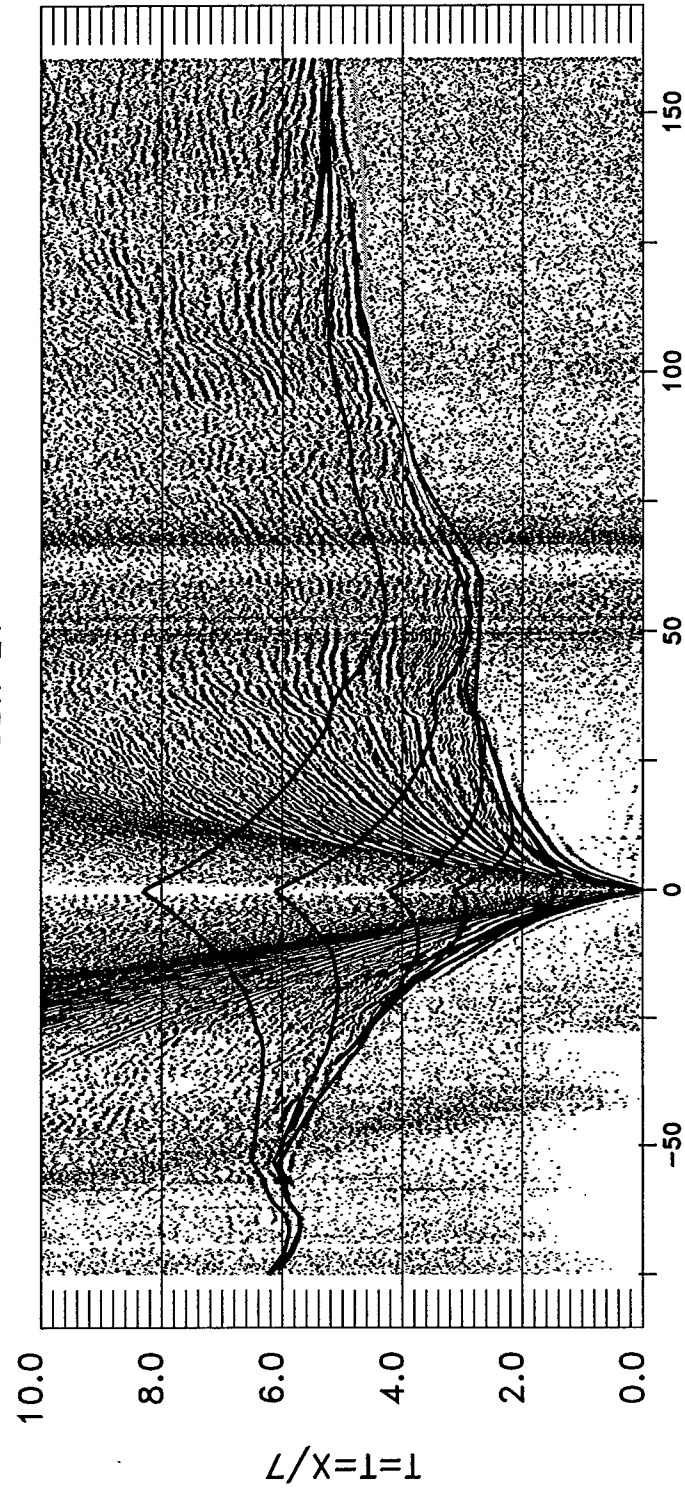
$T=T-X/7$

OBH 17

$T=T=X/7$

Figure 4.7g.1

OBH 17

$T=T-X/7$

Figure 4.7g,2

OBS A3

T=T=X/7

Figure 4.7h,2

OBS A3

Figure 4.7h,1

T=T=X/7

OBH 21

$T=T-X/7$

Figure 4.7i,1

OBH 21

$T=T-X/7$

Figure 4.7i,2

OBH 16

$T=T-X/7$

Figure 4.7j,1

OBH 16

Figure 4.7j,2

OBS A2

$T=T-X/7$

Figure 4.7k,1

OBS A2

Figure 4.7k,2

OBS C1

T=T=X/7

Figure 4.7I,1

173

OBS C1

$T=T-X/7$

Figure 4.7I,2

174

OBH 25

T=T=X/7
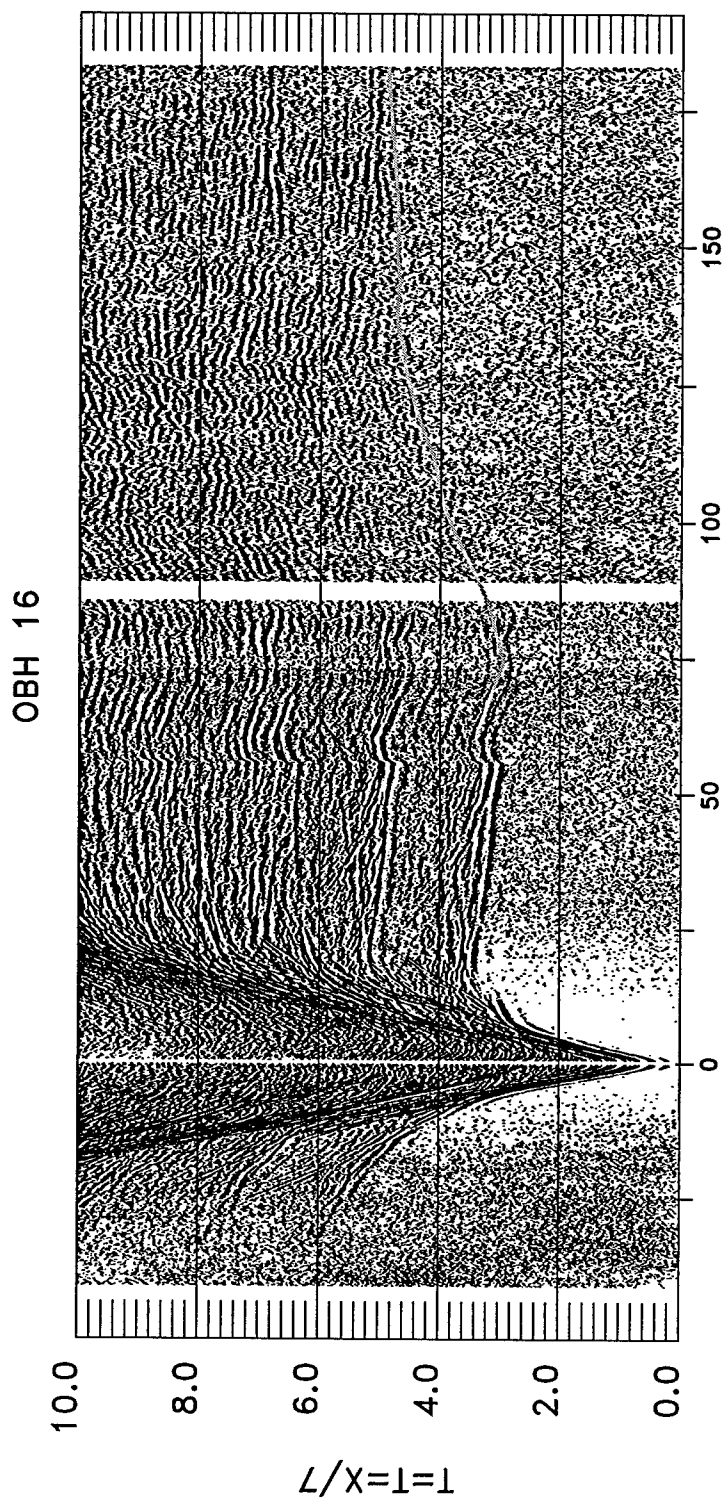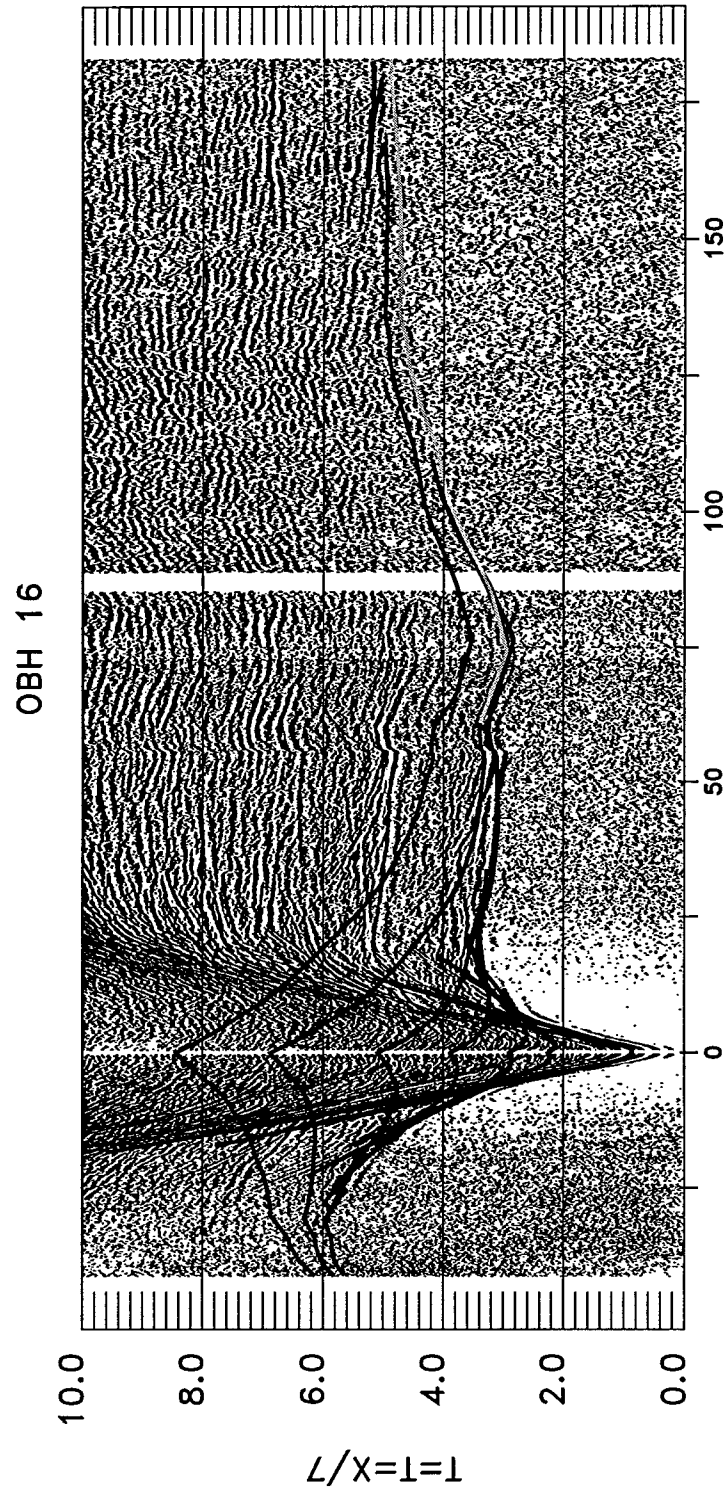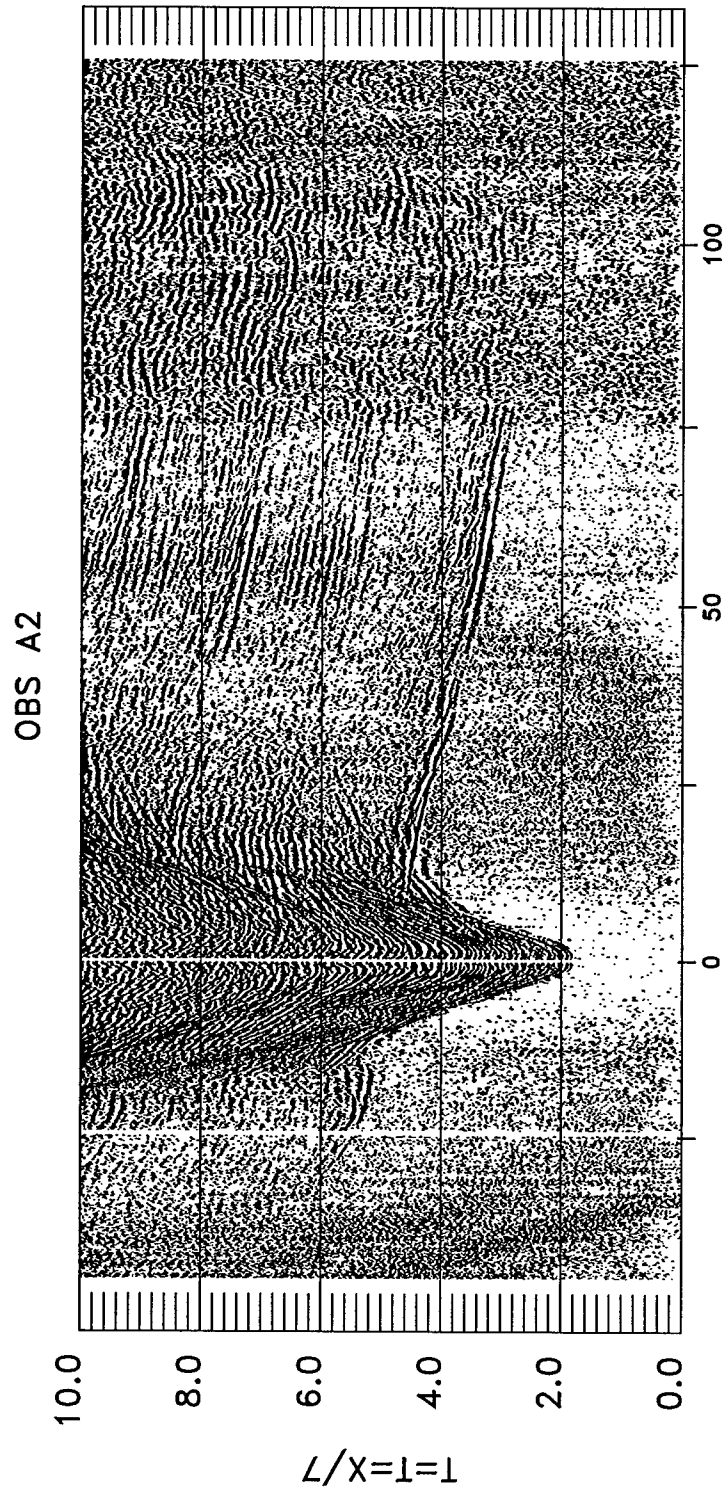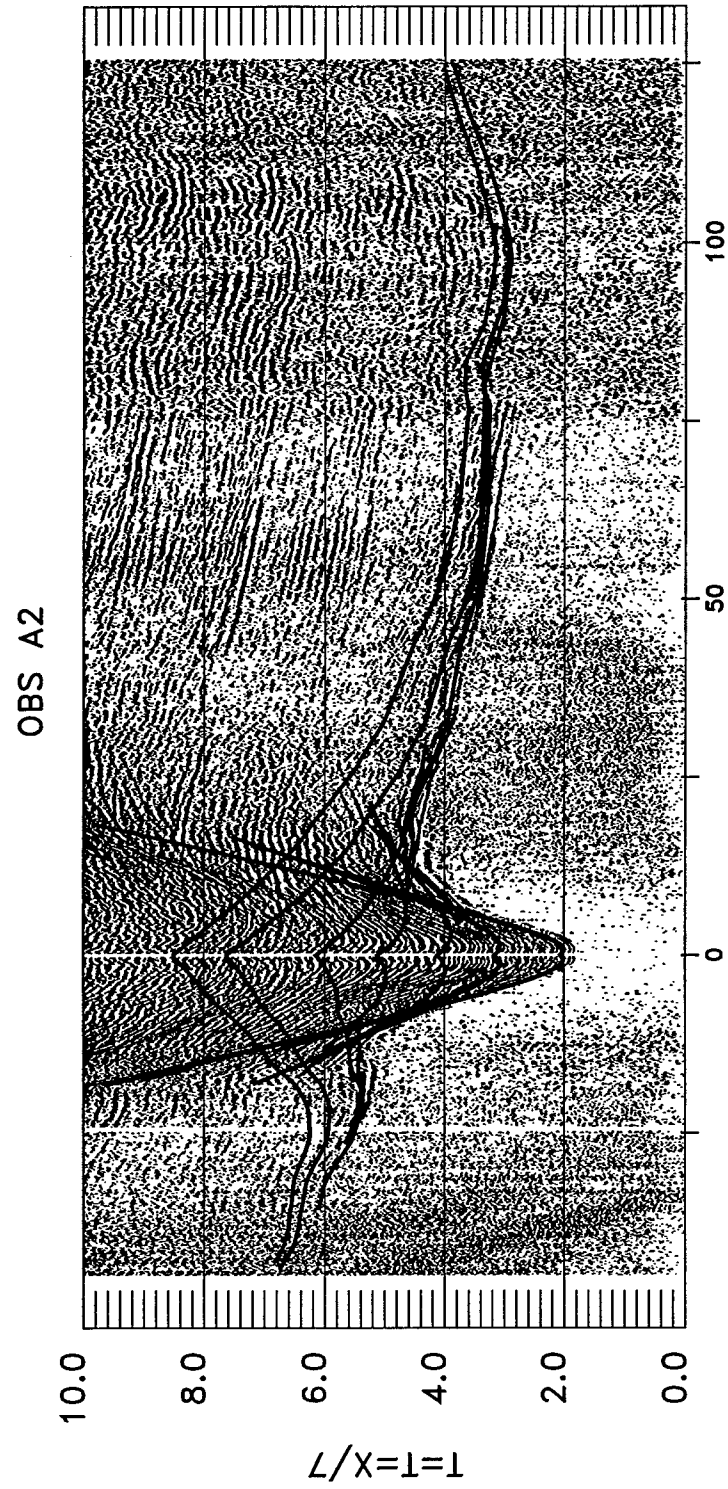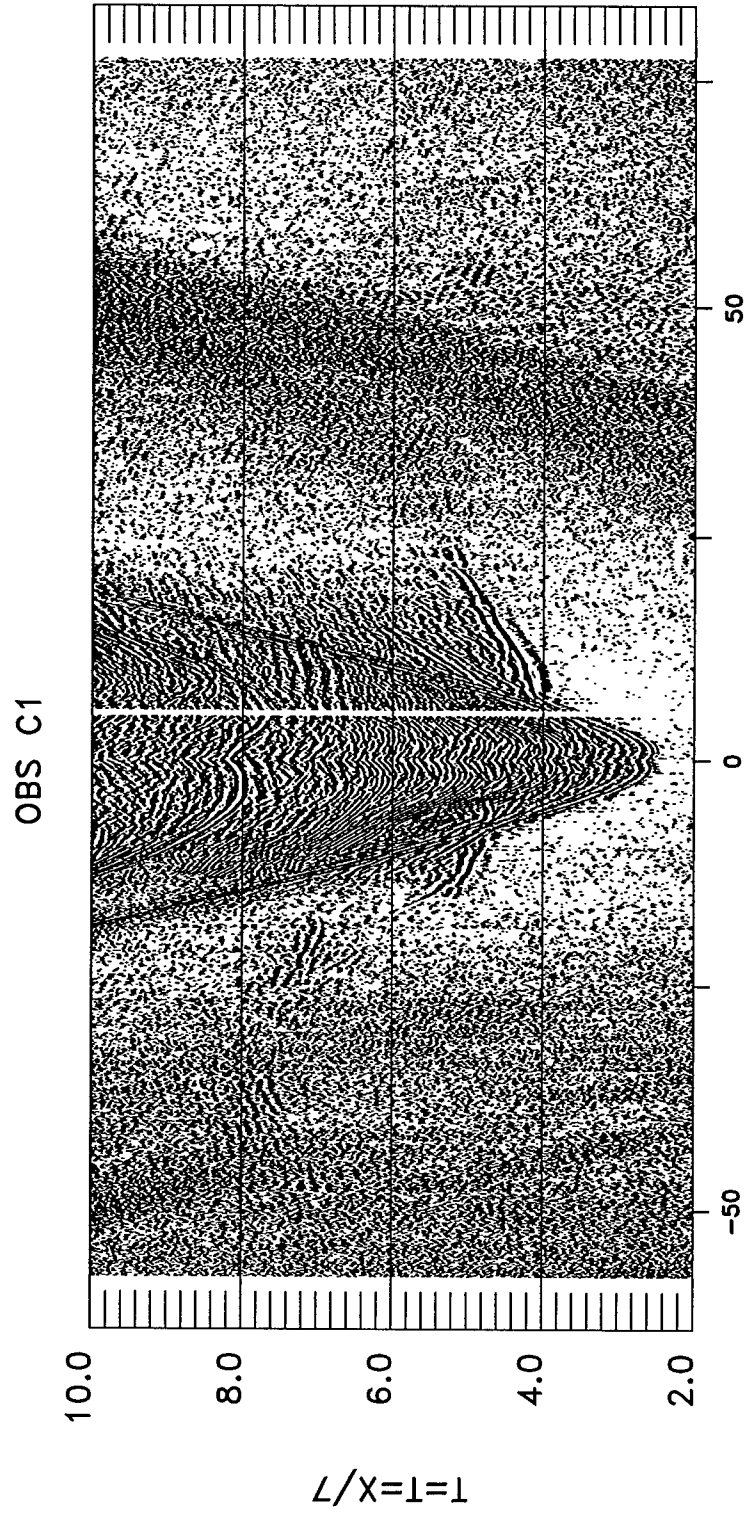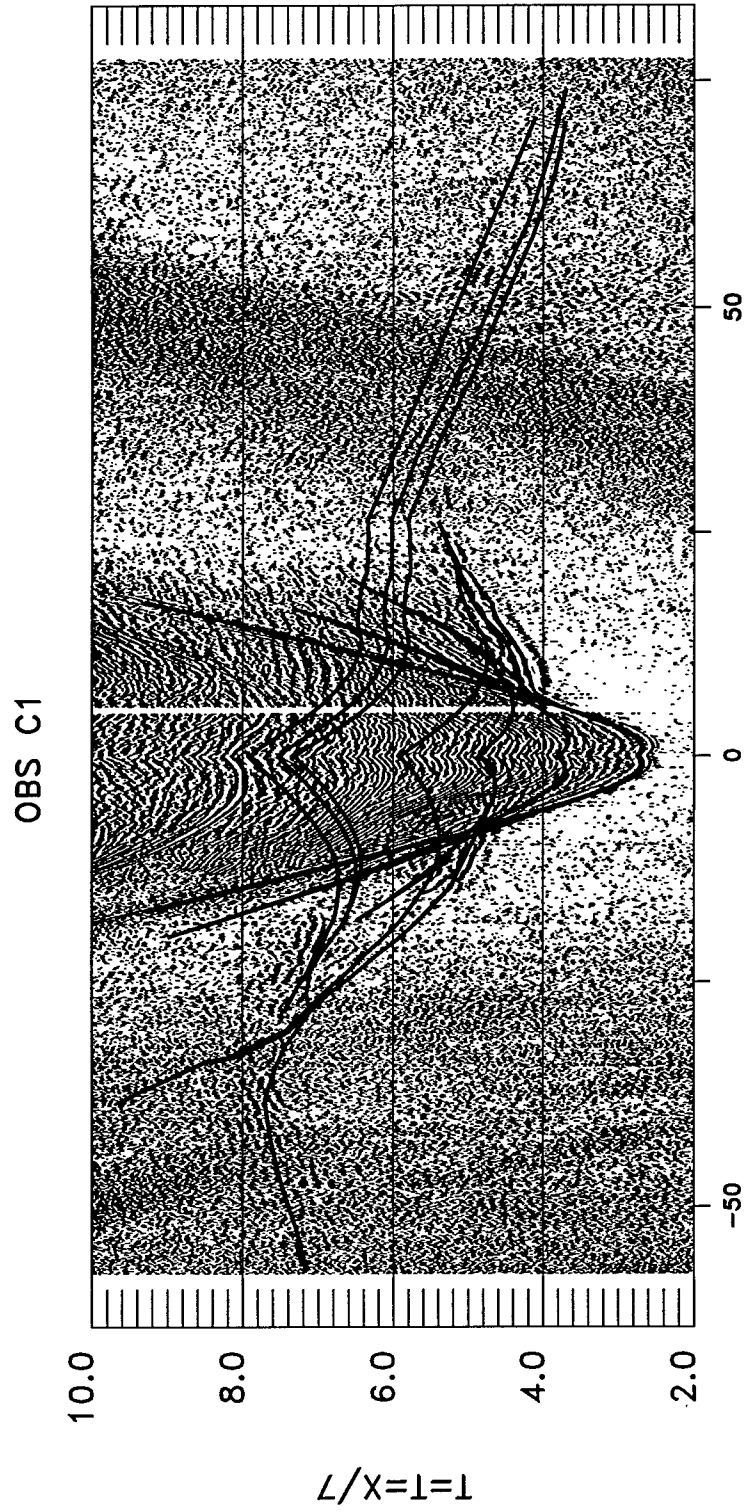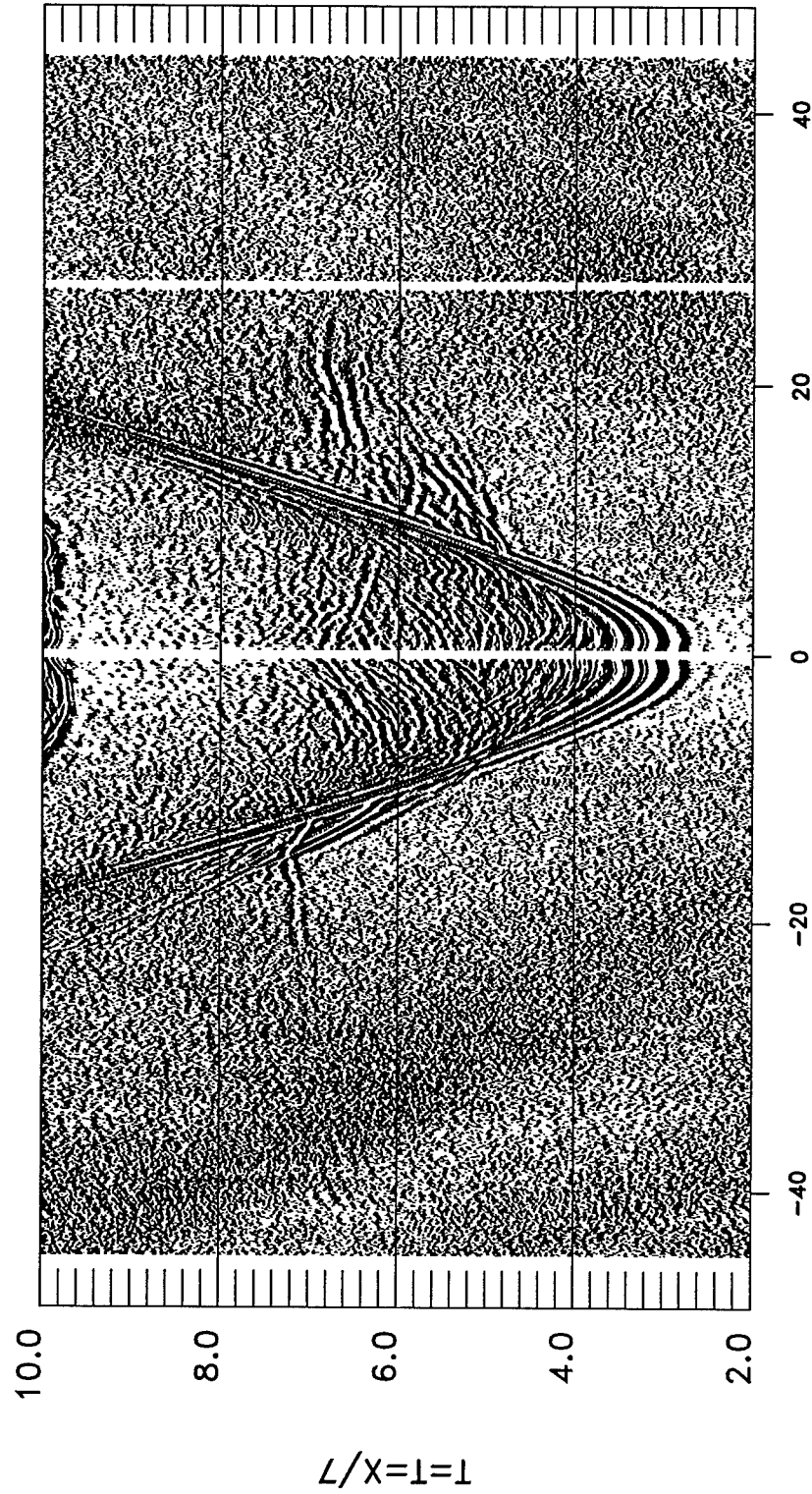
Figure 4.7m,1

OBH 25

Figure 4.7m,2

OBH 23

$T=T-X/7$

Figure 4.7n,1

OBH 23

$T=T-X/7$
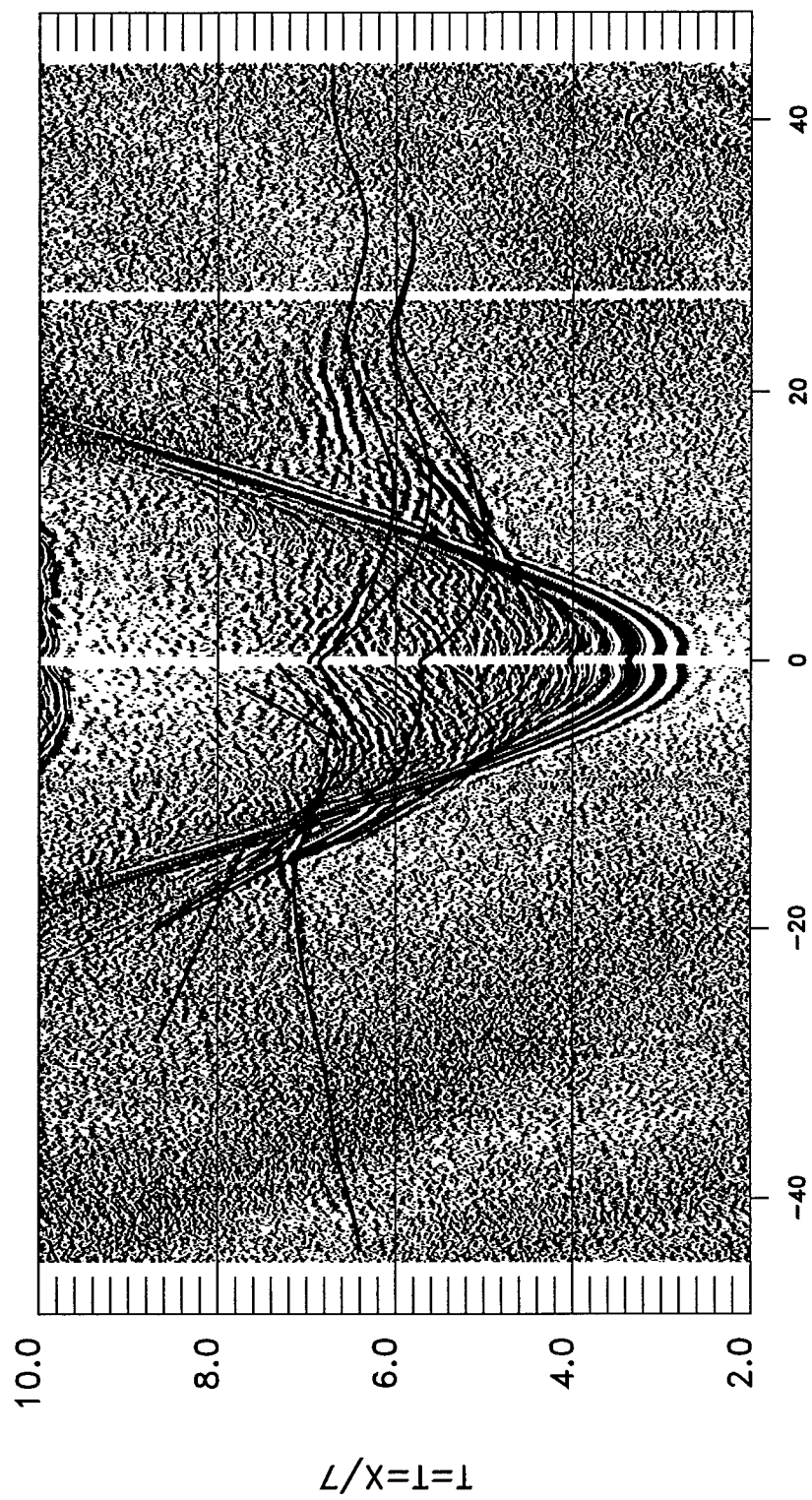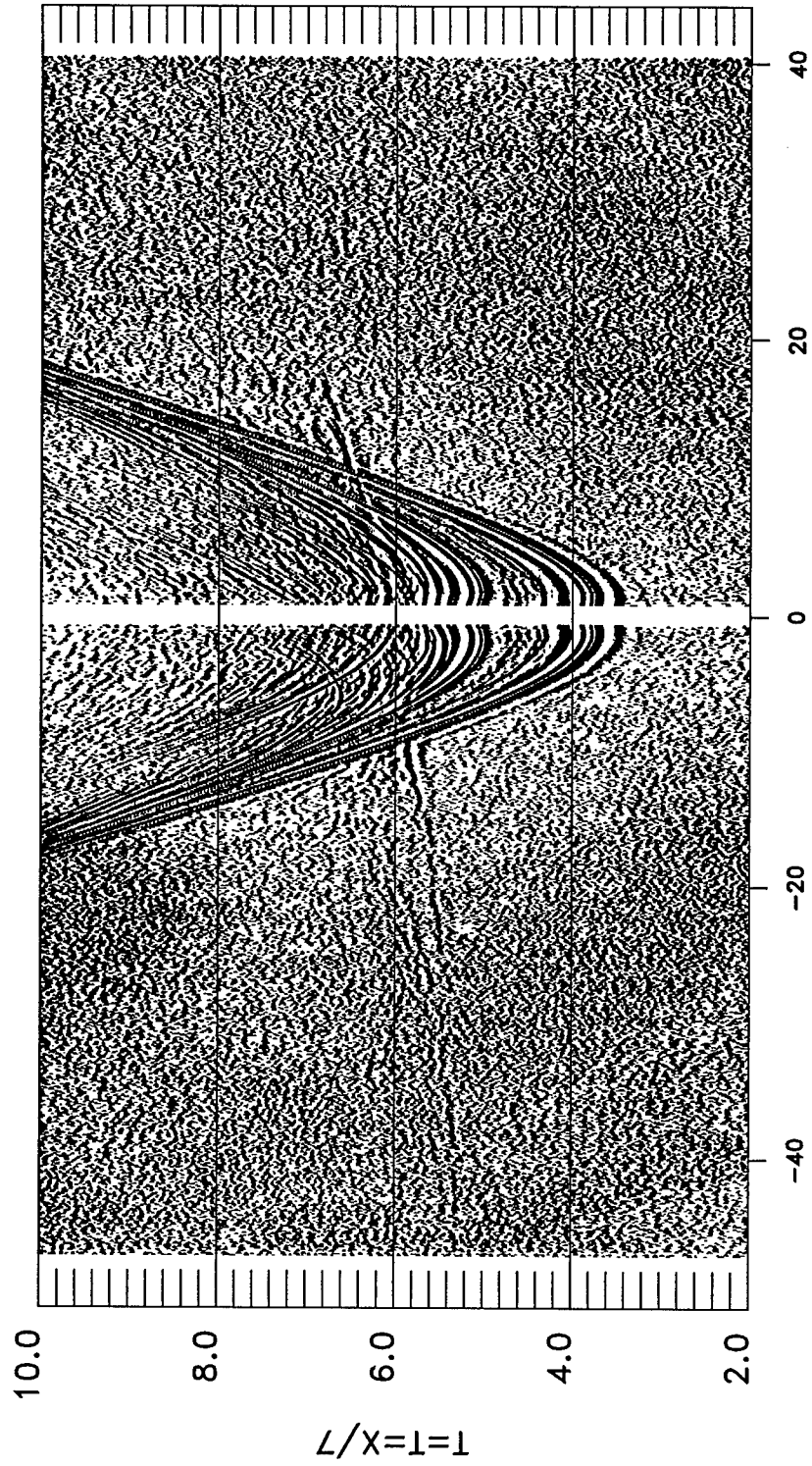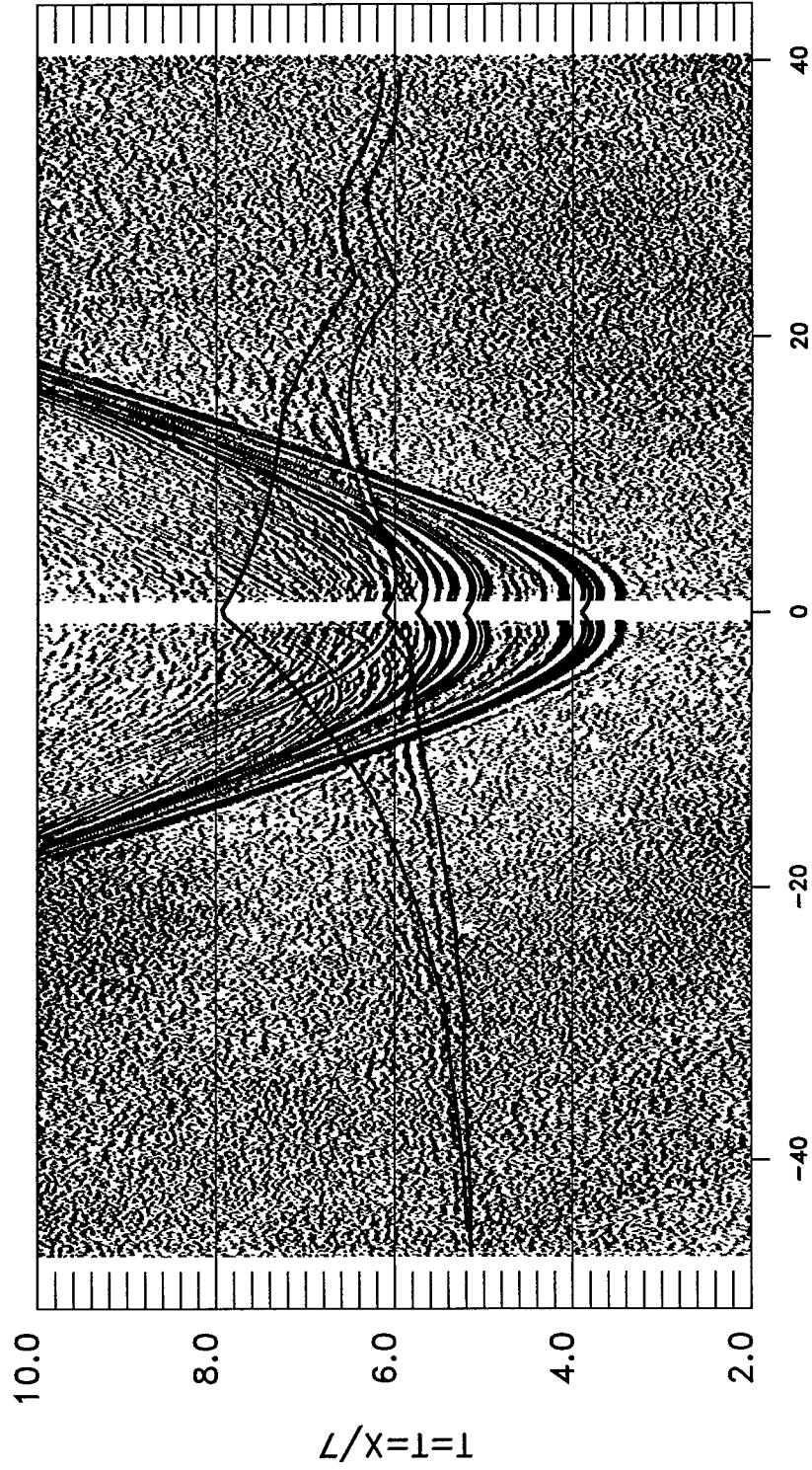
Figure 4.7n,2

OBH 24

Figure 4.7o,1

OBH 24

T=T=X/7
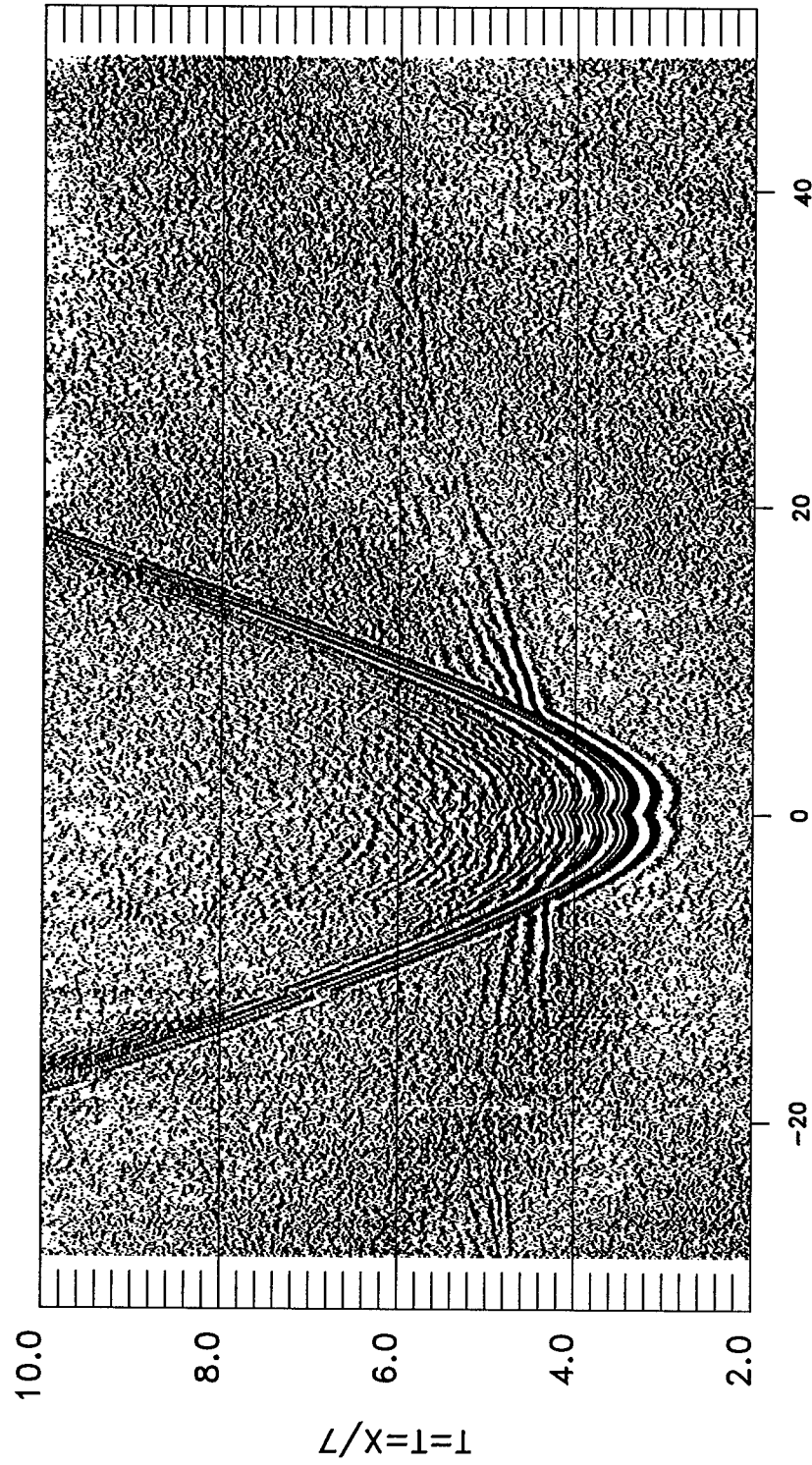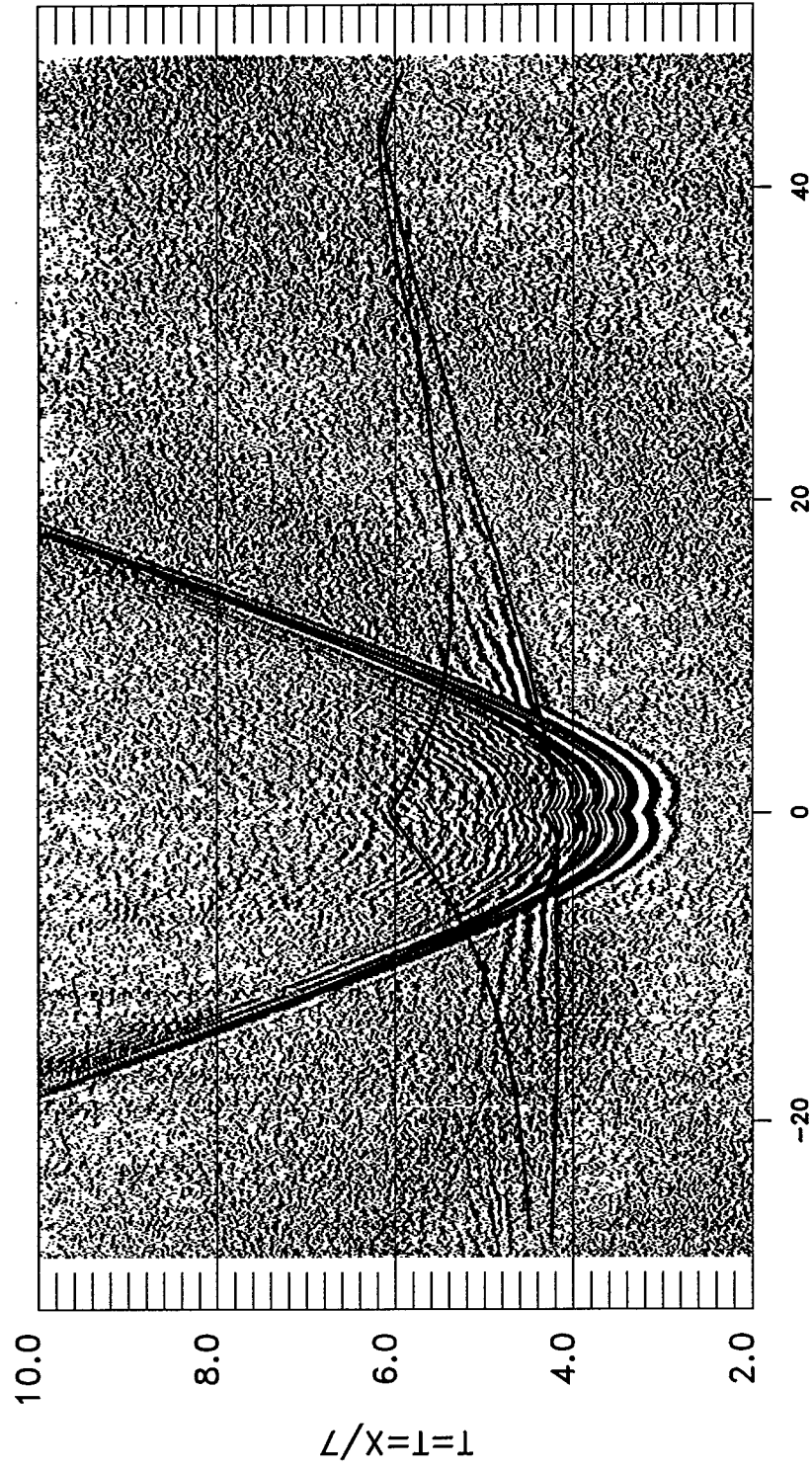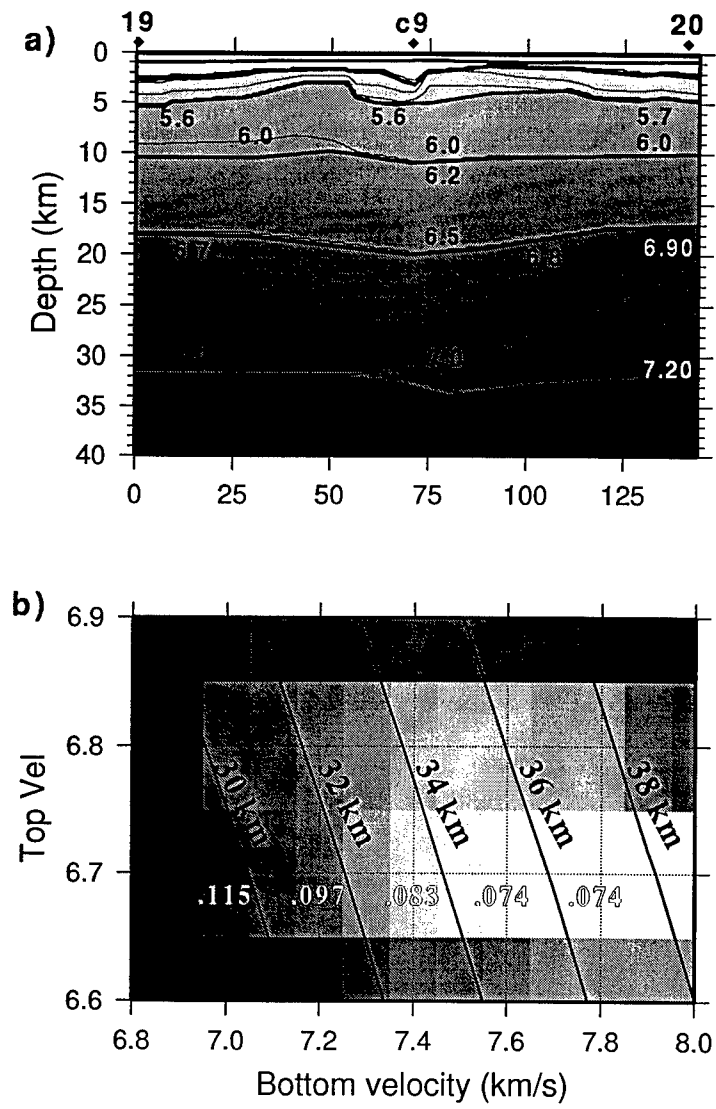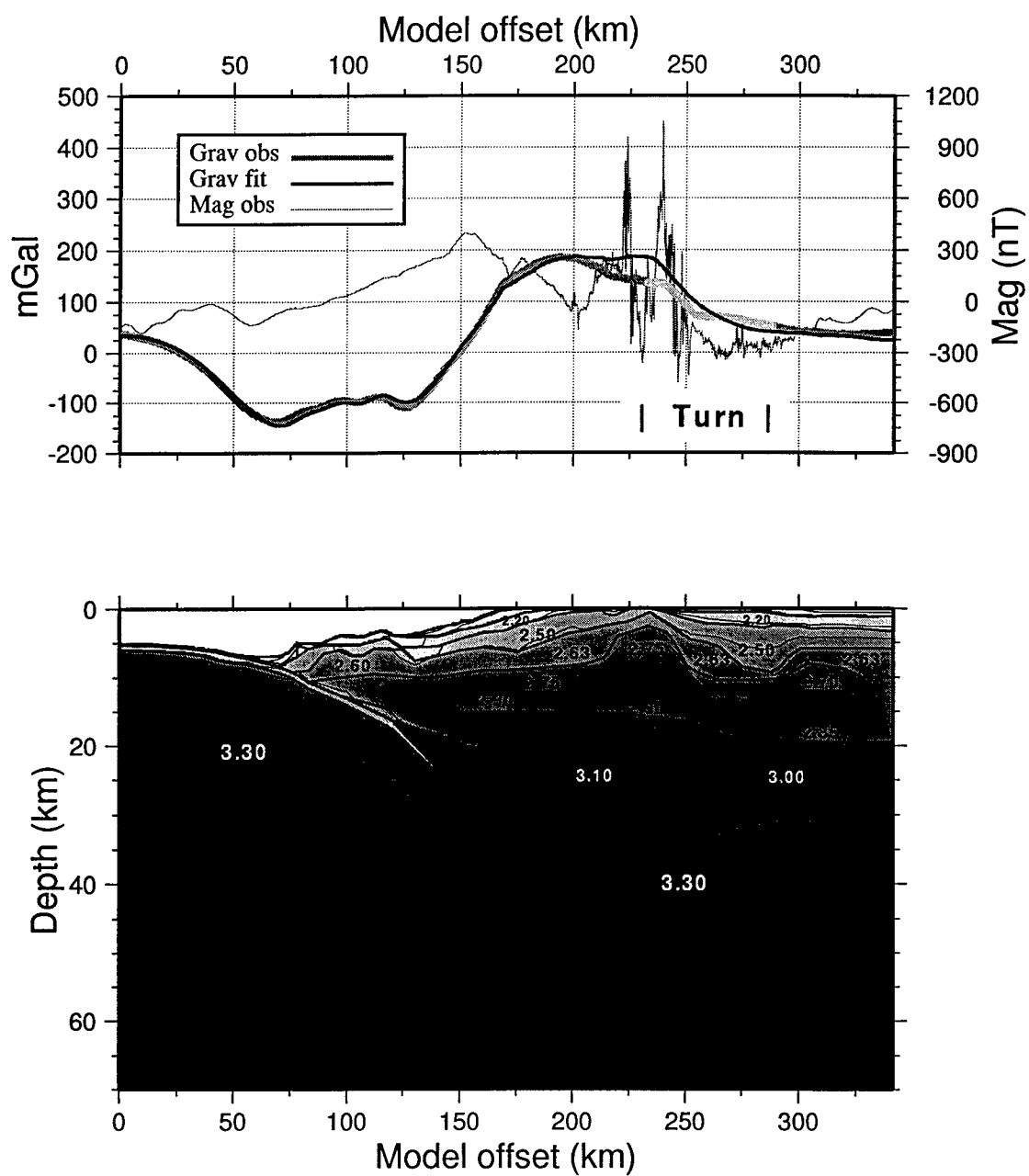
Figure 4.7o,2
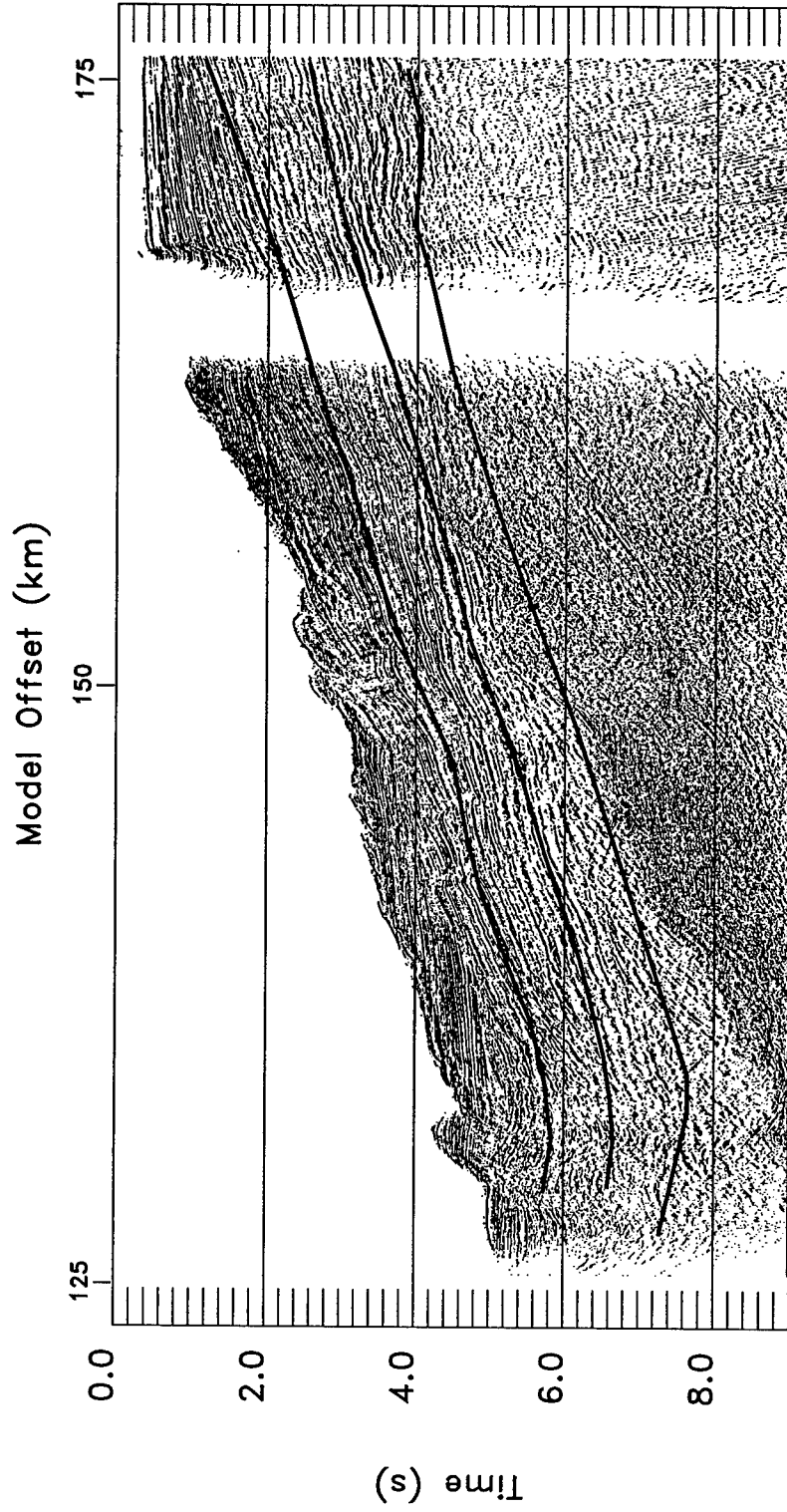
Figure 4.8
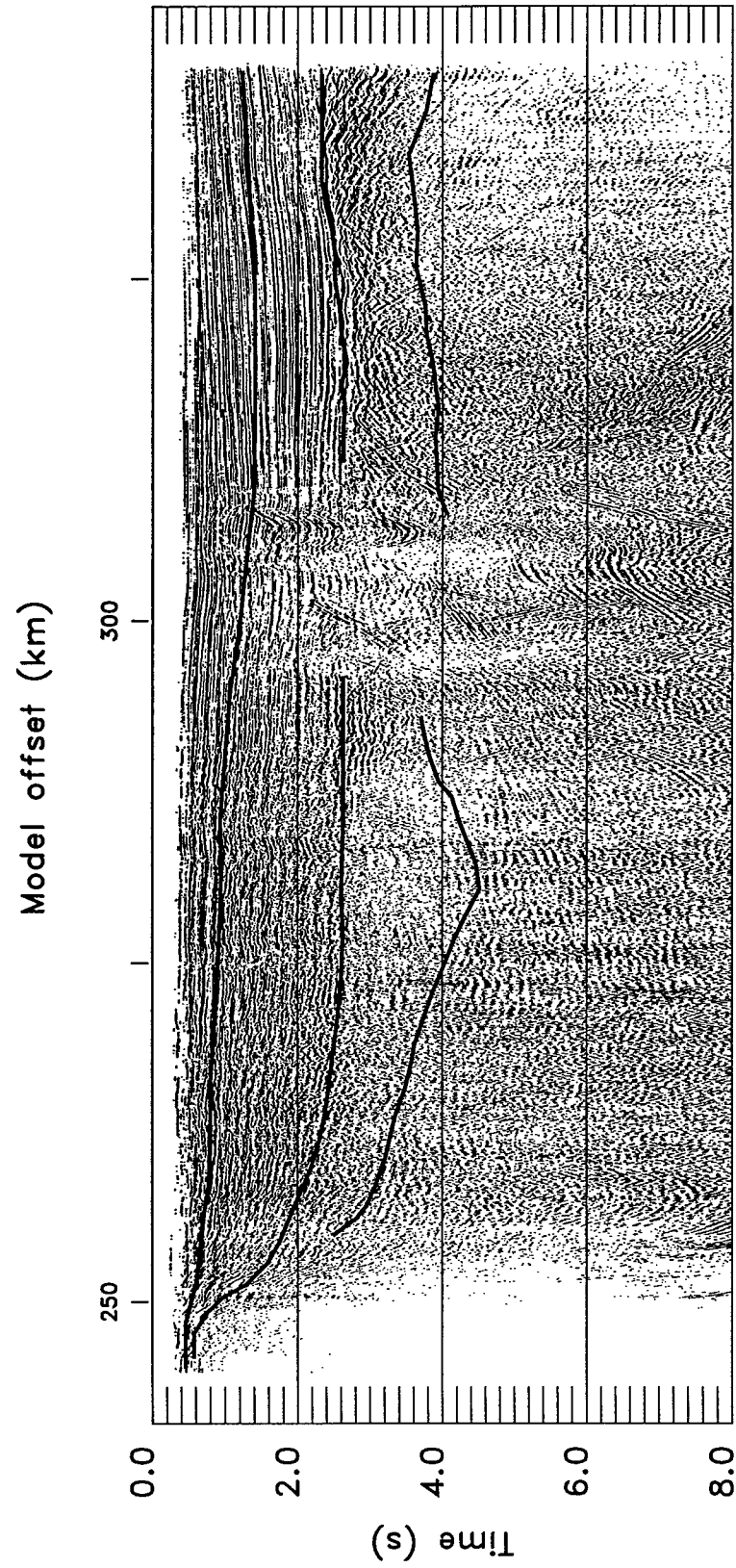
Figure 4.9
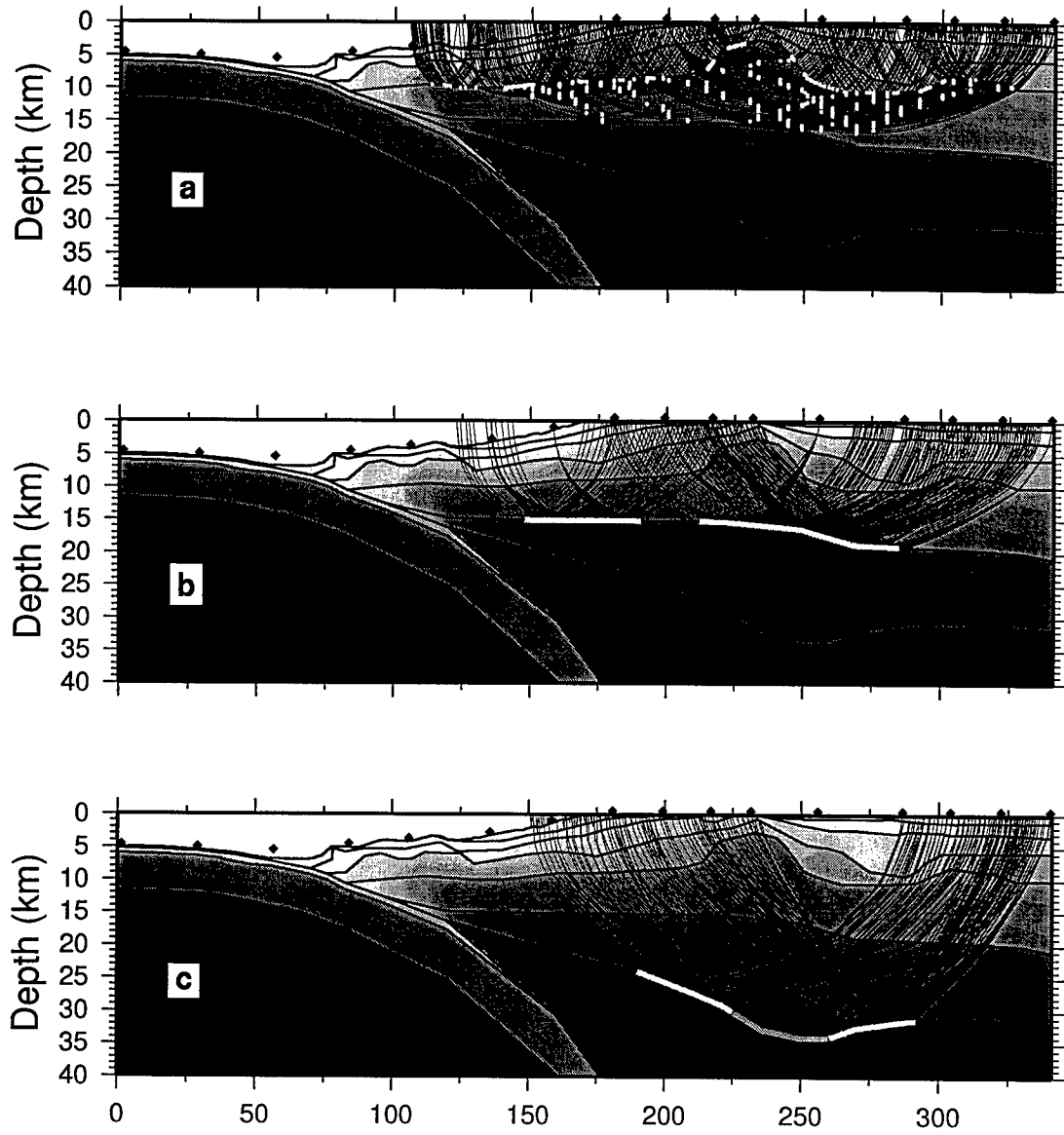
Figure 4.10
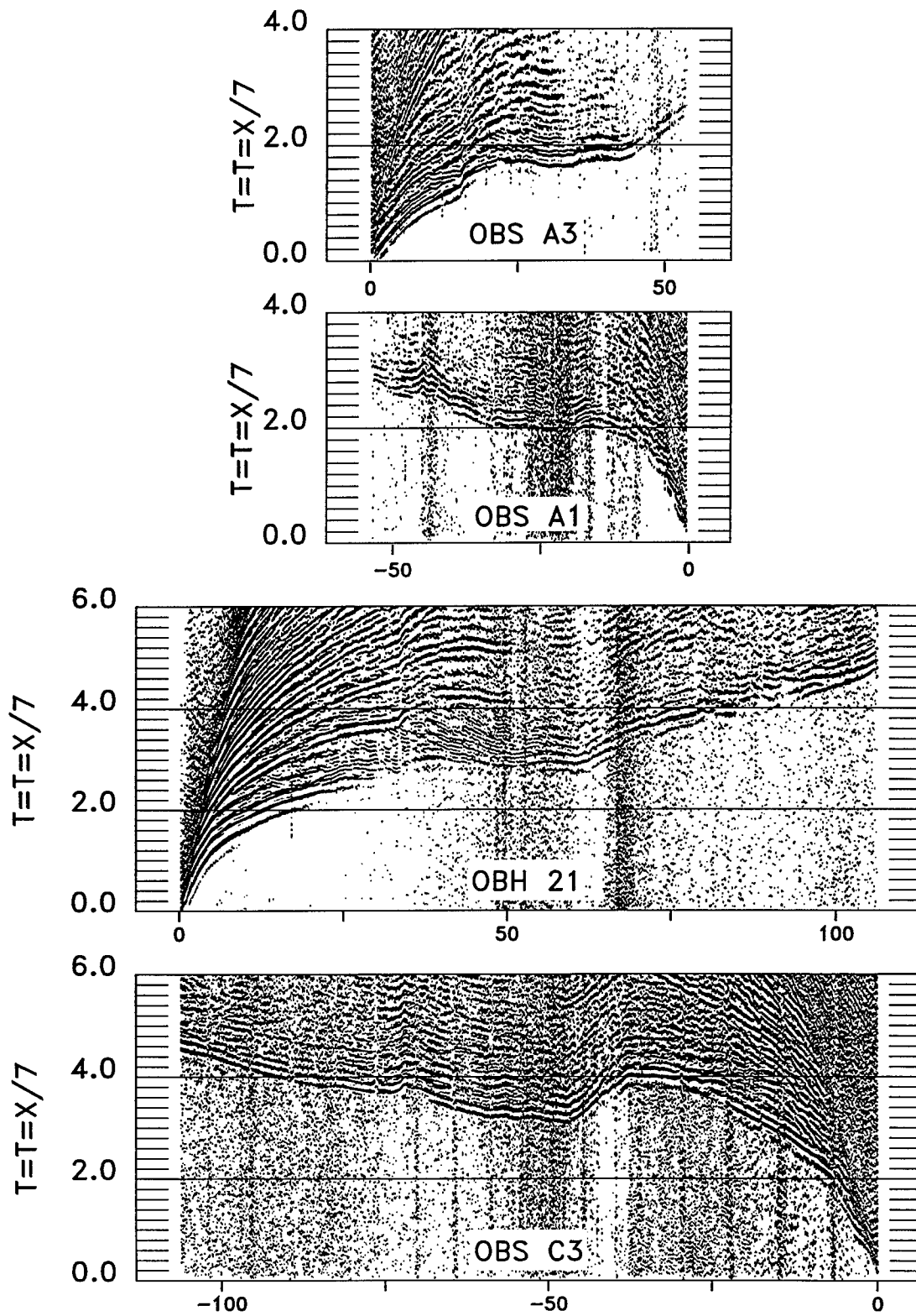
Figure 4.11

Layer 5 Sensitivity
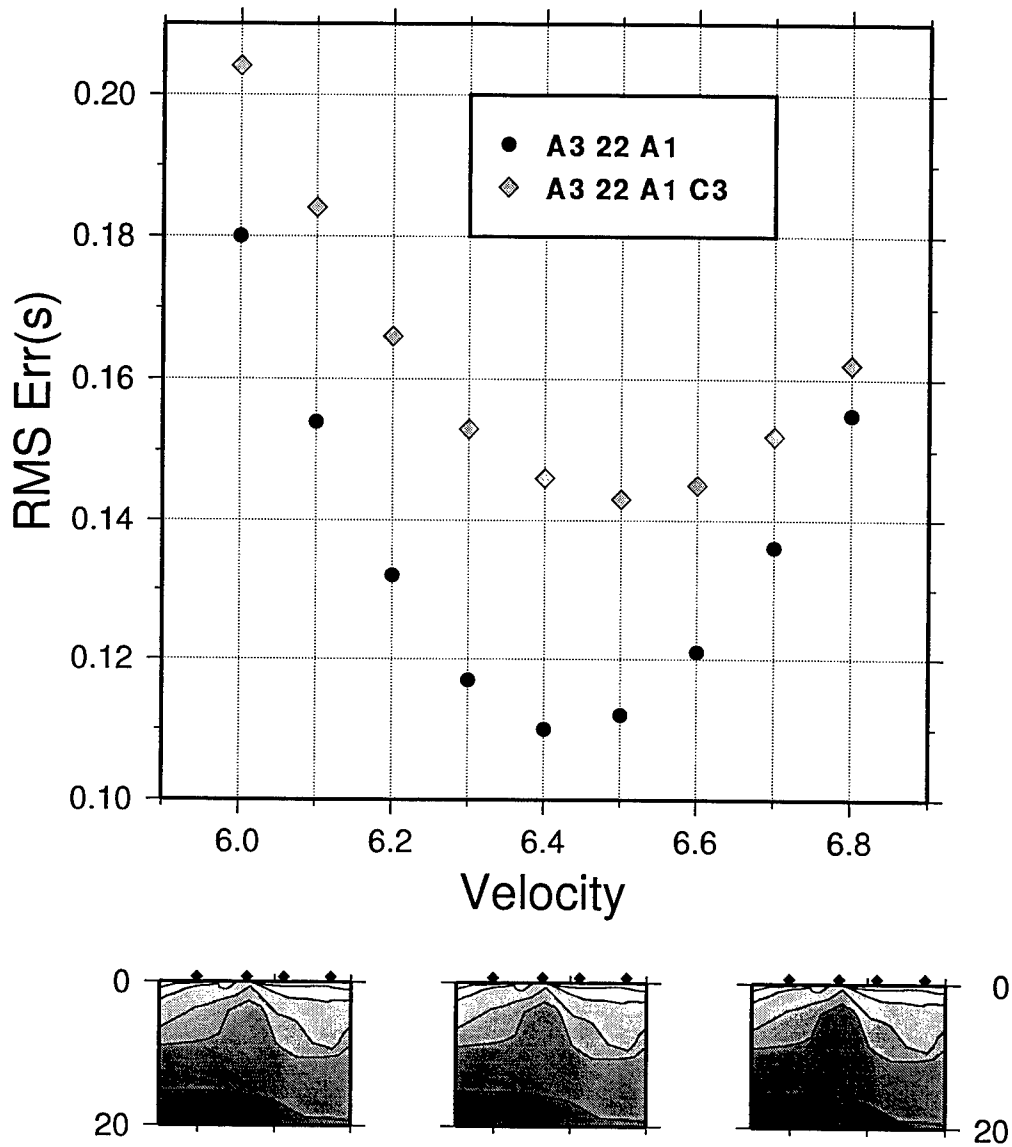
Figure 4.12
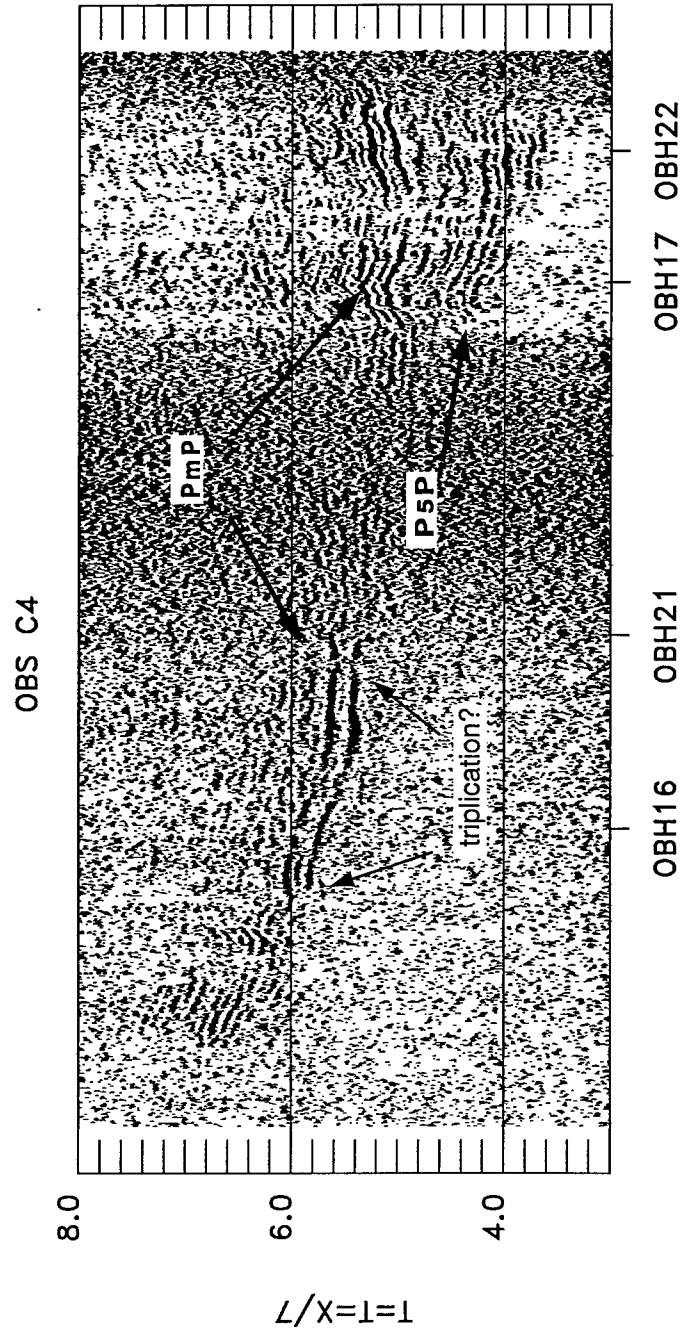
Figure 4.13
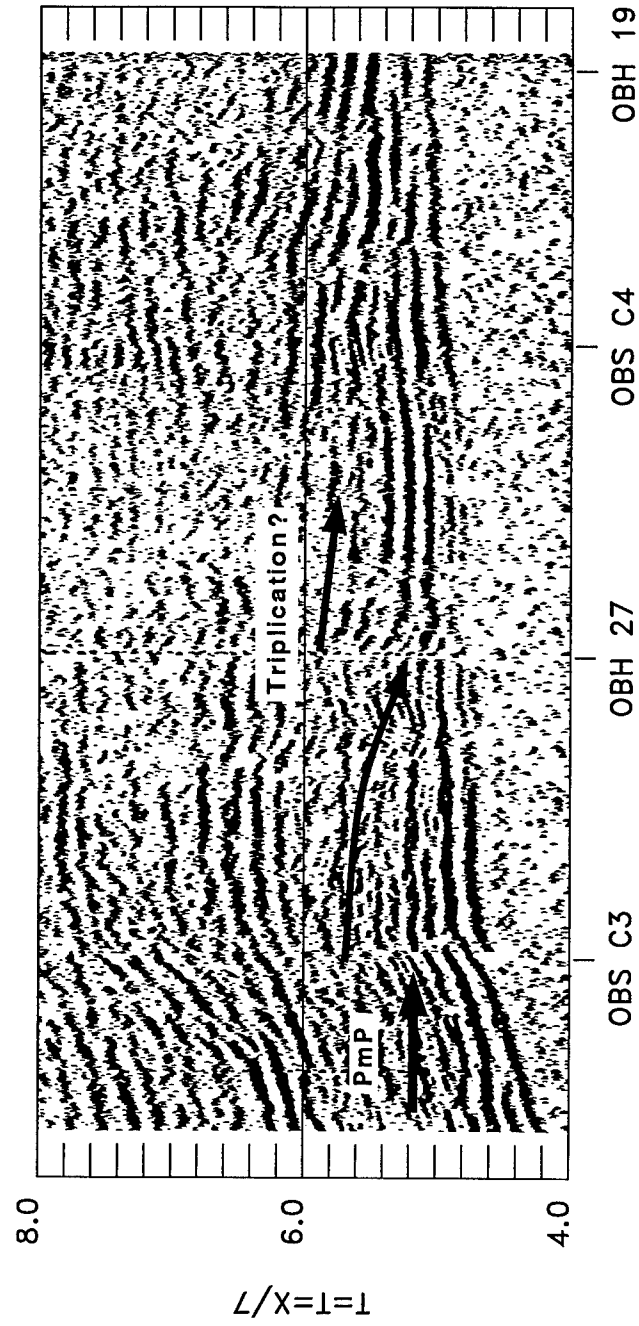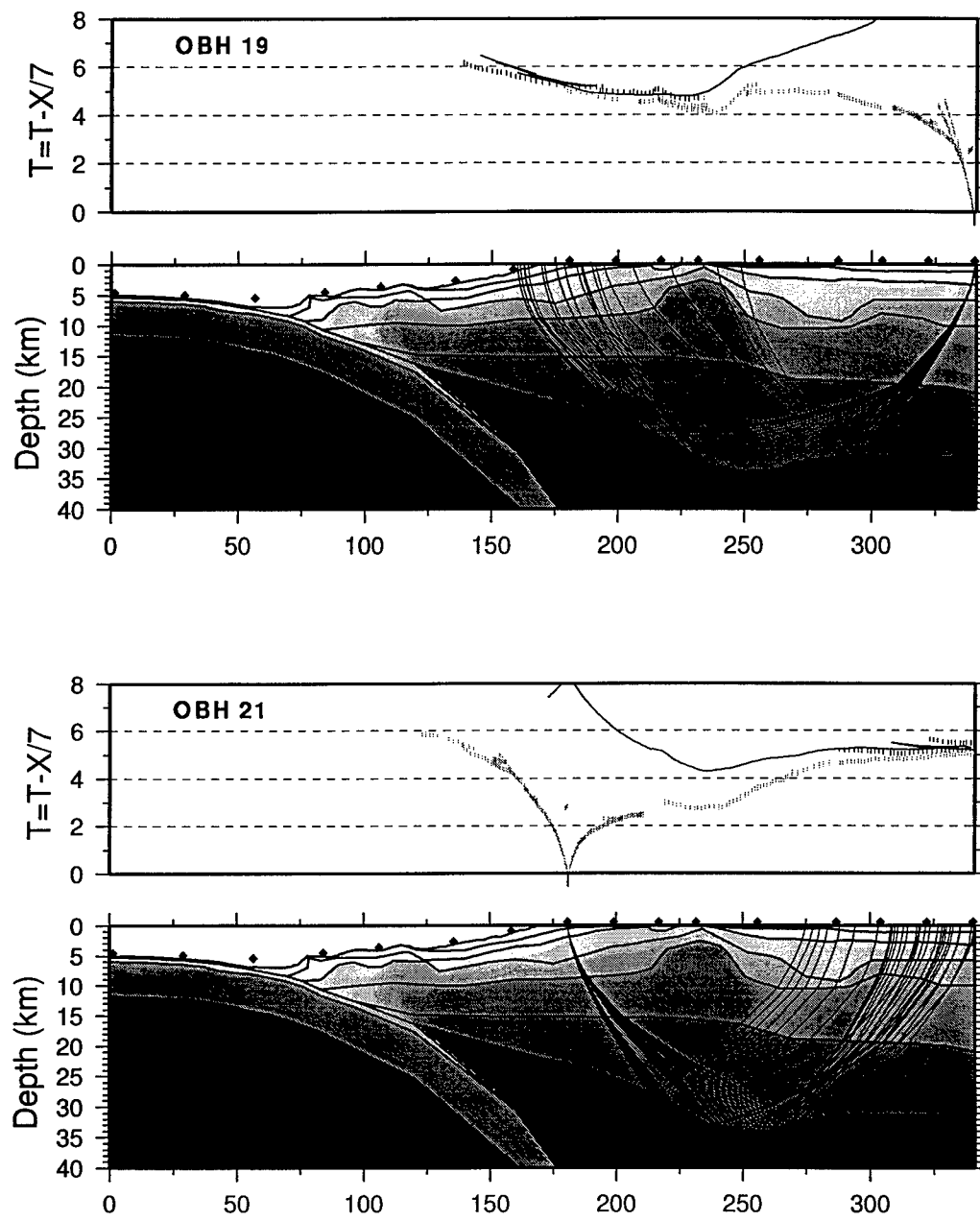
Figure 4.14

Figure 4.15

Figure 4.16

189

Figure 4.17

Figure 4.18

OBH 19

Figure 4.19a

OBS C9

$T=T-X/7$
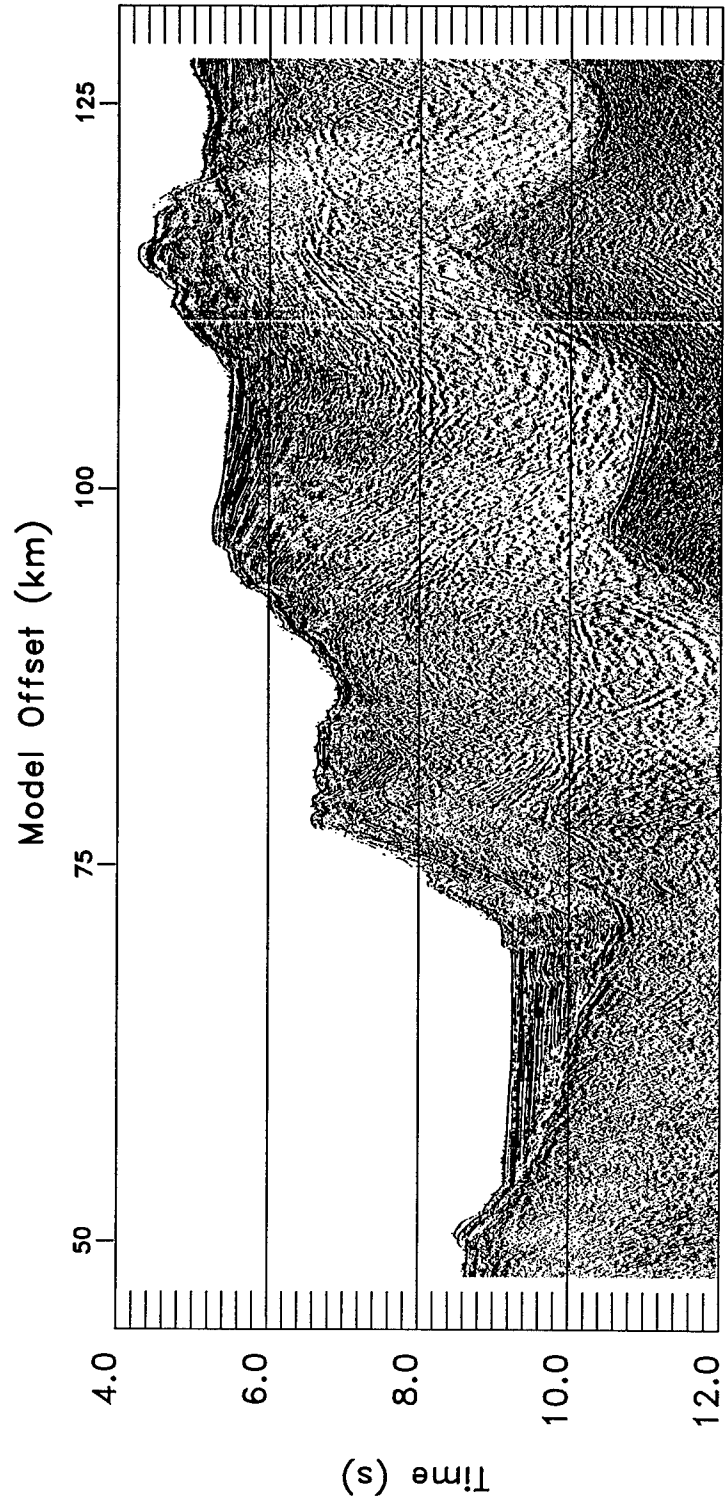
Figure 4.19b

OBH 20

$T=T-X/7$
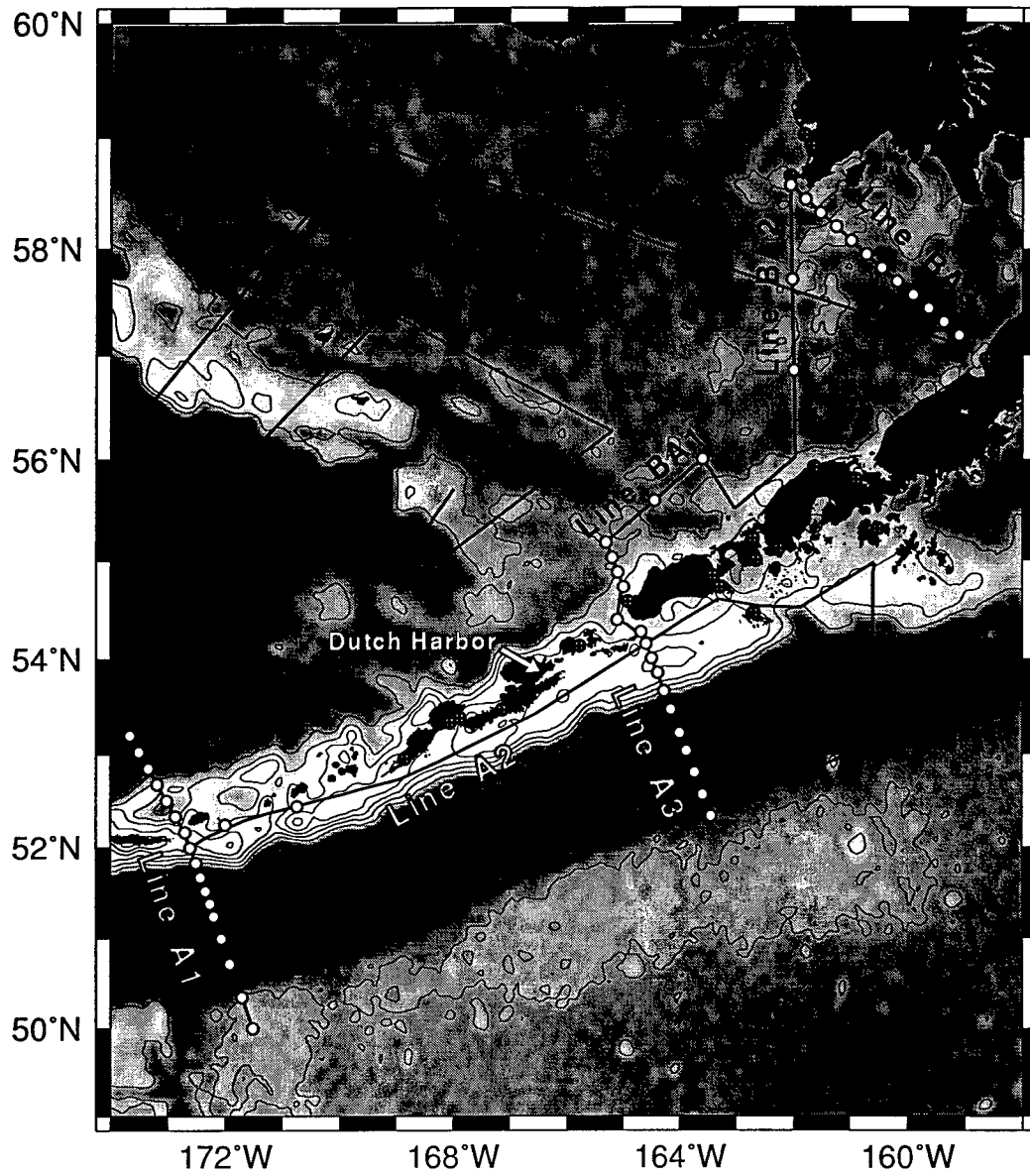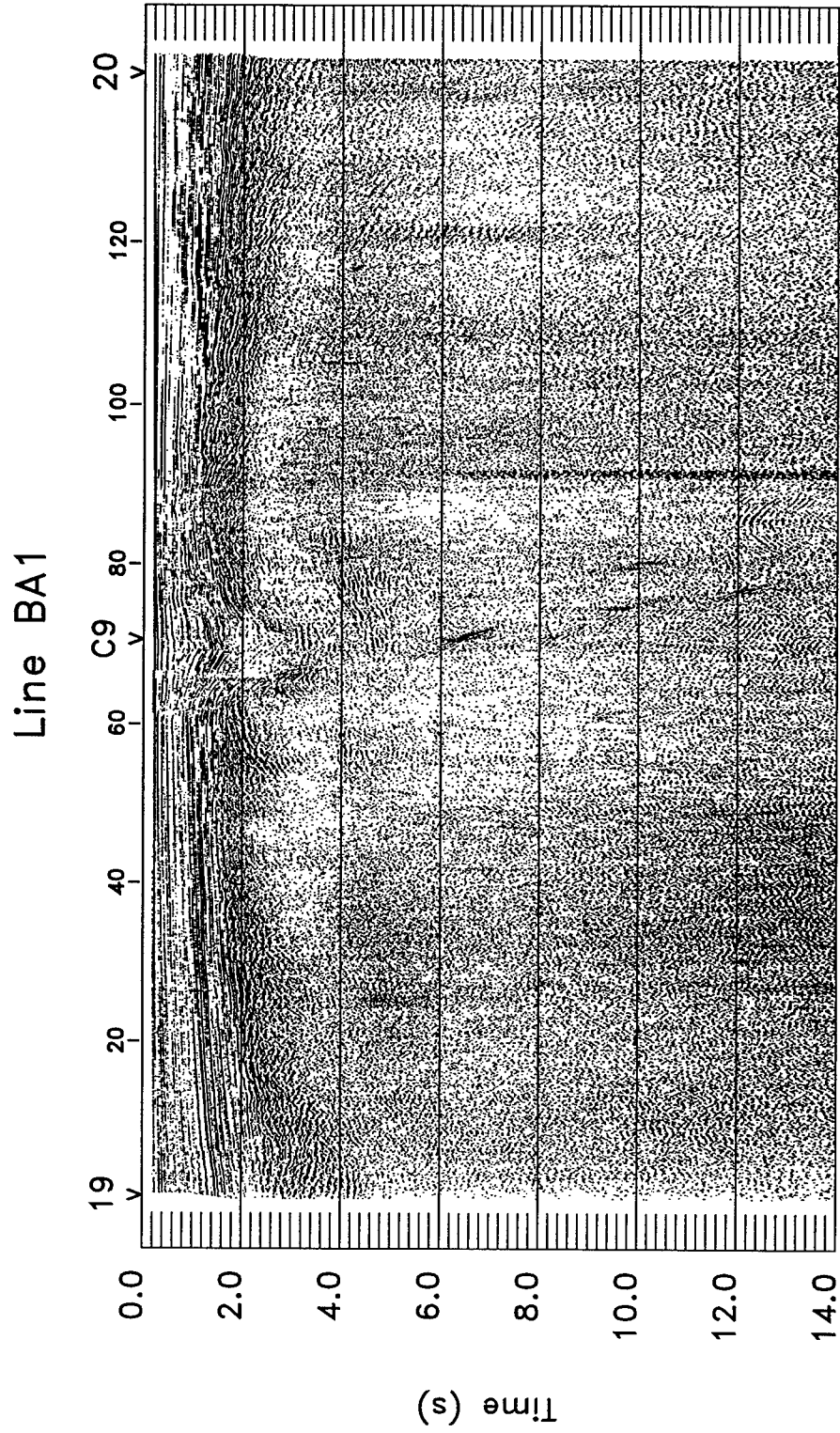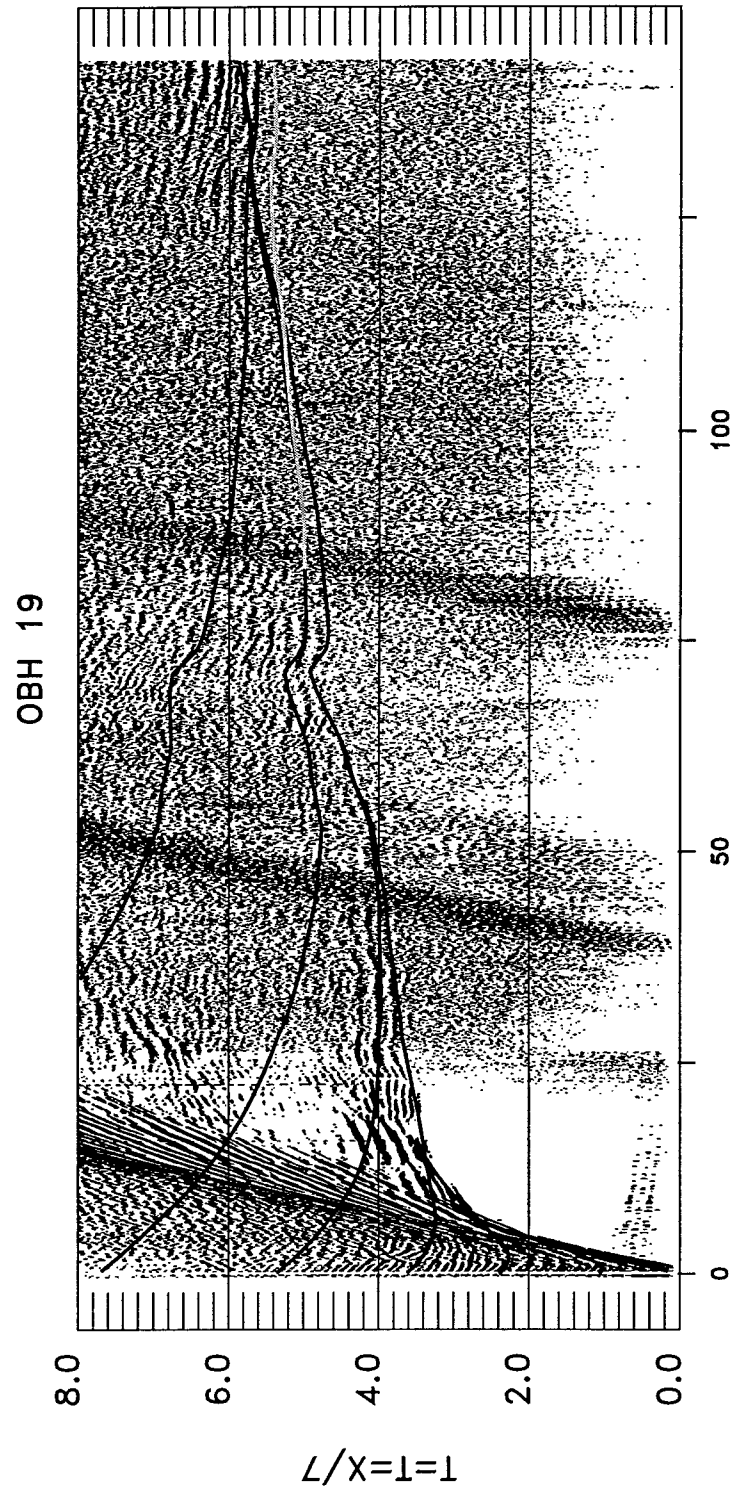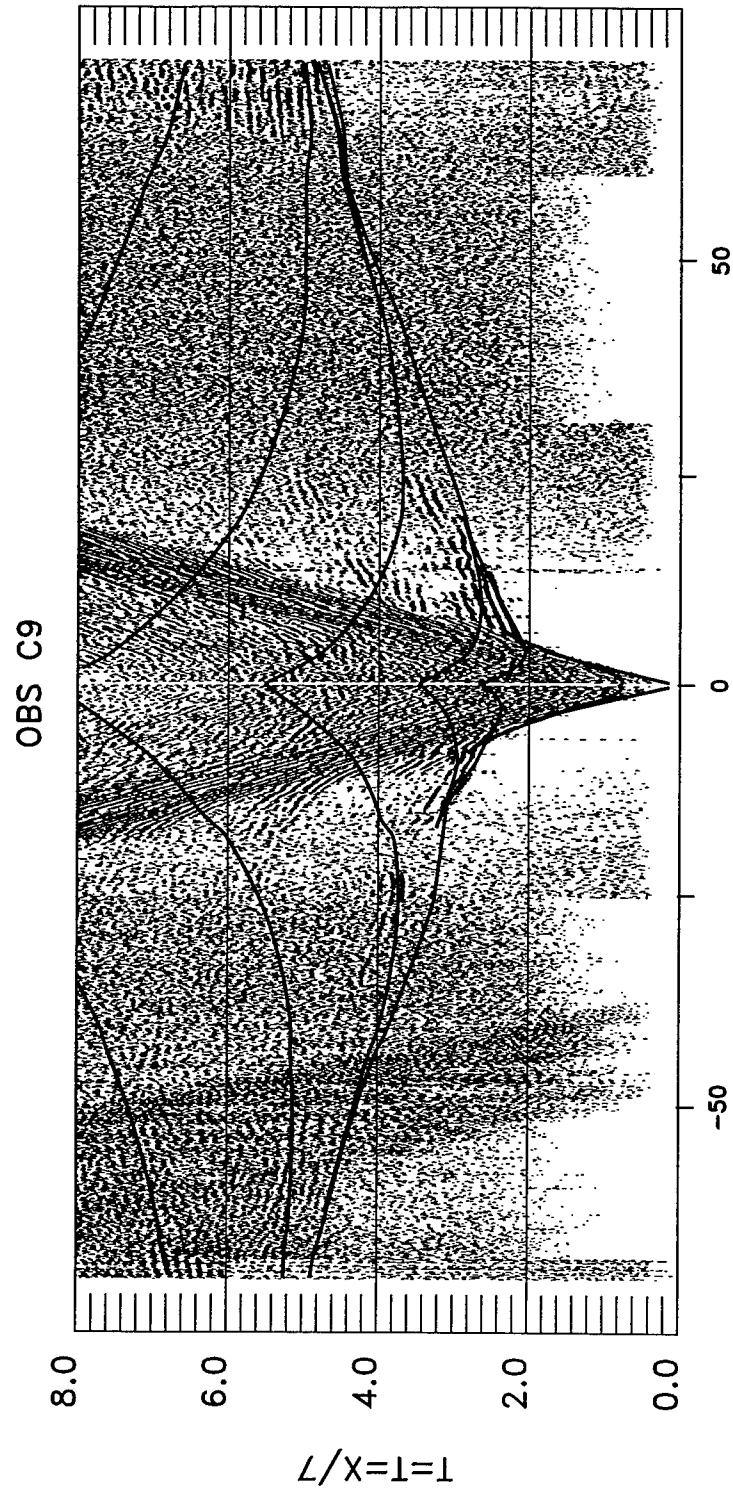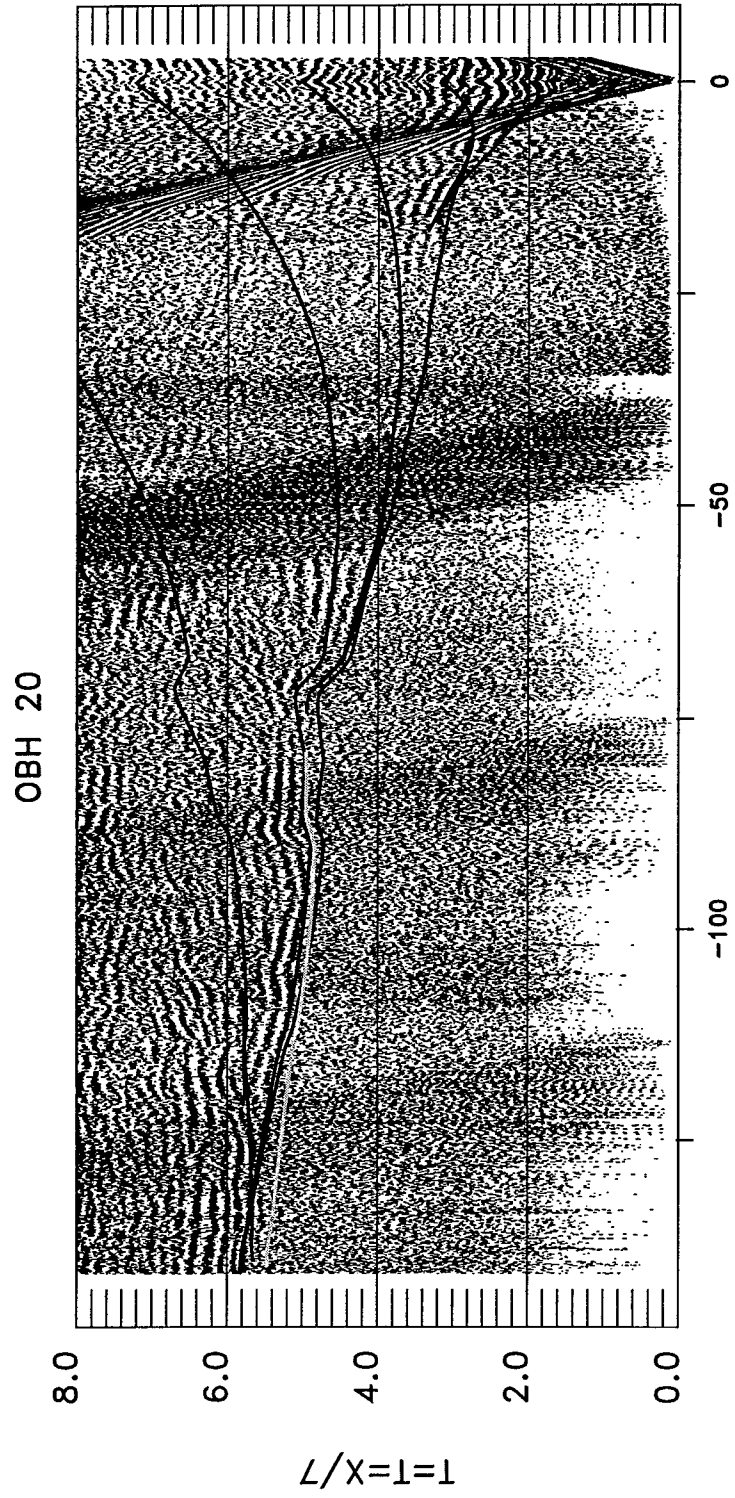
Figure 4.19c

Line BA1

Figure 4.20
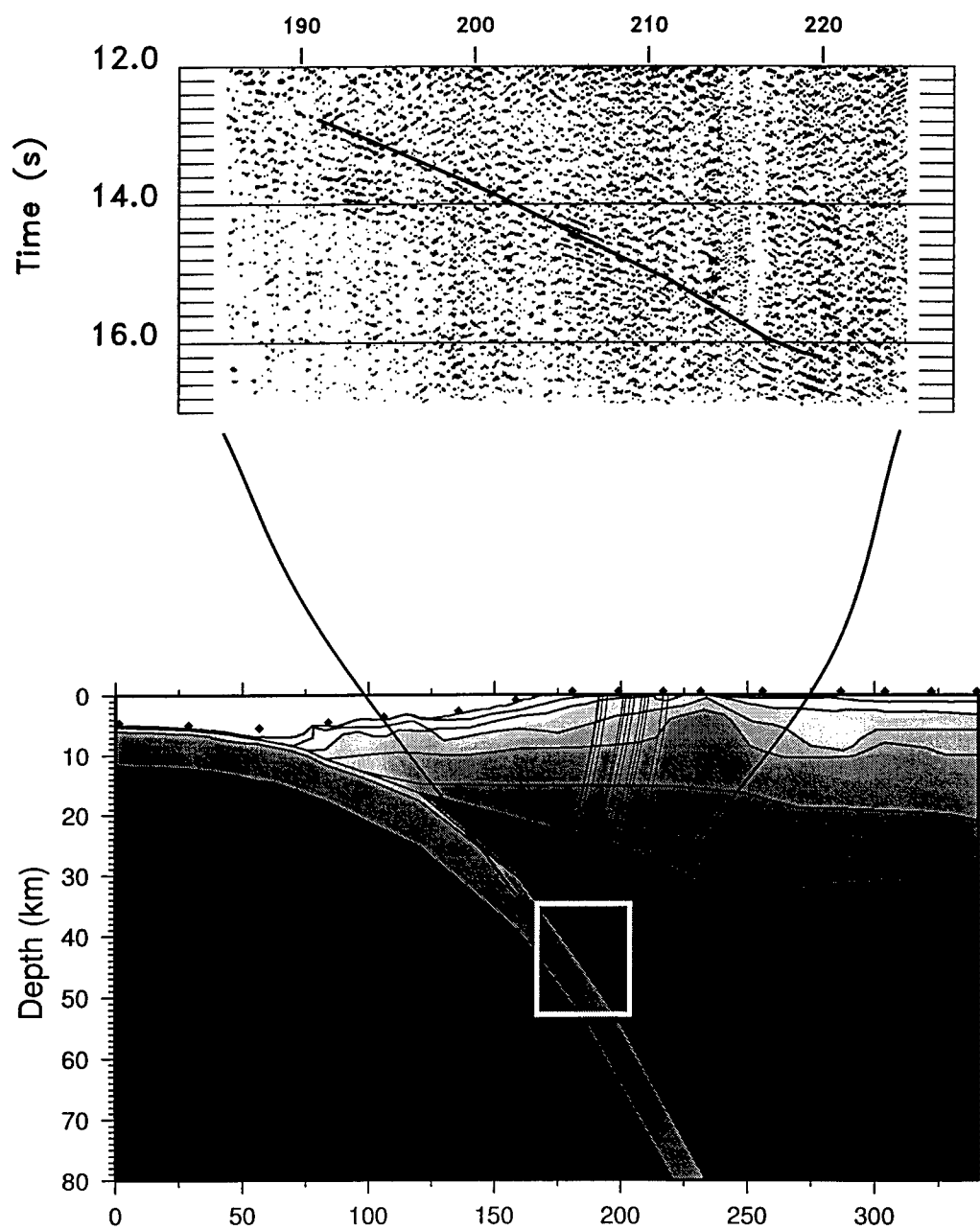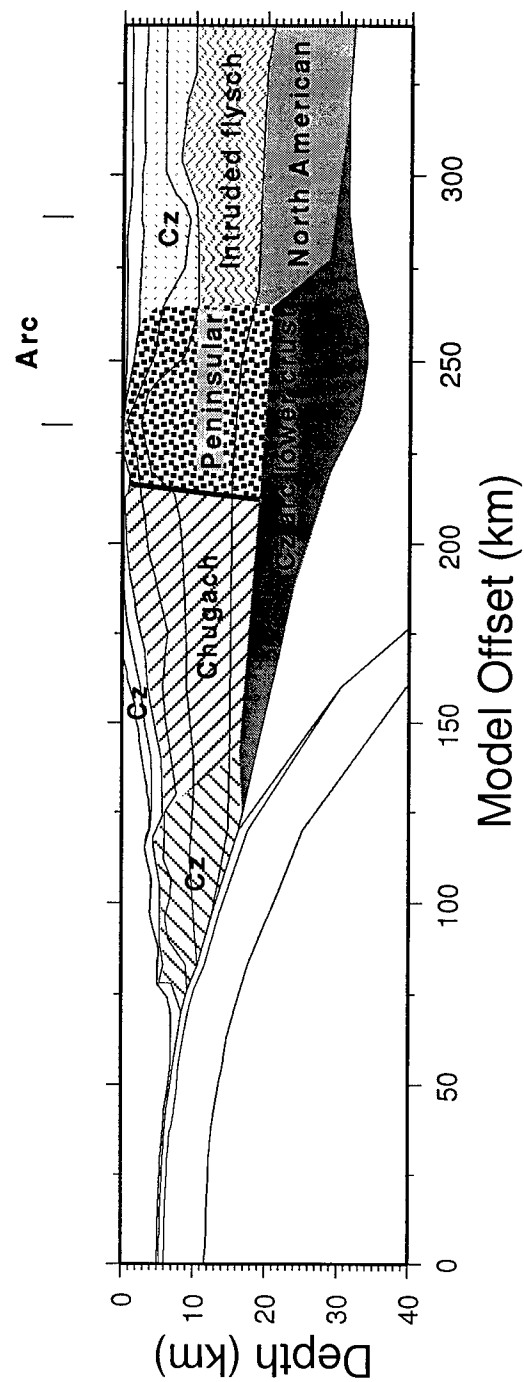
Figure 4.21
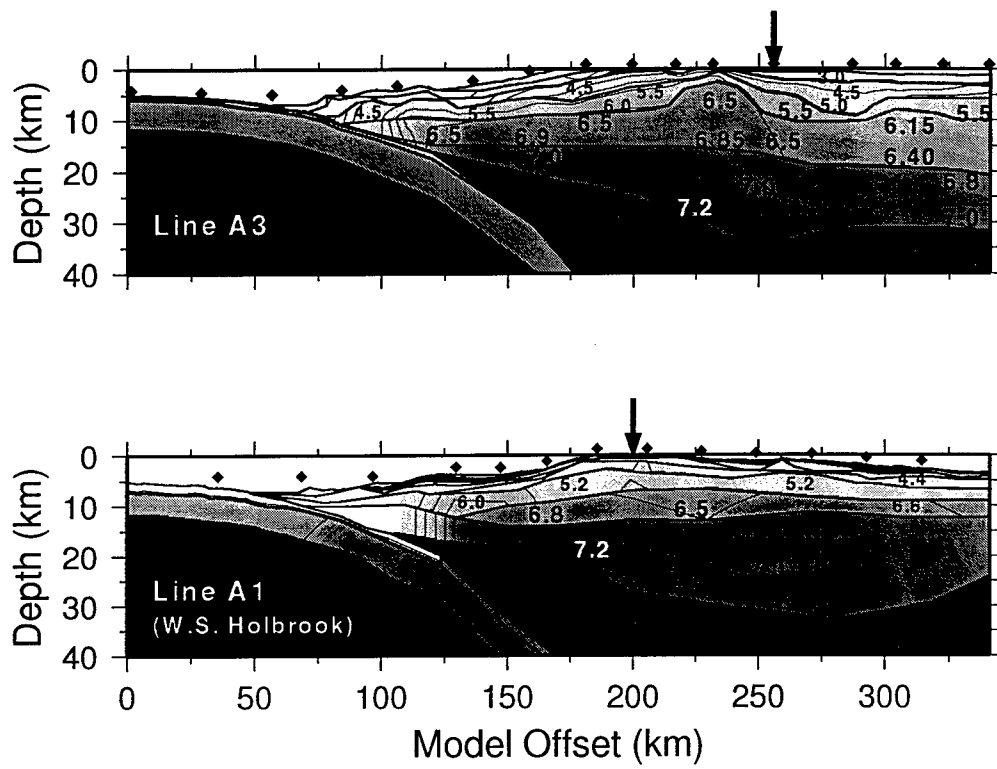
Figure 4.22

Figure 4.23

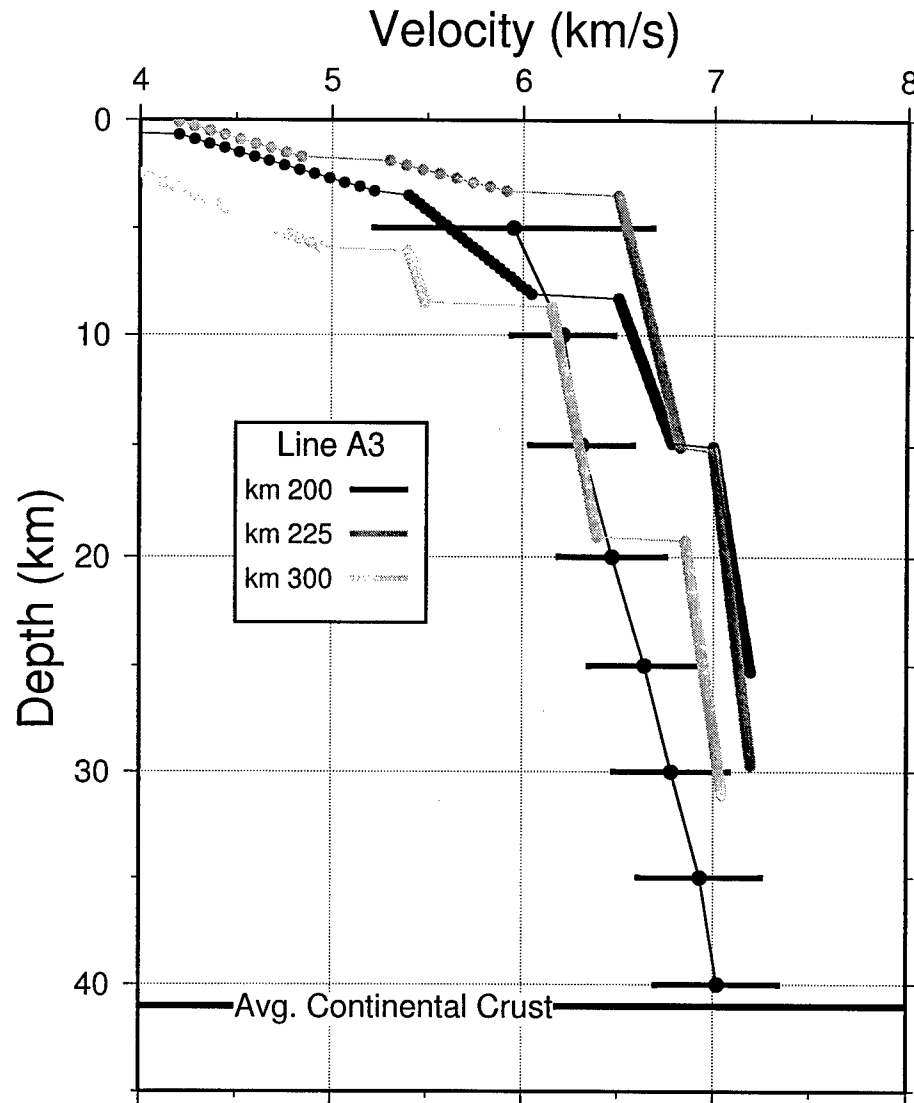Figure 4.24

Figure 4.25

Figure 4.26

Chapter 5
Crustal Structure of Bristol Bay, Alaska:
Amalgamation of Accreted-Terrane Crust

Introduction

The focus of this chapter follows from the themes of Chapter 4, namely the evolution of continental crust through the accretion and amalgamation of oceanic terranes. In this chapter we present results from a seismic transect across Bristol Bay, Alaska (Line BA3, Figure 1). Similar to the peninsular margin of Line A3, the crust of the Bristol Bay area consists of oceanic-arc terranes accreted in the late Jurassic. The history of this crust since accretion has been considerably more tumultuous, however, involving transpressional deformation and translation as well as episodes of subduction-related and anatectic intrusion. In terms of the evolution of continental crust, we can consider the crust of Bristol Bay to be more mature than that of the Line A3 transect. A primary conclusion of Chapter 4 was that accretion and reintrusion have not substantially altered the bulk properties of the accreted crust along Line A3. In this chapter we investigate the effects that terrane amalgamation and subsequent tectonic and magmatic activity have on bulk crustal properties.

Geologic and tectonic setting

The geology of the Bristol Bay region is complex, consisting of at least twenty mapped terranes and subterranes whose relationships and correlations are in many cases still unclear [*Decker et al.*, 1994]. For our purposes, it is sufficient to realize that these are oceanic-arc, back-arc, and accretionary-complex terranes. Most of the terranes are related in some way to the Togiak-Koyukuk oceanic arc, which was accreted to the northwestern North American margin in the Late Jurassic (20-40 m.y. prior to the accretion of the Peninsular terrane), and to flysch derived from the Peninsular terrane [*Decker et al.*, 1994].

Rifting and subsequent opening of the Arctic Ocean basin at about 130 Ma resulted in ~60° counterclockwise rotation of the western Alaska accreted terranes. This rotation was accommodated by right lateral displacements of more than 150 km along major strike slip faults, such as the Denali Fault system (Figure 2). During the Cretaceous and Tertiary, this rotation had the effect of bringing together the northwest-margin terranes (Togiak, etc.) and the southern-margin terranes (Peninsular, etc.), much like the closing of a pair of scissors. Thick sequences of flysch (slope and submarine turbidites composed of volcanogenic graywacke, siltstone and mudstone) accumulated and were tectonically thickened between the approaching terranes. Onshore this flysch lies between the Denali Fault system to the north and the Peninsular terrane to the south and is referred to as the Kahiltna terrane.

The northern boundary of the Kahiltna flysch may pass near the center of Line BA3 along the offshore extension of the Kulukat fault (Figure 1). It is likely that crust of the Togiak-Koyukuk oceanic-arc complex is present beneath the northwestern half of Line BA3 and crust of the Kahiltna terrane is present beneath the southeastern half. The transition may be marked by the prominent gravity gradient bisecting Line BA3. The eastern gravity low is associated with the Bristol Bay Basin, which extends along the length of the peninsula and may be genetically related to the Kahiltna terrane [*Plafker and Berg*, 1994].

In addition to the substantial geologic modifications that accompanied accretion and rotation, the Bering Sea region crust has been subjected to two episodes of widespread magmatism. The first and most voluminous of these episodes occurred along three major magmatic belts during the latest Cretaceous to early Tertiary (Figure 2), around the time of the plate reorganization that trapped Kula-plate crust and established the Aleutian arc [*Moll-Stalcup*, 1994]. These magmatic belts are characterized by abundant granitic and tonalitic plutons, have an average intermediate to felsic composition, and all have light-rare-earth-element characteristics of arc magmas [*Moll-Stalcup*, 1994]. The petrogenesis of the

northern magmatic belts, the Kuskokwim and Yukon-Kanuti belts, is still debated, however. It is thought that these belts may have either been part of an anomalously wide (400-600 km) volcanic arc, or that they are derived from anatectic melts [*Decker*, 1994; *Moll-Stalcup*, 1994].

The second magmatic episode affecting the Bristol Bay region crust began at 6 Ma with an initially voluminous extrusion of alkalic and tholeiitic volcanism. This magmatism continues to the present, though with reduced production rates. These volcanics are found on most islands of the Bering Sea and near the coastal termination of the Denali Fault in Bristol Bay. Major-element, trace-element and isotopic compositions suggest an ocean-island-basalt source for these rocks, which are more similar to Hawaiian volcanics than to normal mid-ocean-ridge basalt (i.e. N-MORB) [*Moll-Stalcup*, 1994]. The origin of these basalts is unclear. They are possibly related to a deep mantle source or back-arc extension and are probably not derived from slab, mantle-wedge, or crustal melting [*Moll-Stalcup*, 1994].

Seismic data acquisition and processing

The seismic data acquisition and processing along Lines BA3 is essentially the same as for Line A3 described in Chapter 4. The R/V *Ewing's* source array and multichannel-seismic (MCS) array were again used, and wide-angle arrivals were recorded by 6 Woods Hole Oceanographic Institution ocean-bottom hydrophones (OBHs) and 2 U.S. Geological Survey ocean-bottom seismometers (OBSs) (Figure 1). Processing of the MCS data is being carried out by other investigators of the experiment and is currently at a very preliminary stage. Consequently, we do not present figures of the MCS data, although these data were used to constrain the basement configuration. The ocean-bottom-data processing flow consisted of previous-shot suppression, predictive deconvolution, 3- to 18-Hz minimum-phase bandpass filter, and a range-varying ($X^{1.0}$) gain.

Seismic data interpretation and velocity model

The Line-BA3 seismic data were used to determine the compressional seismic velocity model shown in Figure 3. The analyses and modeling of the seismic data followed a similar approach to that described in preceding chapters of this thesis, including phase identification and traveltime picking, model parameterization, and a layer-stripping application of inverse and forward traveltime modeling to arrive at a final model. The wide-angle data with fit traveltime curves overlain are shown in Figure 4. The profiles of Figure 4 are all plotted at the same scale and include all shots fired along the line, facilitating comparison of location-dependent features between profiles. The wide-angle data are of high quality but are flawed by noisy conditions over the northern half of the line. (The source of this noise is uncertain, as weather conditions were calm during shooting of the entire profile.) In most cases, however, important phases can be correlated through this noisy interval on appropriately scaled displays.

The final velocity model consists of seven layers. Five layers make up the upper crust, with depths to 17 km. These are the best constrained layers of the model, with velocities and thicknesses based on both refractions and reflections. Layer 1 is a 1.8-km/s sedimentary layer which is quite thin over most of the model but thickens to ~2 km in the south over the Bristol Bay Basin. Layers 2 and 3 are ~1.5 km and ~2.0 km thick over most of the model but thin dramatically north of km 25. Layer 4 has velocities ranging from 5.9 to 6.2 km/s, with slightly higher velocities beneath the northern half of the line. Layer 4 is thicker in the north (~7 km) than in the south (~4 km), shallows to near the surface north of km 25, and shoals by ~1.5 km near km 125. Layer 5 has a fairly uniform structure, with a thickness of ~7 km and velocities of 6.2 to 6.3 km/s. The mid- and lower-crustal layers, Layers 6 and 7, are constrained by wide-angle reflections, are each ~10 km thick, and dip northward. Moho structure is constrained between km 50 and km 175. Crustal thickness is 40 km at km 50 and thins to 33 km at km 175.

The interpreted wide-angle phases used to constrain the velocity model include the diving-wave phases from the upper 5 layers, $P_1 - P_5$, reflecting phases P_4P, P_5P, P_6P, and P_MP from the base of Layers 4, 5, 6, and 7, and the mantle diving-wave phase P_n observed on one instrument, OBH26. Layer 1 velocity structure is constrained by the basement configuration delineated on the MCS profile and the P_1 phase. The P_1 phase is strikingly linear on OBSA1 and OBH20, revealing a thick layer of very slow 1.8-km/s material with only a slight vertical velocity gradient. The northward thinning of this layer is apparent in the progressively earlier times to the P_2 first break observed on instruments north of OBSA1.

The basement surface underlying Layer 1 is rough on a 1- to 5-km horizontal scale, giving an undulatory appearance to the wide-angle arrivals. The most prominent basement disturbance, apart from the Bristol Bay Basin, occurs near km 25. This is a likely location for the intersection of the Denali Fault with Line BA3. The basement disturbance at this location is apparent as strong diffractions emanating from all events crossing it.

The structure of Layers 2 and 3 is constrained by the P_2 and P_3 phases. The P_2 and P_3 phases are strong refractions through the top of the basement. The phases have distinct slopes in some cases (e.g. OBS C3) and merge into a continuous curvature in others (e.g. OBH20). In most cases, the P_3 phase becomes a first arrival at 10- to 20-km offset and remains a first arrival until ~35 km offset. The lateral resolution of Layer-3 structure is thus quite good, even across instrument gaps in the line.

Layer-4 structure is constrained by the P_4 and P_4P phases. The P_4 phase is a first arrival between 30 km and 100 km offset on most instruments. Ray coverage for this phase is excellent (Figure 5a). The slope of the P_4 first arrival is perturbed by the elevated Layer 4 structure near km 125. Comparing OBSC3 and OBH27, for example, we see the P_4 slope increase, decrease, and then increase again on both instruments across the center of the line. This pattern is characteristic of a structural high and is the basis for the Layer 4

structure near km 125. We note that the northern flank of this feature may be steeper than that of the model, as suggested by the strong diffractions, or back reflections, of crossing phases observed on OBSC3 near 65 km offset. The P_4P reflection is a distinct phase, well separated from the first arrival on all of the instruments. The P_4P phase is the earliest reflected phase with computed traveltimes curves overlain on the wide-angle profiles (Figure 4). Bounce points for the picked events are concentrated mostly near the center of the line, but the events on OBH23 and negative offsets of OBH25 have bottoming points near km 30.

Layer-5 structure is constrained by the P_5 and P_5P phases. The P_5 refraction is the first arrival beyond ~100 km offset. Ray coverage for this phase is very good, with bottoming points concentrated towards the top of the layer between km 75 and km 200 (Figure 5b). There is little change in slope from the P_4 phase, indicative of the small change in velocity between Layers 4 and 5. The P_5P reflection is a prominent event on most profiles and is particularly strong on OBSC3. Bottoming points of the reflection lie all along the interface across the center of the line defining a nearly flat base to the layer.

Layer-6 structure is based on the P_6P reflection. This is a prominent phase, but it is obscured within the noisy interval on the southern instruments OBSA1 and OBH20. The phase can be correlated through the noise on OBH27, however, and reversals of this event and a pieces of P_6P on OBSA1 and OBH20 provide reasonable constraints for the structure of Layer 6 (Figure 5c).

Layer-7 and Moho structure are constrained by P_MP phases observed on most of the instruments and the P_n phase observed on OBH26. The P_MP reflection is a strong, distinct phase only on OBH26, where it is particularly strong. The phase is weak and complicated on other south-looking instruments. The north-looking instruments are, again, obstructed by noise, but the reversal of OBH26 with OBH27 can be confidently correlated back into the noise and provides reasonable constraints on this layer's structure (Figure 5d).

We analyzed the sensitivity of the P_MP and P_N fits to velocity by performing a suite of inversions with velocities fixed in various configurations. For each test inversion we held the velocity at the top and bottom of the layer fixed and inverted for the best fitting Moho structure. We ran tests for a range of top and bottom velocities from 6.5 km/s to 7.2 km/s. The results of these inversion runs are shown in Figure 6 for three sets of traveltime data, one using all picks, on using only the OBH26 and OBH27 picks, and one using only the OBH26 picks. The best fit models were generally insensitive to velocity gradient and so we show only the average layer velocity for each inversion in Figure 6. These tests show that the entire dataset is not particularly sensitive to velocity variations of as much as 0.20 km/s and suggest an average velocity of 6.8 km/s for the lower crust. The runs using the reduced traveltime datasets of the most confident picks show considerable sensitivity to average velocity and prefer slower velocities. The best fit models for these runs tend to include more extreme Moho structure than runs using the entire dataset, and fits to the unused traveltimes using these models are poor. We conclude that the 6.8 km/s average velocity for the lower crust is constrained to within ±0.20 km/s. The structure of the Moho may be more complex than in our model. The dramatic change in appearance of the P_MP phase between OBH26 and OBH23, for example, is not easily explained by a simple Moho structure.

Discussion

The geology and tectonic history of the region surrounding Bristol Bay suggest that the crust beneath Line BA3 is built of Togiak-Koyukuk ocean-arc-terrane rocks to the north and Kahiltna-terrane flysch-dominated rocks to the south of the Kulakat Fault, which probably passes near the center of the line and is possibly marked by the Layer 4 structure near km 125. This configuration is similar to our interpretation of Line A3 at the western end of the Alaska Peninsula, where we inferred the origin of crustal components from the

margin's tectonic history, the seismic characteristics of laterally distinct crustal units, and by comparison with the oceanic-arc crust of Line A1. The velocity structures of these two transects are quite different, however. The Line-BA3 crust is thicker and has generally lower velocities than that of Line A3, and the 10-km-thick pile of low-velocity (<6.0 km/s) material observed beneath Line A3 is absent beneath Line BA3, where we observe an upper crust with an average velocity of ~6.0 km/s. One of the major conclusions of Chapter 4 is that the crust beneath Line A3 does not bear a strong resemblance to average continental crust. The principal result of the present chapter is that the crust beneath Line BA3 does have the velocity structure of average continental crust (Figure 7a).

The contrast in seismic structure observed between Line A3 and Line BA3 highlights the underlying themes of this chapter and of Chapter 4, the generation of crust with average continental properties (Line BA3) from mafic arc and accreted-arc crust (Line A3). This contrast is especially significant if, as the onshore geology implies, the Bristol Bay crust has been built of terranes of similar origin as those that make up the crust beneath Line A3. If this is the case, then it is reasonable to infer that the Togiak-Koyukuk terrane crust initially had a seismic structure similar to that of Line A1 or the southern portion of Line A3, and that the Kahiltna-terrane crust once resembled the crust beneath the northern portion of Line A3. These inferences imply that the crust beneath Line BA3 has undergone a dramatic transformation, and, to the extent that these inferences are correct, our results along Line BA3 provide evidence that oceanic-arc-type crust can and has evolved into crust with average continental crust properties.

The transformation of Line-A3 type crust to that of Line BA3 requires at least two processes: crustal thickening and removal of the mafic (>7.0 km/s) lower crust. Significant crustal thickening may have accompanied the 50° crustal rotation and 150 km crustal translation associated with the opening of the Arctic ocean. This thickening may have promoted erosion and metamorphism of low-velocity Line-A3-type upper crustal

material. Removal of the mafic/ultramafic (> 7.0 km/s) lower crust may have been accomplished either by eclogitization and delamination during crustal thickening, or by incorporation into the upper mantle as the residue of intracrustal melting Intracrustal melting, perhaps triggered by crustal thickening, occurred at 50-75 Ma in the southwestern Alaskan magmatic belts (Figure 2), which are characterized by extensive felsic-to-intermediate upper-crustal plutonism [*Moll-Stolcup*, 1994]. The mafic/ultramafic residue of this melting is absent from Line BA3 crust, so it presumably lies below the Moho. This may be suggested by the 40-km crustal thickness at the northern end of Line BA3, which seems inconsistent with an elevation below sea level. It is possible that a dense residual upper mantle is compensating the crustal root at the northern end of Line BA3, holding the crust below sea level. Thus, although we lack sufficient data to propose a definitive scenario for the transformation of Line-A3-type crust to Line-BA3-type crust, the geologic and tectonic history of the region is consistent with the processes — crustal thickening, crustal melting, and the removal of an ultra-mafic residue of crustal melting — that must be invoked to explain such a transformation [e.g. *Nelson*, 1991; *Mooney and Meissner*, 1991].

Although we favor the scenario described above, in which the intermediate-composition components of accreted crust are selectively preserved and thickened, we lack direct evidence that such a sequence of events occurred. Alternative models are also possible; for example, the Togiak-Koyukuk oceanic-arc terranes may not extend offshore, in which case they may have an origin completely unrelated to Line-A3-type crust. In any case, the value of the results presented in this chapter lies in the identification of a region where an important change in crustal properties occurs over a relatively short distance, the 400 km separating Lines A3 and BA3. It should be possible, perhaps with existing MCS and sonobuoy data from the Aleutian Seismic Experiment, to test the various explanations for this transition from mafic arc crust to continental crust.

Conclusions

We have presented results from a seismic experiment over crust formed through the amalgamation of oceanic-arc, back-arc and accretionary complex terranes. Comparison of the crustal structure along this transect with the Line A3 and Line A1 crustal structures discussed in Chapter 4 leads to the following conclusions.

1) The crust of the Bristol Bay region may have once been more mafic and had a structure similar to the peninsular margin. Now, however, the Bristol Bay crust has a seismic velocity structure of average continental crust.

2) The geologic and tectonic evolution the region is consistent with commonly proposed scenarios for continental crustal evolution in which the intermediate-composition components of accreted are crust are selectively preserved through crustal thickening, erosion, and removal of a significant mafic component below the Moho.

3) The identification of continental crust beneath Line BA3 delineates a convenient location for a more complete study of the transition from mafic arc crust to continental crust, a study that can begin with existing data from the Aleutian Seismic experiment.

References

Bickford, M.E., The formation of continental crust: Part 1. A review of some principles; Part 2. An application to the Proterozoic evolution of southern North America, *GSA Bull.*, *100*, 1375-1391, 1988.

Christensen, N.I., and W.D. Mooney, Seismic velocity structure and composition of the continental crust: A global view, *J. Geophys. Res.*, *100*, 9761-9788, 1995.

Fountain, D.M., and N.I. Christensen, Composition of the continental crust and upper mantle: A review, in Geophysical Framework of the Continental United States, edited by L. C. Pakiser and W.D. Mooney, *Mem. Geol. Soc. Am.*, *172*, 711-742, 1989.

Kay, R.W.., and S.M. Kay, Delamination and delamination magmatism, *Tectonophysics*, 219, 177-189, 1993.

Kay, S.M., and R.W. Kay, Aleutian magmas in space and time, in *The Geology of North America*, vol. G-1, *The Geology of Alaska*, edited by G. Plafker, and H.C. Berg, pp. 687-722, Geological Society of America, Boulder, Colo., 1994.

Miller, T.P., Pre-Cenozoic plutonic rocks in mainland Alaska, in *The Geology of North America*, vol. G-1, *The Geology of Alaska*, edited by G. Plafker, and H.C. Berg, pp. 535-554, Geological Society of America, Boulder, Colo., 1994.

Moll-Stalcup, E.J., Latest Cretaceous and Cenozoic magmatism in mainland Alaska, in *The Geology of North America*, vol. G-1, *The Geology of Alaska*, edited by G. Plafker, and H.C. Berg, pp. 589-619, Geological Society of America, Boulder, Colo., 1994.

Mooney, W.D., and R. Meissner, Continental crustal evolution observations, EOS. Trans., 72, 537-585, 1991.

Nelson, J.D., A unified view of craton evolution motivated by recent deep seismic reflection and refraction results, *Geophys. J. Int.*, *105*, 25-35, 1991.

Plafker, G., and H.C. Berg, Overview of the geology and tectonic evolution Alaska, in *The Geology of North America*, vol. G-1, *The Geology of Alaska*, edited by G. Plafker, and H.C. Berg, pp. 989-1021, Geological Society of America, Boulder, Colo., 1994.

Plafker, G., J.C. Moore, and G.R. Winkler, Geology of the southern Alaska margin, in *The Geology of North America*, vol. G-1, *The Geology of Alaska*, edited by G. Plafker, and H.C. Berg, pp. 389-449, Geological Society of America, Boulder, Colo., 1994.

Figure Captions

Figure 1: Location map for the Line BA3 transect. MCS track line and ocean-bottom instrument locations plotted on satellite-based free-air gravity anomaly pattern. Gravity contours are 10 mGal. The Denali and Kulukat strike-slip faults are indicated.

Figure 2: Cenozoic and Pre-Cenozoic magmatic belts of southwestern Alaska. The pre-Eocene location of subduction along the Beringian margin, the location of the Border Ranges Fault (BRF), the Southern Margin Composite terrane, and the tracks of the instrumented lines of the 1994 Aleutian seismic experiment are also indicated. [Adapted from *Plafker et al,* 1994; *Plafker and Berg,* 1994; and *Moll-Stolcup,* 1994]

Figure 3: Gray-shade and contour plot of the Line BA3 final velocity model. Velocities are indicated in km/s and contoured at 0.5 km/s. Bold lines on interfaces represent wide-angle reflection bounce points. Boxed numbers are Layer numbers referred to in text.

Figure 4: Record sections with and without calculated traveltime curves overlain for Line BA3 ocean-bottom instruments. Reduction velocity is 7 km/s for all sections. Horizontal and vertical scales are the same for all profiles.

Figure 5: Two-point ray diagrams (i.e. only rays to traveltime picks) for the (a) P_4, (b) P_5, (c) P_6P and (d) P_MP phases.

Figure 6: RMS misfit versus average Layer-7 velocity for a suite of inversions in which velocity at the top and bottom of the layer was held fixed and Moho structure was inverted for. RMS error was insensitive to vertical velocity gradient. These results demonstrate the sensitivity of the data under simple conditions and indicate a preferred lower-crustal velocity of 6.8 km/s.

Figure 7: Left: Comparison of Line BA3 vertical velocity profiles from km 75 and km 175 (circles with thin lines) with the in-situ velocity structure of average continental crust [*Christensen and Mooney*, 1994] shown with standard deviations. Right: Comparison of Line A3 vertical velocity profiles (see Chapter 4) with average continental crust.
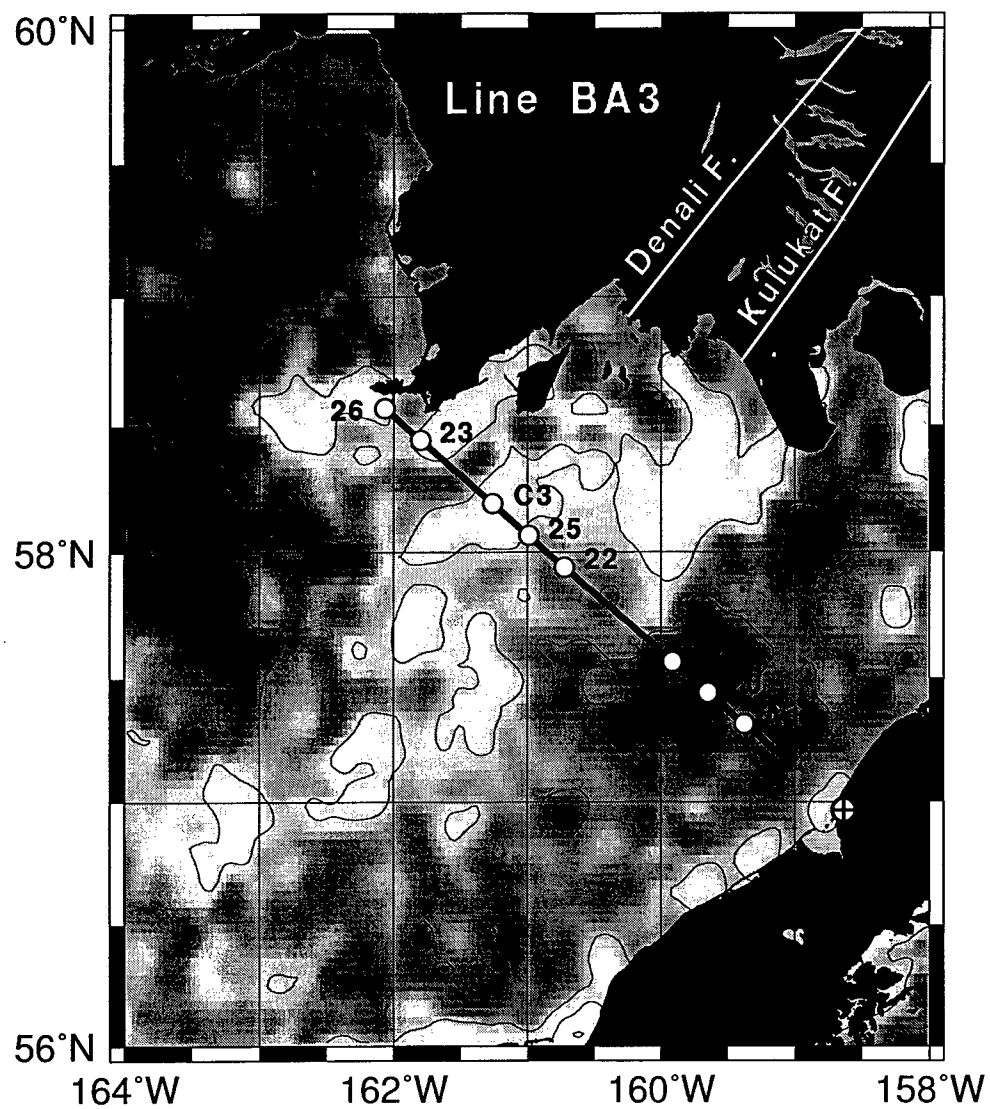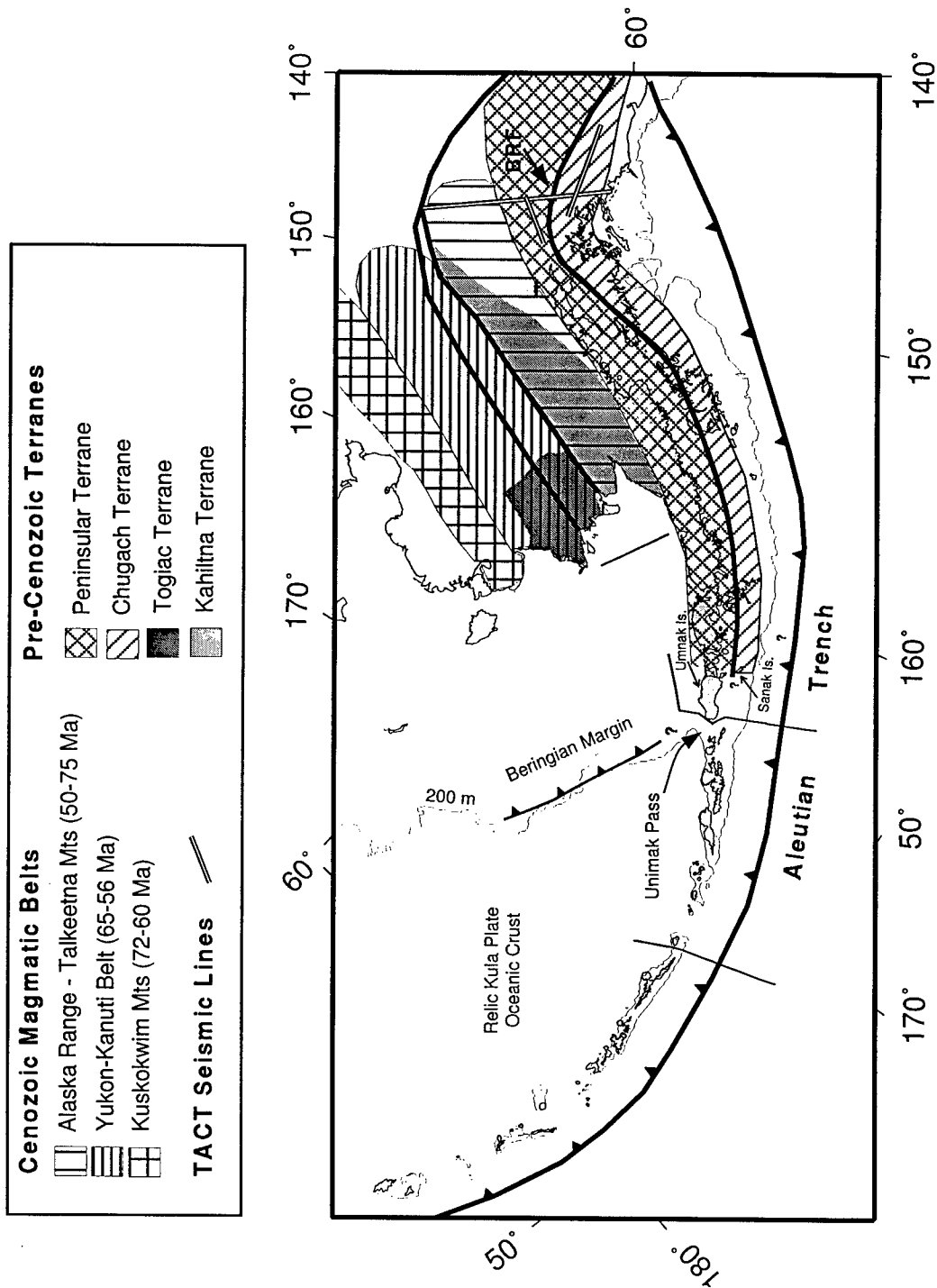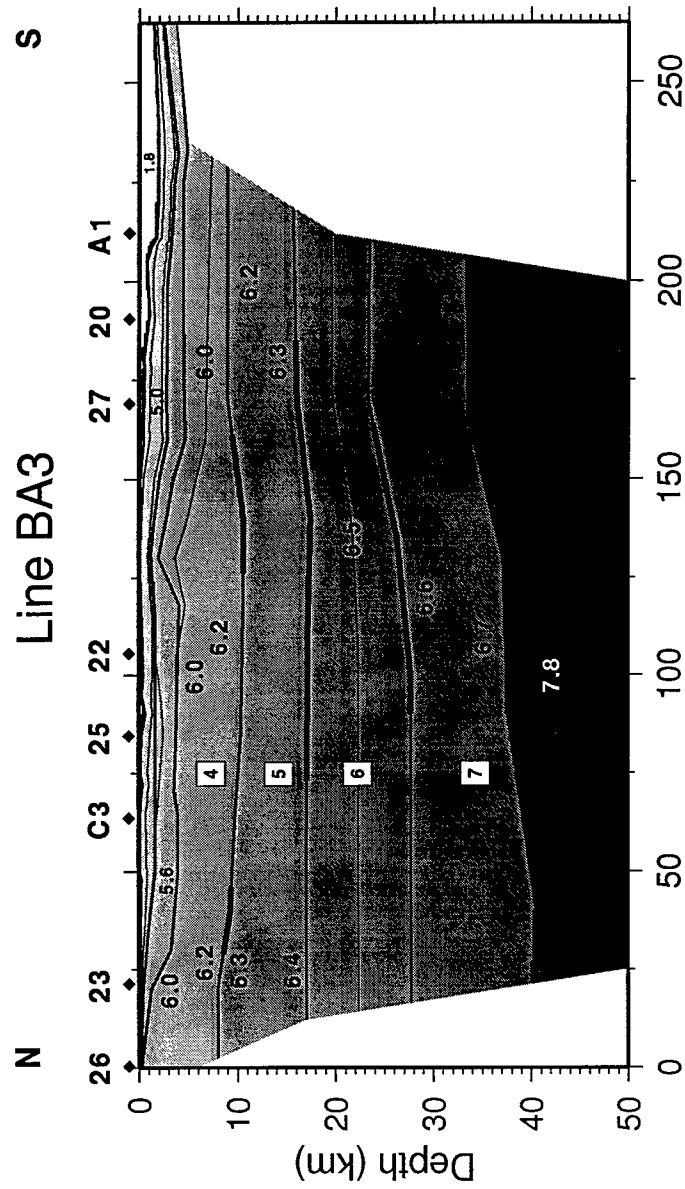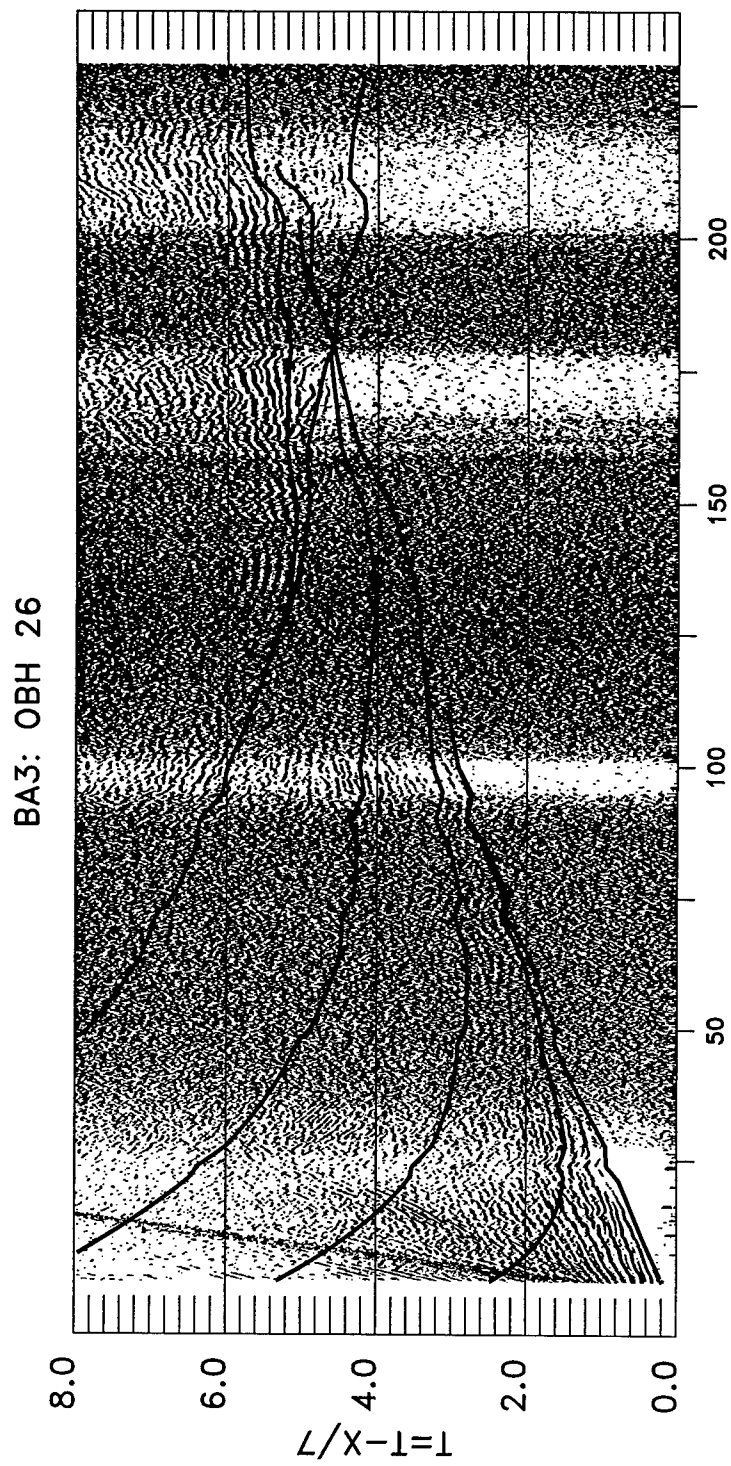
Figure 5.1

Cenozoic Magmatic Belts

Alaska Range - Talkeetna Mts (50-75 Ma)

Yukon-Kanuti Belt (65-56 Ma)

Kuskokwim Mts (72-60 Ma)

TACT Seismic Lines

Pre-Cenozoic Terranes

Peninsular Terrane

Chugach Terrane

Togiac Terrane

Kahiltna Terrane

Relic Kula Plate
Oceanic Crust

200 m

Beringian Margin

Unimak Pass

Umnak Is.

Sanak Is.

Aleutian Trench

Figure 5.2

Figure 5.3

BA3: OBH 26

T=T−X/7

Figure 5.4a

BA3: OBH 23

T=T−X/7

Figure 5.4b

BA3: OBS C3

$T = T - X/7$

Figure 5.4c

BA3: OBH 25

T=T-X/7
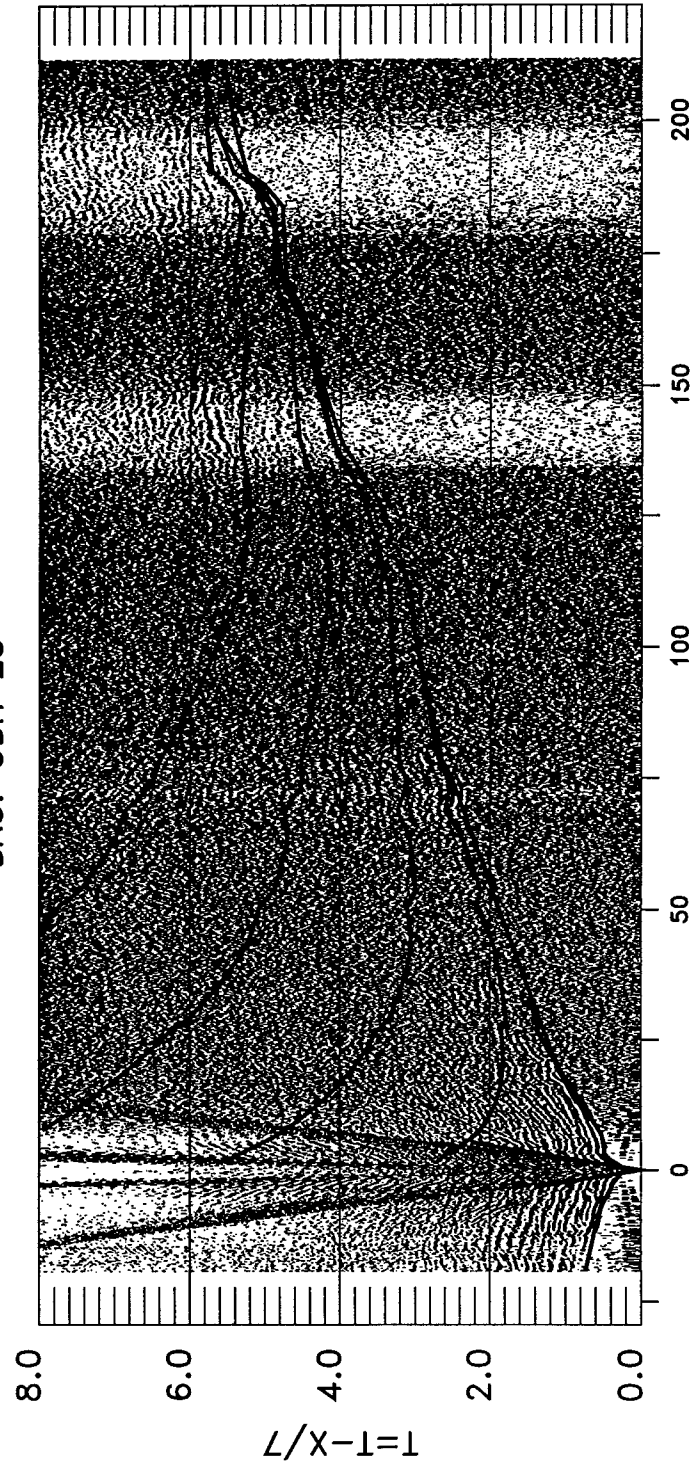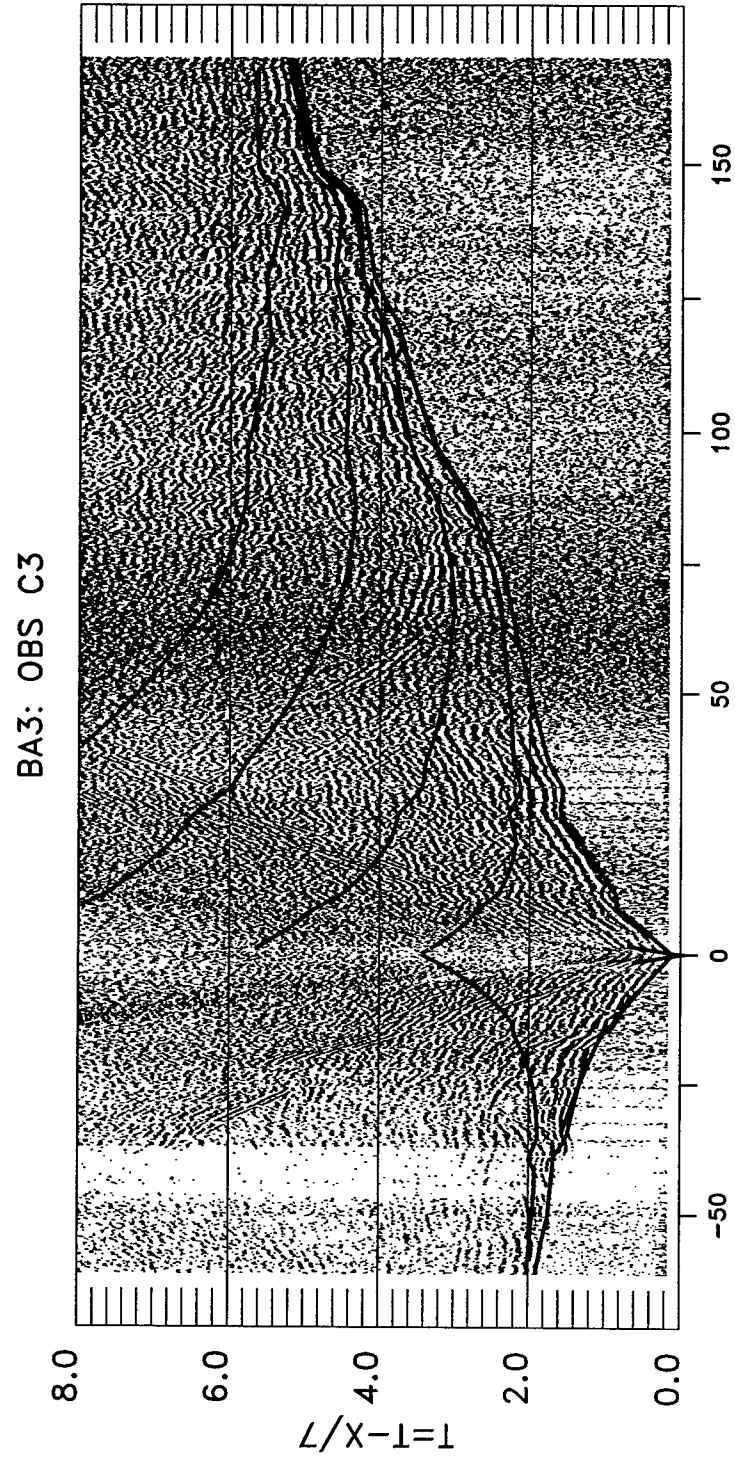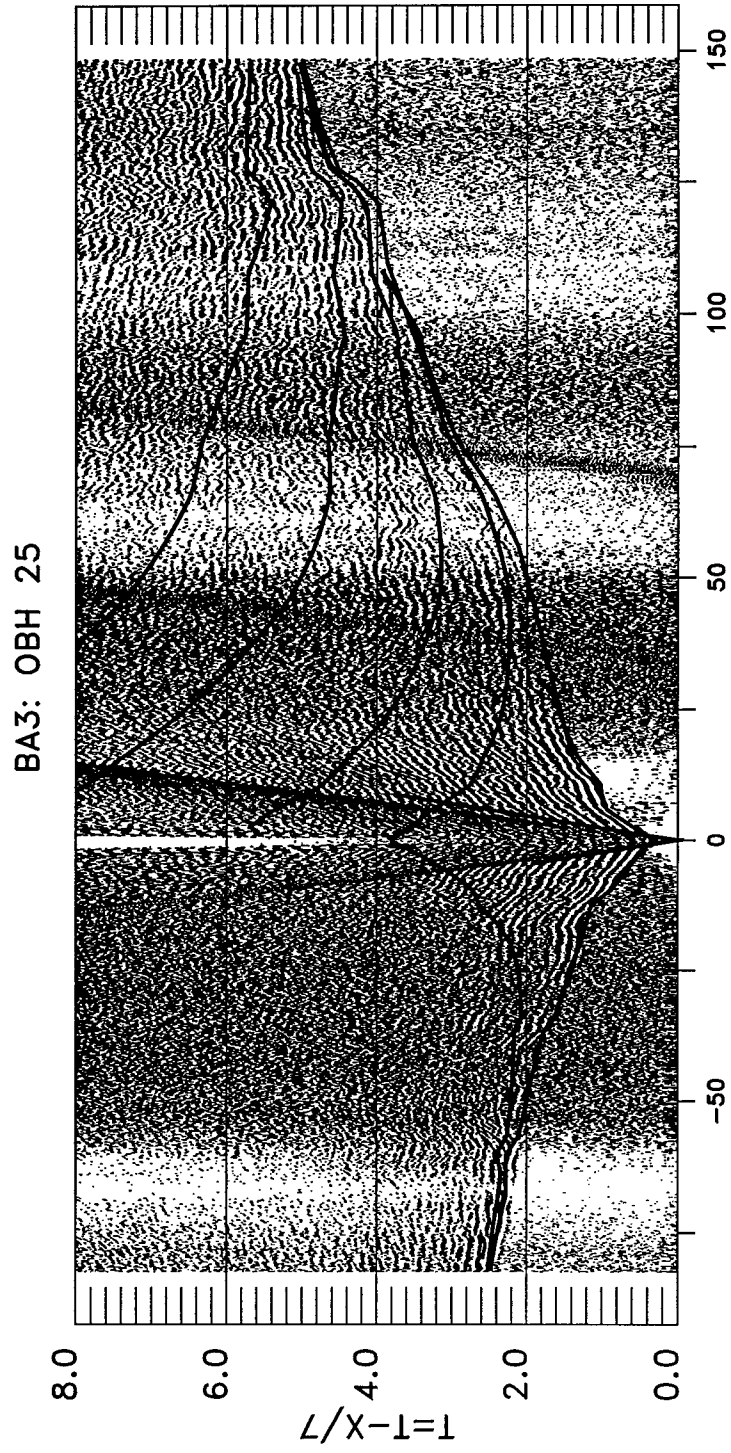
Figure 5.4d

BA3: OBH 22

T=T-X/7
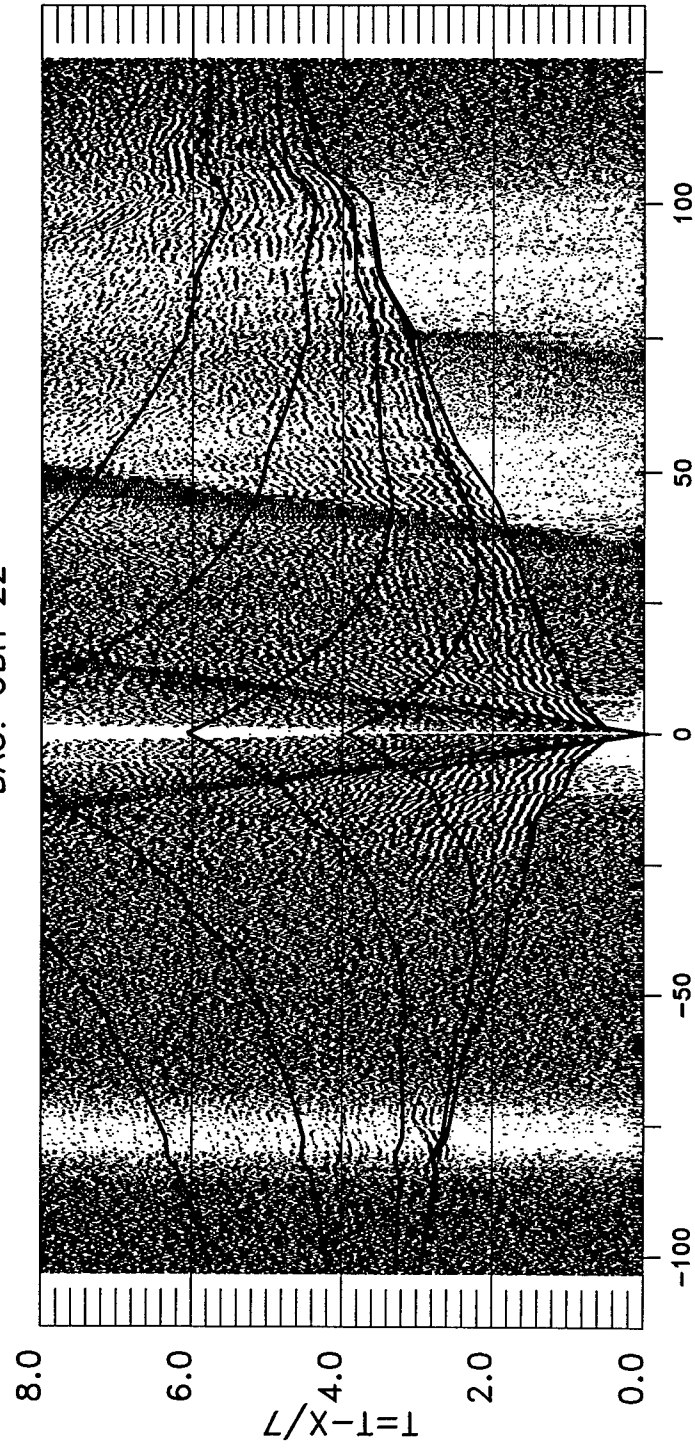
Figure 5.4e

BA3: OBH 27

Figure 5.4f

BA3: OBH 20

T=T-X/7

Figure 5.4g

BA3: OBS A1

Figure 5.4h

T=T−X/7
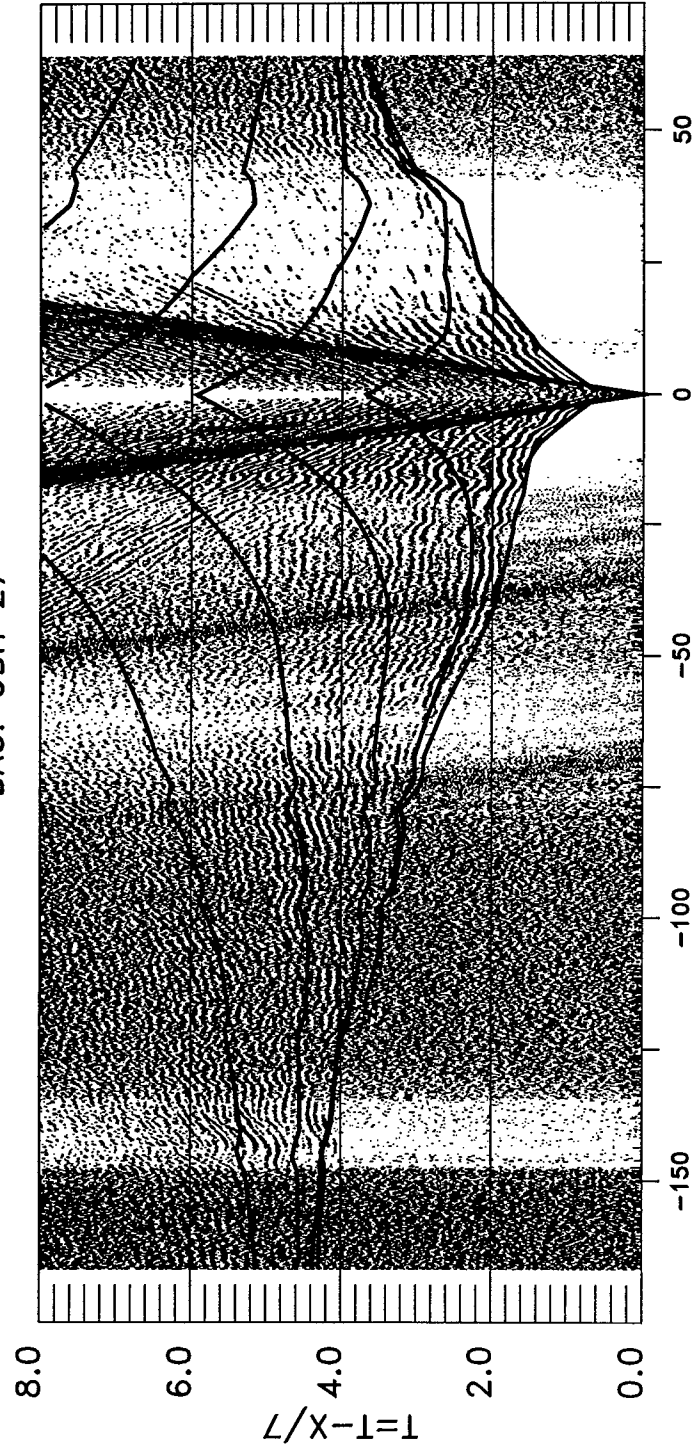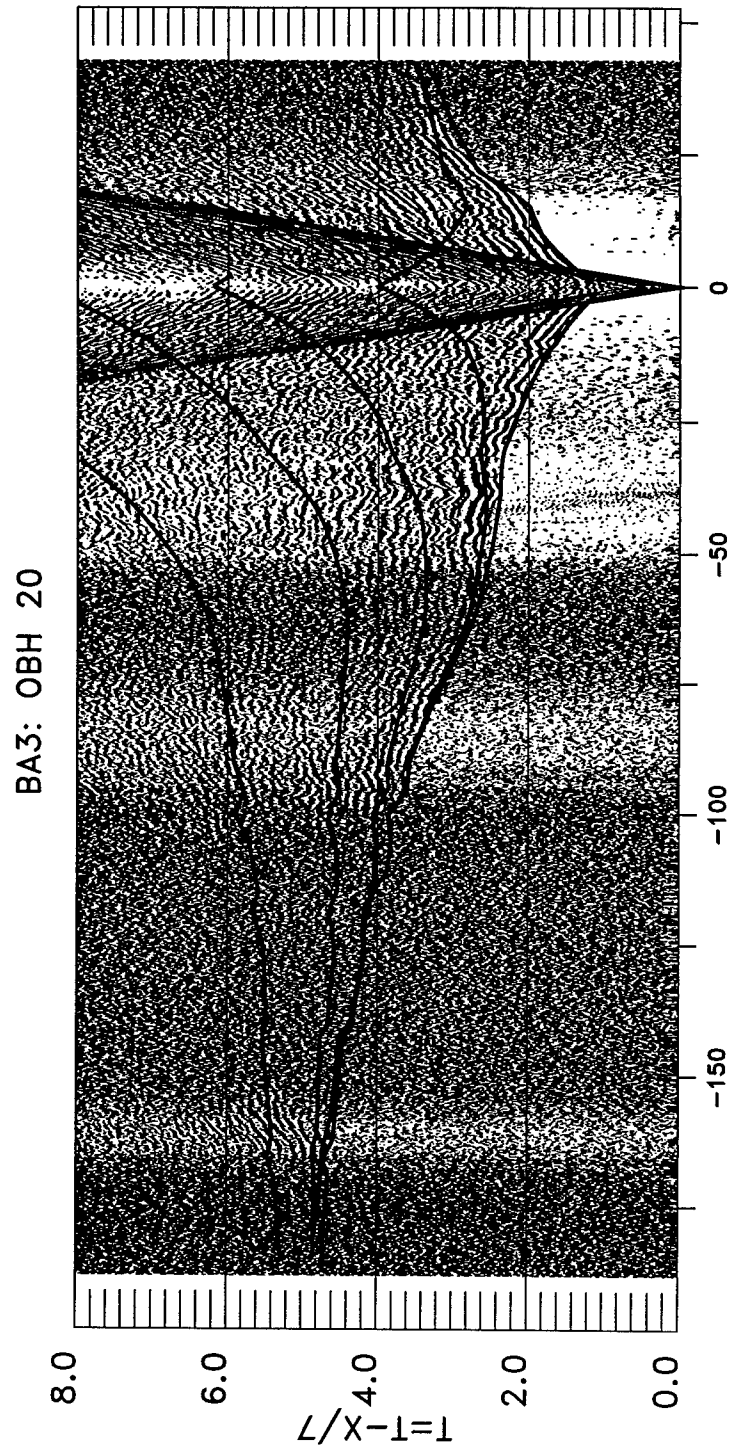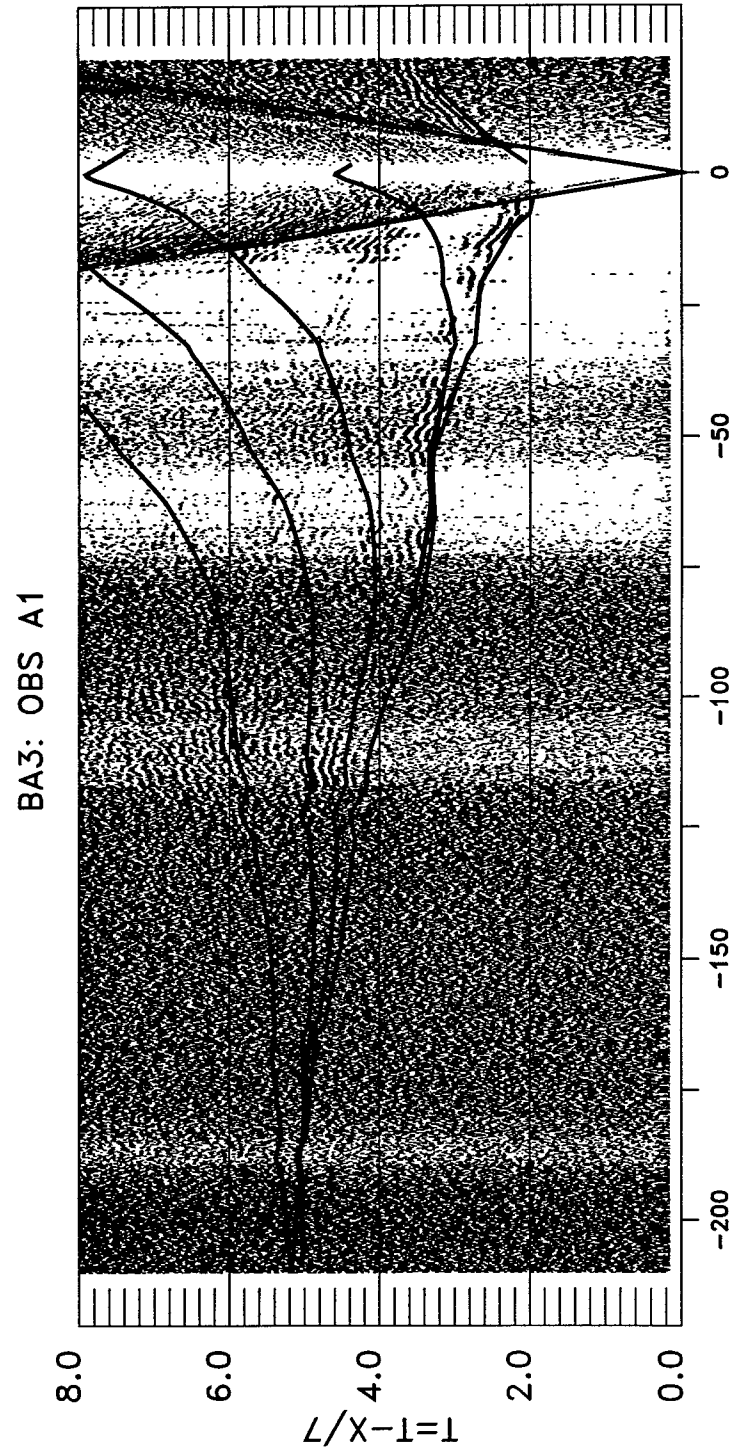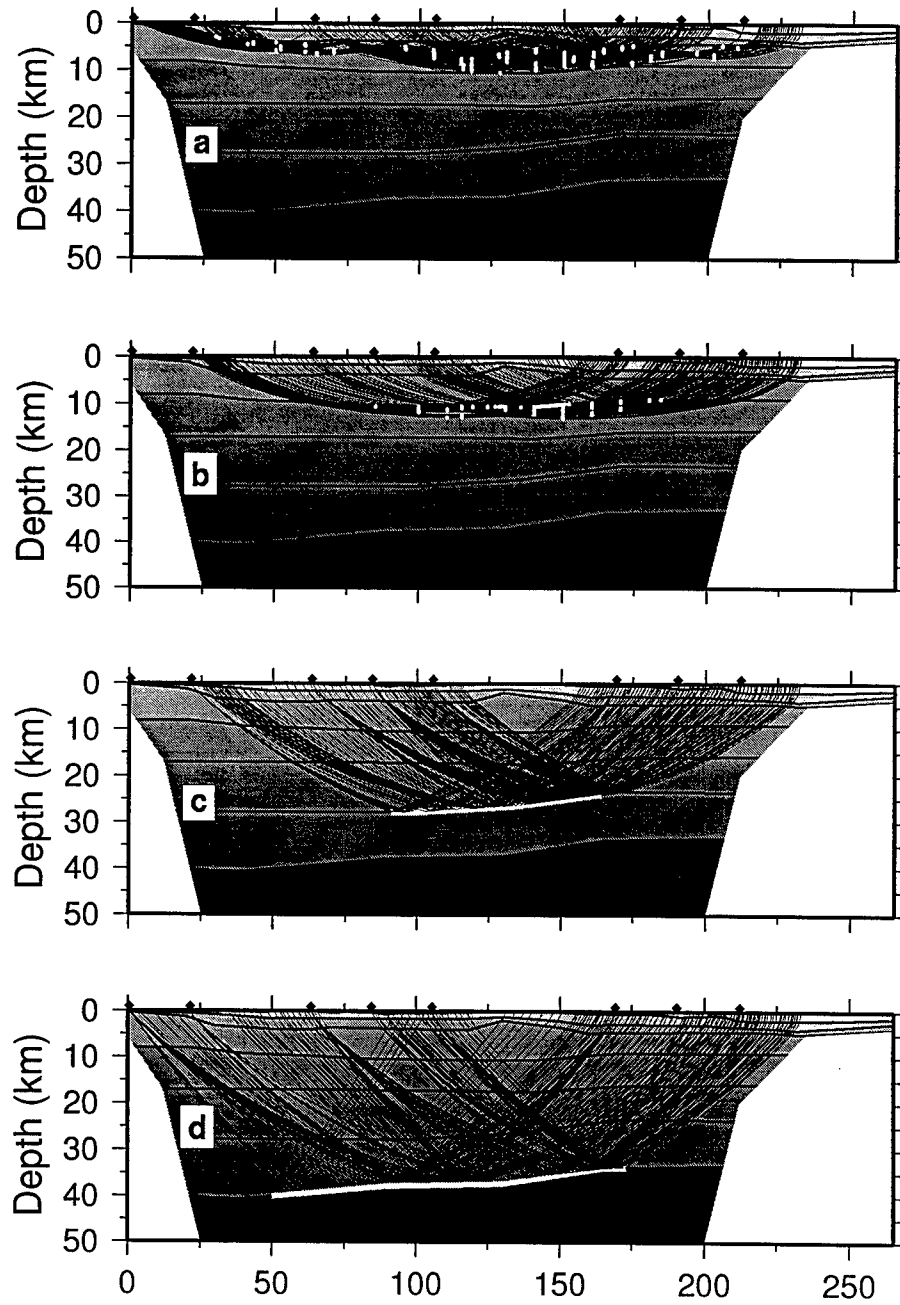
Figure 5.5

BA-3 Lat Cons Vel LC
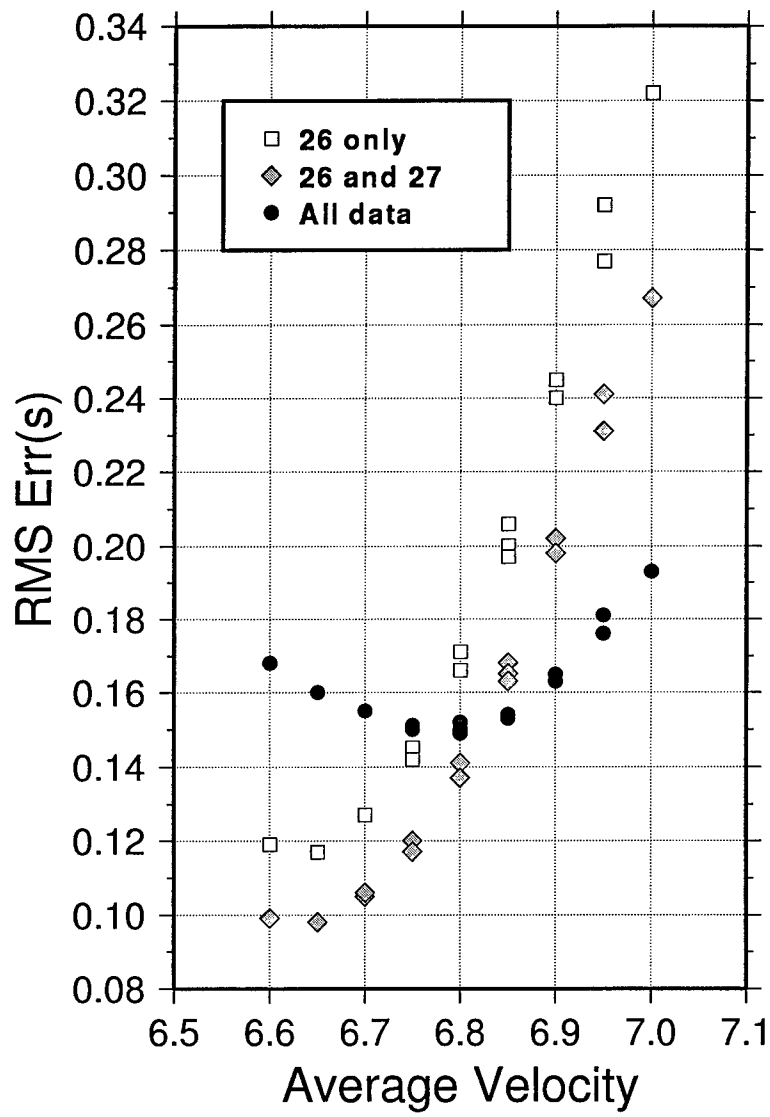
Figure 5.6
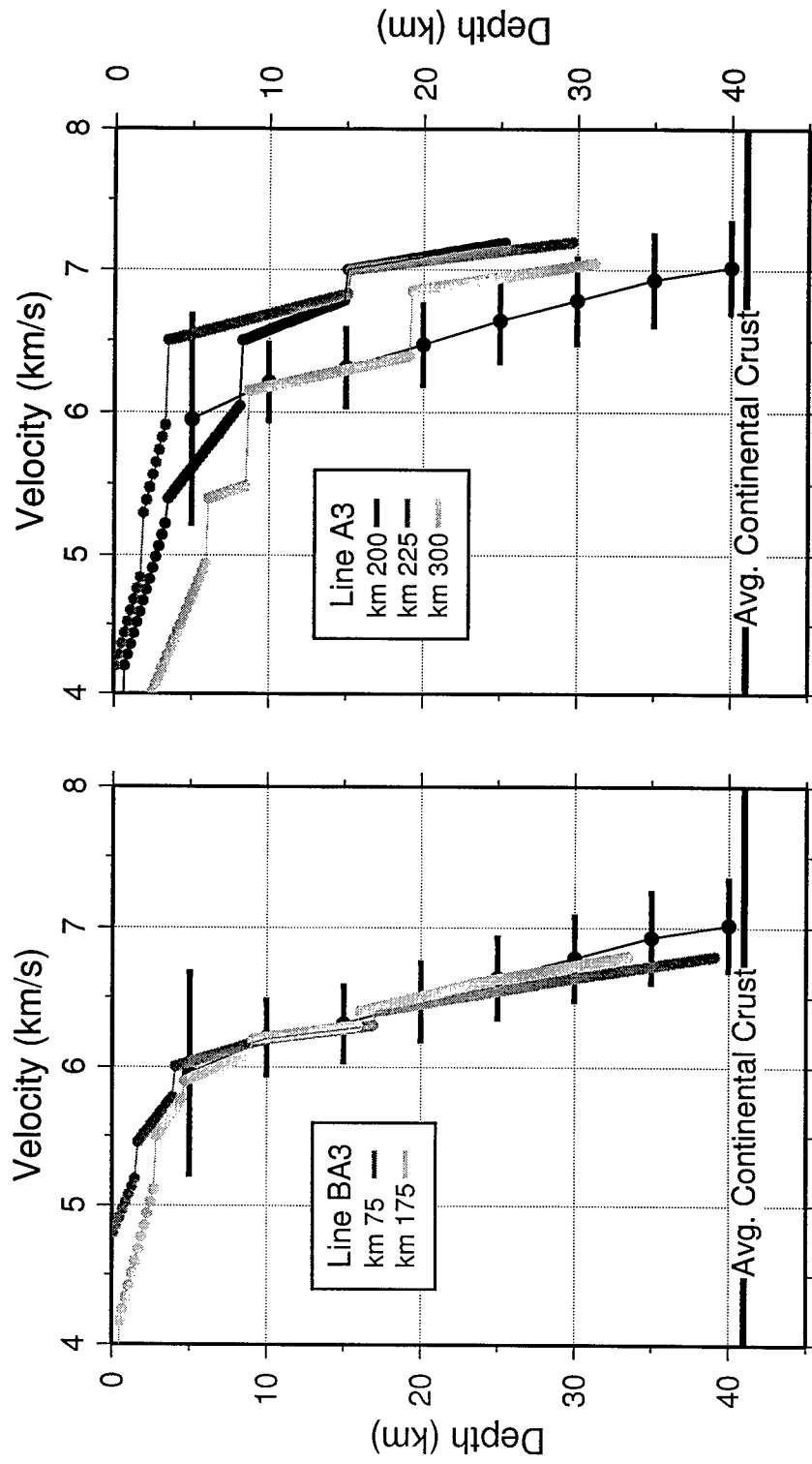
Figure 5.7

University of California, San Diego
SIO Library 0175C
9500 Gilman Drive
La Jolla, CA 92093-0175

Hancock Library of Biology & Oceanography
Alan Hancock Laboratory
University of Southern California
University Park
Los Angeles, CA 90089-0371

Gifts & Exchanges
Library
Bedford Institute of Oceanography
P.O. Box 1006
Dartmouth, NS, B2Y 4A2, CANADA

Commander
International Ice Patrol
1082 Shennecossett Road
Groton, CT 06340-6095

NOAA/EDIS Miami Library Center
4301 Rickenbacker Causeway
Miami, FL 33149

Research Library
U.S. Army Corps of Engineers
Waterways Experiment Station
3909 Halls Ferry Road
Vicksburg, MS 39180-6199

Institute of Geophysics
University of Hawaii
Library Room 252
2525 Correa Road
Honolulu, HI 96822

Marine Resources Information Center
Building E38-320
MIT
Cambridge, MA 02139

Library
Lamont-Doherty Geological Observatory
Columbia University
Palisades, NY z10964

Library
Serials Department
Oregon State University
Corvallis, OR 97331

Pell Marine Science Library
University of Rhode Island
Narragansett Bay Campus
Narragansett, RI 02882

Working Collection
Texas A&M University
Dept. of Oceanography
College Station, TX 77843

Fisheries-Oceanography Library
151 Oceanography Teaching Bldg.
University of Washington
Seattle, WA 98195

Library
R.S.M.A.S.
University of Miami
4600 Rickenbacker Causeway
Miami, FL 33149

Maury Oceanographic Library
Naval Oceanographic Office
Building 1003 South
1002 Balch Blvd.
Stennis Space Center, MS, 39522-5001

Library
Institute of Ocean Sciences
P.O. Box 6000
Sidney, B.C. V8L 4B2
CANADA

National Oceanographic Library
Southampton Oceanography Centre
European Way
Southampton SO14 3ZH
UK

The Librarian
CSIRO Marine Laboratories
G.P.O. Box 1538
Hobart, Tasmania
AUSTRALIA 7001

Library
Proudman Oceanographic Laboratory
Bidston Observatory
Birkenhead
Merseyside L43 7 RA
UNITED KINGDOM

IFREMER
Centre de Brest
Service Documentation - Publications
BP 70 29280 PLOUZANE
FRANCE

50272-101

REPORT DOCUMENTATION PAGE	1. REPORT NO. MIT/WHOI 97-24	2.	3. Recipient's Accession No.

4. Title and Subtitle

Crustal Structure of Rifted and Convergent Margins:

The U.S. East Coast and Aleutian Margins

5. Report Date June 1997	
6.	

7. Author(s) Daniel Lizarralde

8. Performing Organization Rept. No.

9. Performing Organization Name and Address

MIT/WHOI Joint Program in Oceanography/Applied Ocean Science & Engineering

10. Project/Task/Work Unit No.
MIT/WHOI 97-24

11. Contract(C) or Grant(G) No.

(C) OCE-89-17599;
OCE-89-17628; OCE-93-45401

(G) OCE-92-16128; OCE-94-01374
OCE-95-03134; EAR-92-18851

12. Sponsoring Organization Name and Address

National Science Foundation

13. Type of Report & Period Covered

Ph.D. Thesis

14.

16. Abstract (Limit: 200 words)

Processes that create and modify continental crust occur at continental margins. We investigate the crustal structure across the U.S. East Coast rifted margin and the convergent margin of Alaska using modern marine seismic techniques. Rifting of the U.S. East Coast margin was characterized by voluminous volcanism. We constrain the landward extent of crustal extension and rift magmatism to within a narrow region beneath the shelf and slope. The crust thinned here by 50-80% and then spreading began. Constraints from seismic imaging show that initial volcanism was accompanied by rapid margin subsidence, suggesting a limited and finite mantle source for the volcanics.

We study the evolution of continental crust through terrane accretion and arc magmatism along transects across the Alaska Peninsula, where subduction occurs beneath accreted oceanic-arc crust, and across older Bristol Bay crust. The velocity structure of the Peninsular accreted terranes is similar to intraoceanic-arc crust and more mafic than continental crust. Accretion has apparently not modified the terranes' composition. The Bristol Bay crust is also composed of accreted oceanic-arc terranes but has a continental velocity structure. If this crust was originally more mafic, then both crustal thickening and removal of a mafic component are required to explain its current structure—processes consistent with the region's history.

17. Document Analysis   a. Descriptors

Crust

Margins

Seismology

b. Identifiers/Open-Ended Terms

c. COSATI Field/Group

18. Availability Statement	19. Security Class (This Report) UNCLASSIFIED	21. No. of Pages 234
Approved for publication; distribution unlimited.	20. Security Class (This Page)	22. Price

(See ANSI-Z39.18)   *See Instructions on Reverse*

OPTIONAL FORM 272 (4-77)
(Formerly NTIS-35)
Department of Commerce